University of Alberta

Characteristics of Turbulence Energy Dissipation and Liquid-Liquid Dispersions in An Agitated Tank

by

Genwen Zhou 

A thesis

submitted to the Faculty of Graduate Studies and Research

in partial fulfillment of the requirements for the degree of

Doctor of Philosophy

Department of Chemical Engineering

Edmonton, Alberta

Spring 1997

University of Alberta

Library Release Form

NAME OF AUTHOR: Genwen Zhou

TITLE OF THESIS: Characteristics of Turbulence Energy Dissipation and Liquid-Liquid Dispersions in An Agitated Tank

DEGREE: Doctor of Philosophy

YEAR THIS DEGREE GRANTED: 1997

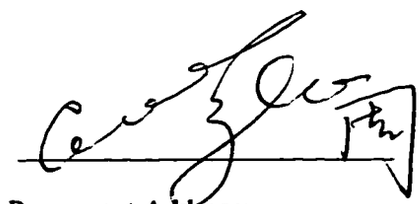

Permanent Address:
c/o: Dr. S. M. Kresta
Department of Chemical Engineering
University of Alberta
Edmonton, Alberta
Canada, T6G 2G6

Date: October 25, 1996

University of Alberta

Faculty of Graduate Studies and Research

The undersigned certify that they have read, and recommend to the Faculty of Graduate Studies and Research for acceptance, a thesis entitled Characteristics of Turbulence Energy Dissipation and Liquid-Liquid Dispersions in An Agitated Tank submitted by GENWEN ZHOU in partial fulfillment of the requirements for the degree of DOCTOR OF PHILOSOPHY.

S. M. Kresta (supervisor)

J. H. Masliyah

S. L. Shah

J. Yokota

P. A. J. Mees

William McCaffrey FOR R.V. Calabrese
R. V. Calabrese (external examiner)

Date: October 10, 1996

To my parents and to Lingling and Brian

Abstract

This thesis covers two major fields in mixing: turbulence energy dissipation and liquid-liquid dispersions in agitated tanks. The main objective of the thesis was to examine the effect of tank and impeller geometry on these variables.

The average turbulence energy dissipation in the impeller regions was investigated for three impellers (the Rushton turbine (RT), the pitched blade turbine (PBT) and the fluidfoil turbine (A310)) using the macroscopic mechanical energy equation. The majority of the input power is dissipated in the small volume of the impeller region for all three impellers. Analysis of the distribution of energy between convective and turbulent flow shows that the A310 is the most efficient at generating convective flow; the RT generates the most turbulence kinetic energy and the PBT derives a large portion of its energy from the return flow.

The equation ($\varepsilon=Av^3/L$), used to estimate the local turbulence energy dissipation rate, was verified by comparing local and integral methods. Here v is a fluctuating velocity; A is a constant and L is macroscale length. The effect of tank geometry (number of baffles (N_b), impeller diameter (D), and off bottom clearance (C or C/D)) on ε_{max} was investigated using three factorial designs for four impellers (PBT, A310, HE3 and RT). The dominant variable was shown to be the impeller diameter. This effect is in addition to the expected scaling with D^2. Clearance is also an important variable, which is best quantified by its dimensionless form, C/D. The number of baffles has no significant effect on ε_{max}.

Silicone oil/water dispersions were also studied with varying tank geometries. The shape of the drop size distribution changes with rotational speed (N). Four characteristic distributions were found; in order of increasing N: long tail, double peak, skew, and skew-normal distribution. Two normal distributions can be combined to represent the last three distributions. The Kolmogoroff length scale (η) cannot be used as an estimate of the minimum drop size present in the dispersions investigated. The cumulative number probability density less than η is negatively correlated with ε_{max}. The Sauter mean diameter (d_{32}) is more closely correlated to ε_{max} and the interaction of ε_{max} with the mean flow than to $P/\rho V_T$. A new correlation for d_{32} is proposed.

Acknowledgments

I would like to take this opportunity to express my deep gratitude to my supervisor Dr. S. Kresta for her guidance, support and encouragement throughout my Ph.D. program. Her inspiration and kindness made my Ph.D. program an enjoyable, learning experience. Her master-touch on every draft of the manuscript has contributed immensely to this thesis.

I would like sincerely to thank Drs. J. H. Masliyah, R. E. Hayes and K. Nandakumar for their advice and teaching throughout my stay at the University of Alberta. I would also like to thank Dr. R. Calabrese for his kindly serving as the external examiner and sharing his insightful ideas in mixing science and technology. Dr. J. Yokota from Department of Mechanical Engineering is gratefully acknowledged for his critical review of this thesis as my outside-department committee member. My appreciation is extended to Drs. S. L. Shah and P. Mees for their careful reading of this thesis and suggestions for its improvement.

All the support staff members are appreciated for making this department like home. Among those I would like to most honorably mention are Cindy Heisler, Walter Boddez and Bob Barton.

The Syncrude Research and the Natural Science and Engineering Research Council of Canada (NSERC) provided financial support for this research. Drs. B. Tipman and J. Spence from Syncrude Research are gratefully acknowledged for their suggestions during this project.

My deep appreciation goes to my wife, Lingling, and my son, Brian, for their encouragement, support and love at all times.

Table of Contents

Content		Page
Chapter 1	Introduction	1
References		6
Chapter 2	Literature Review - Flow Characteristics in Agitated Tanks	7
2.1	Introduction	7
2.2	Geometric variables	7
2.2.1	Classification of Impellers	7
2.2.2	Geometry of Impellers	8
2.2.3	Geometry of An Agitated Tank	9
2.3	Characteristics of the Flow Generated by Different Impellers	9
2.3.1	Mean and Fluctuating Velocities and Pressure	10
2.3.2	Methods of Studying Flow Characteristics	11
2.3.3	General Flow Characteristics	12
2.3.3.1	The Propagation of Turbulence with Increase of Reynolds Number	13
2.3.3.2	Effect of Baffles on the Flow	13
2.3.3.3	Characteristics of the Vortices in Agitated Tanks	14
2.3.3.4	Local Isotropy of the Flow in the Impeller and Impeller Discharge Region	16
2.3.3.5	Velocity Profiles for the Radial Flow Impeller (RT)	16
2.3.3.6	Flow Fields for the Axial Flow Impeller (PBT)	17
2.4	Dimensionless Groups	19
2.4.1	Reasons and Ways	19
2.4.2	Variables Affecting Fluid Motion	20
2.4.3	Important Dimensionless Groups	20
2.4.3.1	Reynolds Number and Froude Number	20
2.4.3.2	Power Number	21
2.4.3.3	Weber Number	21
2.4.4	Power Characteristics of Mixing Impellers	22
2.5	Turbulence Energy Spectrum and Turbulence Energy Dissipation Characteristics	23
2.5.1	Turbulence Energy Spectrum	24
2.5.2	Relative Velocity in Local Isotropic Turbulence	29
2.5.3	Experimental Investigations of Turbulence Energy Dissipation Characteristics	31
2.5.3.1	Average Energy Consumption	31
2.5.3.2	Local Turbulence Energy Dissipation	32

Tables		40
Figures		43
References		46
Chapter 3	Literature Review - Mechanisms of Drop Breakup and Mean Drop Size	52
3.1	Introduction	52
3.2	The Mechanisms of Drop Breakup	52
3.2.1	Deformation and Breakup of Drops	52
3.2.2	Force (or Energy) Balance during Drop Breakup and Coalescence	54
3.3	Correlations for the Mean Drop Size and the Characteristics of Drop Size Distribution	58
3.3.1	Measuring Methods	60
3.3.2	Correlations for Mean Drop Diameter	61
3.3.3	Drop Size Distributions in Agitated Tanks	62
3.4	The Scope of This Study	63
Tables		66
Figures		71
References		72
Chapter 4	Validation of the Experimental Equipment	75
4.1	Introduction	75
4.2	The Laser Doppler Technique	76
4.2.1	The Basic Principles of LDA	76
4.2.2	Measurement of the Doppler Shift	78
4.2.3	The Process of Velocity Measurement	78
4.3	The LDA	80
4.4	Validation of Experimental Data	84
4.4.1	Dimensionless Variables and the Measuring Traverses and Volume	85
4.4.2	Reproducibility of Experimental Data	85
4.4.3	Symmetry of the Flow Field	86
4.4.4	Comparison of Experimental Data with Those of Previous Investigators	86
4.4.5	Mass Conservation	86
4.5	Conclusion	87
Tables		88
Figures		89
References		100

Chapter 5	Turbulence Energy Dissipation in the Impeller Regions	101
5.1	Derivation of the Macroscopic Mechanical Energy Balance Equation	101
5.1.1	Introduction	101
5.1.2	Derivation	101
5.2	Methods Used by Previous Investigators to Estimate the Average and Local Dissipation Rates	110
5.2.1	Previous Measurements of the Average Dissipation	110
5.2.2	Previous Estimates of the Local Dissipation	112
5.3	Experimental Determination of the Turbulence Energy Dissipation Rates in the Impeller Regions	114
5.3.1	Apparatus	114
5.3.2	Methods	115
5.4	Results	118
5.4.1	Comparison of the Local and Integral Methods	118
5.4.2	Comparison of the Three Impellers	119
5.5	Conclusions	123
Tables		125
Figures		128
References		134
Chapter 6	Impact of Tank Geometry on the Maximum Turbulence Energy Dissipation Rate	136
6.1	Introduction	136
6.2	Experimental	138
6.2.1	The LDA	138
6.2.2	Geometry of the Baffled Tank and the Impellers	138
6.2.3	Experimental Design	138
6.2.3.1	Rotational Speed	139
6.2.3.2	Factorial Design in N_f, D and C	139
6.2.3.3	Factorial Design in N_f, D and C/D	139
6.3	Results	140
6.3.1	Determination of the Location of ε_{max}	140
6.3.2	Effect of Rotational Speed on ε_{max}	142
6.3.3	Range of Variation in Scaled ε_{max}	142
6.3.4	Effect of Tank Geometry on ε_{max}	143
6.3.4.1	Criteria Used to Evaluate the Statistical Significance of the Effects	144
6.3.4.2	Discussion of Significant Effects	145
6.4	Conclusions	151
Tables		153

Figures		161
References		177
Chapter 7	Particle Size measurement Using the Phase Doppler Particle Analyzer	178
7.1	Introduction	178
7.2	Phase Doppler Particle Analyzer	178
7.2.1	Interference Behavior of a Droplet	179
7.2.2	Geometric Optics Approach	179
7.2.3	Optical Configuration of a PDPA	180
7.2.4	Experimental Parameters	181
7.3	Choice of Fluids and Tank Material	183
7.4	Validation of PDPA Size Measurement	187
7.4.1	PDPA Size Measurement Using Standard Particles	187
7.4.2	Repeatability of the Instrument and of the Experiment	188
7.4.2.1	Volume Fraction of Silicone Oil	189
7.4.2.2	Repeatability of the Instrument and Sample Size	189
7.4.2.3	Rinse Procedure and Repeatability of the Experiment	190
7.4.3	Feasibility of Using a Step-Change in N	191
7.4.3.1	Equilibrium Time of the Silicone Oil/Water Dispersion	191
7.4.3.2	Effect of a Step-Change in N	193
7.5	Conclusions	193
Tables		195
Figures		202
References		208
Chapter 8	Characterization of Liquid-Liquid Dispersions	209
8.1	Experimental Design	210
8.1.1	Impellers and Tank Geometry	210
8.1.2	Measurement Locations	211
8.1.3	Experimental Parameters and Procedure	212
8.2	Preliminary Experiments to Investigate the Effect of the Extra Water Layer and Oil Addition on the Flow Field	213
8.2.1	Effect of an Extra Water Layer on the Flow Field	213
8.2.2	Effect of Oil Addition on the Flow Field	214
8.3	Drop Size Distributions	215
8.3.1	Drop Size Distributions Proposed by Previous Researchers	215
8.3.2	Changes in the Drop Size Distribution with Increasing Rotational Speed	218
8.3.3	Characterization of the Drop Size Distribution Using Two	222

	Superimposed Normal Distributions	
8.3.4	**Conclusions about the Drop Size Distribution**	224
8.4	**Minimum Drop Size**	225
8.4.1	**Kolmogoroff Length Scale**	225
8.4.2	**Experimental Results of the Minimum Drop Size**	227
8.4.3	**Correlation of F(η)with Flow Field and with Drop Size Distribution**	229
8.4.4	**Conclusions about the Minimum Drop Size**	230
8.5	**Sauter Mean Diameter**	231
8.5.1	**d_{max} in the Turbulent Flow in Agitated Tanks**	232
8.5.2	**Relationship between d_{32} and d_{max}**	233
8.5.3	**Scaleup of Geometrically Similar Dispersion Systems**	235
8.5.4	**Conclusions about the Sauter Mean Diameter**	239
8.6	**Summary**	239
Tables		241
Figures		250
References		276
Chapter 9	Synthesis	278
References		284
Appendix-1	Drop size distribution data	285
Appendix-2	Cumulative number probability density data	299
Appendix-3	Parameters of the regression for each case	313
Appendix-4	Viscosity of silicone oil	315

List of Tables

Table		Page
2-1	Power numbers for the Rushton turbine.	40
2-2	Values of the constant (from Kresta and Wood, 1993b).	41
2-3	Values of the constant (L is set to D/10).	42
3-1	Correlations for mean drop diameter in liquid-liquid mixing tanks.	66
4-1	Geometric and operating variables of the impeller and the baffled tank in the experiments used to optimize the LDA parameters.	88
4-2	Geometric and operating variables for volume conservation	88
5-1	Experimental conditions and selected results for the three impellers.	125
5-2	Comparison of the two methods for the impeller discharge stream. All results are based on unscaled data.	126
5-3	Distribution of power between convective terms, turbulent fluctuations and dissipation.	127
6-1	Experimental Design and Results-PBT.	153
6-2	Experimental Design and Results-A310.	154
6-3	Experimental Design and Results-HE3.	155
6-4	Experimental Design and Results-RT.	156
6-5	Calculated effects of geometric variables and interactions on ε_{max}/N^3D^2 for the factorial design based on N_f, D and C.	157
6-6	Calculated effects of geometric variables and interactions on ε_{max}/N^3D^2 for the factorial design based on N_f, D and C/D.	158
6-7	Calculated effects of geometric variables and interactions on ε_{max} for the factorial design based on N_f, D and C/D.	159
6-8a	95% confidence intervals calculated from ε_{max}/N^3D^2 values for the 5 runs with varying N.	160
6-8b	95% confidence intervals calculated from ε_{max} values for the 5 runs	160

with varying N.

7-1 Diameter measurement ranges. 195

7-2 Physical properties and operating parameters of the dispersion systems used by previous investigators. 196

7-3 Experimental results with standard polystyrene particles. 200

7-4 Repeatability of the PDPA instrument. 200

7-5 Repeatability of the experiment 200

7-6 Time evolution of mean drop size, d_{32}. 201

7-7 Step-change measurement of mean drop size, d_{32}. 201

8-1 Cases investigated. 241

8-2 Mean drop size at different radial traverses. 241

8-3 Sampling points for mean drop size measurements. 242

8-4 Maximum turbulence energy dissipation rates (no extra water layer). 243

8-5 List of d_{10}, $\sigma(d)$, d_{20}, d_{30}, η and $F(\eta)$ at different rotational speeds. 244

8-6 Constant (c) values in the equation $d_{32}=c \cdot d_{max}$ obtained by previous investigators. 246

8-7 Constant (c) values in the equation $d_{32}=c \cdot d_{max}$ obtained in this work. 247

8-8 Values of the exponent of D in typical correlations of d_{32} if D is considered as an independent variable. 248

8-9 Sauter mean drop sizes at different rotational speeds for the four impellers. 249

List of Figures

Figure		Page
2-1	Schematic drawings of the three impellers-PBT, A310 and RT.	43
2-2	Geometry of the stirred tank (T=0.240 m, H=T).	43
2-3	Schematic three dimensional view of the trailing vortex pair produced by the RT (from Van't Riet and Smith, 1975).	44
2-4	Schematic drawing of the second circulation loop created by the PBT (from Kresta, 1993).	44
2-5	General flow patterns for the PBT, A310 and RT.	45
2-6	Form of the three-dimensional energy spectrum function E(k,t) in the various wavenumber ranges (from Hinze, 1975).	45
3-1	The two common breakup mechanisms in liquid dispersion	71
4-1	LDA measuring volume as envisioned by the fringe interpretation (from George, 1988).	89
4-2	Optical orientations for the determination of three components of velocity as defined in cylindrical coordinates (from Kresta, 1991).	90
4-3	The importance of proper alignment of the laser beams (from Hanson, 1974).	91
4-4	"Thumb" diagram showing the velocity component (from Kresta, 1991).	92
4-5	Arrangement of laser Doppler anemometer.	92
4-6	Axial velocity measurements using three tracks.	93
4-7	Axial velocity measurements with varying voltages.	93
4-8	Axial velocity measurements with varying signal sampling frequencies.	94
4-9	Axial velocity measurements with varying sample time.	94
4-10	Axial velocity measurements with varying sampling size.	95
4-11	The measuring traverses and control volume for mass conservation.	95
4-12	Reproducibility of the data (left side of upper edge).	96
4-13	Reproducibility of the data (left side of lower edge).	96
4-14	Symmetry of the flow at the upper edge of the impeller blades.	97
4-15	Symmetry of the flow at the lower edge of the impeller blades.	97
4-16	Symmetry of the flow at the tip of the impeller blades.	98
4-17	Comparison of experimental data with Kresta's data.	99
5-1	A control volume in an agitated tank in cylindrical coordinates (r, θ, z).	128
5-2	The three impellers studied, with tuft visualization of the trailing vortices at the blade tip.	128
5-3	The control volumes and local dissipation traverses for the three impellers.	129
5-4a	Axial profiles of mean and fluctuating velocities at r=63 mm for the RT.	130
5-4b	Radial profiles of mean and fluctuating velocities at z=10.5 mm for the	130

PBT.

5-4c Radial profiles of mean and fluctuating velocities at z=9.0 mm for the A310. 131

5-5a Comparison of the turbulence kinetic energy (q) calculated from 3 RMS velocities with q estimated from the radial RMS velocity, RT, tip of the impeller blades. 131

5-5b Comparison of the turbulence kinetic energy (q) calculated from 3 RMS velocities with q estimated from the axial RMS velocity, PBT, below the impeller blades. 132

5-5c Comparison of the turbulence kinetic energy (q) calculated from 3 RMS velocities with q estimated from the axial RMS velocity, A310, below the impeller blades. 132

5-6 Percent of the power dissipated, and average dissipation $\overline{\varepsilon_i}$ (m^2/s^3) calculated from the macroscopic energy balance for all control volumes. Units of the r and z are in mm. The results are based on equal power input 133

6-1 Schematic drawing of the stirred tank and the measuring traverses (- - - - -) used to locate ε_{max} for each of the four impellers. 161

6-2 Velocity profiles used to locate ε_{max}: 161

a) **PBT**; radial profiles of v_z.

b) **A310**; radial profiles of v_z. 162

c) **RT**; axial profiles of v_r. 162

6-3 Validation of the scaling of ε with N^3. 163

a) **PBT**; D=T/3, 2z/Wp=1.35.

b) **A310**; D=0.475T, 2z/Wp=1.30. 163

c) **HE3**; D=T/3, 2z/Wp=1.46. 164

d) **RT**; D=T/3, 2r/D=1.08. 164

6-4 Comparison of the scaled ε_{max}'s for all experiments. 165

6-5 Normal probability plots of the effects of geometric variables on ε_{max}/N^3D^2 showing the 95% confidence interval around zero effect for the factorial design based on N_f, D and C.

5a) **PBT** 166

5b) **A310** 166

5c) **HE3** 167

5d) **RT** 167

6-6 Profiles of ε/N^3D^2 showing the details of the experimental results for the factorial design based on N_f, D and C.

6a) **PBT** 168

6b) **A310** 168

6c) **HE3** 169

6d) **RT** 169

6-7 Normal probability plots of the effects of geometric variables on ε_{max}/N^3D^2 showing the 95% confidence interval around zero effect for the factorial design based on N_f, D and C/D.

7a) **PBT** 170

7b) **A310** 170

7c) **HE3** 171

7d) **RT** 171

6-8 Profiles of ε/N^3D^2 showing the details of the experimental results for the factorial design based on N_f, D and C/D.

8a) **PBT** 172

8b) **A310** 172

8c) **HE3** 173

8d) **RT** 173

6-9 Comparison of scaling based on constant power (closed symbols) vs. scaling based on constant ε_{max} (open symbols) when the impeller diameter is changed from D=T/2 to D=T/4. 174

6-10 Normal probability plots of the effects of geometric variables on ε_{max} showing the 95% confidence interval around zero effect for the factorial design based on N_f, D and C/D.

a) **PBT**; ε_{max}'s for the four cases with D=T/4 were divided by 8. 175

b) **A310**; ε_{max}'s for the four cases with D=0.375T were divided by 3.88. 175

c) **HE3**; ε_{max}'s for the four cases with D=T/4 were divided by 8. 176

d) **RT**; ε_{max}'s for the four cases with D=T/4 were divided by 8. 176

7-1 Ray trace for light incident on a spherical, transparent particle with an index of refraction higher than that of its surroundings. 202

7-2 The schematic of the scattering lobes for a spherical, transparent silicone oil droplet with a refractive index of 1.495. 202

7-3 Schematic of an Aerometrics PDPA optical configuration. 203

7-4 Particle and air bubble measurement in deionized ultra-filtered water.

4a) Largest diameter was set at 170 μm. 203

4b) Largest diameter was set at 50 μm 203

4c) air bubble measurement in deionized ultra-filtered water. 204

7-5 Size histogram measured in silicone oil/DIUF water dispersion. 204

7-6 Typical size histogram of standard particles.

6a) Particle size histogram (without sealing water). 205

6b) Particle size histogram (with sealing water). 205

7-7 Drop size distribution for the 4 runs with the same tank geometry and N measured on 4 consecutive days. 206

7-8 Equilibrium time for silicone oil/DIUF water dispersion. 207

	Step-change measurement: d_{32} vs time at varying N's.	207
8-1	Comparison of RMS velocities between the two cases with and without extra water layer when no silicone oil was added.	
	1a) HE3	251
	1b) PBT	251
8-2	Comparison of RMS velocities between the two cases with and without silicone oil when no extra water layer was added.	
	2a) HE3	252
	2b) PBT	252
8-3	Plots of drop size distributions at different rotational speeds for the case: A310: D=0.350T, C/D=1, 2r/D=0.50.	253
8-4	Plots of arithmetic mean drop sizes and standard deviations vs N's.	
	4a) A310: D=0.350T, C/D=1.	256
	4b) A310: D=0.350T, C/D=1/2.	256
	4c) A310: D=0.550T, C/D=1/2.	256
	4d) HE3: D=T/4, C/D=1.	257
	4e) PBT: D=T/4, C/D=1.	257
	4f) RT: D=T/4, C/D=1.	258
	4g) RT: D=T/4, C/D=1/2.	258
8-5	Comparison of experimental distribution and predicted distribution. A310. D=0.350T, C/D=1	
	5a) Double peak distribution	259
	5b) Skew distribution	259
	5c) Skew-normal distribution	260
8-6	Kolmogoroff length η vs turbulence energy dissipation rate ε	261
8-7	Plots of cumulative number probability density vs d at different rotational speeds. PBT, D=T/4, C/D=1, 2r/D=0.30.	261
8-8a	Plots of $F(\eta)$ vs N for all seven cases.	264
8-8b	Plots of $F(\eta)$ vs ND for all seven cases.	264
8-8c	Plots of $F(\eta)$ vs Re for all seven cases.	265
8-8d	Plots of $F(\eta)$ vs ε_{max} for all seven cases.	265
8-8e	Plots of $F(\eta)$ vs $P/\rho V_T$ for all seven cases.	266
8-9a	Plots of $F(\eta)$ vs d_{10} for all seven cases.	266
8-9b	Plots of $F(\eta)$ vs d_{30} for all seven cases.	267
8-9c	Plots of $F(\eta)$ vs d_{32} for all seven cases.	267
8-10a	Plots of $F(\eta)$ vs d_{30}/d_{10} for all seven cases.	268
8-10b	Plots of $F(\eta)$ vs d_{32}/d_{10} for all seven cases.	268
8-11a	Plots of the constant c vs N for all seven cases.	269
8-11b	Plots of the constant c vs ND for all seven cases.	269
8-11c	Plots of the constant c vs Re for all seven cases.	270

8-11d	**Plots of the constant c vs ε_{max} for all seven cases.**	270
8-11e	**Plots of the constant c vs $P/\rho V_T$ for all seven cases.**	271
8-12a	**Plots of Sauter mean diameter vs ND for all seven cases.**	271
8-12b	**Plots of Sauter mean diameter vs ε_{max} for all seven cases.**	272
8-12c	**Plots of Sauter mean diameter vs $P/\rho V_T$ for all seven cases.**	272
8-13	**Plot of Sauter mean diameter vs $\varepsilon_{max}\cdot(D/D_0)^2$ for the A310, D_0=0.350T**	273
8-14	**Plot of Sauter mean diameter vs $\varepsilon_{max}\cdot(D/D_0)^{-8/3}$ for the A310, D_0=0.350T**	273
8-15a	**Plots of Sauter mean diameter vs ($\varepsilon_{max}\cdot$ND) for all seven cases**	274
8-15b	**Plots of Sauter mean diameter vs ($\varepsilon_{max}\cdot ND^2$) for all seven cases**	274
8-15c	**Plots of Sauter mean diameter vs $\varepsilon_{max}\cdot(ND)^2$ for all seven cases**	275
8-16a	**Plots of Sauter mean diameter vs ($P/\rho V_T\cdot$ND) for all seven cases**	275
8-16b	**Plots of Sauter mean diameter vs ($P/\rho V_T\cdot ND^2$) for all seven cases**	276
8-16c	**Plots of Sauter mean diameter vs $P/\rho V_T\cdot(ND)^2$ for all seven cases**	276

Nomenclature

A, A'	constant	
A_a	total area around a control volume	(m^2)
A_e	area of entrances and exits around a control volume	(m^2)
$A(h_0)$	adhesion force	(kg m/s^2)
c	the constant in $d_{32}=c \cdot d_{max}$	(-)
$c, c_1, c_2, \ldots$	constant	
C	off bottom clearance	(m)
d	drop diameter	(μm)
d_{10}	arithmetic mean drop diameter	(μm)
d_{20}	area-mean drop diameter	(μm)
d_{30}	volume-mean drop diameter	(μm)
d_{32}	Sauter mean drop diameter	(μm)
D	impeller diameter	(m)
dA	area integration element	(m^2)
dr	integration element in r direction	(m)
dQ	volume integration element	(m^3)
dz	integration element in z direction	(m)
$E(k,t)$	energy spectrum function	(m^3/s^2)
$\dot{E}v$	total rate of viscous dissipation to internal energy in a control volume	(kg m^2/s^3)
F	adhesion force	(kg m/s^2)
f_D	Doppler shift frequency	(s^{-1})
$F(k,t)$	energy-transfer-spectrum function	(m^3/s^3)
$f_n(d)$	number probability density	(-)

$f_V(d)$	volumetric probability density	(-)
$F_n(d)$	Cumulative number probability density	(-)
Fr	Froude number, $\frac{DN^2}{g}$	(-)
g	gravity acceleration	(m/s^2)
H	liquid height	(m)
$\hat{I}$	unit tensor	(-)
k	wavenumber in **Chapter 2**	(m^{-1})
k	kinetic energy in **Chapter 6**	(m^2/s^2)
k_d	wavenumber corresponding to the maximum of energy spectrum in the range of energy-containing eddies	(m^{-1})
k_e	wavenumber corresponding to the main contribution to the total dissipation in energy spectrum	(m^{-1})
L	characteristic length	(m)
L_b	length of impeller blades	(m)
$\vec{n}$	unit normal vector of a surface	(-)
N	rotation speed of the impeller	(s^{-1})
N_b	number of blades	(-)
N_f	number of baffles	(-)
N_p	power number, $\frac{P}{\rho N^3 D^5}$	(-)
n_r, n_θ, n_z	components of $\vec{n}$ in r ,θ, z directions, respectively	(-)
N_{Vi}	viscosity group defined by Eq.(3-3)	(-)
p	pressure	(kg/s^2 m)
p'	fluctuating pressure	(kg/s^2 m)
$\overline{p}$	average pressure	(kg/s^2 m)

P	power input	(kg m^2/s^3)
q	kinetic energy	(m^2/s^2)
r	radial coordinate	(m)
r_1, r_2	radial coordinates	(m)
Re	Reynolds number, ND^2 / ν	(-)
$Re_{,\lambda}$	Reynolds number defined by Eq.(2-20)	(-)
$Re_{,L}$	Reynolds number defined by Eq.(2-21)	(-)
R_E	autocorrelation function defined in Eq.(2-46)	(-)
rms or RMS	root-mean-square of fluctuating velocity	(m/s)
t	time	(s)
$\bar{t}(n)$	stress vector defined by $\bar{t}_{(n)} = \bar{n} \bullet \hat{T}$	(kg/m s^2)
T	tank diameter	(m)
$\hat{T}$	stress tensor	(kg/m s^2)
u	Kolmogoroff's velocity scale	(m/s)
V_a	a control volume	(m^3)
V	instantaneous velocity	(m/s)
$\overline{V}$	average velocity	(m/s)
v'	fluctuating velocity	(m/s)
v	intensity of turbulence, or rms of fluctuating velocity	(m/s)
$\overline{V_r}, \overline{V_z}, \overline{V_\theta}$	radial, axial and tangential mean velocities, respectively	(m/s)
v'_r, v'_z, v'_θ	radial, axial and tangential fluctuating velocities, respectively	(m/s)
v_r, v_z, v_θ	rms of radial, axial and tangential fluctuating velocities, respectively	(m/s)

$\overline{V^2(r)}$ or $\overline{V^2(d)}$	mean-square of the relative velocity between two points	(m^2/s^2)
W	width of impeller blades	(m)
W_b	width of baffles	(m)
$\bar{W}$	velocity of moving control volume surface	(m/s)
$\dot{W}$	rate of the shaft work input to a control volume	$(kg\ m^2/s^3)$
We	Weber number, $\frac{\rho_c \overline{V^2(d)} d}{\sigma}$	(-)
We_T	Weber number in mixing tank, $\frac{\rho_c N^2 D^3}{\sigma}$	(-)
W_p	projected width of blades	(m)
x	component of spatial coordinates	(m)
z	axial coordinate	(m)
z_1, z_2	axial coordinates	(m)

Greek

ε	turbulence energy dissipation rate	(m^2/s^3)
$\bar{\varepsilon}$	mean energy dissipation rate	(m^2/s^3)
η	Kolmogoroff length	(m)
θ	tangential coordinate, or the angle between two beams	(°)
λ	wavelength of light	(m)
λ_g	microscale of turbulence	(m)
μ	absolute viscosity	(kg/m s)
ν	kinematic viscosity	(m^2/s)
σ	interfacial tension	(kg/s^2)

ρ	density	(kg/m^3)
ϕ	a scalar defined in Eq.(5-4)	(m^2/s^2)
	or volume fraction of dispersed phase	(-)
Φ	rate of conversion to thermal energy	
	per unit volume defined in Eq.(5-5)	($kg/m\ s^3$)
$\hat{\tau}$	viscous stress tensor	($kg/m\ s^2$)
τ	external forces	($kg/m\ s^2$)

Superscripts

–	vector
^	tensor

Subscripts

c	continuous phase
crit	critical value
d	dispersed phase
i,j	principal coordinates, r,θ,z.
max	maximum
min	minimum
r,θ,z	radial, tangential, axial coordinate in cylindrical coordinates

Abbreviation

LDA	laser Doppler anemometer
PDPA	phase Doppler particle analyzer
RT	the Rushton turbine
PBT	the pitched blade turbine
A310	the fluidfoil turbine
HE3	the high efficiency turbine

Chapter 1

Introduction

All chemical processing involves the mixing or interpenetrating of one substance with another. The mixing of immiscible liquids is among the most important chemical engineering operations and mechanically agitated tanks are very common industrial equipment for liquid-liquid dispersions. One of the important industrial parameters in transfer phenomena is the area per unit volume (a) in dispersions which is related with the Sauter mean diameter (d_{32}) and determined by drop size distribution: thus, research on the mechanisms of drop breakup and the effects of physical properties of fluids, of flow in agitated tanks and of tank geometries on liquid-liquid dispersions is of great significance and has been an active research field since the 1950's.

Research on liquid-liquid dispersions and on the flow characteristics in agitated tanks is not reviewed in detail in this first chapter since there are two following chapters to be dedicated to this purpose. A review of the study of flow characteristics and liquid-liquid dispersions are given in detail in **Chapters 2** and **3**, respectively. Here, only the main findings and the discrepancies among investigators are explained in order to highlight why and how this project is designed and the main objectives of the work.

A review of the literature in this field shows that the ligament stretching mechanism and the turbulent fragmentation mechanism (turbulent pressure fluctuation breaking) can explain most of the phenomena involved in drop breakup in dispersions in agitated tanks (Ali et al., 1981, Hinze, 1955). The viscous shear breaking mechanism, which occurs only when the magnitude of the drop size is of order of the Kolmogoroff length, is not the usual case in liquid-liquid dispersions in turbulent flows.

Both the ligament stretching and the turbulent fragmentation mechanisms occur in *the vortex system trailing from the impeller blade tips*. Taking the example of oil as a dispersed phase fluid:

a) The ligament stretching mechanism consists of two sequential steps: when the oil enters the region of the vortex, first the velocity gradient between the vortex and the

surrounding liquid causes the oil to be stretched into ligaments or elongated sheets, then the ligament breaks into small droplets when the stretching becomes sufficient to create an unstable interfacial condition;

b) The turbulent fragmentation mechanism occurs at higher Reynolds numbers (higher rotation speed and lower viscosity of dispersed fluids). When the large oil drop enters the vortex region near the *impeller tip*, a rapid disintegration of the drop occurs, which forms a resultant droplet cloud.

Calabrese (1979) studied the breakup of highly viscous dispersed phases in stirred tanks. He argued that highly viscous dispersed droplets may break up by a ligament stretching mechanism and low viscosity droplets undergo a turbulent fragmentation mechanism when the disruptive forces in the continuous phase are much larger than that needed to break up the droplets.

Therefore, one may conclude that the droplets in a liquid-liquid dispersion in an agitated tank mainly experience the ligament stretching breakup when the dispersed phase is viscous and/or the Reynolds number is low; and that the turbulent fragmentation mechanism dominates when the viscosity of the dispersed phase is low and/or the Reynolds number is very high. Put another way, when the dispersed phase is viscous and/or the Reynolds number is low, correlations of drop size with the flow should mainly consider the velocity gradient; and when the viscosity of the dispersed phase is low and/or the Reynolds number is very high, correlations of drop size with the flow should mainly consider the turbulent pressure fluctuation which is represented by local turbulence energy dissipation rate, ε.

Many different correlations for drop size have been proposed, but it is difficult to evaluate them for the purpose of scaling up liquid-liquid dispersion systems because a variety of fluids and/or geometric variables have been used, with no common base case (see **Table 3-1**). Most of the existing correlations of drop size are based on the pressure fluctuation breaking mechanism in which the turbulent energy dissipation rate should be used to represent the pressure fluctuations, but almost always the average power input per unit mass ($P/\rho V_T$) is used instead of ε . In some cases, two different scale-up rules (equal

tip speed (πND) and equal power input per unit mass ($P/\rho V_T$)) are proposed for almost identical dispersions (Godfrey and Grilc, 1977, Okufi et al., 1990).

The discrepancies among the existing correlations for drop size (discussed in detail in **Chapter 3**) may be partly caused by the fact that it is not clear which parameter is the best parameter to correlate the Sauter mean drop size: the mean flow (ND), or the average energy consumption rate on the scale of the whole tank, or the average turbulence energy dissipation rate on the scale of the impeller region, or the maximum turbulent energy dissipation rate in the flow field of a tank. To include the average power input explicitly or implicitly in correlations for mean drop size confuses the local characteristics of drop breakup. According to Park and Blair (1975) and other investigators' work, drop breakup occurs only near the impeller and droplet coalescence predominates at other locations. Park and Blair found that beyond distances from the impeller region of the order of only 1/6 the impeller diameter, breakup is virtually nonexistent. Several researchers have pointed this out. Calabrese et al. (1986) argued that for extremely viscous drops "it seems that no model based on power per unit mass of liquid ($P/\rho V_T$) will provide a reasonable correlation." Nishikawa et al. (1987) found experimentally that neither the impeller speed, Reynolds number or average power input per unit mass of liquid can be used as the scale-up standard to keep the interfacial area of emulsion constant, though they are often used as the scale-up standard for various phenomena in the mixing vessel.

Another possibility for the discrepancies between correlations for mean drop size is that the effects of some geometric variables of impellers and tanks such as the ratio of impeller diameter to tank diameter, off bottom clearance and the number of baffles on the flow (reflected in ε) are not accounted for.

This project is designed to fill the gap between the model and the real physics. The main concept is to try to use the local turbulence energy dissipation rate near the impeller blades, especially the maximum turbulence energy dissipation rate, ε_{max}, to represent the external deforming force on droplets since drop breakup occurs in this region and the mean drop size may be correlated well with the ε_{max}. This is especially

true for dilute liquid-liquid dispersions in which coalescence in the bulk of the tank is not significant.

A phase Doppler particle analyzer (PDPA) is used in this study. It can measure the diameter and the velocity of drops simultaneously ((PDPA) mode), or the velocity only (laser Doppler anemometer (LDA) mode). Four impellers are used, one radial flow turbine (Rushton turbine (RT)) and three axial flow turbines (pitched blade turbine (PBT) and fluidfoil turbine (A310) and a modified pitched blade turbine (HE3)). A cylindrical tank with a diameter of 0.240 m is used.

This project is divided into two parts:

i) Characterization of the turbulence energy dissipation in impeller regions.

Both the average and the local turbulence energy dissipation rate, especially the maximum turbulence energy dissipation rate, are investigated to characterize the turbulence energy dissipation in impeller regions.

For the average turbulence energy dissipation rate, a macroscopic mechanical energy balance equation needs to be derived since a discrepancy is found in published works of previous investigators (Wu and Patterson, 1989, Ranade and Joshi, 1989, Ranade et al., 1992). The average turbulence energy dissipation rate in impeller regions is calculated with the derived equation and the data measured with a validated LDA. Emphasis is put on checking the conflicts between the magnitude of energy dissipation in the impeller region and in the impeller discharge region for the RT (Cutter, 1966, Gunkel and Weber, 1975, Wu and Patterson, 1989). Further experiments were performed with the PBT and the A310.

For the local turbulence energy dissipation rate, ε, the commonly used estimate equation ($\varepsilon=Av^3/L$) is verified in the impeller regions by first examining the assumption of isotropic flow which is inherent in the equation; then the length scale L and the constant A are determined experimentally.

The effects of geometric variables (number of baffles, N_f, impeller diameter, D, off bottom clearance, C, or the ratio of C/D) on ε_{max} are investigated using factorial designs. The maximum turbulence energy dissipation rate, ε_{max}, is estimated using the

verified equation for the local dissipation rate. First, the location of ε_{max} in the flow field is determined. The dominating effects and interactions will be highlighted and used in the study of liquid-liquid dispersions. Four impellers (the PBT, the A310, the HE3 and the RT) are used which represent the full spectrum of impellers currently used for turbulent mixing in industry.

ii) Characterization of liquid-liquid dispersions in agitated tanks.

Preliminary experiments were carried out to validate the PDPA; the choice of the fluid in the dispersed phase; and to examine the effect of the dispersed phase addition on the flow field.

Drop sizes are measured over a wide range of rotational speeds using a validated PDPA. Four impellers are used. Data analysis is focused on the drop size distribution, minimum drop size and Sauter mean diameter. The two scale-up rules mentioned above and the new approach using ε_{max} to replace $P/\rho V_T$ are examined simultaneously using all the data obtained for the four impellers and varying tank geometries to determine which is the best parameter to be used in correlations with d_{32}. A new scale-up principle is proposed from the data analysis. From the data of minimum drop sizes, the suitability of Kolmogoroff length scale $[\eta=(\nu^3/\varepsilon)^{1/4}]$ is examined. This length scale is often used to estimate the minimum drop size in dispersions in agitated tanks.

This thesis is composed of the following six parts: (1) literature reviews of a) the flow characteristics of agitated tanks (**Chapter 2**) and b) mechanisms of drop breakup and correlations for mean drop size (**Chapter 3**); (2) validation of the experimental equipment used (**Chapter 4** for LDA mode, **Chapter 7** for PDPA mode); (3) a study of the average turbulence energy dissipation rate in the impeller regions (**Chapter 5**); (4) the local and maximum turbulence energy dissipation rate, ε_{max}, and the effect of tank geometry (number of baffles (N_f) , impeller diameter (D), off bottom clearance (C) and/or the ratio of C/D) on ε_{max} (**Chapter 6**); (5) measurement of the drop size distribution, the minimum and mean drop sizes and correlation of the mean drop size with flow (**Chapter 8**); and (6) summary of main conclusions drawn from this work and suggestions for future research needs related to this project (**Chapter 9**).

References

Ali, A. M., Yuan, H. H. S., Dickey, D. S. and Tatterson, G. B., 1981, Liquid dispersion mechanisms in agitated tanks: Part I. Pitched blade turbine. *Chem. Eng. Commun.* **10**, 205-213.

Calabrese, R. V., 1979, The effect of dispersed phase viscosity on drop breakup in agitated liquid-liquid systems. presented at Joint Japanese-North American Mixing Conference, AIChE, 72nd Annual Meeting.

Calabrese, R. V., Chang, T. P. K. and Dang, P. T., 1986, Drop breakup in turbulent stirred-tank contactors, Part I: Effect of dispersed-phase viscosity. *AIChE J.* **32**, 657-666.

Cutter, L. A., 1966, Flow and turbulence in a stirred tank. *AIChE J.* 12, 35-45.

Godfrey, J. C. and Grilc, V., 1977, Drop size and drop size distribution for liquid-liquid dispersions in agitated tanks of square cross-section. *Second European Conference on Mixing,* Cambridge, England, BHRA Fluid Engineering: Cranfield, UK, C1-1 to C1-20.

Gunkel, A. A. and Weber, M. E., 1975, Flow phenomena in stirred tanks: Part I. the impeller stream. *AIChE J.* **21**, 931-949.

Hinze, J. O., 1955, Fundamentals of the hydrodynamic mechanism of splitting in dispersion processes. *AIChE J.* **1**,.289-295.

Nishikawa, M., Mori, F., Fujieda, S. and Kayama, T., 1987, Scale-up of liquid-liquid phase mixing vessel. *J. Chem. Eng. Japan* **20**, 454-459.

Okufi, S., Perez de Ortiz, E. S. and Sawistowski, H., 1990, Scale-up of liquid-liquid dispersions in stirred tanks. *Can. J. Chem. Eng.* **68**, 400-406.

Park, J. Y. and Blair, L. M., 1975, The effect of coalescence on drop size distribution in an agitated liquid-liquid dispersion. *Chem. Eng. Sci.* **30**, 1057-1064.

Ranade, V. V. and Joshi, J. B., 1989, Flow generated by pitched blade turbines I: Measurements using laser Doppler anemometer. *Chem. Eng. Commun.* **81**, 197-224.

Ranade, V. V., Mishra, V. P., Saraph, V. S., Deshpande, G. B. and Joshi, J. B., 1992, Comparison of axial flow impellers using a laser Doppler anemometer. *Ind. Eng. Chem. Res.* **31**, 2370-2379.

Wu, H. and Patterson, G. K., 1989, Laser Doppler measurements of turbulent-flow parameters in a stirred mixer. *Chem. Eng. Sci.* **44**, 2207-2221.

Chapter 2

Literature Review-Flow Characteristics in Agitated Tanks

2.1 Introduction

The formation of liquid-liquid dispersions has been an active field of study in chemical engineering science since the 1950's. The drop size distribution, which is itself an important process variable, also determines the surface area per unit volume, and thus the mass and energy transfer rates. Because of its importance, a lot of research has been done on the mechanisms of drop breakup and on correlation of mean drop size with the turbulent flow in agitated tanks. In the next two chapters, the literature pertinent to this investigation is reviewed, with particular emphasis on the results obtained for stirred tanks. In this chapter the work of various researchers on the flow characteristics in agitated tanks is reviewed. In **Chapter 3** the proposed mechanisms of drop breakup and correlations for mean drop size are reviewed.

In order to make previous investigations easy to present, some general definitions for the study of liquid-liquid dispersions in agitated tanks will be presented wherever they are necessary.

First, we begin with some definitions about the geometry of an agitated tank and impellers.

2.2 Geometric Variables of An Agitated Tank and Impellers

2.2.1 Classification of Impellers

Different impellers create different flow patterns and are used in liquid-liquid dispersion systems for various purposes. Several methods are used to classify impellers, each of which has advantages and disadvantages. The most commonly used method is to group impellers by flow regime and by blade shape. Using this method, impellers can be classified into five distinct categories: propeller, turbine, paddle, close clearance impeller and reciprocating impeller.

Reciprocating impellers have little commercial importance (Uhl and Gray, 1966) except in reciprocating plate columns. Propellers are essentially high-speed impellers of the axial flow-type (discharge flow parallel to the agitator shaft), and may be used in low viscosity liquids almost without restriction as to the size and the shape of the tank. The basic paddle is based on operation in the laminar range, or in the transition and turbulent range without baffles. Close clearance impellers are mainly used for high viscosity and non-Newtonian fluids. In this thesis project, only turbines will be used; the rest are less relevant for liquid-liquid dispersion operations.

The turbine is defined in the AIChE "Standard Test Procedure for Impeller-Type Mixing Equipment" (AIChE, 1960) as "an impeller with essentially constant blade angle with respect to a vertical plane, over its entire length or over finite sections, having blades either vertical or set at an angle less than 90° with the vertical". The blades may be curved or flat. The number of blades is not important and can be two or more. There are two kinds of turbines: the flat-blade radial discharging style and the pitched-blade axial thrust type (there is a small radial component to the discharge velocity from this turbine). All others are modifications of these, e.g. disk flat blade, curved blade and tilted blade, pitched curved blade.

Most of the reported studies on liquid-liquid dispersions were done with turbines. In this study both the flat-blade radial discharging style and the pitched-blade axial thrust type turbines are used as well as the newer A310 fluidfoil axial and the modified pitched-blade axial (HE3) impeller. Because turbines are also commonly called impellers, in the following chapters the words impeller and turbine are used interchangeably for the mixing agitators.

2.2.2 Geometry of Impellers

Schematic drawings of the axial-flow impellers (pitched blade turbine (PBT), and fluidfoil turbine (A310)) and the radial-flow impeller (Rushton turbine, RT) are shown in **Figure 2-1**. Although some other types of impellers have been used by previous investigators, the PBT and RT (especially the RT) are the most common. All three impellers are shown in **Figure 2-1** in their standard configurations. The PBT has a pitch

angle of 45°; the blade width, W, of the PBT and RT is $D/5$; the blade length of the RT is $D/4$. The modified pitched blade turbine HE3 (not shown here) is a newcomer, so published research is rare in the literature. It is similar to the PBT, but with three blades and a smaller pitch angle and a flat corner on each blade.

2.2.3 Geometry of An Agitated Tank

The schematic drawing of a typical agitated tank used for study of mixing is shown in **Figure 2-2**. For this study the agitated tank is a cylindrical tank with its diameter, T, equal to the liquid height, H (=0.240 m); and vertical rectangular baffles (their width, $W_b=T/10$) equally spaced around the periphery of the tank. The number of baffles, N_f, can range from four to zero. The off bottom clearance, C, is defined as the distance between the bottom of the tank and the center line of the impeller blades. The radius of the impeller, D/2, is the distance from the impeller shaft axis to the tip of one blade. The origin of the cylindrical coordinates is defined as the cross point of the shaft axis and the center line from a baffle to a baffle at the center line of the impeller blades.

2.3 Characteristics of the Flow Generated by Different Impellers in Agitated Tanks

The stable mean drop size is determined by the balance of the external forces (viscous stress and turbulent pressure fluctuations) and the restoring forces (interfacial tension and viscous stress due to the deformation and the internal motion of the drop (Hinze, 1955)). The external forces are determined by the flow conditions in the continuous phase around the drop. Generally speaking, for a specific mixing system flow conditions are determined by the type of the impeller, the rotational speed and the geometry of the stirred tank. Most of the work investigating the flow conditions focuses on the flow created by the RT and the PBT. The detailed flow characteristics for the A310 have not yet been systematically investigated in the open literature.

At present, a purely theoretical treatment of the flow within an agitated tank is impossible due to the randomness of turbulence, the three dimensionality of the flow, and the nonlinearity of the governing equations of motion. In recent years more and more numerical experiments on the flow using computational fluid dynamics (CFD) have been

presented. Verification of their accuracy is based on experimental measurements and on appropriate boundary conditions obtained from experimental measurements.

2.3.1 Mean and Fluctuating Velocities and Pressure

Before we review the work of previous investigators on the characteristics of the flow generated by different impellers in agitated tanks, we introduce the definitions of mean and fluctuating velocities and pressure.

In most practical situations the flow in an agitated tank is fully turbulent. Hinze (1975, pg 2) formulated a definition for turbulent flow as follows: "Turbulent fluid motion is an irregular condition of flow in which the various quantities show a random variation with time and space coordinates, so that statistically distinct average values can be discerned". Because of its irregularity, a turbulent motion cannot be characterized by its scale alone; the violence of the fluctuations is as important as the mean value. Furthermore, the value of a variable at a spatial point at an instant time has little practical relevance for a turbulent flow; thus all variables which characterize the turbulent flow have time or space averaged properties.

The momentary values of the velocity and pressure are written as

$$V = \overline{V} + v' \tag{2-1}$$

$$p = \overline{p} + p' \tag{2-2}$$

respectively, where the overscore denotes the average value, so that by definition the mean of turbulent fluctuations, $\overline{v'}$ is zero. The average value can be either a time average or a space average value. For a quasi-steady, or stationary random turbulent flow field the time average value is used; for a homogeneous turbulence flow field the space average value is used. The averages are defined as follows:

Time average for stationary turbulence:

$$\overline{V}(x_0) = \lim_{T\to\infty} \frac{1}{2T} \int_{-T}^{+T} V(x_0, t)dt \tag{2-3}$$

Space average for homogeneous turbulence:

$$\bar{V}(t_0) = \lim_{x\to\infty} \frac{1}{2X} \int_{-X}^{+X} V(x, t_0)dx \qquad (2\text{-}4)$$

In practical use the X and T have finite values.

The fluctuating velocity is defined by the root-mean-square (rms, or RMS) of the turbulent fluctuations

$$v = \sqrt{\overline{v'^2}} \qquad (2\text{-}5)$$

and the relative intensity of the turbulence fluctuations is defined by the ratio

$$\text{turbulence intensity} = \frac{v}{\bar{V}} \times 100\%$$

2.3.2 Methods of Studying Flow Characteristics

There are two categories of experimental methods to study the flow in an agitated tank. One is flow visualization with tracer particles added in the tank (Rushton and Oldshue, 1953a, 1953b, Sachs and Rushton, 1954, Metzner and Taylor, 1960) or tufts attached on parts of the mixing equipment (Shen and Baird, 1991, Kresta and Wood, 1991). The other is the direct measurement of the flow in the tank.

Flow visualization methods can give an excellent overall picture of the more complex time varying aspects of the flow, which are difficult to reproduce from a local time averaged experiment. Its improvement relies on the development of more powerful cameras with higher speeds and possibly programmable motion (Winardi et al., 1988, Van't Riet and Smith, 1973, 1975).

Direct measurement of the flow can be done in many ways. In the fifties, photographic measuring methods were the main methods used to measure fluid velocities (Rushton and Oldshue, 1953a, 1953b, Sachs and Rushton, 1954, Metzner and Taylor, 1960). On account of the simple experimental set-up, they are still successfully being applied (Cutter, 1966, Schwartzberg and Treybal, 1968, Levis and Glastonbury, 1972, Ali et al., 1981, Winardi et al., 1988); however, the experimental results obtained by this method can only approximately reproduce an overall pattern of the flow and mean velocities. Since the early sixties, pressure probes [pitot tube: Kim and Manning, 1964, Desouza and Pike, 1972, Rao and Brodkey, 1972], and convection probes [hot wire:

Baldwin and Walsh, 1961, Mujimdar et al., 1970, Gunkel and Weber, 1975; and hot film: Nishikawa et al., 1976, Bertrand et al., 1980, Okamoto et al., 1981] have been widely used. Using these methods both the mean and fluctuating velocities are recorded. However, these methods require the introduction of probes into the flow field in an agitated tank, and the flow will be affected by the presence of the probes. In the fine turbulent structure of the flow, the distorting effect of the measuring probe may be substantial. A technique developed in the late seventies - laser Doppler anemometry (LDA) - allows non-intrusive measurement of the flow, and records an almost instantaneous response to velocity fluctuations, with unambiguous separation of the three directional components of velocity. The development of LDA allowed substantial improvement of the understanding of the flow in an agitated tank. The first investigation published on the flow in an agitated tank with LDA was conducted by Reed et al. (1977). Since then, many other investigations using LDA have been published (Van der Molen and Van Maanen, 1978, Laufhutte and Mersmann, 1985, 1987, Jaworski et al., 1988, Costes and Couderc, 1988a, 1988b, Wu and Patterson, 1989, Wu et al., 1989, Ranade and Joshi, 1989, Jaworski et al., 1991, Ranade et al., 1992, Kresta and Wood, 1993a, Dyster et al., 1993). Among the methods summarized above, the most successful has been laser Doppler anemometry.

2.3.3 General Flow Patterns in Agitated Tanks

In papers about the flow characteristics and liquid-liquid dispersions in agitated tanks, the phrases "impeller region", "impeller stream" or "impeller discharge stream (or region)", and "bulk" are often used by investigators to specify the regions around, near and away from the impeller blades. Such definitions are quite qualitative. It is necessary to define these regions more quantitatively for different impellers in order to make the following analysis more meaningful. *Impeller region* stands for the region around impeller blades. The fluid in this region is about 5% of the total volume of the fluid in the tank; however, the actual scale for this region differs among investigators, depending on the measuring methods used. *Impeller stream*, or *impeller discharge stream*, or *impeller discharge region* refers to the region near impeller blades to which the fluids

discharged by an impeller go. It has a different meaning for axial flow and radial flow impellers because of their different discharge characteristics. For radial flow impellers like the RT, the impeller discharge region is the region neighboring the impeller region in the radial direction (defined above with the same axial coordinates); for the axial flow impellers like the PBT, the A310 and the HE3, impeller discharge region is usually the region under the impeller blades, into which the main discharge stream goes. The fluids enclosed in the impeller region and the impeller discharge region occupy about 10% of the fluids in the tank. Regions other than the impeller region and the impeller discharge region are called "the bulk of the tank".

2.3.3.1 The Propagation of Turbulence with Increase of Reynolds Number

Nagata et al. (1959, 1960) extensively investigated the flow conditions in an agitated tank with or without baffles for laminar, transitional and turbulent flow. The flow conditions in an agitated tank are different from those in a pipe, but they have the same trend with the change of Reynolds numbers ($\mathrm{Re} = \frac{ND^2}{\nu}$). At low Reynolds numbers the flow is laminar throughout the tank. Around the impeller the liquid velocity is high and decays rapidly away from the impeller blades. With increasing Reynolds numbers, the flow around the impeller becomes turbulent and the flow in the bulk of the tank is still laminar. Further increases of Reynolds number result in the propagation of the turbulent state to the bulk away from the neighborhood of the impeller, and finally the flow in the whole tank becomes turbulent.

Nagata et al. did not clearly specify Reynolds numbers for laminar flow and turbulent flow. From visualization and direct measurement of the flow field in agitated tanks and from the results of investigating the power characteristics of impellers (described in detail in section **2.4.4**), the flow in agitated tanks is laminar when $\mathrm{Re} \leq 20$; and the flow is turbulent when $\mathrm{Re} \geq 10^4$, between these two Reynolds numbers, the flow is in transitional (from laminar to turbulent) state.

2.3.3.2 Effect of Baffles on the Flow in Agitated Tanks

Aiba (1958) investigated flow patterns of three types of impellers (paddle, turbine and propeller) with and without baffles using a tracer method. He found that in the case of unbaffled agitation, irrespective of the type of impeller, two flow regions existed in the tank relating to the tangential velocity component. In the region around the center of the tank the liquid seems to rotate as a whole, as if it were a solid (cylindrical forced vortex). In the other region, between the former and the tank wall, the liquid rotates along with the cylindrical vortex (free vortex). In the turbulent region flow patterns for a given agitation system are independent of the impeller speed. This does not hold true for the case of viscous liquids, when agitation is far from turbulent. From his data, we can deduce that for an unbaffled tank tangential velocities produced by all three types of impellers are high relative to radial and axial components. In the case of fully baffled operation the tangential velocity component decreases.

Nagata et al. (1959, 1960) deduced a similar conclusion from their experimental results. They found that the flow pattern is more erratic with baffles than without. For an unbaffled tank tangential velocities produced by turbine impellers are high relative to radial and axial components. In case of fully baffled operation the flow pattern is characterized by a decrease in tangential velocity components. The radial components remain almost unchanged.

2.3.3.3 Characteristics of the Vortices Formed in Agitated Tanks

Many investigators found the existence of vortices in agitated tanks (see **Figure 2-3**). Van't Riet and Smith (1973, 1975) carried out the first quantitative investigation on the trailing vortex system produced by the *RT* using a photographic method. They showed that a pair of vortices exists, one above and one below the impeller disc plane behind impeller blades. The vortices behind the blades maintain their identity for two to three blade lengths and the vortex axis is very nearly horizontal with position independent of speed for Reynolds numbers above 5000. By measuring the velocity and pressure distributions within the trailing vortex, they found that velocity and pressure can be scaled up in terms of the Reynolds number only, and that the flow is turbulent even at

Re=300. Van't Reit, Bruijn and Smith (1976) examined the impeller flow with a stationary hot-film probe and observed that the vortices were broken up at the baffles and the tank walls. Van der Molen and Van Maanen (1978) drew similar conclusions and reported that the circulation velocity in the vortices is dependent on the impeller geometry and in particular on the blade thickness. Yianneskis et al. (1987) studied the vortex structure in detail, and the influence of geometrical variables, using laser-slit photography to provide a visualization of the flow and a laser Doppler anemometer to measure the velocity characteristics in both the discharge stream and the bulk of the tank. They found that the velocities in the vortices were of the order of 0.25 of the blade tip velocity (πND), and that the impeller diameter affected the shape of the ring vortices and, to a lesser extent than the clearance, the inclination of the impeller stream. Their measurements of the radial and tangential average velocities below the impeller showed a vortical structure in planes perpendicular to the tank axis, with a helical vortex present behind each baffle and large regions of the flow rotating in a sense opposite to that of the impeller. The flow was controlled mainly by the balance of pressure and inertial forces.

Vortices also exist in the flow field generated by axial flow impellers. The investigation of them, however, is much less extensive than that of the vortex system created by the RT. Tatterson et al. (1980) examined the flow around the impeller blades for a PBT. They found that the vortices move down through the tank, and considered the shedding and decay of the trailing vortices as the impeller rotates. They concluded that the flow produced by a PBT is a combination of "high-speed jets", or streaming flow, and trailing vortices; and that the dominant flow depends on the number of blades, and/or the scale of the experiment. Kresta and Wood (1991) used particle and tuft visualization experiments to examine the flow generated by a PBT. They found that in contrast to the single primary circulation loop filling the entire tank for all geometric configurations which was illustrated by classic fluid mixing texts (e.g. Oldshue, 1983, Uhl and Gray, 1986) and reaffirmed by the experimental results of Rewatkar and Joshi (1991), the primary circulation loop is accompanied by a weak secondary circulation loop which forms in the lower corners of the tank for some geometric configurations, and the primary

circulation loop is much smaller than previously reported. Above the impeller in the upper third of the tank, there is very little circulation and many of the weaker circulation patterns are unstable. They specified that a trailing vortex forms at the tip of impeller blades, and no vortex action exists in the inner part of the impeller blades. The vortices created by the PBT and the second circulation loop for some geometric configurations are shown in **Figure 2-4.**

2.3.3.4 Local Isotropy of the Flow in the Impeller and the Impeller Discharge Region

From the analysis above, we know that the flow in an agitated tank is non-homogeneous, and that big differences of mean or fluctuating velocities between different regions exist. The flow around the impeller blades is more turbulent than that away from the impeller, and it is non-homogeneous as well. Several investigators have assumed that the flow in the impeller and the impeller discharge region is isotropic (Cutter, 1966, Shinnar, 1961, Arai et al., 1977). Experiments to check the isotropy of the flow in the impeller and impeller discharge region were done by Jaworski et al. (1987) and Kresta and Wood (1991).

Jaworski et al. (1987) investigated the flow characteristics for the region surrounding a PBT using a photographic method. By analyzing the radial distribution of the fluctuating velocity components they concluded that local isotropy of those components exists for the entire investigated area around the impeller blades. They actually measured only the radial and axial components of the mean and fluctuating velocities. For the flow formed by the PBT, the tangential component of velocity is not too small to be neglected, so their data are not sufficient to confirm the existence of the isotropy of the flow in impeller region. Kresta and Wood (1991) checked the flow in both the impeller and impeller discharge region for the PBT. They found that the three fluctuating velocities are nearly the same, and concluded that the flow in these regions is approximately locally isotropic. The check of isotropy of the flow in impeller region and impeller discharge region for three impellers (RT, PBT and A310) will be reexamined in **Chapter 5.**

2.3.3.5 Velocity Profiles for the Radial Flow Impeller (RT)

Sachs and Rushton (1954) measured the radial velocity profiles in the discharge stream for the RT using a photographic method. They obtained roughly parabolic profiles of radial velocities near and away from the impeller tip in the discharge stream. The momentum diffuses and the velocity profiles flatten out as the radial distance increases. The radial volumetric flow rate (through various cylindrical surfaces bounded by vertical planes extending through the top and bottom of the impeller blades) is proportional to the impeller speed at various radial distances from the impeller. A large volume of fluid is entrained by the discharge stream as it flows away from the impeller.

Cooper and Wolf (1968) measured velocity and angle profiles near the RT impeller tip with varying impeller diameters, blade widths and blade lengths in both air and water using a hot wire anemometer probe and two and three dimensional pitot tubes. They found that the radial velocity profile is parabolic in shape, while the tangential profile is flatter. The radial velocity profile normalized with the maximum radial velocity is independent of turbine speed and independent of turbine diameter for geometrically similar turbines. The angle of the discharge flow varies across the width of the blade, with the flow becoming increasingly radial towards the centerline of the turbine. The discharge angle is independent of speed and turbine size for geometrically similar turbines.

Nouri et al. (1987) investigated the flow with varying impeller diameters and rotational speeds using a laser Doppler anemometer. The findings obtained with this totally different technique are in close agreement with those of Cooper and Wolf (1968).

2.3.3.6 Flow Fields for the Axial Flow Impeller (PBT)

Most of the extensive investigations on the flow generated by the PBT have been done using LDA. The only detailed investigation on this flow using a method other than LDA is Fort and co-workers' work. Fort and co-workers (Fort et al., 1969) used the axial velocity (measured with pitot tube) and the circulation time data to characterize the flow generated by pitched blade turbines. They studied the effects of number of blades, angle

of blades, D/T ratio and impeller location on the flow by measuring the variation of pumping capacity with these variables.

Ranade and Joshi (1989) investigated the flow generated by the PBT extensively using LDA. They used two sizes of tanks and examined the effects of off bottom clearance, of the geometry of the impeller (blade angle (30°-60°), blade width (0.2D-0.4D)) and impeller diameter (0.25T-0.5T) on the flow. They found that 1) in the impeller region, pitched blade turbines generated strongly accelerated downward flow through the impeller region when impeller diameters are less than T/2; 2) the mean velocities and turbulence intensities were approximately proportional to the impeller speed within the range of Reynolds numbers studied ($4x10^4$-$1.4x10^5$); 3) the angle of the blade significantly affected the flow; the blade width affected the flow as well, but to lesser extent; 4) the large impeller (D/T=0.5) generated entirely different flow-radially outward flow through the vertical periphery of the swept surface; 5) in the bulk region three distinct zones exist viz., cone shaped region below the impeller (with upflow of liquid), a highly turbulent region below the impeller center plane and a relatively less turbulent zone above the impeller.

Jaworski et al. (1991) studied the flow generated by a standard PBT with varying off bottom clearances (C=T/4 and C=T/2) using LDA. They found that near the bottom of the tank off bottom clearance decisively influenced the flow pattern, in the case of D/T=0.5, a low intensity flow reversal prevailed over the entire bottom whilst only a small but significant core of reverse flow was found at the lower clearance.

Kresta and Wood (1993a) investigated the flow created by a PBT in detail using a combination of flow visualization and LDA, focusing especially on the impeller discharge stream and bulk circulation flow. They defined two distinct bulk circulation patterns based on their experimental data: with a secondary circulation loop for higher off bottom clearances and without a secondary circulation loop for lower clearances. They found that the circulation patterns had a substantial impact on the discharge stream, even very close to the edge of the impeller blades. The secondary circulation loop displaces the impeller discharge stream, changing the axial velocity profile, and increasing the radial velocity.

General flow patterns for the RT and the PBT are depicted schematically in **Figure 2-5**. In **Figure 2-5** the flow pattern of the fluidfoil impeller (A310) is also drawn, which is based on the experimental data of this study (detailed velocity profiles for the A310 are presented in **Chapters 4, 5, and 6**). For the A310, the general flow pattern is similar to that of the PBT, with smaller radial velocities in the impeller discharge region (under impeller blades). The angle between the axis of the impeller shaft and the discharge stream is smaller for the A310 than for the PBT.

2.4 Dimensionless Groups

2.4.1 Reasons and Ways to Get Dimensionless Groups

The fundamental physical laws governing transfer to particles immersed in fluids are Newton's second law, the principle of conservation of mass, and the first law of thermodynamics. Application of these laws to an infinitesimal element of material or to an infinitesimal control volume leads to the Navier-Stokes, continuity, and the energy equation. Exact analytical solutions to these equations have been derived only under restricted conditions. It is practically impossible to get exact analytical solutions to these equations for turbulent flow in an agitated baffled tank. More usually, it is necessary to solve the equations numerically or to resort to approximate techniques where certain terms are omitted or modified in favor of those which are known to be more important. Most often, in the case of turbulent flow in a stirred baffled tank, the governing equations are used to suggest relevant dimensionless groups with which to correlate experimental data.

Dimensionless groups are the direct result of dimensional analysis. Dimensional analysis combines independent variables into dimensionless parameters with mathematical or physical significance. There are two methods used to get dimensionless groups. One is the Π-theorem, developed by Buckingham (1914). The background and development of this theorem has been well presented by Hixson and Luedeke (1937), Johnstone and Thring (1957), Rushton et al. (1950), and recently Dickey (1993), and will not be repeated here. A point worth mentioning is that the Π-theorem starts directly with an uncertain equation which is no more than a complete list of unknowns and potential

correlating variables. Another method, proposed by Rayleigh (1915), uses a governing equation and substitutes a few characteristic variables into the governing equation to get dimensionless groups. The two methods give the same results.

2.4.2 Variables Affecting Fluid Motion in the Mixing of Liquids

Variables which affect fluid motion in mixing are of three types.

First, the kinematic and dynamic characteristics of flow such as velocity, power input or resisting forces, e.g. the interfacial tension in the case of drop breakup, and the force of gravity.

Second, the fluid physical properties such as density, ρ, viscosity, μ, and interfacial tension, σ.

Third, geometrical dimensions of the impeller and tank such as: impeller diameter, D, tank diameter, T, liquid depth (height), H, off bottom clearance, C, pitched angle of the impeller, θ_p , length of impeller blades, L_b , width of blades, W, width of baffles, W_b, number of blades, N_b , number of baffles, N_f.

2.4.3 Important Dimensionless Groups for the Fluid Motion in the Mixing of Liquids

2.4.3.1 Reynolds Number and Froude Number

For a constant-density, Newtonian liquid, the Navier-Stokes equation for momentum balance in terms of local pressure and velocity (Bird et al., 1960) is:

$$\rho\frac{DV}{Dt} = -\nabla p + \mu\nabla^2 V + \rho\bar{g} \qquad (2\text{-}6)$$

To get dimensionless groups, we first choose characteristic quantities to represent the principal dimensions of length, time and mass (D for length, $1/N$ for time, ND for velocity, $\rho(ND)^2$ for pressure). Substituting the characteristic quantities into Eq.(2-6), and rearranging coefficients yields a dimensionless form of the Navier-Stokes equation:

$$\frac{DV^*}{Dt^*} = -\nabla^* p^* + [\frac{\mu}{ND^2\rho}]\nabla^{*2} V^* + [\frac{g}{DN^2}]\frac{\bar{g}}{g} \qquad (2\text{-}7)$$

where * denotes dimensionless variables. Two dimensionless groups appear as parameters in Eq.(2-7). The Reynolds number for agitation, $\frac{ND^2\rho}{\mu}$, appears in reciprocal form as the coefficient for the viscous dissipation term. The Reynolds number for agitation (simply called the Reynolds number in following chapters) represents the ratio of *inertial* to *viscous forces*. Another dimensionless group, $\frac{g}{DN^2}$, is the reciprocal of the Froude number. The Froude number represents the ratio of *inertial* to *gravitational forces*.

2.4.3.2 Power Number

Using the Π-theorem (Rushton et al. 1950) or the relation between power and rotational speed and applied torque (Dickey and Fenic, 1976), we can get a dimensionless group—power number, N_p,

$$N_p = \frac{P}{\rho N^3 D^5} = f(Re, Fr) \qquad (2\text{-}8)$$

The power number relates *imposed forces* to *inertial forces*, and is a function of the Reynolds number and the Froude number.

2.4.3.3 Weber number

When two immiscible liquids are agitated, a dispersion is formed in which continuous breakup and coalescence of drops occurs. The drop is assumed to be broken by *viscous shear forces* and *turbulent pressure fluctuations*. The elastic stress generated due to *interfacial tension* on the other hand, tends to restore the drop to the original shape. In the inertial subrange, a balance between the elastic stress, σ / d, and turbulent pressure fluctuation represented by $\rho_c \overline{V^2(d)}$, determines the maximum stable drop size. The ratio of the turbulent pressure fluctuations and the elastic stress is called the Weber number, or Weber group:

$$We = \frac{\rho_c \overline{V^2(d)}d}{\sigma} \tag{2-9}$$

where d is the diameter of the drop. Expressing the mean-square of the relative velocity, $\rho_c \overline{V^2(d)}$,by $\rho_c N^2 D^2$, and replacing drop diameter, d , with the impeller diameter, D, we get the Weber number in a mixing tank:

$$We_{,T} = \frac{\rho_c N^2 D^3}{\sigma} \tag{2-10}$$

The qualification "in a mixing tank" is added to distinguish between the Weber number on the scale of drop diameter, d, and that on the scale of the mixing equipment. Strictly speaking, the Weber number refers to the definition by Eq.(2-9). There is an alternative way to derive Weber number in a mixing tank, which will be given in section **3.2.2** of **Chapter 3**.

2.4.4 Power Characteristics of Mixing Impellers

The main function of agitation is to introduce energy into the tank with the aid of a rotating impeller, thus converting mechanical energy into hydrodynamic motion. The power consumption characteristics of mixing impellers are one of the most decisive parameters needed to characterize mixing impellers and the flow generated by them in the tank.

Rushton et al. (1950a, 1950b) were the first investigators to systematically study the power characteristics of three types of impellers - propellers, paddles and radial flow turbines (RT). Their data cover a wide range of Reynolds numbers - from laminar flow. Reynolds numbers<20, to fully turbulent flow, Reynolds numbers$\geq 10^4$. They related the power number to the Reynolds number and the Froude number. For agitated tanks, the effect of the gravity force on the power number is negligible, so the power number is generally considered a function of the Reynolds number. For both propellers and Rushton turbines, the power number decreases linearly with the Reynolds number in the laminar flow (on the logarithmic plots). In the transition region (laminar to fully turbulent flow) the power number shows different trends for propellers and Rushton

turbines: for propellers the power number decreases slowly with the Reynolds number. for Rushton turbines the power number first slowly decreases, then increases with the Reynolds number. In the fully turbulent region the power number is no longer a function of the Reynolds number for any of the impellers studied.

Bates et al. (1963) studied the power characteristics of both radial flow turbines and axial flow turbines. Their data cover a wide range of Reynolds numbers (10^{-1} to 10^{5}) as well. The data for radial flow turbines agrees well with that of Rushton and co-workers. They also investigated the effects of some shape factors (impeller blade width, number of blades, blade angle, off bottom clearances, number of baffles, baffle width) on impeller power.

The power numbers in the fully turbulent region for the RT and PBT are used in the following chapters, so a summary of the reported values of these power numbers for the RT and PBT is given in **Table 2-1**.

Data on the power number for the PBT is much less plentiful than for the RT. Bates et al. (1963) obtained a value of 1.4 for the power number of the PBT in the fully turbulent region. Nienow and Miles (1971) obtained a value of 1.4 when D/T=1/2, C/T=1/4; and a value of 1.8 when D/T=1/4, C/T =1/4 to 1/2 in the range of Reynolds numbers ($2x10^{4}$ to 10^{5}). Ranade et al. (1992) studied the power number of the PBT with varying pitch angles and blade width; they got a value of 1.47 for the power number of the PBT when its pitched angle is 45° and blade width is D/5. The values of power numbers used for this work are based on these studies.

2.5 Turbulence Energy Spectrum and Turbulence Energy Dissipation Characteristics in Agitated Tanks

As mentioned before, directly applying the Navier-Stokes equation for turbulent motion in an agitated tank is difficult and practically impossible because the variables in the equation refer to instantaneous values at a local point. From the analysis in the sections above, we know that the flow fields vary from time to time and from point to point, so it is necessary to use some statistical average and a measure of the deviation from the average.

By expressing the instantaneous value of a variable as a sum of an average value and a fluctuating value, and taking the time average of the Navier-Stokes equations, we can obtain the following equations:

$$\rho\left(\frac{\partial \overline{V_i}}{\partial t} + \overline{V_j}\frac{\partial \overline{V_i}}{\partial x_j}\right) = -\frac{\partial \overline{p}}{\partial x_i} + \mu\frac{\partial^2 \overline{V_i}}{\partial x_j^2} - \rho\frac{\partial \overline{v'_i v'_j}}{\partial x_j} + \rho g_i \qquad (2\text{-}11)$$

In the time averaged Navier-Stokes equations, a new term, $\rho\overline{v'_i v'_j}$, appears. This term represents the stresses due to the turbulent velocity fluctuations, known as the Reynolds stresses; thus the Navier-Stokes equations in the form of Eq.(2-11) are often called the Reynolds equations. There are three Reynolds equations with 10 unknowns, but we can add only one more equation - the continuity equation by mass conservation - to make 4 total equations. Six more equations are needed to solve the Reynolds equations. There are several ways to overcome this obstacle: the first is to use functional expression for the Reynolds stresses - for example, Boussinesq's Theory, Prandtl's Mixing Length Theory, Taylor's Vorticity Transport Theory, the k-ε model; the second is to directly use statistical correlations for the fluctuating velocities; the third is to convert the differential momentum conservation of Navier-Stokes equations to the integral mechanical energy balance (Tennekes and Lumley, 1972), if an energy balance is our goal. In all three approaches some information about the turbulence structure will be lost.

Most of the phenomenological theories and assumptions proposed so far are directly or indirectly related to turbulence energy theory. In next two sections the theory of turbulence energy is reviewed.

2.5.1 Turbulence Energy Spectrum

When a flow is in the turbulent state, varying sizes of turbulent eddies are formed which range from the very smallest (on the viscous scales) to the largest (which are limited only by the boundaries of the mixing equipment). Different sizes of eddies have their own energy transfer characteristics which are depicted by the energy spectrum equation. For isotropic turbulence the following equation, describing the energy

spectrum, can be obtained by taking the Fourier transform of the Karman-Howarth equation (Hinze, 1975, pg 215).

$$\frac{\partial}{\partial t}E(k,t) = F(k,t) - 2\nu k^2 E(k,t) \qquad (2\text{-}12)$$

k is the wavenumber and is often considered to be the reciprocal of an eddy size; E(k,t) is the three-dimensional energy spectrum function related to the Fourier transform of second-order velocity-correlation tensor and indicates the way in which the energy associated with each velocity component is distributed over various wave numbers or frequencies; and F(k,t) is the three-dimensional transfer spectrum function related to the Fourier transform of third-order velocity-correlation tensor and is associated with energy transfer between wave numbers or eddy sizes, so it is frequently referred to as the energy-transfer-spectrum function. Eq.(2-12) is indeterminate due to the unknown behavior of the transfer spectrum function F(k,t). Two ways can be used to overcome this difficulty: 1) assume some appropriate functional form for F(k,t) as in the case of Reynolds stresses; or 2) directly draw some conclusions about the functional form of E(k,t). Various forms of F(k,t) and E(k,t) have been suggested to be used in solving Eq.(2-12).

In the case of no energy supply we integrate Eq.(2-12) from zero to infinity over k by taking into consideration that the integral of F(k,t) is zero because there is no net transfer over all the wave numbers. Thus a relationship between the turbulence energy dissipation per unit mass, ε, and the energy spectrum function is established, since the time derivative of the integration of E(k,t), $\frac{\partial}{\partial t}\int_0^\infty E(k,t)dt$, is nothing but the change of the total kinetic energy of turbulence which must equal the turbulence energy dissipation rate.

$$\varepsilon = 2\nu\int_0^\infty E(k,t)k^2 dk \qquad (2\text{-}13)$$

In isotropic turbulence, we can express ε as follows:

$$\varepsilon = 15\nu\frac{v^2}{\lambda_g^2} \tag{2-14}$$

So, for isotropic turbulence we have

$$\varepsilon = 15\nu\frac{v^2}{\lambda_g^2} = 2\nu\int_0^\infty E(k,t)k^2 dk \tag{2-14'}$$

where v is the turbulence intensity (the root mean square of fluctuating velocity), and λg is the dissipation scale characterizing the size of eddies mainly responsible for dissipation, often referred to as the microscale of turbulence. Eq.(2-13) and (2-14') can be used to evaluate ε in some regions of turbulence where E(k,t) can be determined analytically or empirically.

For the simplest case, in which the interaction among eddies of various wave numbers is assumed to be negligibly small (i.e. F(k,t) is negligible with respect to the other terms), we can easily get an exponential form of solution for E(k,t) by integrating Eq.(2-12).

$$E(k,t) = E(k,t_0)\exp[(-2\nu k^2(t-t_0)] \tag{2-15}$$

Eq.(2-15) can also be considered the solution for the case in which the viscous effects are predominant corresponding to low values of the Reynolds number and/or viscous fluids.

The energy spectrum for the more general case of higher Reynolds numbers has been the subject of many theoretical and experimental studies. Paraphrasing the explanation from Hinze (1975, pg 221), we consider the energy cascade of turbulence model. In this model, the flux of energy through the wavenumber range and energy dissipation is continuous, i.e. the curve of the energy spectrum function E(k,t) vs. wavenumber *k* is continuous. In order to make the analysis of the turbulence energy spectrum easier, we introduce some definitions used by Hinze (1975, pg 221): "The range of the energy spectrum where the eddies make the main contribution to the total kinetic energy of turbulence will be called the range of the energy-containing eddies". The maximum in the energy spectrum appears in this range, and the wavenumber corresponding to this maximum is denoted as k_e. As mentioned before, energy

dissipation is continuous. Dissipation by viscous effects increases as the wavenumber increases, up to a maximum for a certain value of the largest wavenumbers (or the smallest eddies). We associate a wavenumber k_d with the size of the eddies that provide the main contribution to the total dissipation.

In the process of turbulence development, the larger eddies produce smaller and smaller eddies through inertial interaction, thereby transferring energy to the small eddies. When the turbulence is fully developed the eddies containing the maximum kinetic energy will be the eddies in a higher-wavenumber range, no longer the largest eddies.

For high Reynolds numbers, the range of the energy-containing eddies and the range of maximum dissipation can be considered to be sufficiently wide apart, i.e. $k_e <<< k_d$. For this case, in the range of higher wavenumbers (smaller eddies) the turbulence is characterized by the large amount of energy transferred through eddies compared with the rate of change of their energy, so we may consider that these eddies are in statistical equilibrium with one another. Kolmogoroff made the following hypothesis based on this fact (Hinze, 1975, pg 227): "At sufficiently high Reynolds numbers there is a range of high wavenumbers where the turbulence is statistically in equilibrium and uniquely determined by the parameters ε and ν. This state of equilibrium is universal." **Figure 2-6** shows how the turbulence energy spectrum may be divided into three ranges: large eddies, energy-containing eddies and the universal equilibrium range (Hinze, 1975, pg 229).

From dimensional reasoning Kolmogoroff defined a length scale η and a velocity scale u

$$\eta = (\nu^3 / \varepsilon)^{1/4} \tag{2-16}$$

$$u = (\nu\varepsilon)^{1/4} \tag{2-17}$$

By this definition the Reynolds number with reference to such a velocity scale and length scale is unity

$$\frac{u\eta}{\nu} = 1$$

The wavenumber k_d where the viscous effects become very strong is of the same order as $1/\eta$. The wavenumber k_e marking the range of the energy-containing eddies is of the same order 1/L where L may be interpreted as the average size of the energy-containing eddies, or macroscale of turbulence. It is usual to define

$$k_d = \frac{1}{\eta} \tag{2-18}$$

$$k_e = \frac{1}{L} \tag{2-19}$$

As mentioned above, for the equilibrium range to exist the wavenumber k_d must be large compared to k_e, in terms of the length scale

$$L >>> \eta$$

and the turbulence is independent of the mean flow and the boundaries. Hence, the unit Reynolds number defined above is not sufficient to characterize the turbulence in the whole wavenumber range. Two other Reynolds numbers can be obtained from local parameters: the microscale Reynolds number $R_{e,\lambda}$

$$R_{e,\lambda} = \frac{v\lambda_g}{\nu} \tag{2-20}$$

and the macroscale Reynolds number $R_{e,L}$

$$R_{e,L} = \frac{vL}{\nu} \tag{2-21}$$

Using these two Reynolds numbers the condition for the existence of the equilibrium range becomes

$$R_{e,\lambda}^{3/2} >>> 1 \tag{2-22}$$

in terms of the microscale Reynolds number, and

$$R_{e,L}^{3/4} >>> 1 \tag{2-23}$$

in terms of the macroscale Reynolds number.

We mentioned before that in the equilibrium range the dissipation increases with the wavenumber. If the Reynolds number is very large it is reasonable to assume that there is a subrange of wavenumbers very far below the region of maximum dissipation in which the dissipation is negligibly small compared with the flux of energy transferred by

inertial effects. In such a subrange the effect of the parameter ν would then vanish. Based on this consideration Kolmogoroff made his second hypothesis: "If the Reynolds number is infinitely large, the energy spectrum in the subrange satisfying the condition ($ke<<k<<k_d$) is independent of ν, and is solely determined by one parameter ε." This subrange is usually called inertial subrange because the inertial transfer of energy is the dominating factor in this subrange. The condition for the existence of this subrange becomes

$$R_{e,\lambda}^{3/4} >>> 1 \tag{2-24}$$

in terms of the microscale Reynolds number, or

$$R_{e,L}^{3/8} >>> 1 \tag{2-25}$$

in terms of the macroscale Reynolds number.

From dimensional analysis Kolmogoroff arrived at the following expression for the energy spectrum in the inertial subrange

$$E(k,t) = c\varepsilon^{2/3}k^{-5/3} \tag{2-26}$$

which has been confirmed theoretically and experimentally for stirred tanks by various investigators (Cutter, 1966, Kim and Manning, 1964, Komasawa et al., 1974, Nishikawa et al., 1976, Gunkel and Weber, 1975, Kresta and Wood, 1991, Hinze, 1975, pg 252).

The higher wavenumber region of the universal equilibrium range is called the viscous dissipation range. Heisenberg obtained a k^{-7} relationship between E(k,t) and k in this subrange. The energy spectrum function is in the form

$$E(k,t) = \left(\frac{c\varepsilon}{2\nu^2}\right)^2 k^{-7} \tag{2-27}$$

An equation applicable for the whole universal equilibrium range has been proposed by Chandrasekhar (1949)

$$E(k) = \left(\frac{8}{9c}\right)^{2/3}(\varepsilon\nu^5)^{1/4}\frac{(k/k_d)^{-5/3}}{\left[1+\frac{8}{3c^2}\left(\frac{k}{k_d}\right)^4\right]^{4/3}} \tag{2-28}$$

Eq.(2-28) reduces to Eq.(2-26) when $k/k_d<<1$ and to Eq.(2-27) when $k/k_d>>1$.

2.5.2 Relative Velocity in Local Isotropic Turbulence

The concept of local isotropy was first proposed by Kolmogoroff. Batchelor (1947, 1951) made a good summary in English. The main points of this concept and the expressions for the relative velocity are summarized briefly here. They will be used extensively in the chapters which follow.

We have already introduced the definitions of turbulence intensity, the wavenumbers k_c and k_d, Kolmogoroff's length scale η and velocity scale u, the turbulence microscale λ_g and the turbulence macroscale L, and the relationship between ε and the energy spectrum function. Now we introduce the definition of the relative velocity between two spatial points:

$$\overline{V^2(\bar{r})} = \overline{[V(r_1) - V(r_2)]^2} \tag{2-29}$$

where r is a component of space coordinates, $\bar{r}$ is the radius vector $r_1 r_2$. If in any small volume of liquid, for any value of $\bar{r}$, $\overline{V^2(\bar{r})}$ is independent of the direction of $\bar{r}$ and time, we say the turbulence is in local isotropy. Any relative velocity in the space should be a function of u^2 (dimension consistence) and the length scale η. Therefore

$$\overline{V^2(r)} = B(\bar{r}, u^2, \eta) \tag{2-30}$$

It can be shown that B must be of the form

$$\overline{V^2(r)} = u^2 B\left(\frac{r}{\eta}\right) \tag{2-31}$$

where B is an universal function, the properties of which are unknown. But for the following limiting cases the values of B can be found:

1) Case 1: $r \ll \eta$

For this case, the energy is dissipated in the region of viscous shear.

The function $\overline{V(r)}$ is an even function of r vanishing with r, therefore $B\left(\frac{r}{\eta}\right)$ must have the same properties. For very small values of r, $\frac{\partial V(r)}{\partial r}$ is constant and V(r) is directly proportional to r. Thus Eq.(2-31) can be written as

$$\overline{V^2(r)} = u^2 c_1 \left(\frac{r}{\eta}\right)^2 = \varepsilon^{1/2}\nu^{1/2} c_1 \frac{r^2}{\varepsilon^{-1/2}\nu^{3/2}} = c_1 \frac{\varepsilon}{\nu} r^2 \qquad (2\text{-}32)$$

2) Case 2: L>>r>>η

This region lies in the inertial subrange where the velocity correlation between the two points satisfying L>>r>>η is a function of ε and $|\vec{r}|$, and is independent of viscosity ν. This velocity correlation $V^2(r)$ between the two points is determined by the eddies having a wave length of the same magnitude as r. As stated in the section above, in this region the motion due to the larger eddies is determined by the constant rate at which each eddy passes energy to its next smaller neighbor, and the proportion of energy dissipated by viscosity is negligible. $V^2(r)$ is therefore independent of ν, which can only be true from dimensional analysis if

$$B\left(\frac{r}{\eta}\right) = c_2 \left(\frac{r}{\eta}\right)^{2/3} \qquad (2\text{-}33)$$

Thus

$$\overline{V^2(r)} = \varepsilon^{1/2}\nu^{1/2} c_2 \left(\frac{r}{\varepsilon^{-1/4}\nu^{3/4}}\right)^{2/3} = c_2 \varepsilon^{2/3} r^{2/3} \qquad (2\text{-}34)$$

The direct verification of Eq.(2-32) and (2-34) experimentally has never been achieved, but many investigators use these two equations to calculate velocity derivatives and to express the inertial force. Their data shows agreement with the theory under the operations used. Detailed comparisons of the results will be reviewed in **Chapter 3**.

2.5.3 Experimental Investigations of Turbulence Energy Dissipation Characteristics in Agitated Tanks

From the First Law of Thermodynamics, the energy balance for the material (system) in a non-flow agitated tank should be simple, since only the shaft work of the impeller and heat are exchanged between the system and its environment. No other forms of energy are transferred if no electrical and/or magnetic work is involved. It is true that all the power consumed by an impeller of any shape or size is converted into heat in a non-flow agitated tank, but the conversion mechanism in the tank is much more

complex than the overall energy balance. As analyzed in **Section 2.5.1**, this conversion mechanism interacts in complex ways through the viscous stresses. Many investigators have studied turbulence energy dissipation characteristics in agitated tanks. They concluded that the micro eddies play an important role in the conversion. Oldshue (1993) defined the micro scale mixing as a qualitative number - beginning at about 100 microns. He argued that the fluctuating part of the velocity goes to make up the micro scale environment, and that this is where the power is ultimately dissipated.

2.5.3.1 The Average Energy Consumption

For the characteristics of average energy consumption in the whole tank, the research results were summarized in **Section 2.4.4**. The power number is constant when the turbulence is fully developed and the Reynolds number is larger than 10^4. This means that the total energy consumption in a stirred tank is independent of the viscosity and is a function of only the geometric design of the impeller and its speed. This is an indication that the energy of the large eddies created by the impellers is independent of viscosity. In terms of the average energy consumption per unit mass, ($\bar{\varepsilon} = P/\rho V_T$), this conclusion can be described as:

$$\bar{\varepsilon} = k' N^3 D^2 \qquad (2\text{-}35)$$

where k' is a constant dependent on the geometry of the tank and the impeller.

2.5.3.2 The Local Turbulence Energy Dissipation

The knowledge of the average energy dissipation is not sufficient to determine the characteristics of the turbulence energy dissipation in an agitated tank. Direct determination of local turbulence energy dissipation ε by experiments, however, is practically impossible, since all three mean and fluctuating velocities and higher order of velocity correlations are needed. Several methods using a combination of theoretical and experimental bases have been proposed.

Cutter (1966) started with the Navier-Stokes equations and derived the following equation to calculate ε

$$2\pi r\int_{-\infty}^{+\infty}\varepsilon dz=\frac{d}{dr}[r2\pi\int_{0}^{\infty}(K^2\overline{V_z}+2\overline{V_\theta v'_r v'_\theta})dz] \qquad (2\text{-}36)$$

where K^2 equals $\overline{V_z}^2+\overline{V_r}^2+\overline{V_\theta}^2+\overline{v'^2_z}+\overline{v'^2_r}+\overline{v'^2_\theta}$. He made the following main assumptions during the derivation of Eq.(2-36):

a) the turbulence is steady, so the time means and variances of velocity at any given point in the tank are independent of time, when estimated from a sufficient number of measurements, taken over a sufficient long interval of time;

b) the viscous forces are negligible in comparison with the inertial forces since the impeller is operating under conditions such that the power consumption is independent of the viscosity;

c) the turbulence is isotropic, so $\overline{v'^2_z}\approx\overline{v'^2_r}\approx\overline{v'^2_\theta}$;

d) axial mean velocities are negligible compared with radial and tangential components for a RT;

e) circular symmetry exists, i.e. $\partial/\partial\theta=0$.

With Eq.(2-36) and the data of the mean and fluctuating components of velocity measured by a photographic method in the flow agitated by the RT, Cutter determined the local turbulence energy dissipation. He concluded that most of the energy supplied to the impeller is dissipated in the impeller region (~20%) and the impeller stream (~50%), with only about 30% being dissipated in the rest of the tank (approximately 90% of the tank volume). He found that the values of the ratio $\varepsilon/\bar{\varepsilon}$ vary tremendously in the tank from 0.25 outside the impeller stream to 70 in the immediate neighborhood of the impeller: this means that there is 270-fold difference between local turbulence energy dissipation rates in the tank.

Gunkel and Weber (1975) measured the flow parameters in a baffled tank agitated by the RT with air as the working fluid by using a hot-wire anemometer. They proposed a totally different picture of the turbulence energy dissipation. They found that most of the energy supplied to the impeller was dissipated outside the impeller stream, that is, in the bulk of the tank. They argued that this disagreement with Cutter's work may be caused by the sufficient scatter of Cutter's data , since the kinetic energy fluxes are

calculated by raising measured velocities to the third power, reliable energy fluxes can only be obtained by accurate experimental data. Gunkel and Weber stated that their data were confirmed by checking the turbulence energy spectrum in the whole universal equilibrium range (inertial and viscous subrange), and mass balance and the power number.

Okamoto et al. (1981) used the integration of the one-dimensional energy spectrum to calculate the local energy dissipation ε. They measured the mean and fluctuating velocities in the flow created by the RT in both the impeller stream and the bulk of tanks in unbaffled and baffled tanks using a hot-film anemometer. In the unbaffled tank the maximum value of the ratio $\varepsilon / \bar{\varepsilon}$ is 11.3 near the tip of the impeller and the minimum value is 0.21 in the bulk outside the impeller stream; in the baffled tank the maximum value of the ratio $\varepsilon / \bar{\varepsilon}$ is 6.50 which is near the tip of the impeller at the center line of blades and the minimum value is 0.16 on the top part region of the bulk. The difference between local turbulence energy dissipation rates in the tank is 54-fold for the unbaffled case and 41-fold for the baffled case. This indicates that the flow in baffled tank is less non-homogenous than the flow in unbaffled tank. Okamoto and co-authors reported the following correlations for the local turbulence energy dissipation rates in the impeller stream ε_i ("right beside the impeller") and the circulation region (bulk) ε_c:

$$\begin{aligned} &\varepsilon_i = 7.8\bar{\varepsilon}(D/T)^{-1.38}\exp(-2.46D/T) \\ &\varepsilon_c = 0.90\bar{\varepsilon}(D/T)^{1.10} \\ &(0.25 \le D/T \le 0.70) \end{aligned} \tag{2-37}$$

They also correlated Sato and co-workers' data and presented the following correlations:

$$\begin{aligned} &\varepsilon_i = c'_1\bar{\varepsilon}(W/T)^{-1.38}\exp(-2.46D/T) \\ &\varepsilon_c = c'_2\bar{\varepsilon}(W/T)^{0.32}(D/T)^{0.78} \\ &(0.05 \le W/T \le 0.30, \qquad 0.25 \le D/T \le 0.70) \end{aligned} \tag{2-38}$$

where c'_1 and c'_2 are constants, the value of c'_1 was 0.85 for the data with six-bladed impeller and four baffle plates. The value of c'_2 was not given.

Costes and Couderc (1988) measured the turbulent flow induced by a RT using LDA. They used energy spectrum analysis to determine the local turbulence energy dissipation and found that

a) near the impeller $\varepsilon / \bar{\varepsilon} \cong 5 \sim 10$.

b) in the bulk of the tank $\varepsilon / \bar{\varepsilon} \cong 0.05 \sim 0.07$ which is much lower than that reported by Cutter and Okamoto et.al. The difference between local turbulence energy dissipation rates in the tank is approximately 100-fold.

Wu and Patterson (1989) also measured the turbulent flow induced by a RT using LDA. They simply used the following equation to calculate ε:

for the kinetic energy flux in radial direction, KE_r

$$KE_r = \rho\pi r \int_{z1}^{z2} \overline{V_r}(\overline{V_z}^2 + \overline{V_r}^2 + \overline{V_\theta}^2 + 3\overline{v'^2_r} + \overline{v'^2_z} + \overline{v'^2_\theta})dz \qquad (2\text{-}39a)$$

for the kinetic energy flux in axial direction, KE_z

$$KE_z = \rho\pi \int_{r_1}^{r2} \overline{V_z}(\overline{V_z}^2 + \overline{V_r}^2 + \overline{V_\theta}^2 + 3\overline{v'^2_z} + \overline{v'^2_r} + \overline{v'^2_\theta})rdr \qquad (2\text{-}39b)$$

By doing the energy balance, they concluded that about 30% of the total energy was dissipated in the impeller region, about the same amount was dissipated in the impeller stream (the fluid in the impeller and the impeller stream region is only 9% of the total), and the rest (about 40%) was dissipated in the bulk of the tank. They only reported the values of ε in the impeller stream. The maximum value of the ratio $\varepsilon / \bar{\varepsilon}$ for their work is about 22 near the tip of the impeller. In **Chapter 5** the derivation of the turbulence energy dissipation in a control volume used in this work is given. It differs somewhat from that used by Wu and Patterson (1989).

Ranade and Joshi (1989), and Ranade et al. (1992) calculated the turbulence kinetic energy flux in the same way as Wu and Patterson, using the LDA data for a PBT, but the equations in the two papers are all multiplied by 2 which should be canceled in the derivation of the equations. Ranade and Joshi reported the profiles of turbulent kinetic energy normalized with the square of impeller tip speed, and the effects of blade angle and blade width on the dimensionless turbulent kinetic energy, but no data about the turbulence energy dissipation in specific regions of the tank were reported. In the

paper of Ranade et al., the authors defined a "hydraulic efficiency" which is the ratio of the rate of kinetic energy flowing out of the impeller swept volume (including the impeller and the impeller stream) to the total energy input rate, so the percent of the total energy dissipated in the impeller and the impeller stream should be $(1-\eta_H)$x100. For the five different geometries of PBT's they studied (pitch angle from 30° to 60°, W/D from 0.2 to 0.4), 46% to 34% of the total energy was dissipated in the impeller and the impeller stream, with the value 46% corresponding with the geometry: pitch angle=45° and W/D=0.2, which is often considered as a standard design.

It has been shown experimentally (Cutter, 1966, Sachs and Rushton, 1954, Aiba, 1958, Ranade and Joshi, 1989, Dyster et al., 1993) that the velocity distribution at Reynolds numbers above 104 is universal, i.e. the ratio of the average flow velocities at two points is constant and independent of Reynolds numbers and fluid properties. Shinnar (1961) argued that in such a case the spatial distribution of local turbulence energy dissipation ε is universal also, and that all local values of ε are then directly proportional to $\bar{\varepsilon}$. That is

$$\varepsilon(x,y,z) = k''(x,y,z)\,N^3 D^2 \tag{2-40}$$

The dimensionless factor k'' is an experimentally determinable function of the coordinates of any point in the tank. This arguments can be deduced directly from the estimate equation of ε proposed by Batchelor (1953).

$$\varepsilon = A\frac{v^3}{L} \tag{2-41}$$

where A is an empirical constant in the order of magnitude O(1), L, as defined on page 28, is the characteristic length of large eddies, and v is the streamwise component of turbulence intensities or commonly called the root-mean square (rms) of fluctuating velocities. It should be briefly mentioned that Eq.(2-41) can be derived in several ways. According to the basic definition of ε as the change of turbulence kinetic energy, Tennekes and Lumley made a dimensional argument to express the time by a fluctuating velocity component and a length scale of turbulence, and got the equation. Starting from

Eq.(2-14) and using Taylor's equation (Hinze, 1975, pg 225) to compute the microscale of the turbulence:

$$\lambda^2 \propto \frac{L\nu}{v} \tag{2-42}$$

equation (2-41) forms. Now we go back to the local turbulence energy dissipation ε. According to Eq.(2-41), if the fluctuating velocity is proportional to ND and L can be set to some fraction of D, then ε is proportional to N^3D^2 as Eq.(2-40). Experimental investigations showed the fluctuating velocity in a fully developed turbulence is exactly proportional to ND (Bertrand et al., 1980, Laufhutte and Mersmann, 1985, Ranade and Joshi, 1989, Dyster, 1993), and the macroscale length L can be set to some fraction of D (Brodkey, 1975).

It should be pointed out that the isotropy of the turbulence is assumed in the derivation of Eq.(2-41), and only in isotropic turbulence can the turbulence kinetic energy be approximated by a single component of fluctuating velocities. In a more general case, all three fluctuating velocities are needed to find the turbulence kinetic energy. Thus the following equation is often used by investigators to estimate ε

$$\varepsilon = A' \frac{q^{3/2}}{L} \tag{2-43}$$

where $q \equiv \frac{1}{2}(\overline{v'^2_z} + \overline{v'^2_r} + \overline{v'^2_\theta})$, or $\equiv \frac{1}{2}(v_z^2 + v_r^2 + v_\theta^2)$. The constant A in Eq.(2-41) or A' in Eq.(2-43) is related to the determination of the macroscale length of turbulence L or L' and the choice of the velocity scale v or $q^{1/2}$. The length scale L can be obtained in two ways: one is to set it as some fraction of the impeller diameter (Brodkey, 1975), another is to calculate it from the integration of autocorrelation functions (Wu et al., 1989, Wu and Patterson, 1989) which is briefly introduced below. Wu and Patterson first related the characteristic length via the mean velocity:

$$L = \bar{V}\,\tau_E \tag{2-44}$$

where τ_E is the Eulerian integral time scale obtained by taking the integral of the autocorrelation function:

$$\tau_E = \int_0^\infty R_E dt \tag{2-45}$$

where the autocorrelation function R_E is defined as:

$$R_E = \frac{\overline{v'(t')v'(t'+t)}}{\overline{v'^2}} = \frac{\overline{v'(t')v'(t'+t)}}{v^2} \tag{2-46}$$

Wu and Patterson suggested that several corrections to these relations are necessary because the flow is three dimensional and the fluctuating velocity contains a periodic component.

Kresta and Wood (1993b) summarized the values of A or A′ corresponding to different characteristic length and velocity scales used by various investigators (see **Table 2-2**). Most of the reported results are for Rushton turbines (Rao and Brodkey, 1972, Laufhutte and Mersmann, 1985, Costes and Couderc, 1988, Wu et al., 1989, Wu and Patterson, 1989). Rao and Brodkey (1972) used several other types of impellers and got the same value for the length scale, while Laufhutte and Mersmann (1987) got nearly the same value for the length scale with a PBT.

If we use $q = \frac{3}{2}v^2$ by assuming local isotropy of the turbulence, **Table 2-3** can be obtained. From **Table 2-3**, we can conclude that the constant is approximately 1 when the streamwise component of turbulence intensities are used and the macroscale length of the turbulence is set to D/10. The value of A obtained by Laufhutte and Mersmann is around 0.6 because they used the estimate equation to calculate ε for *whole tank*: turbulence energy dissipation rate in the bulk of the tank is much smaller than that in the impeller regions, so when L is set to D/10 the constant A is well smaller than 1.

Schwartzberg and Treybal (1968) obtained an approximate value for L based on the scale of turbulence reported by Cutter (1966) for the energy-containing eddies in the impeller discharge stream of the tank. They presented the following relation

$$\frac{1}{k_e} = L = 0.08D \tag{2-47}$$

which is in excellent agreement with the values L=D/10 in **Table 2-3**.

Estimated results of ε using Eq.(2-41) or (2-43) showed that differences of the order of tens or hundreds of times in the turbulence energy dissipation rates at different positions in the tank exist due to the appreciable differences in the state of turbulence at different positions within the tank.

From the analysis of **Section 2.5.2**, we know that relative velocity (determining the external forces deforming droplets) is related to local turbulence energy dissipation rate, ε, in the universal equilibrium range. It is clear that ε is a critical variable to determine the mean drop size and drop size distribution in an agitated tank. This will be discussed further in the next chapter, when the mechanisms of drop breakup and the correlations for mean drop size in agitated tanks are reviewed.

In **Chapters 5** and **6**, Eq.(2-41) will be used to estimate the local turbulence energy dissipation rate. Isotropic flow, an assumption inherent in Eq.(2-41), will be checked in the measurement regions - the impeller region and impeller discharge region. The macroscale turbulence length L in Eq.(2-41) will be compared for the three impellers - the RT, the PBT and the A310, with emphasis on the less studied impeller - A310. Effects of geometric variables (impeller diameter, number of baffles, off bottom clearance) and rotational speed of the impeller on ε will be investigated, and the main variables affecting ε will be chosen to be studied in the experiments to measure mean drop sizes. The experimental results of local turbulence energy dissipation rates, especially the maximum turbulence energy dissipation rates, will be related to the mean drop sizes and presented in **Chapter 7** and the following chapters.

Tables in Chapter 2

Table 2-1 Power numbers for the Rushton turbine in fully turbulent flow

Series	Investigators	Power number N_p
1	Rushton et al., 1950	6.2
2	Flynn and Treybal, 1955	6.0
3	Laity and Treybal, 1957	5.5
4	Calderbank, 1958	5.5
5	Bates et al., 1963	5.0
6	Esch, 1971	5.1
7	Nienow and Miles, 1971	5.0
8	Brauer et al., 1972	5.1*
9	Pharamond, 1973	5.1*
10	Boon-Long, 1976	5.5*
11	Bertrand et al., 1980	5.1
12	Yianneskis et al., 1987	4.8
Average (series from 1 to 11)**		5.4

* From Bertrand et al., 1980.

** D from T/4 to T/2, C from T/4 to T/2, in baffled tanks.

Table 2-2 Values of the constant in Eq. (2-41) or Eq. (2-43) (from Kresta and Wood. 1993b)

Reference	Velocity Scale	Length Scale	Value of A or A′
Laufhutte and Mersmann, 1985	v	D	6 to 6.6
Laufhutte and Mersmann, 1987	v	D	5.5 to 7.2, recommends 6.25
Costes and Couderc (1988)	$q^{1/2}$	D	4.4±2.4
Rao and Brodkey, 1972	v	D/2	4.4
Wu et al., 1989	$q^{1/2}$	from autocorrelation	0.946
Wu and Patterson, 1989	$q^{1/2}$	from autocorrelation	0.85±10%
Cutter, 1966	v	from correlation coefficient	0.51
Stoots and Calabrese, 1989	$q^{1/2}$	D/5	1

Table 2-3 Values of the constant in Eq. (2-41) or Eq. (2-43) when L is set to D/10

Reference	Velocity Scale	Length Scale	Value of A or A′
Laufhutte and Mersmann, 1985	v	D/10	0.6 to 0.66 *
Laufhutte and Mersmann, 1987	v	D/10	0.55 to 0.72, * recommends 0.625
Costes and Couderc (1988)	$q^{1/2}$ replaced by v	D/10	0.81±0.44
Rao and Brodkey, 1972	v	D/10	0.88
Stoots and Calabrese, 1989	$q^{1/2}$ replaced by v	D/10	0.92

* based on whole tank.

Figures in Chapter 2

Figure 2-1 Schematic drawings of the three impellers-PBT, A310 and RT.

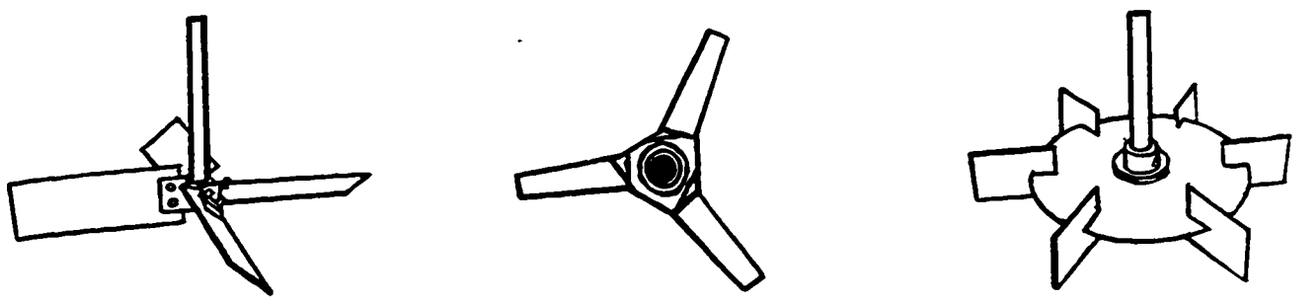

Pitched Blade Turbine (PBT) Fluidfoil Impeller (A310) Rushton Turbine (RT)

Figure 2-2 Geometry of the stirred tank (T=0.240 m, H=T).

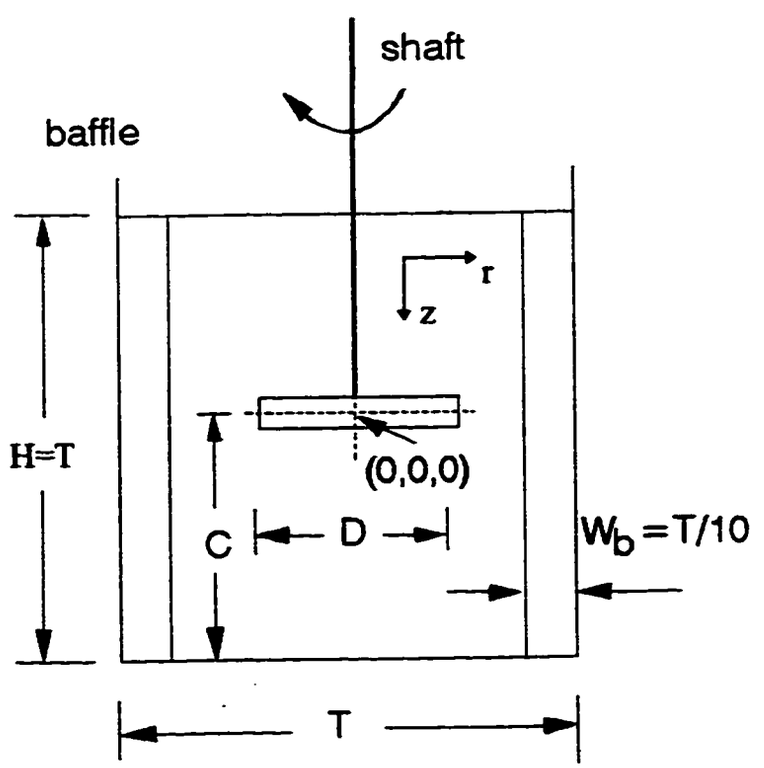

Figure 2-3 Schematic three dimensional view of the trailing vortex pair produced by the RT (from Van't Riet and Smith, 1975).

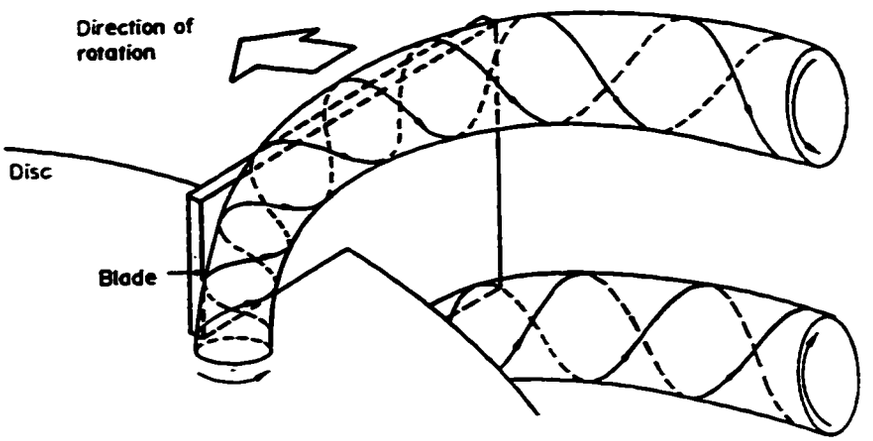

Figure 2-4 Schematic drawing of the second circulation loop created by the PBT (from Kresta and Wood, 1993). (a) tank mid-section; (b) flow at the tank wall; (c) impingement at the bottom of the tank.

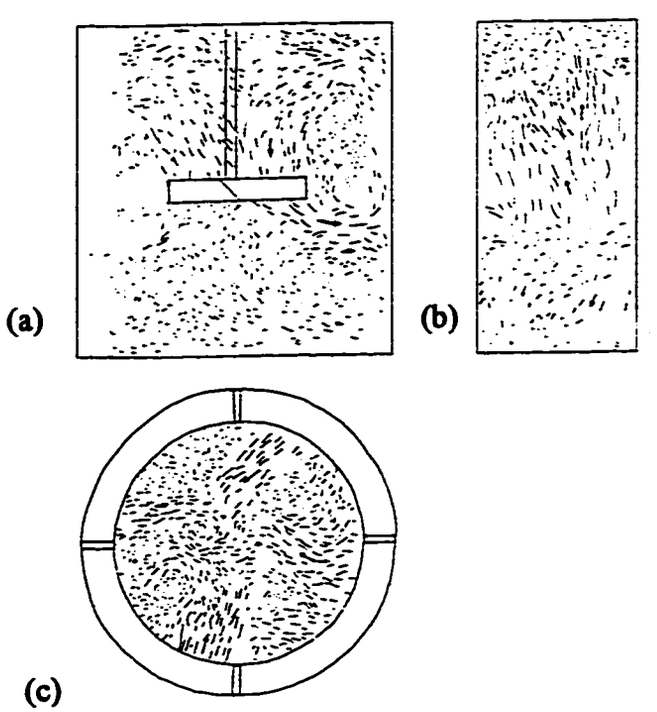

Figure 2-5 General flow patterns for the PBT, A310 and RT.

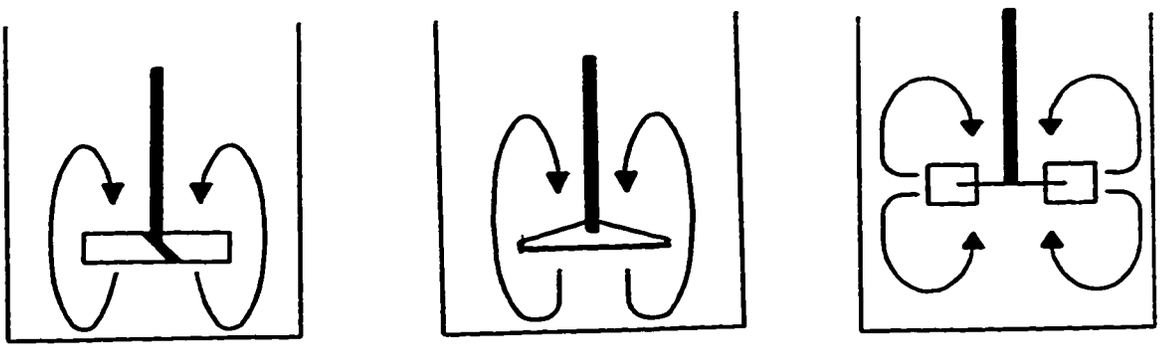

Figure 2-6 Form of the three-dimensional energy spectrum function E(k,t) in the various wavenumber ranges (from Hinze, 1975, pg 229).

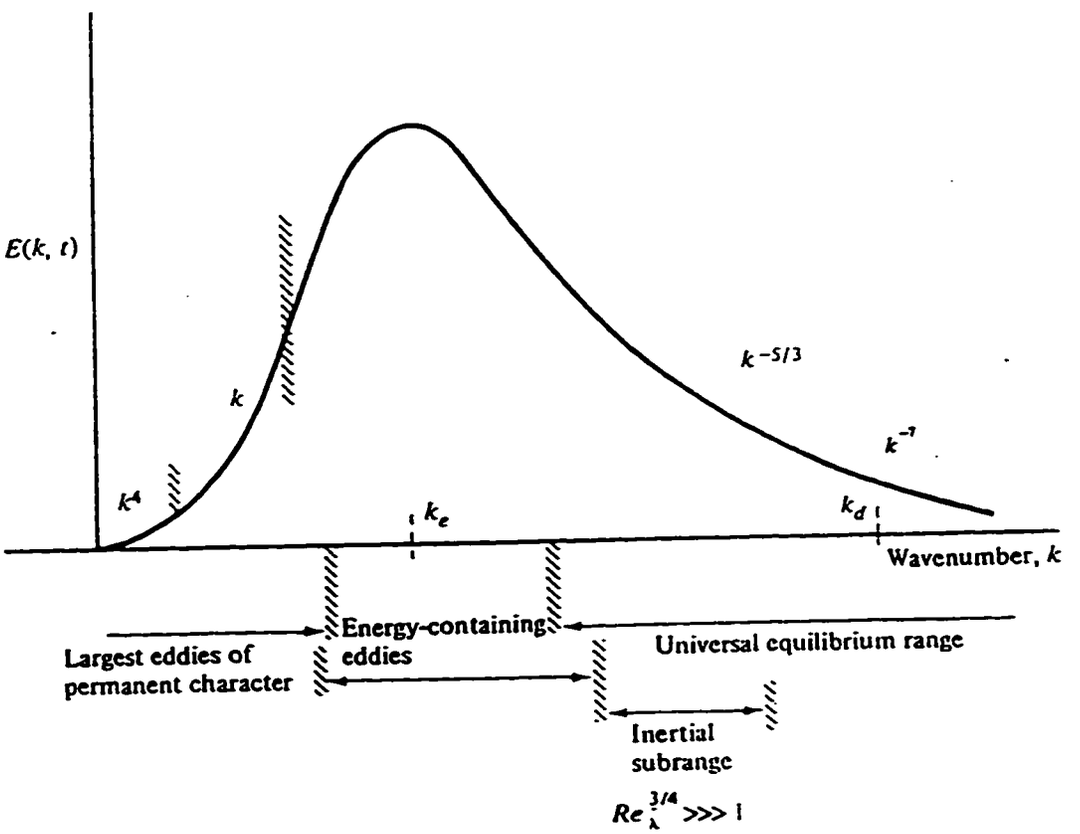

References

Aiba, S., 1958, Flow patterns of liquids in agitated vessels. *AIChE J.* **4**, 485-489.

AIChE, 1960, *Standard testing procedure, impeller-type mixing equipment*, AIChE, New York.

Ali, A. M., Yuan, H. H. S., Dickey, D. S. and Tatterson, G. B., 1981, Liquid dispersion mechanisms in agitated tanks: Part I. pitched blade turbine. *Chem. Eng. Commun.* **10**, 205-213.

Arai, K., Konno, M., Matunaga, Y. and Saito, S., 1977, Effect of dispersed-phase viscosity on the maximum stable drop size for breakup in turbulent flow. *J. Chem. Eng. Japan* **10**, 325-330.

Baldwin, L. V. and Walsh, T. J., 1961, Turbulent diffusion in the core of fully developed pipe flow. *AIChE J.* **7**, 53-61.

Bertrand, J., Couderc, J. P. and Angelino, H., 1980, Power consumption, pumping capacity and turbulence intensity in baffled stirred tanks: comparison between several turbines. *Chem. Eng. Sci.* **35**, 2157-2163.

Batchelor, G.K., 1947, *Cambridge Phil. Soc. Proc.* **43**, 533.

Batchelor, G.K., 1951, *Cambridge Phil. Soc. Proc.* **47**, 359.

Bird,, R. B., Stewart, W. E. and Lightfoot, E. N., 1960, *Transport phenomena*, Wiley, New York.

Buckingham, E., 1914, On physically similar systems: illustrations of the use of dimensional equations. *Phys. Rev.* **IV(4)**, 345.

Calderbank, P. H., 1958, Physical rate processes in industrial fermentation, Part I: The interfacial area in gas-liquid contacting with mechanical agitation. *Trans. IChemE.* **36**,.443-463.

Chandrasekhar, S., 1949, The theory of statistical and isotropic turbulence. *Phys. Rev.* 75, 896.

Cooper, R. G. and Wolf, D., 1968, Velocity profiles and pumping capacities for turbine type impellers. *Can. J. Chem. Eng.* **46**, 94-100.

Costes, J. and Couderc, J. P., 1988a, Study by laser Doppler anemometry of the turbulent flow induced by a Rushton turbine in a stirred tank: influence of the size of the units-I. mean flow and turbulence. *Chem. Eng. Sci.* **43**, 2751-2764.

Costes, J. and Couderc, J. P., 1988b, Influence of the size of the units-II. spectral analysis and scales of turbulence. *Chem. Eng. Sci.* **43**, 2765-2772.

Cutter, L. A., 1966, Flow and turbulence in a stirred tank. *AIChE J.* 12, 35-45.

Desouza, A. and Pike, R. W., 1972, Fluid dynamics and flow patterns in stirred tanks with a turbine impeller. *Can. J. Chem. Eng.***50**, 15-23.

Dickey, D. S. and Fenic, J. C., 1976, Dimensional analysis for fluid agitation system. *Chem. Eng.* **January** 5, 139-145.

Dickey, D. S., 1993, Dimensional analysis, similarity and scale-up. *Process mixing-chemical and biochemical applications: Part II, AIChE Symposium Series, New York,* **89**,143-150.

Dyster, K. N., Koutsakos, E., Jaworski, Z. and Nienow, A. W., 1993, An LDA study of the radial discharge velocities generated by a Rushton turbine: Newtonian fluids, Re≥5. *Trans IChemE*, **71**, Part A,11-23.

Esch, D. D., D'Angelo, P. J. and Pike, R. W., 1971, On minimum power requirements for emulsification of two-phase, liquid systems. *Can. J. Chem. Eng.* **49**, 872-875.

Flynn, A. W. and Treybal, R. E., 1955, Liquid-liquid extraction in continuous-flow agitated extractors. *AIChE J.* **1**, 324-328.

Fort, I, Podivinska, J. and Baloun, R., 1969, The study of convective flow in a system with a rotary mixer and baffles. *Collection Czechoslov. Chem. Commun.* **34**, 959-974.

Gunkel, A. A. and Weber, M. E., 1975, Flow phenomena in stirred tanks: Part I. the impeller stream. *AIChE J.* **21**, 931-949.

Hinze, J. O., 1955, Fundamentals of the hydrodynamic Mechanism of splitting in dispersion processes. *AIChE J.* **1**,.289-295.

Hinze, J. O., 1975, *Turbulence*, Second Edition, McGraw-Hill, New York.

Hixson, A. W. and Luedeke, V. D., 1937, *Ind. Eng. Chem.* **29**, 927.

Jaworski, Z., Fort, I. and Strek, F., 1988, Turbulent flow characteristics for pitched blade turbine. *Collect. Czech. Chem. Commun.***53**, 957-967.

Jaworski, Z., Nienow, A. W., Koutsakos, E., Dyster, K. and Bujalski, W., 1991, An LDA study of turbulent flow in a baffled vessel agitated by a pitched blade turbine. *Trans. I.Chem.E.* **69**, 313-320.

Johnstone, R. E. and Thring, M. W., 1957, *Pilot plants, models and scale-up methods in chemical engineering*, McGraw-Hill, New York.

Kim, W. J. and Manning, F. S., 1964, Turbulence energy and intensity spectra in a baffled, stirred vessel. *AIChE J.***10**, 747-752.

Komasawa, I., Kuboi R. and Otake, T., 1974, Fluid and particle motion in turbulent dispersion. *Chem. Eng. Sci.* **29**, 641.

Kresta, S. M., 1991, *Characterization, measurement and prediction of the turbulent flow in stirred tanks*, Ph.D. Thesis.

Kresta, S. M. and Wood, P. E., 1993a, The mean flow field produced by a 45° pitched blade turbine: changes in the circulation pattern due to off bottom clearance. *Can. J. Chem. Eng.***71**, 42-53.

Kresta, S. M. and Wood, P. E., 1993b, The flow field produced by a pitched blade turbine: characterization of the turbulence and estimate of the dissipation rate. *Chem. Eng. Sci.* **48**, 1761-1774.

Laity, D. S. and Treybal, R. E., 1957, Dynamics of liquid agitation in the absence of an air-liquid interface. *AIChE J.* **3**, 176-180.

Laufhutte, H. D. and Mersmann, A., 1985, Laser-Doppler velocimetry as a suitable measuring technique for the determination of flow behaviour in stirred fluids. *Ger. Chem. Eng.* **8**, 371-379.

Laufhutte, H. D. and Mersmann, A., 1987, Local energy dissipation in agitated turbulent fluids and its significance for the design of stirring equipment. *Chem. Eng. Technol.***10**, 56-63.

Levins, D. M., and Glastonbury, J. R., 1972, Particle-liquid hydrodynamics and mass transfer in a stirred vessel: Part I-particle-liquid motion. *Trans.IChemE.* **50**, 32-41.

Metzner, A. B. and Taylor, J. S., 1960, Flow patterns in agitated vessels. *AIChE J.* **6**, 109-114.

Mujumdar, A. S., Huang, B., Wolf, D., Weber, M. E. and Douglas, W. J. M., 1970, Turbulence parameters in a stirred tank. *Can. J. Chem. Eng.* **48**,.475-483.

Nagata, S., Yamamoto, K. and Hashimato, K., 1959, Flow patterns of liquids in acylindrical mixing vessel with baffles. *Mem. Fac. Eng., Kyoto University* **21**, 260.

Nagata, S., Yamamoto, K. and Hashimato, K., 1960, Studies on the flow patterns of liquids in acylindrical mixing vessel over a wide range of Reynolds number. *Mem. Fac. Eng., Kyoto University* **22**, 68.

Nienow, A. W. and Miles, D., 1971, Impeller power numbers in closed vessels. *Ind. Eng. Chem. Process Des. Develop.* **10**, 41-43.

Nishikawa, M., Okamoto, Y., Hashimoto, K. and Nagase, S., 1976, Turbulence energy spectra in baffled mixing vessels. *J. Chem. Eng. Japan* **9**, 489-494.

Nouri, J. M., Whitelaw, J. H. and Yianneskis, M., 1987, The scaling of the flow field with impeller size and rotational speed in a stirred reactor. *Second International Conference on Laser Anemometry - Advances and Applications*, Strathclyde, UK, (Sept.).

Okamoto, Y., Nishikawa, M. and Hashimoto, K., 1981, Energy dissipation rate distribution in mixing vessels and its effects on liquid-liquid dispersion and solid-liquid mass transfer. *Int. Chem. Eng.***21**, 88-94.

Oldshue, J. Y., 1993, Geometric relationships for scale-up of diverse mixing processes. *Process Mixing-chemical and biochemical applications: Part II. AIChE Symposium Series* **89**, New York, 158-163.

Ranade, V. V. and Joshi, J. B., 1989, Flow generated by pitched blade turbines I: measurements using laser Doppler anemometer. *Chem. Eng. Commun.* **81**, 197-224.

Ranade, V. V. and Joshi, J. B., 1989, Flow generated by pitched blade turbines II: Simulation using $k-\varepsilon$ model. *Chem. Eng. Commun.* **81**, 225-248.

Ranade, V. V., Mishra, V. P., Saraph, V. S., Deshpande, G. B. and Joshi, J. B., 1992, Comparison of axial flow impellers using a laser Doppler anemometer. *Ind. Eng. Chem. Res.* **31**, 2370-2379.

Rao, M. A. and Brodkey, R. S., 1972, Continuous flow stirred tank turbulence parameters in the impeller stream. *Chem. Eng. Sci.* **27**, 137-156.

Rayleigh, J. W. S., 1915, *Nature*, **95**, 66.

Reed, X. B., Princz, M. and Hartland, S., 1977, Laser Doppler measurements of turbulence in a standard stirred tank. *Second European Conference on Mixing*, Cambridge, England.

Rushton, J. H., Costich, E. W and Everett, H. J., 1950a, Power characteristics of mixing impellers-Part I. *Chem. Eng. Prog.* **46**, 395-404.

Rushton, J. H., Costich, E. W and Everett, H. J., 1950b, Power characteristics of mixing impellers-Part II. *Chem. Eng. Prog.* **46**, 467-476.

Rushton, J. H. and Oldshue, J. Y., 1953a, Mixing-present theory and practice-Part I. *Chem. Eng. Prog.* **49**, 161-168.

Rushton, J. H. and Oldshue, J. Y., 1953b, Mixing-present theory and practice-Part II. *Chem. Eng. Prog.***49**, 267-275.

Sachs, J. P. and Rushton, J. H., 1954, Discharge flow from turbine-type mixing impellers. *Chem. Eng. Prog.* **50**, 597-603.

Schwartzberg, H. G. and Treybal, R. E., 1968, Fluid and particle motion in turbulent stirred tanks-fluid motion. *I. & E. C. Fund.***7**, 1-6.

Shen, Z. J. and Baird, M. H. I., 1991, The delta mixing impeller- some hydrodynamic studies. *Chem. Eng. Res. Des.* **69**, 143.

Shinnar, R., 1961, On the behaviour of liquid dispersions in mixing vessels. *Fluid Mech.* **10**, 259-275.

Tennekes, H. and Lumley, J. L., 1972, *A First Course in Turbulence*, MIT Press, Cambridge, Mass..

Uhl, V. W. and Gray, J. B., 1966, *Mixing, theory and practice, Volume 1*. Academic Press, New York.

Van der Molen, K. and van Maanen, H. R. E., 1978, Laser-Doppler measurements of turbulent flow in stirred vessels to establish scaling rules. *Chem. Eng. Sci.* **33**, 1161-1168.

Van't Riet, K. and Smith, J. M., 1973, The behaviour of gas-liquid mixtures near Rushton turbine blades. *Chem. Eng. Sci.* **28**, 1031-1037.

Van't Riet, K. and Smith, J. M., 1975, The trailing vortex system produced by Rushton turbine agitators. *Chem. Eng. Sci.* **30**, 1093-1105.

Van't Riet, K., Bruijn, W. and Smith, J. M., 1976, Real and pseudo-turbulence in the discharge stream from a Rushton turbine. *Chem. Eng. Sci.* **31**, 407.

Winardi, S., Nakao, S. and Nagase, Y., 1988, Pattern recognition in flow visualization around a paddle impeller. *J. Chem. Eng. Japan* **21**, 503-508.

Wu, H. and Patterson, G. K., 1989, Laser Doppler measurements of turbulent-flow parameters in a stirred mixer. *Chem. Eng. Sci.* **44**, 2207-2221.

Wu, H., Patterson, G. K. and Van Doorn, M., 1989, Distribution of turbulence energy dissipation rates in a Rushton turbine stirred mixer. *Expts in Fluids* **8**, 153-160.

Yianneskis, M., Popiolek, Z. and Whitelaw, J. H., 1987, An experimental study of the steady and unsteady flow characteristics of stirred reactors. *Fluid Mech.* **175**, 537-555.

Chapter 3

Literature Review-Mechanisms of Drop Breakup and Mean Drop Size

3.1 Introduction

When two immiscible liquids are agitated, a dispersion is formed in which continuous breakup and coalescence of drops occurs. The drops are broken by viscous shear forces and turbulent pressure fluctuations. The elastic stress generated due to interfacial tension, on the other hand, tends to restore the drop to the original shape. As the diameter of the drop decreases, the deforming stress across it also decreases, whereas the restoring stress increases. A diameter is finally reached where the deforming stress is unable to break the drop. This diameter is normally referred to as d_{max}, the maximum stable drop diameter which is encountered in the impeller zone of an agitated tank where the maximum of the deforming force occurs. Simultaneously, coalescence may occur when drops collide. The probability of coalescence is related to the collision energy - also at a maximum in the impeller zone. After some time a dynamic equilibrium is established between breakup and coalescence, and a spectrum of drop sizes results. The average drop size and the drop size distribution will depend upon the conditions of agitation as well as the physical properties of the two liquids. In **Chapter 2** the flow characteristics of agitated tanks were reviewed. In this chapter the theoretical and experimental studies of the mechanisms of drop breakup, and of the mean drop size and drop size distribution will be reviewed in detail.

3.2 The Mechanisms of Drop Breakup

Drop breakup is often characterized in one of two ways. The first is to visualize the deforming stages and features of drop breakup, the other is to analyze the force balance (or energy balance) during drop breakup.

3.2.1 Deformation and Breakup of Drops

In general the disintegration of drops takes place in stages. Initially, when two immiscible fluids are stirred by an agitator, the fluid to be dispersed is present in bulk.

This bulk of fluid deforms and breaks into chunks of fluid which break up further into smaller parts. Hinze (1955) made a good summary of the existing theories of breakup. He postulated a mechanism to account for the disintegration of liquids, namely the penetration of lamellae and ligaments of one fluid into the other. These ligaments then break up into droplets which may further split up into small parts. Since the ligaments at the moment of breakup are not equally thick, drops of different sizes will be formed during this disintegration process. Hinze (1955) divided breakup processes into three different types. This classification is qualitative, and is based on photographic studies of droplet breakup.

a) *Lenticular Breakup.* The droplet flattens into an oblate ellipsoid which may be curved depending on the magnitude of the external forces (flow field) causing the deformation. The droplet in flattened form may change later into a toroid, which further breaks up into small droplets, but it may also undergo an irregular shattering process. Lenticular breakup is often observed in the bursting of droplets in air. It occurs at higher Weber numbers than elongated breakup, which will be described below.

b) *Elongated Breakup.* The droplet is first deformed into a prolate ellipsoid, which further elongates to a cylindrical thread. The thread breaks up later into several droplets. Elongated breakup is especially important in liquid-liquid dispersions.

c) *Bulgy Breakup.* As the surface of the droplet is deformed locally, bulges and protuberances occur. If the disturbance is strong enough, a small droplet may separate from the droplet.

Ali et al. (1981) investigated the mechanisms in an oil-water dispersion agitated by a PBT in a baffled tank using a photographic method. They found that two different dispersion mechanisms were responsible for the breakup of oil drops, namely the ligament stretching mechanism and the turbulent fragmentation mechanism. Both mechanisms occurred in the vortex system trailing from the impeller blade tips.

The ligament stretching mechanism consists of two sequential steps: when the oil enters the region of the vortex, first the velocity gradient between the vortex and the surrounding liquid causes the oil to be stretched into ligaments or elongated sheets, then the ligament breaks into small droplets when the stretching becomes sufficient to create

an unstable interfacial condition. Here, the ligament stretching mechanism is like the elongated breakup Hinze defined.

The turbulent fragmentation mechanism occurs at higher Reynolds numbers (higher rotation speed and lower oil viscosity). When the large oil drop enters the vortex region near the impeller tip, a rapid disintegration of the drop occurs, which forms a resultant droplet cloud.

Calabrese (1979) studied the breakup of highly viscous dispersed phases in stirred tanks. He argued that highly viscous dispersed droplets break up by a ligament stretching mechanism and low viscosity droplets undergo a turbulent fragmentation mechanism when the disruptive forces in the continuous phase are much larger than that needed to break up the droplets.

From the analysis above, we may conclude that the droplets in a liquid-liquid dispersion in agitated tanks mainly experience ligament stretching breakup when the dispersed phase is viscous and/or the Reynolds number is low; and that the turbulent fragmentation mechanism dominates when the viscosity of the dispersed phase is low and/or the Reynolds number is very high. **Figure 3-1** clearly shows the common two breakup mechanisms encountered in liquid-liquid dispersion.

3.2.2 Force (or Energy) Balance during Drop Breakup and Coalescence

As mentioned before, whether or not a drop can be broken depends on the relative magnitude between the restoring forces and the external deforming forces. In other words, a drop can be broken only when it can gain enough energy to compensate for its surface energy increase due to the increase of the total surface area. There are two main external forces, a dynamic pressure (turbulent pressure fluctuation) and a viscous stress set up in the surrounding continuous phase. τ is denoted as the external force per unit surface area. The restoring forces could be the interfacial tension σ/d, the viscous stress τ_d , and the dynamic pressure due to the deformation of the droplet. We first specify all the forces, starting with the restoring forces.

The dynamic pressure due to the deformation of the droplet may be considered as the pressure difference across the surface of the droplet, which can be calculated by the following equation:

$$p_i - p_o = \frac{4\sigma}{d} \tag{3-1}$$

where the indexes i and o refer to inner and outer phase respectively. $p_i - p_o$ is a restoring force, but it can be included in the interfacial tension from Eq.(3-1). Thus this force is often implicitly neglected in the force balance around the droplet.

Hinze (1955) argued that the viscous stresses inside the droplet are of the order of magnitude $\frac{\mu_d}{d}\sqrt{\frac{\tau}{\rho_d}}$, where the subscript d refers to the dispersed phase. He suggested two dimensionless groups to account for the force balance when both surface and dispersed-phase viscous forces contribute to drop stability. One is a generalized Weber group, W_e, another is a viscosity group, N_{Vi}.

$$W_e = \frac{\tau d}{\sigma} \tag{3-2}$$

$$N_{Vi} = \frac{\mu_d}{\sqrt{\rho_d \sigma d}} \tag{3-3}$$

The external or deforming force, τ, can be either turbulent pressure fluctuations $\rho_c\overline{V^2(d)}$, or viscous shear forces $\mu_c\frac{\partial V}{\partial r}$, where the subscript c refers to the continuous phase.

It is clear that the forces described above are actually force per unit area, which is in the same unit as energy per unit volume. Therefore, the force balance will give results similar to the energy balance. For the sake of simplicity, only a force balance or an energy balance is analyzed for a specific case below.

Hinze (1955) argued that the greater the external force τ compared with the counteracting interfacial tension force σ/d, the greater the deformation. At a critical value $(We)_{crit}$, breakup occurs. When both surface and dispersed-phase viscous forces contribute to drop stability, he proposed the following form of function

$$(W_e)_{crit} = c[1+\varphi(N_{Vi})] \tag{3-4}$$

where φ represents some function of the viscosity group. The restoring effects of both surface and dispersed-phase viscous forces are incorporated in Eq.(3-4). When $N_{vi} \rightarrow 0$, the function φ decreases to zero. That is

$$(We)_{crit} = \text{constant}$$

In the following analysis, $(We)_{crit}$ is simply written as *We*.

When the diameter of a droplet is much larger than the Kolmogoroff length η defined by Eq. (2-16), the viscous stresses are negligible compared with the turbulent pressure fluctuations. In this case,

$$W_e = \frac{\rho_c \overline{V^2(d)}d}{\sigma} = \frac{c_1 \rho_c \varepsilon^{2/3} d_{max}^{5/3}}{\sigma} \tag{3-5}$$

with the use of Eq.(2-34), $\overline{V^2(d)} \propto \varepsilon^{2/3} r^{2/3}$, if the turbulence is isotropic. Here d_{max} is used instead of d because drops with diameters larger than d_{max} will be broken by the external force, so d_{max} is the maximum stable drop diameter. By using Eq.(2-40), $\varepsilon \propto N^3 D^2$, we obtain the following equation

$$\frac{d_{max}}{D} = c_2 \left(\frac{\rho_c N^2 D^3}{\sigma}\right)^{-3/5} \tag{3-6}$$

or

$$\frac{d_{max}}{D} = c_2 (W_{e,T})^{-3/5} \tag{3-6'}$$

for $d >> \eta$, where $W_{e,T}$ is the Weber number in mixing tank.

In contrast to this, when a drop is smaller than η the dominant forces acting on the drop are the viscous shear forces. In this case the corresponding equation for the breakup of a drop was derived by Taylor (1932)

$$\mu_c \frac{\partial V}{\partial r} \frac{d}{\sigma} = f\left(\frac{\mu_d}{\mu_c}\right) \tag{3-7}$$

where f is a function of μ_d / μ_c. Shinnar (1961) then, derived the following equation using the relation for locally isotropic flow $(\partial V / \partial r)^2 = 2\varepsilon / 15\nu$,

$$d_{max} = c_3 \frac{\sigma}{\mu_c} \left(\frac{\nu_c}{\varepsilon}\right)^{1/2} f\left(\frac{\mu_d}{\mu_c}\right) = c_4 \frac{\sigma}{\mu_c} \nu_c^{1/2} N^{-3/2} D^{-1} f\left(\frac{\mu_d}{\mu_c}\right) \qquad (3\text{-}8)$$

for $d \ll \eta$.

It should be noted that Eqs.(3-6), or (3-6′) and (3-8) should apply only in dilute dispersions with a non-viscous dispersed phase where the viscous energy within a drop is negligible compared with the surface energy of the drop and the average drop size is determined by the breakup of droplets.

Calabrese et al. (1986a) derived the following equation including the contribution of the viscous energy within a drop as a restoring energy:

$$\frac{\rho_c \bar{(\varepsilon)}^{2/3} d_{max}^{5/3}}{\sigma} = c_5 \left[1 + c_6 \left(\frac{\rho_c}{\rho_d}\right)^{1/2} \frac{\mu_d \bar{(\varepsilon)}^{1/3} d_{max}^{1/3}}{\sigma} \right] \qquad (3\text{-}9)$$

One of the methods commonly used to deal with the possible coalescence in concentrated dispersions is to correct the equations above with a linear function of holdup fraction (volume fraction, ϕ), which will be given in detail in the next section. Using such a correction, Eq.(3-6′) will be in the form

$$\frac{d_{max}}{D} = c_7 (1 + c_8 \phi)(W_{e,T})^{-3/5} \qquad (3\text{-}10)$$

Although this project did not address the coalescence of drops, the force balance for coalescence of drops is reviewed for completeness and as background to the correlations for mean drop size.

Local turbulent velocity fluctuations of the dispersion cause the drops to collide with each other. After two drops collide, providing they can stay together for a sufficient time for the continuous phase liquid film separating them to drain out, coalescence occurs. Shinnar (1961) assumed that there are adhesive forces which tend to hold the two colliding drops together. He argued that the force of adhesion is a function of the drop diameter, and that there is a minimum drop diameter d_{min} below which the turbulent eddies will not be able to separate the two colliding droplets and therefore will not be able to prevent their coalescence. The energy of adhesion is expressed as $A(h_0)d$, both $A(h_0)$ and h_0 are constant and independent of the droplet diameter d in any given dispersion as

long as h_0/d is small. The kinetic energy of the droplets is proportional to $\rho_c \overline{V^2(d)} d^3$. The ratio of $\rho_c \overline{V^2(d)} d^3$ to $A(h_0)d$ determines if the two drops coalesce or separate again. The critical ratio is given by

$$\frac{\rho_c \overline{V^2(d)} d^2}{A(h_0)} = \text{const.}$$

Substituting the relation for locally isotropic flow, $\overline{V^2(d)} \propto (\varepsilon d)^{2/3}$ when $d >> \eta$ and $\varepsilon \propto N^3 D^2$, Shinnar obtained

$$d_{min} = c_9 \rho_c^{-3/8} \varepsilon^{-1/4} A(h_0)^{3/8} = c_{10} \rho_c^{-3/8} N^{-3/4} D^{-1/2} A(h_0)^{3/8} \qquad (3\text{-}11)$$

for $d >> \eta$.

In contrast to this, when $d << \eta$ the dominating force preventing coalescence is the viscous shear stress. The critical ratio which determines if two droplets coalesce is given by Sprow (1967a)

$$\mu_c \frac{\partial V}{\partial r} \frac{d^2}{F} = \text{const.} \qquad (3\text{-}12)$$

where F is the adhesion force. Substituting the relation for locally isotropic flow, $\frac{\partial V}{\partial r} \propto \left(\frac{\varepsilon}{\nu_c}\right)^{1/2}$ when $d << \eta$ and $\varepsilon \propto N^3 D^2$, Sprow obtained

$$d_{min} = c_{11} \mu_c^{-1/2} F^{1/2} \varepsilon^{-1/4} \nu_c^{1/4} = c_{12} \mu_c^{-1/2} \nu_c^{1/4} N^{-3/4} D^{-1/2} F^{1/2} \qquad (3\text{-}13)$$

for $d << \eta$.

3.3 Correlations for the Mean Drop Size and the Characteristics of Drop Size Distribution

The maximum stable drop diameter d_{max} and the minimum stable drop diameter d_{min} have already been introduced. Here some other definitions of mean drop diameters are introduced.

a) Arithmetic-mean diameter, d_{10}

$$d_{10} = \frac{\sum_i n_i d_i}{\sum_i n_i} \tag{3-14}$$

where n_i is the number of drops with diameter d_i

b) Area-mean diameter, d_{20}

$$d_{20} = \left[\frac{\sum_i n_i d_i^2}{\sum_i n_i} \right]^{1/2} \tag{3-15}$$

c) Volume-mean diameter, d_{30}

$$d_{30} = \left[\frac{\sum_i n_i d_i^3}{\sum_i n_i} \right]^{1/3} \tag{3-16}$$

d) Sauter mean diameter, d_{32}

$$d_{32} = \frac{\sum_i n_i d_i^3}{\sum_i n_i d_i^2} \tag{3-17}$$

In general, we can define the mean drop diameter by following equation

$$d_{mn} = \left[\frac{\sum_i n_i d_i^m}{\sum_i n_i d_i^n} \right]^{1/(m-n)} \tag{3-18}$$

where m=1, 2, 3; n=0, 1, 2; and m>n.

Among all the mean diameters, the Sauter mean diameter d_{32} is the most important since it is directly related to the interfacial area per unit volume, a. The relationship between the Sauter mean diameter d_{32} and the interfacial area per unit volume, a, is as follows

$$a = \frac{6\phi}{d_{32}} \tag{3-19}$$

To correlate the Sauter mean diameter with properties of fluids, operating conditions and geometric variables through force or energy analysis (as in the case of the maximum stable drop diameter) many uncertainties related to the statistics of varying drop sizes must be overcome. Fortunately, in most cases there is a linear function between the Sauter mean diameter and the maximum stable drop diameter. It was Sprow (1967b) who first assumed that d_{32} =const.× d_{max}, and then verified this relation with his experimental data. He found that d_{32} =0.380 d_{max} for a non-coalescing dispersion. Several other investigators have also reported this relation:

—Brown and Pitt (1972) obtained d_{32} =0.70 d_{max}.

—Coulaloglou and Tavlarides (1976) found that d_{32} =0.67d_{max} for a continuous process of mixing.

—Calabrese et al. (1986) obtained d_{32}=(0.48~0.60)d_{max} for μ_d from 0.0960 to 10.51 Pa.s. They also analyzed the data reported by Chen and Middleman (1967) and got d_{32}=0.64 d_{max}.

—Nishikawa et al. (1987) investigated liquid-liquid dispersions in both the breakup region (near impeller blades) and in the coalescence region (bulk) in agitated tanks. They found that d_{32}=0.50 d_{max} for breakup region, and d_{32} =0.45 d_{max} for coalescence region.

—Berkman and Calabrese (1988) obtained d_{32}=0.67d_{max} for a liquid-liquid dispersion in a static mixer. This suggests that the relation between the Sauter mean diameter and the maximum stable drop size is independent of the geometry of impellers (agitators) and tanks, and of the type of mixing process - batch or continuous.

Based on these experimental results, the equations for the maximum stable drop diameter are also valid for Sauter mean drop diameter, with the use of different constants.

3.3.1 Methods of Measuring Drop Sizes

Experimental methods for measuring drop sizes have been reviewed by Groves and Freshwater, 1968, Shah et al., 1972, Tavlarides and Stamatoudis, 1981. Since 1981, some new methods have been introduced for the measurement of drop size distributions of particular interests. The major categories reviewed by these authors are summarized below.

a) *In Situ Measurements.* This technique directly measures the dispersion without drawing samples by using photograph or high-speed cinephotograph. Photographs can be taken either with photo probes inserted in the dispersion or just through a window of the tank. Photo probes can be used to measure the dispersion with high holdup fraction, but the flow is affected. Taking photographs through a window of the tank cannot be used for high holdup fraction due to the interference of drops with the optical path.

b) *Sample Withdrawal Measurements.* In this technique, a sample of the dispersion is first withdrawn, then drop size distributions are measured from the sample by microscopic examination, photograph, or photomicrograph. The critical issue for the success of this technique is the prevention of drop coalescence in the sample. Usually surfactants are added to the sample. Although this technique has no holdup fraction limitations, it disturbs the dispersion hydrodynamics, and the drop size distribution can not be measured without distortion if the positions for sampling are not chosen properly and the size of the sample is not sufficient.

Phase doppler particle analyzer (PDPA)

The phase Doppler particle analyzer measures drop size distribution locally like the sample withdrawal method. It can only be applied to a dilute dispersion with a transparent continuous phase since the laser beams used in this technique can not pass through dense clusters of drops to reach photodetectors if the holdup fraction is high. The principle of this technique will be discussed in detail in **Chapter 7**.

3.3.2 Correlations for Mean Drop Diameter

The first systematic experimental investigation to correlate mean drop size with physicochemical properties of fluids, operating conditions and geometric variables was done by Vermeulen et al. (1955). Since then many investigators have reported their correlations for mean drop size, usually the Sauter mean drop diameter. The Sauter mean diameter depends on the physicochemical properties of the system, the flow field, and the holdup fraction if coalescence occurs. It is necessary to summarize the most important reported correlations with the ranges of operating variables and physical parameters. **Table 3-1** gives such a summary in chronological order.

From **Table 3-1**, it is clear that Eq.(3-6') is used when the holdup fraction is low and coalescence is negligible; Eq.(3-10) is used when the holdup fraction is high and possible coalescence occurs. For the system with high viscosity of dispersed phase, Eq.(3-4) is often used.

3.3.3 Drop Size Distributions in Agitated Tanks

The mean drop size alone can not fully characterize a dispersion system because dispersions with different drop size distributions can have the same Sauter mean drop diameter. To describe a dispersion system, both the mean drop size and the drop size distribution are needed. Several functions have been proposed by various investigators.

a) *Log-normal Distribution*

The number probability distribution function of drops was found to be a log-normal distribution by several investigators (Keey and Glen, 1969, Nagata and Yamaguchi, 1960, Yamaguchi et al., 1963, cited from Tavlarides and Stamatoudis, 1981):

$$f_n(d) = \frac{1}{\sqrt{2\pi}\log\sigma}\exp[-\frac{(\log d - \log d_{10})^2}{2(\log\sigma)^2}] \qquad (3\text{-}20)$$

where d_{10} is the arithmetic mean drop diameter, σ is the standard deviation.

Parthasarathy and Ahmad (1994) investigated the bubble size distribution in a gas-sparged tank agitated by a Rushton turbine. They found that with increasing agitation, the drop size distribution changes from unimodal to bimodal, and again to unimodal, as the bubble population moves progressively down the size scale. They summed two log-normal distributions, each with its distinct statistical parameters, to deal with the bimodal distribution.

b) *Normal Distribution*

The volumetric probability distribution function can be represented by a normal distribution function. Chen and Middleman (1967) used the following equation to fit their data

$$f_v\left(\frac{d}{d_{32}}\right) = \frac{1}{0.23\sqrt{\pi}}\exp[-9.2\left(\frac{d}{d_{32}} - 1.06\right)^2] \qquad (3\text{-}21)$$

Brown and Pitt (1972) obtained an equation similar to Eq.(3-21)

$$f_V\left(\frac{d}{d_{32}}\right) = \frac{1}{0.20\sqrt{\pi}} \exp\left[-12.5\left(\frac{d}{d_{32}} - 1.07\right)^2\right] \qquad (3\text{-}22)$$

By a detailed examination, they noticed that a bimodal form of distribution exists.

Nishikawa et al. (1991) used a combination of normal distributions to express both the number density distribution and the volumetric probability distribution in order to fit whole range of drop sizes. They found that a combination of three normal distributions gives a good fit for the volumetric drop size distribution and that a combination of two normal distributions can fit the number density distribution.

c) *Other Distributions*

Several other distributions have been proposed, such as the Erlang distribution, the Weibull distribution, and the Gamma distribution, but they are less common. The distribution given by Schwarz-Bezemer, however, was found to fit the drop size distribution very well (Sprow, 1967a)

$$\ln V\% = \ln 100 + d_c / d_{max} - d_c / d \qquad (3\text{-}23)$$

where V% is the cumulative volume percent of drops below diameter d, d_c is a characteristic diameter related to the maximum of the distribution function, and d_{max} is the largest drop diameter in the dispersion. Another distribution function worth mentioning is that proposed by Gal-Or and Hoelscher (1966, cited from Tavlarides and Stamatoudis, 1981) which directly relates drop size distribution with the rotational speed and holdup fraction

$$f(d) = 4\left(\frac{\alpha^2}{\pi}\right)^{1/2} d^2 \exp(-\alpha d^2) \qquad (3\text{-}24)$$

in which

$$\alpha = (16\pi^{1/2} N / 3\phi)^{2/3} > 0$$

More investigators found that a single distribution function is not able to describe the whole range of drop sizes, especially small or large drop sizes, so the current trend is to use a combination of distribution functions of the same form to express the drop size distribution (see Nishikawa et al. (1991) and Parthasarathy and Ahmad (1994)).

3.4 The Scope of This Study

From **Table 3-1**, we have noticed that although most of the correlations for mean drop size fall in the forms of Eq.(3-4), (3-6') or (3-10), the difference between constants or exponentials is not small. The same conclusion can be made for the relation between the Sauter mean drop diameter and the maximum stable drop diameter. By examination of the correlations an assumption is found to have been used in relating the local turbulence energy dissipation rate to the average energy input, $\varepsilon \propto P/\rho V_T$, i.e. the distribution of the main flow velocity in the tank is universal. This is true only for the impeller and impeller discharge region (around and near impeller blades), but the mean drop diameter is often obtained experimentally in both the impeller and impeller discharge region and the bulk of the tank. This means that a gap between the model and the real physics of a phenomenon exists. To include the mean power input explicitly or implicitly in correlations for mean drop size confuses the local characteristics of drop breakup. According to Park and Blair (1975) and other investigators' work, drop breakup occurs only near the impeller and droplet coalescence predominates at other locations. Park and Blair found that beyond distances from the impeller region of order of only 1/6 the impeller diameter, breakup is virtually nonexistent. Several researchers have pointed this out. Calabrese et al. (1986a) argued that for extremely viscous drops "it seems that no model based on power per unit mass ($P/\rho V_T$) will provide a reasonable correlation." Nishikawa et al. (1987b) found experimentally that neither the impeller speed, Reynolds number or average power input per unit mass of liquid ($P/\rho V_T$) can be used as the scale-up standard to keep the interfacial area of emulsion constant, though they are often used as the scale-up standard for various phenomena in the mixing vessel. Another possibility for the discrepancies between correlations for mean drop size is that the effects of some geometric variables of impellers and tanks such as the ratio of impeller diameter to tank diameter, off bottom clearance and the number of baffles on the flow (reflected in ε) are not accounted for. This project is designed to fill the gap between the model and the real physics. It will:

a) **Investigate the local energy dissipation rate,** namely ε_I, in the impeller regions where drop breakup dominates, and try to find if there is some more direct relation between ε_I and the mean drop diameter. Emphasis is also put on checking the conflicts about the magnitude of energy dissipation in the impeller region and in the impeller discharge region for the RT. A method to determine ε_I will be proposed by using an equation with a good theoretical basis and more reliable experimental data.

b) **Investigate the effect of impellers and tank geometry** such as the ratio of impeller diameter to tank diameter, off bottom clearance, and the number of baffles on the local turbulence energy dissipation rate, especially on the maximum turbulence energy dissipation rate in the tank, and try to shine some light on which geometric variables should be included in i) correlating drop size and ii) scaling up a dispersion system.

c) **Measure the mean drop size and size distribution** in an agitated tank using the PDPA with variation of some operating conditions, especially those which seem to be more important in determining the mean drop size.

Four impellers - 1 radial flow impeller (RT) and 3 axial flow impellers (PBT, A310 and HE3) will be used. Research with the impellers A310 and HE3 has not been done before, and drop size data for the PBT is rare.

Tables in Chapter 3

Table 3-1 Correlations for mean drop diameter in liquid-liquid mixing tanks

Investigators	Correlation	Physical properties					Operating conditions/Geometric parameters				Impeller/ Measurement techniques and Comments
		$\rho_d(g/cm^3)$	$\rho_c(g/cm^3)$	$\mu_d(cp)$	$\mu_c(cp)$	$\sigma(\frac{dynes}{cm})$	D(cm)	T(cm)	ϕ	N(rps)	
Vermeulen et al., 1955	$\frac{d_{32}}{D} = Bf_{\phi}(W_{e,T})^{-0.6}$	0.693-1.595	0.693-1.595	0.378-184	1.81-65.4	3.1-55.1	-	25.4, 50.8	0.10-0.40	1.80-6.67	4-bladed paddles/In-situ (light transmittance)
Roger et al., 1956	$\frac{d_{32}}{D} = B(D/T)^{-b}(W_{e,T})^{-0.36}$	0.761-1.101	1.0	0.578-3.91	1.0	2.1-49	5.1-30.0	15.5, 45.7	0.5	1-20	6-bladed RT/In situ (photography, light transmittance)
Calderbank 1958	$\frac{d_{32}}{D} = 0.06(1+3.75\phi)(W_{e,T})^{-0.6}$	-	-	-	-	35-40	5.8-25.4	17.8, 38.1	0-0.2	-	4-bladed paddles/In situ (light transmittance)
	$\frac{d_{32}}{D} = 0.06(1+9\phi)(W_{e,T})^{-0.6}$	-	-	-	-	35-40	5.8-25.4	17.8, 38.1	0-0.2	-	6-bladed RT/In situ (light transmittance)
Shinnar 1961	$\frac{d_{32}}{D} = B(W_{c,T})^{-0.6}$ (breakage control)										No experiments
	$\frac{d_{32}}{D} = B(\sigma D)^{-3/8}(W_{c,T})^{-3/8}$ (coalescence control)	-	-	22.5	0.4	-	12.7	29.0	0.05	2.6-10.5	Paddle turbine/Sample withdrawal
Chen and Middleman 1967	$\frac{d_{32}}{D} = 0.053(W_{e,T})^{-0.6}$	0.703-1.101	0.997-1.001	0.52-25.8	0.890-1.270	4.75-48.3	5.1-15.2	10.0-45.7	0.001-0.005	1.33-16.7	6-bladed RT/In situ (photograph)

where B, b are constants.

Cont'd **Table 3-1** Correlations for mean drop diameter in liquid-liquid mixing tanks

Investigators	Correlation	Physical properties					Operating conditions/Geometric parameters				Impeller/ Measurement techniques and Comments
		$\rho_d(g/cm^3)$	$\rho_c(g/cm^3)$	$\mu_d(cp)$	$\mu_c(cp)$	$\sigma(\frac{dynes}{cm})$	D(cm)	T(cm)	ϕ	N(rps)	
Sprow, 1967	$\frac{d_{32}}{D} = 0.0524(We_{,T})^{-0.6}$	0.692	1.005	0.51	0.99	41.8	3.2-10.0	22.2, 30.5	0-0.015	4.2-33.4	6-bladed RT, modified turbine /Sample withdrawal (Coulter counter)
Brown and Pitt, 1970	$\frac{d_{32}}{D} = 0.051(1+3.14\phi)(We_{,T})^{-0.6}$	0.783-0.838	0.972-0.998	0.59-3.30	1.0-1.28	1.9-50.0	10	30	0.05-0.3	4.2-7.5	6-bladed RT/In situ (photograph)
Van Heuven and Beek, 1971	$\frac{d_{32}}{D} = 0.047(1+2.5\phi)(We_{,T})^{-0.6}$	-	0.998	-	-	8.5-49.5	3.75-40.0	12.5-120	0.04-0.35	-	6-bladed RT/Encapsulation, sample withdrawal
Mlynek and Resnick, 1972	$\frac{d_{32}}{D} = 0.058(1+5.4\phi)(We_{,T})^{-0.6}$	1.055	1.0	-	1.0	41	10	29	0.025-0.34	2.3-8.3	6-bladed RT/In situ (photograph) sample withdrawal (drop encapsulation)
Weinstein and Treybal, 1973	$d_{32} = 10^{(-2.316+0.672\bar{\phi})}\nu_c^{0.0722}\varepsilon^{-0.194}(\sigma g_c/\rho_c)^{0.196}$ for batch process $d_{32} = 10^{(-2.066+0.732\bar{\phi})}\nu_c^{0.047}\varepsilon^{-0.204}(\sigma g_c/\rho_c)^{0.274}$ for continuous process	0.831-0.997	0.831-0.997	0.722-7.43	0.722-7.43	3.76-36.0	7.62-12.7	24.5, 37.2	0.079-0.593	2.5-10.33	6-bladed RT, unbaffled tank/In situ (light transmittance)[a]

a for batch process: $\varepsilon = (P g_c / V(1-\bar{\phi})\rho_c)$, V is the volume of the fluids.

for continuous process $\varepsilon = \frac{(P - 6Q_d\sigma/\overline{d_{32}})g_c}{V(1-\bar{\phi})\rho_c}$, Q_d is the flow rate of dispersed phase

Cont'd **Table 3-1** Correlations for mean drop diameter in liquid-liquid mixing tanks

Investigators	Correlation	Physical properties					Operating conditions/Geometric parameters				Type of Impeller/ Measurements techniques and Comments
		$\rho_d(g/cm^3)$	$\rho_c(g/cm^3)$	$\mu_d(cp)$	$\mu_c(cp)$	$\sigma(\frac{dynes}{cm})$	D(cm)	T(cm)	ϕ	N(rps)	
Brown and Pitt, 1974	$d_{32} = B(\sigma/\rho\bar{\varepsilon}t_c)^{0.6}$	0.783-0.838	0.972-0.998	0.59-3.30	1.0-1.28	1.9-50.0	10, 15	30	0.05	2.1-7.5	6-bladed RT/In situ (light transmittance)[b]
Coulaloglou and Tavlarides, 1976	$\frac{d_{32}}{D} = 0.081(1+4.47\phi)(W_{e,T})^{-0.6}$ for continuous process	0.972	1.0	1.3	1.0	43	10.0	24.5	0.025-0.15	3.2-5.2	6-bladed RT/In situ (photomicrography)
Godfrey and Grilc, 1977	$\frac{d_{32}}{D} = 0.058(1+3.6\phi)(W_{e,T})^{-0.6}$ or $d_{32} = 10^{(-3.18+0.74\bar{\phi})}\frac{\bar{\varepsilon}}{(\sigma/\rho_c)^{0.1787}}^{-0.2755}$	0.783-0.829	0.986-0.997	2.05-8.6	0.89-1.19	1.9-34.5	5.1	15.2	0.05-0.5	8.33-15.0	6-bladed RT,unbaffled square tank/Sample withdrawal
Arai et al., 1977	$\frac{d_{max}}{d_{max,0}} = (1+9N'_{Vi})^{3/5}$	0.879-0.922	1.00	0.78-1500	0.97	22	incorrect value of (D/10) is given in the paper	12.7	<0.003	2.5-13.7	6-bladed RT/In situ (photograph)[c]
Lagisetty et al., 1986	$\frac{d_{max}}{D} = 0.125(1+4.0\phi)^{1.2}(W_{e,T})^{-0.6}$	0.88-1.47	0.78, 1.0	non-Newtonian	1.0, 2.1	20, 45.2, 50	7.25	14.5	0.02	3.33-10	6-bladed RT/Sample withdrawal. Correlation is based on Voigt model; limited experiments used for verification of the model.

b In the equation of Brown and Pitt (1974), t_c is the circulation time.

c based on Voigt model. $d_{max,0}$ is the d_{max} when $N'_{Vi} \rightarrow 0$. $N'_{Vi} = \mu_d \bar{\varepsilon}^{1/3} d_{max}^{1/3}/\sigma$.

Cont'd **Table 3-1** Correlations for mean drop diameter in liquid-liquid mixing tanks

Investigators	Correlation	Physical properties					Operating conditions/Geometric parameters				Type of Impeller/ Measurements techniques and Comments
		$\rho_d(g/cm^3)$	$\rho_c(g/cm^3)$	$\mu_d(cp)$	$\mu_c(cp)$	$\sigma(\frac{dynes}{cm})$	D(cm)	T(cm)	ϕ	N(rps)	
Calabrese et al., 1986a	$\frac{d_{32}}{d_0} = (1+11.5N''_{Vi})^{5/3}$	0.960, 0.970	0.997	96.0, 486	0.893	37.8	7.1-19.6	14.2-39.1	<0.0015	0.93-5.95	6-bladed RT/In situ (photograph)[d]
	$N''_{Vi}<1$ for moderate-viscosity, μ_d										
	$\frac{d_{32}}{D} = 2.1(\mu_d/\mu_c)^{3/8}Re^{-3/4}$	0.971-0.975	0.997	971-10510	0.893	37.8	7.1-19.6	14.2-39.1	<0.0015	0.93-5.95	
	for high viscosity, μ_d										
Wang and Calabrese 1986	$\frac{d_{32}}{D} = 0.053(We_{,T})^{-0.6}$ $(1+0.97Vi^{0.79})^{3/5}$	0.834-0.986	0.792-0.997	0.81-459	0.52-0.89	0.21-47	7.1-15.6	14.2-31.2	<0.002	1.4-4.7	6-bladed RT/In situ (photograph)[e]
Calabrese et al., 1986b	$\frac{d_{32}}{D} = 0.053(We_{,T})^{-0.6}$ $(1+0.91Vi^{0.84})^{3/5}$	0.692-1.101	0.792-1.005	0.51-520	0.52-1.27	0.21-48.3	7.1-19.6	14.2-39.1	<0.005	0.93-33.4	mainly 6-bladed RT/Correlate Calabrese et al. (1986a), Wang and Calabrese (1986), Arai et al. (1977) and Sprow (1967b)
Berkman and Calabrese 1988	$\frac{d_{32}}{D} = 0.49(W'_e)^{-0.6}$ $(1+1.38Vi(d_{32}/D)^{1/3})^{3/5}$	0.852-0.967	~1	0.63-204	-	31.8-41.6	-	1.91	0.00057-0.001	-	Kenics static mixer/In situ (photograph)[f]

d d_0 is the d_{32} for an inviscid dispersed phase. $N''_{Vi} = (\rho_c/\rho_d)^{1/2}\mu_d\bar{\varepsilon}^{1/3}d_{32}^{1/3}/\sigma$.

e $Vi = \frac{\mu_d ND}{\sigma}(\frac{\rho_c}{\rho_d})^{1/2}$.

f D is the diameter of the pipe, and $\overline{V}$ is the mean velocity in the pipe. $W'_e = \rho_c\overline{V}^2D/\sigma$ and $Vi = (\mu_d\overline{V}/\sigma)(\rho_c/\rho_d)^{1/2}$

Cont'd **Table 3-1** Correlations for mean drop diameter in liquid-liquid mixing tanks

Investigators	Correlation	Physical properties					Operating conditions/Geometric parameters				Type of Impeller/ Measurements techniques and Comments
		$\rho_d(g/cm^3)$	$\rho_c(g/cm^3)$	$\mu_d(cp)$	$\mu_c(cp)$	$\sigma(\frac{dynes}{cm})$	D(cm)	T(cm)	ϕ	N(rps)	
Nishikawa et al., 1987a	$\frac{d_{32}}{D} = 0.095N_p^{-2/5}(W_{e,T})^{-0.6}(1+2.5\phi^{2/3})(\mu_d/\mu_c)_d^{1/5}(\mu_d/\mu_c)_c^{1/8}$ (breakup region) $\frac{d_{32}}{D} = 0.035N_p^{-1/4}(W_{e,T})^{-3/8}D^{-3/8}(1+3.5\phi^{3/4})(\mu_d/\mu_c)_d^{1/5}(\mu_d/\mu_c)_c^{1/8}$ (coalescence region)	0.81	0.972	17.0	0.356	17.9	12.5	25.0	0.0045-0.36	1.3-5.0	6-bladed RT/Sample withdrawal The suffix d or c outside the bracket (μ_d/μ_c) means to keep the viscosity of dispersed phase or the viscosity of continuous phase constant.
Nishikawa et al., 1987b	$\frac{d_{32}}{D} = 0.095N_p^{-2/5}(W_{e,T})^{-0.6}(T/T_0)^{-2/5}(1+2.5(T/T_0)^{1/2}\phi^{2/3})(\mu_d/\mu_c)_d^{1/5}(\mu_d/\mu_c)_c^{1/8}$ (breakup region) $\frac{d_{32}}{D} = 0.035N_p^{-1/4}(W_{e,T})^{-3/8}(T/T_0)^{-1/4}(1+3.5(T/T_0)^{1/2}\phi^{3/4})(\mu_d/\mu_c)_d^{1/5}(\mu_d/\mu_c)_c^{1/8}D^{-3/8}$ (coalescence region)	0.81	0.972	17.0	0.356	17.9	T/2	12-50	0.005-0.36	1.0-10.0	6-bladed RT/Sample withdrawal The suffix d or c outside the bracket (μ_d/μ_c) means to keep the viscosity of dispersed phase or the viscosity of continuous phase constant.
Chatzi et al., 1989	$\frac{d_{32}}{D} = 0.056(1+10.97\phi)(W_{e,T})^{-0.6}$	0.8792, 0.9014	0.9881, 0.9971	0.4591, 0.7303	0.5502, 0.9147	7.4, 11.5	7.5	15	0.01-0.03	2.50-5.00	4-bladed turbine/Sample withdrawal. Suspending agent (polyvinyl alcohol) added in the tank)

Figures in Chapter 3

Figure 3-1 The two common breakup mechanisms in liquid dispersion

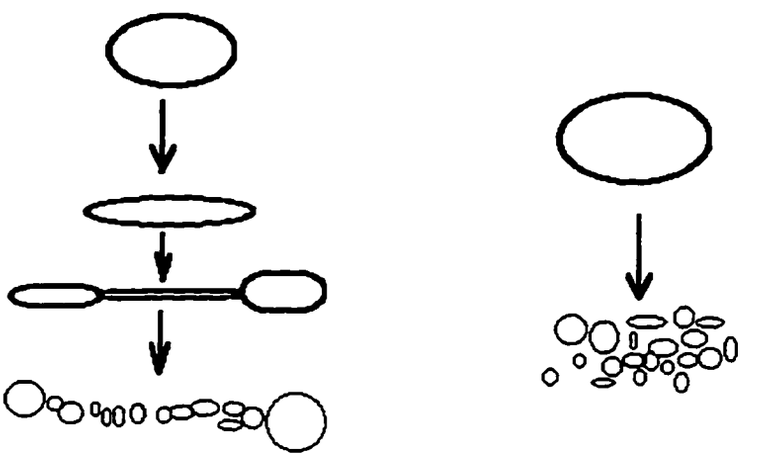

a) Ligament stretching mechanism

b) Turbulent fragmentation mechanism

References

Ali, A. M., Yuan, H. H. S., Dickey, D. S. and Tatterson, G. B., 1981, Liquid dispersion mechanisms in agitated tanks: Part I. pitched blade turbine. *Chem. Eng. Commun.* **10**, 205-213.

Arai, K., Konno, M., Matunaga, Y. and Saito, S., 1977, Effect of dispersed-phase viscosity on the maximum stable drop size for breakup in turbulent flow. *J. Chem. Eng. Japan* **10**, 325-330.

Berkman, P. D. and Calabrese, R. V., 1988, Dispersion of viscous liquids by turbulent flow in a static mixer. *AIChE J.* **34**, 602-609.

Brown, D. E. and Pitt, K., 1970, Drop breakup in a stirred liquid-liquid contactor. *Proc. Chemeca 1970* **83**, Melbourne and Sydney.

Brown, D. E. and Pitt, K., 1972, Drop size distribution of stirred non-coalescing liquid-liquid system. *Chem. Eng. Sci.***27**, 577-583.

Brown, D. E. and Pitt, K., 1974, Effect of impeller geometry on drop break-up in a stirred liquid-liquid contactors. *Chem. Eng. Sci.* **29**, 345-348.

Calabrese, R. V., 1979, The effect of dispersed phase viscosity on drop breakup in agitated liquid-liquid systems. presented at joint Japanese-North American Mixing Conference, AIChE, 72nd Annual Meeting.

Calabrese, R. V., Chang, T. P. K. and Dang, P. T., 1986a, Drop breakup in turbulent stirred-tank contactors, Part I: Effect of dispersed-phase viscosity. *AIChE J.* **32**, 657-666.

Calabrese, R. V., Wang, C. Y. and Bryner, N. P., 1986b, Drop breakup in turbulent stirred-tank contactors, Part III: Correlations for mean size and drop size distribution. *AIChE J.* **32**, 677-681.

Calderbank, P. H., 1958, Physical rate processes in industrial fermentation, Part I: The interfacial area in gas-liquid contacting with mechanical agitation. *Trans. IChemE.* **36**,.443-463.

Chatzi, E. G., Gavvrielides, A. D. and Kiparissides, C., 1989, Generalized model for prediction of the steady-state drop size distributions in batch stirred vessels. *Ind. Eng. Chem. Res.* **28**, 1704-1711.

Chen, H. T. and Middleman, S., 1967, Drop size distribution in agitated liquid-liquid systems. *AIChE J.* **13**, 989-995.

Coulaloglou, C. A. and Tavlarides, L. L., 1976, Drop size distribution and coalescence frequencies of liquid-liquid dispersions in flow vessels. *AIChE J.* **22**, 289-297.

Groves, M. J. and Freshwater, D. C., 1968, *J. Pharm. Sci.* **57**, 1273.

Godfrey, J. C. and Grilc, V., 1977, Drop size and drop size distribution for liquid-liquid dispersions in agitated tanks of square cross-section. *Second European Conference on Mixing,* Cambridge, England, BHRA Fluid Engineering: Cranfield, UK, C1-1 to C1-20.

Hinze, J. O., 1955, Fundamentals of the hydrodynamic Mechanism of splitting in dispersion processes. *AIChE J.* **1**,.289-295.

Lagisetty, J. S., Das, P. K., Kumar, R. and Gandhi, K. S., 1986, Breakage of viscous and non-Newtonian drops in stirred dispersions. *Chem. Eng. Sci.* **41**, 65-72.

Mlynek, Y. and Resnick, W., 1972, Drop size in an agitated liquid-liquid system. *AIChE J.* **18**, 122-127.

Nishikawa, M., Mori, F. and Fujieda, S., 1987a, Average drop size in a liquid-liquid phase mixing vessel. *J. Chem. Eng. Japan* **20**, 82-88.

Nishikawa, M., Mori, F., Fujieda, S. and Kayama, T., 1987b, Scale-up of liquid-liquid phase mixing vessel. *J. Chem. Eng. Japan* **20**, 454-459.

Nishikawa, M., Mori, F., Kayama, T. and Nishioka, S, 1991, Drop size distribution in a liquid-liquid phase mixing vessel. *J. Chem. Eng. Japan* **24**, 88-94.

Rodger, W. A., Trice, V. G. and Rushton, J. H., 1956, Effect of fluid motion on interfacial area of dispersions. *Chem. Eng. Progs* **Dec.**, 515-520.

Park, J. Y. and Blair, L. M., 1975, The effect of coalescence on drop size distribution in an agitated liquid-liquid dispersion. *Chem. Eng. Sci.* **30**, 1057-1064.

Parthasarathy, R. and Ahmed, N., 1994, Bubble size distribution in a gas sparged vessel agitated by a Rushton turbine. *Ind. Eng. Chem. Res.* **33**, 703-711.

Shah, P. S., Fan, L. T., Kao, I. C. and Erickson, L. E., 1972, *Adv. Appl. Microbiol.* **15**, 367.

Shinnar, R. and Church, J. M., 1960, Statistical theories of turbulence in predicting particle size in agitated dispersions. *Ind. Eng. Chem.* **52**, 253-256.

Shinnar, R., 1961, On the behaviour of liquid dispersions in mixing vessels. *Fluid Mech.* **10**, 259-275.

Sprow, F. B., 1967a, Drop size distributions in strongly coalescing agitated liquid-liquid systems. *AIChE J.* **13**, 995-998.

Sprow, F. B., 1967b, Distribution of drop sizes produced in turbulent liquid-liquid dispersion. *Chem. Eng. Sci.***22**, 435-442.

Tavlarides, L. L. and Stamatoudis, M., 1981, The analysis of interphase reactions and mass transfer in liquid-liquid dispersions. *Adv. Chem. Eng.* **11**, 199-273.

Taylor, G. I., 1932, The viscosity of a fluid containing small drops of another fluid. *Pro. Roy. Soc.* **A138**, 41-48.

Van Heuven, J. W. and Beek, W. J., 1971, Proc. Int. Solvent Extr. Conf., Hague, *Soc. Chem. Ind.* **70**, Paper 51.

Vermeulen, T., Williams, G. M. and Langlois, G. E., 1955, Interfacial area in liquid-liquid and gas-liquid agitation. *Chem. Eng. Progs* **51**, 85F-95F.

Wang, C. Y. and Calabrese, R. V., 1986, Drop breakup in turbulent stirred-tank contactors, Part II: Relative influence of viscosity and interfacial tension. *AIChE J.* **32**, 667-676.

Weinstein, B. and Treybal, R. E., 1973, Liquid-liquid contacting in unbaffled agitated vessels. *AIChE J.* **19**, 304-312.

Chapter 4

Validation of the Laser Doppler Anemometer (LDA)

4.1 Introduction

A phase Doppler particle analyzer (PDPA), which can measure one of the three components of velocity and the diameter of a droplet simultaneously, or the velocity only (acting as a LDA), is used in this study. The equipment consisting of (PDPA and a baffled agitated tank) described below was installed at the University of Alberta at the beginning of this experimental program. Although the technique of phase Doppler particle analyzer has been used for about two decades, the accuracy of measurements with new instruments can not be taken for granted, so it was necessary to validate the equipment.

With PDPA the validation rate, which is calculated using validated samples/attempted samples×100, decreases to a significant extent when both the velocity and the diameter of a drop are measured simultaneously. Furthermore, velocities measured in this way only characterize the motion of the drop, not of the continuous phase. When drops pass through the measuring volume of the PDPA the velocities of the drops are measured; however, these velocities can not characterize the continuous phase flow field or the turbulence energy dissipation characteristics estimated using this flow field. It is the continuous phase flow field which is experienced by the drops and actually determines the size distribution in the liquid-liquid dispersion. Therefore, the velocity field in an agitated tank was measured first. Another important reason for measuring fluid velocities and drop diameters separately is that in this way we can distinguish the effects of some operating conditions and geometric variables on the velocity field, the mean drop size and the drop size distribution. The relationship between the turbulence energy dissipation field determined from the velocity field and the mean drop size measured separately is possible when the introduction of the dispersed phase does not significantly change the flow field in the tank. This is true when the holdup fraction of the dispersed phase is very low, the dispersed phase is not viscous, and the difference

between the density of the continuous phase and that of the dispersed phase is not large. It will be shown in later chapters that these conditions are satisfied in this study.

In order to avoid confusion, when only velocity is measured using PDPA, we say the instrument is in LDA mode because in this situation the PDPA acts as a laser Doppler anemometer; when both the velocity and the diameter of a drop are measured , the instrument is in PDPA mode. The validation of the LDA, i.e. velocity measurements, is documented in this chapter.

4.2 The Fundamental Principles of the Laser Doppler Technique

Before the detailed analysis of experiments with LDA is presented, it is necessary to review the development and some basic principles of the laser Doppler technique.

The technique of using laser light to determine velocities was first used in the middle 1960's. Since then, the laser Doppler anemometer (LDA), or the laser Doppler velocimeter (LDV) has been used in many velocity fields. Its application continues to expand into more difficult environments; including combustion, supersonic and hypersonic flows, due to the improvement of Doppler signal processing methods. Its application to the study of turbulence is the most important for our research.

4.2.1 Basic Principles

The basic principles of laser Doppler anemometry can be interpreted in two ways: Doppler shift interpretation and virtual fringes interpretation.

a) *Doppler Shift Interpretation*

When a beam of light with a given frequency reaches a moving object, the light will change its frequency. In any form of wave propagation, frequency changes occur due to movement of the source, receiver, propagation medium, or an intervening reflector or scatter. This phenomenon is called "*Doppler shift*" after the Austrian physicist who first considered the phenomenon in 1842. The relation between the Doppler shift frequency f_D and a moving object scattering the light is (Drain, 1980)

$$f_D = \frac{2V}{\lambda_0}\sin(\frac{\theta}{2}) \qquad (4\text{-}1)$$

where V is the velocity of the object, θ the angle between two illuminating beams, and λ_o the wavelength of the light. By measuring the Doppler shift frequency for a given wavelength and angle of two beams, we can determine the speed of the object which is scattering the beams. There must be some particles to scatter the light. These may be seeding particles or naturally occurring impurities in the fluid. In our case, the 1 micron particles in tap water are the perfect particles to serve as the scattering medium.

b) *Virtual Fringes Interpretation*

To construct the LDA measuring volume, two beams of linearly polarized laser light are crossed at the beam waists, as shown in **Figure 4-1**. Where the beams cross, the combined light will have a maximum intensity when the maximum intensities of the light waves (represented by the black lines) coincide. When the minimum intensities of the light waves coincide, the combined intensity will be at a minimum. The aggregate effect of these combinations within the measuring volume is the production of apparent "fringes" of light with a known spacing. The orientation of these fringes is exactly parallel to the bisector of the angle between the two incoming laser beams. When particles cross the measuring volume described above, they scatter laser light with a modulated intensity corresponding to their passage through the fringes. The frequency of this modulation can be directly related to the component of fluid velocity perpendicular to the fringes, and in the plane of the two laser beams, as follows:

fringe spacing

$$\delta_f = \frac{\lambda_o}{2\sin(\theta/2)} \tag{4-2}$$

Doppler frequency

$$f_D = \frac{V}{\delta_f} \tag{4-3}$$

Eqs.(4-2) and (4-3) are combined to give Eq.(4-1). This is refereed to as the fringe interpretation of LDA.

4.2.2 Measurement of the Doppler Shift

Two main techniques are proposed to measure the Doppler shift. One is called "optical beating", and the other the "differential Doppler" technique.

The *optical beating technique* is suitable for measuring very small Doppler shifts by using the principle of *heterodyning* or "beating" of two frequencies in a device having a non-linear response. The output of the detector contains a signal of the difference frequency between two beams; a beam with high intensity scattered by particles moving with the fluid is compared with a reference beam having the same path length but less intensity.

The *differential Doppler technique* is the most commonly used technique; it requires no reference beam. Two beams of equal intensity (generated from the same source) are focused and crossed at the point under investigation. Scattered light from this region is focused onto the photodetector. Since light scattered from the beams reaches the detector simultaneously, a beat is obtained of frequency equal to the difference in Doppler shifts corresponding to the two angles of scattering. Because of the dominant use of the differential Doppler technique, and its use in the LDA in this study, only the differential Doppler velocimeter is discussed in the following section.

4.2.3 The Process of Velocity Measurement

A simple differential Doppler velocity measurement system consists of: a laser, a beam splitter, a Bragg cell for frequency shifting, focusing lenses, photodetectors, amplifiers and a signal processor.

The commonly available continuous wave *lasers* cover a wide range of wavelengths and light output power: 0.3250 μm (Helium-Cadmium) - 0.4880 μm (Argon) - 0.6328 μm (Helium-Neon) - 10.6 μm (Carbon Dioxide) (Encyclopedia of Chemical Technology, 1981); 1 mW (Helium-Cadmium, Helium-Neon) - 18 W (Argon) (Encyclopedia of Chemical Technology, 1981) - 1000W (Carbon dioxide) (Drain, 1980). In our case, the argon-ion laser radiates in the 457 nm to 514.5 nm regime, at powers ranging from 10 mW to 500 mW. Since the two laser beams from a laser source experience several reflections and passages through some mediums, the intensities of the

two laser beams reaching the measuring volume generated by them is much less than that from the source; about 100 mW at the exit from the transmitting optics.

The *beam splitter* (often a prism) separates the laser beam into two beams with the same intensity, then a *lens* focuses the beams at the probe volume (region to be investigated). When particles travel through the probe volume, the light is scattered at the Doppler frequency (see **Figure 4-1**). The scattered light is collected by a *photodetector* via a *focusing lens* and an optical aperture.

A Bragg cell producing a frequency shift is to get around the velocity sign ambiguity. The fringe pattern mentioned above, which is produced at the crossing of the two beams, is stationary. Thus, the frequency of the modulated light has no information of the sign of the particle velocity. To distinguish the velocity sign requires introduction of a frequency shift in the transmitting optics to one of the two beams. As a result, a particle moving in the measuring volume scatters light modulated such that the difference between the modulation frequency and the shift frequency is proportional to the velocity; moving in the same direction to the fringe movement reduces the modulation frequency, while moving in opposite direction increases it. In the Aerometrics LDA and PDPA systems a 40 MHz shift is produced by a Bragg cell.

Two types of photodetectors are available at present, namely *photomultipliers* and *photodiodes*. They both convert changes in light intensity into electrical signals. We have three photomultipliers in our receiver.

The signal is analyzed by a *signal processor* after being amplified.

Signal processors can be classified into two categories: the *time domain processors* (namely the counter and the covariance processors) and the *frequency domain processors* , which use a Fourier transform. The counter processor is relatively simple and provides accurate measurements, but it can only be used in situations where the signal to noise ratio (*SNR*) is relatively high (Ibrahim et al., 1990). It has been shown that the Fourier transform method gives the optimum frequency and phase estimation in terms of the maximum likelihood criteria (Bachalor, 1994). In our case, the Doppler signal analyzer (DSA) uses frequency domain burst detection to convert signals. In the frequency domain the discrete Fourier transform (DFT) of 16x16 samples is used. The

DSA combines the power approach with the DFT approach. It keeps the time domain in order to lock out the surrounding "ringing" frequency in the time domain. At the same time, the signal to noise ratio is less of an issue for detection because the DFT looks at the signal in the Fourier domain, where most of the noise is filtered out. DFT is used by Aerometrics because by detecting the well defined frequency, one bit sampling can be used.

Three components of velocity can be determined in a cylindrical coordinate system by changing the optical orientations (see **Figure 4-2**). In this work, the velocity vector in cylindrical coordinates is defined as:

a) the direction of positive radial velocity is radially outward;

b) the direction of positive tangential velocity is horizontally perpendicular to the radial velocity and counter clockwise as observed from above the vessel;

c) the direction of positive axial velocity is vertically downward.

Although the accuracy of velocity measurement by LDA depends partly on the quality of the components in the LDA system, it is determined mainly by the following considerations, which are critical to fringe visibility:

1) *Alignment.* The laser beams must be aligned correctly, otherwise, the beams will not cross exactly at the beam waists and the fringes will not be parallel (see **Figure 4-3**).

2) *Polarization.* The plane of polarization of the light is adjusted to be perpendicular to the plane of the beams. This sets up the interference fringes (see **Figure 4-4**).

3) *Coherence.* This is a property of the laser light.

4) *Beam intensity.* The two beams should have the same intensity. The Bragg cell is also adjusted to obtain equal intensities.

Among the four qualities critical to the accuracy of LDA measurements, only the beam intensity can be adjusted by LDA users, the others either require professional knowledge or are determined by the laser source itself.

4.3 The LDA

The layout of the LDA is shown in **Figure 4-5**.

An argon-ion laser (1) was used. Two laser beams passed the transmitting and focusing optics (2) including a Bragg cell which applies a frequency shift to one of the two beams. The intersection of the two beams forms a measuring volume within a cylindrical, baffled tank (3) surrounded by a square tank. All walls of both tanks are made from perspex, and both tanks were filled with water to minimize optical distortion. The two tanks are moved together horizontally using computer controlled traverses (6), and vertically using a manual traverse (7). The speed of the motor was measured using an optical tachometer (4). The receiving optics (5) with photodetectors are operated in a forward scattering mode. An Aerometrics Doppler signal analyzer (DSA) (8) was used to convert analog signals from the receiving optics into Doppler frequencies and velocities. Both the DSA and the traverse controller (9) [Unidex 11] are connected to a computer (10).

There are a few parameters to be chosen in LDA:

a) *tracks*. There are three different tracks corresponding to different beam separations:

Track	Beam separation, m
1	0.01691
2	0.03404
3	0.06307

The focal length (500 mm) is the same for all three tracks.

b) *voltages*. The voltage applied to the photodetectors in receiving optics can be varied from less than 200V to the maximum 800V.

c) *velocity range*. This range determines the minimum and the maximum velocities that can be measured.

d) *signal sampling frequency or sampling rate*. Sample frequency determines how fast the *signal* sampling is done. In general, it can be changed from a few thousands per second (kHz) to more than 80 MHz. This is not the same as the data rate, which is determined by the rate of particle arrival in the measuring volume, and by the high voltage setting.

e) *sample size*. The sample size defines how many validated velocity samples are to be taken to get the average value and the root-mean square of fluctuating values of a variable for one measurement. The qualifier "validated" is added because in most cases the validation of samples is less than 100%; thus the validated samples are not equal to the attempted samples. The relationship between the sample size or validated samples and the attempted samples is

$$\text{sample size} = \text{validation percent} \times \text{attempted samples}$$

f) *sample time or run time*. This is an alternative parameter for sample size. The sample time and sample size can not be set simultaneously. The sample time defines the total time of measurement.

All of the parameters described above have optimum operation ranges for a specific application; thus the optimization of these parameters was carried out before acquiring data.

The geometric and operating variables for the experiments used to optimize the LDA parameters are summarized in **Table 4-1.** The geometry of the impeller and the baffled tank is standard. The definitions of the geometric variables are as depicted in **Figure 2-1**. Measurements were carried out at z=10.5 mm (2 mm below the impeller blades) and r=54 mm ($2r/D$=0.9) where the turbulent flow is strong for the PBT with D=T/2. Except for the check of sample size, sample size was 10,000.

a) *Comparison of tracks*. Different tracks have different beam separations. Although beam separation is critical to the measurement of drop diameter, it has less effect on the measurement of velocity alone. Experimental data with different tracks confirmed this expectation. **Figure 4-6** shows that the average value and the RMS of axial fluctuating velocities with a sample size of 10,000 are almost the same for all three tracks, but the data obtained using track 1 (minimum beam separation) give the best reproducibility for velocity measurements. Therefore track 1 was chosen for all measurements in LDA mode.

b) *Voltage applied to photodetectors*. When the sample rate or sample frequency is high enough and sample size is fixed, high voltages enhance the signal burst detection and

thus reduce the total sample time. Excessively high voltages make the sample time too short to give accurate mean values, since the measurements cover very few passages (or cycles) of the impeller blades; while very low voltages limit detection to signals with very high magnitudes, so the measurements are biased. Experimental results (**Figure 4-7**) with varying voltages and fixed sampling frequency and sample size showed that voltages from 400V to 680V give very stable measurements. It should be noted that when the signal is very strong voltages less than 400V can also give stable measurements.

c) *Velocity ranges.* Experimental results showed that the velocity range does not affect velocity measurements. As long as the velocity range is set to cover the whole range of possible velocities encountered in the measurement volume, no differences in velocity measurements are found.

d) *Signal sampling frequency or sample rate.* Like the velocity range, the signal sampling frequency does not substantially affect velocity measurements if it is chosen properly. Although very a high sampling frequency can guarantee the total randomness of signal sampling, the validation rate decreases, which increases the file size when the data are stored. It is not necessary to explain how the Doppler signal analyzer (DSA) works in detail, but a few words about it may bring out some useful information to account for why file sizes are a concern. The DSA software can create data files and graphics. Velocity measurements of 30 spatial points with 10,000 velocity samples each occupy more than 10 MB (mega bytes) of computer memory if the percent validation is 100%. If the percent validation of samples is below 100%, the same measurements need well above 10 MB memory. Even with a hard drive of 300 MB, the data need to be backed up nearly every day. **Figure 4-8** shows that a sampling frequency between 2.5 MHz and 10 MHz gives both stable velocity measurements and high validation percent of samples.

e) *Sample size and sample time.* Experimental results showed that both the sample size and the sampling time are critical to velocity measurements, so they should be set properly. One setting can not guarantee the accurate and reproducible measurement of velocities. It was found that the sample time must be long enough to cover at least 80 passages of impeller blades, i.e. for an impeller with 4 blades rotating at 400 rpm, the

sampling time should be no less than 3 seconds (i.e. 3×4×400/60=80 passages of blades). If the sample time is too short, the reproducibility of velocity measurements is poor even with sample sizes larger than 10,000 data points. When the velocity signal is very strong and the voltage on the photodetectors is high, measurements with a large sample size can be completed within a short sampling time. Fortunately, this situation can be avoided by setting a proper voltage. When the sampling time is sufficient, a sample size of at least 4,000 is required to obtain accurate and stable measurement of velocities. **Figures 4-9** and **4-10** show how important the sampling time and sample size are for velocity measurement.

From the above analysis, the experimental parameters for the LDA were chosen as follows:

Track 1

voltage - 450~680 V

velocity range - -3~+3 m/s

signal sampling frequency - 2.5~10 MHz

velocity sampling time - $\geq 120\times60/(N\times N_b)$ seconds, (covering 120 or more passages of the impeller blades, N in rpm here)

velocity sample size - ≥4,000, typically 10,000

4.4 Validation of Velocity Measurements

After the optimization of the LDA parameters, validation of velocity measurements was carried out using these parameters. The validation was composed of four parts: reproducibility of experimental data, symmetry of the flow field, comparison of experimental data with that of previous investigators and mass conservation. The off bottom clerance was T/2. The sample size was 10,000.

One experiment was used to test the reproducibility of experimental data, the symmetry of the flow field, and to compare the experimental data with that of previous investigators. The PBT with D=T/2 was used for all tests, and for mass conservation both the PBT and the RT were used. Before the experimental results for the validation of

velocity measurements are presented, some definitions of dimensionless variables are introduced below.

4.4.1 Definition of Dimensionless Experimental Variables and the measuring traverse and volume

In order to compare the data with that of previous investigators, some dimensionless variables are introduced. The tip speed of an impeller (πND) is the maximum speed flow in an tank can reach, so it is often used to obtain dimensionless velocities.

dimensionless axial, radial and tangential velocities: $\frac{\overline{V_z}}{\pi ND}, \frac{\overline{V_r}}{\pi ND}, \frac{\overline{V_\theta}}{\pi ND}$

dimensionless axial, radial and tangential RMS velocities: $\frac{v_z}{\pi ND}, \frac{v_r}{\pi ND}, \frac{v_\theta}{\pi ND}$

dimensionless radial and axial coordinates: $\frac{2r}{D}, \frac{2z}{W_p}$, where W_p is the projected blade width, i.e. $W_p = W \times \sin(\text{pitch angle})$. The pitch angle for the PBT is 45°, so $W_p = W \times 0.707$. The blades on the RT are not pitched.

The measuring traverses and the control volume for mass conservation (not to scale) are shown in **Figure 4-11**. The symmetry check of the flow field is done along traverses: 2 mm above the upper edges and 2 mm below the lower edges of the impeller blades on both sides of the impeller shaft, which is the strongest turbulence region in the agitated tank. The control volume for the mass conservation check (see **section 4.4.5**) is enclosed in the region around the impeller with four dotted lines: one is 2 mm below the impeller blades; one is 2 mm above the impeller blades; and the other two are 3 mm from the impeller tip.

4.4.2 Reproducibility of Experimental Data

The reproducibility of the experimental data was checked in the impeller region where both instantaneous velocities and fluctuating velocities are very high. Even in this highly turbulent region, the reproducibility of the data was fairly good. **Figures 4-12** and

4-13 show the data measured on traverses of left side of the upper edge, and the left side of the lower edge of the impeller blades, respectively. The flow at the upper edge of the impeller blades is less stable than that at the lower edge of the impeller blades.

4.4.3 Symmetry of the Flow Field

Previous investigators have assumed axial symmetry of the flow field in agitated tanks. The symmetry of the flow field in an agitated tank is determined by the geometrical symmetry of the tank and impellers. Since impeller geometries are standard, the check of the symmetry of flow field is mainly to determine whether the tank and baffles are symmetric and whether the shaft is exactly in the center of the tank. By confirming the symmetry of the flow field, measurements can be taken on only one side of the impeller shaft. Experimental results show that the flow field in the agitated tank is perfectly symmetric (**Figures 4-14, 4-15, and 4-16**) *close to the impeller*.

4.4.4 Comparison of Experimental Data with That of Previous Investigators

By choosing the same geometry of a baffled agitated tank and an impeller, and the same rotational speed of the impeller, the data obtained with this equipment can be compared with the data of Kresta and Wood (1991). **Figure 4-17** shows that the two sets of data are in good agreement.

4.4.5 Mass Conservation

While checking the reproducibility of experimental data only determines whether or not the measurements are stable and repeatable, comparing the data of this study with other investigators' data can serve as a means to verify the accuracy of the data; and checking mass conservation can give us information on both the accuracy and self-consistency of the data.

Continuity demands that the mass flowing into a control volume must be equal to that flowing out of the control volume if there is no mass accumulation. The measuring volume can be considered as a constant volume if we assume that the density of the fluid (water) in an agitated tank is constant, which is true for the experimental conditions used.

In this case, mass conservation is equivalent to volume conservation. The control volume for checking volume conservation is drawn schematically in **Figure 4-11**. The volume conservation experiments were carried out with two impellers - PBT and RT. The equations used to calculate volumetric flow rates are as follows:

a) The axial volumetric flow rate passing through the upper edge or low edge of impeller blades, $Q_{z,i}$:

$$Q_{z,i} = 2\pi \int_{r_1}^{r_2} (\overline{V_z})_i r dr \qquad (4\text{-}4)$$

where i=U (representing the upper edge), or L (the lower edge of impeller blades). r_1 and r_2 are the integration limits in the radial direction.

b) The radial volumetric flow rate passing through the tip of the impeller blades, Q_r:

$$Q_r = 2\pi r_2 \int_{z_1}^{z_2} \overline{V_r} dz \qquad (4\text{-}5)$$

where z_1 and z_2 are the integration limits in axial direction. The origin of the two coordinates (r, z) is depicted in **Figure 2-1**.

The geometric and operating variables for volume conservation are given in **Table 4-2**.

The results for mass conservation were reasonably good for such strongly turbulent flow. The relative error between the total inlet volumetric flow rate and the total outlet volumetric flow rate was 6.5% for the RT, and 7.3% for the PBT. For the PBT two sets of data were obtained with the same geometric and operating variables. If the two sets of data are averaged and used in Eqs (4-4) and (4-5), the relative error between the total inlet volumetric flow rate and the total outlet volumetric flow rate reduces to 5.6% for the PBT.

4.5 Conclusion

Accurate and reproducible velocity profiles have been obtained using this LDA. The geometry of the baffled tank close to the impeller is symmetric, as are the velocity profiles on either side of the impeller shaft.

Tables in Chapter 4

Table 4-1 Geometric and operating variables of the impeller and the baffled tank in the experiments used to optimize the LDA parameters

Tank Variables		Impeller Variables	
number of baffles, N_f	4	impeller	PBT
width of baffles, W_b	$T/10$=0.024 m	number of blades	4
agitated liquid	water at 20°C	width of blades, W	0.024 m
liquid height, $H=T$	0.240 m	pitch angle	45°
diameter, T	0.240 m	off bottom clearance, $C=T/2$	0.120 m
Reynolds number, Re	97300	diameter, $D=T/2$	0.120 m
		rotation speed, N	407 rpm

Table 4-2 Geometric and operating variables for volume conservation

Variable	PBT	RT
D	0.120 m	0.120 m
C	0.120 m	0.120 m
N	400 rpm	221 rpm
r_1	0	0
r_2	1.05D/2	1.05D/2
z_1	$-0.70W_p$	$-0.583W$
z_2	$+0.70W_p$	$+0.583W$

where W=0.024 m, W_p=0.707W.

Figures in Chapter 4

Figure 4-1 LDA measuring volume as envisioned by the fringe interpretation (from George, 1988).

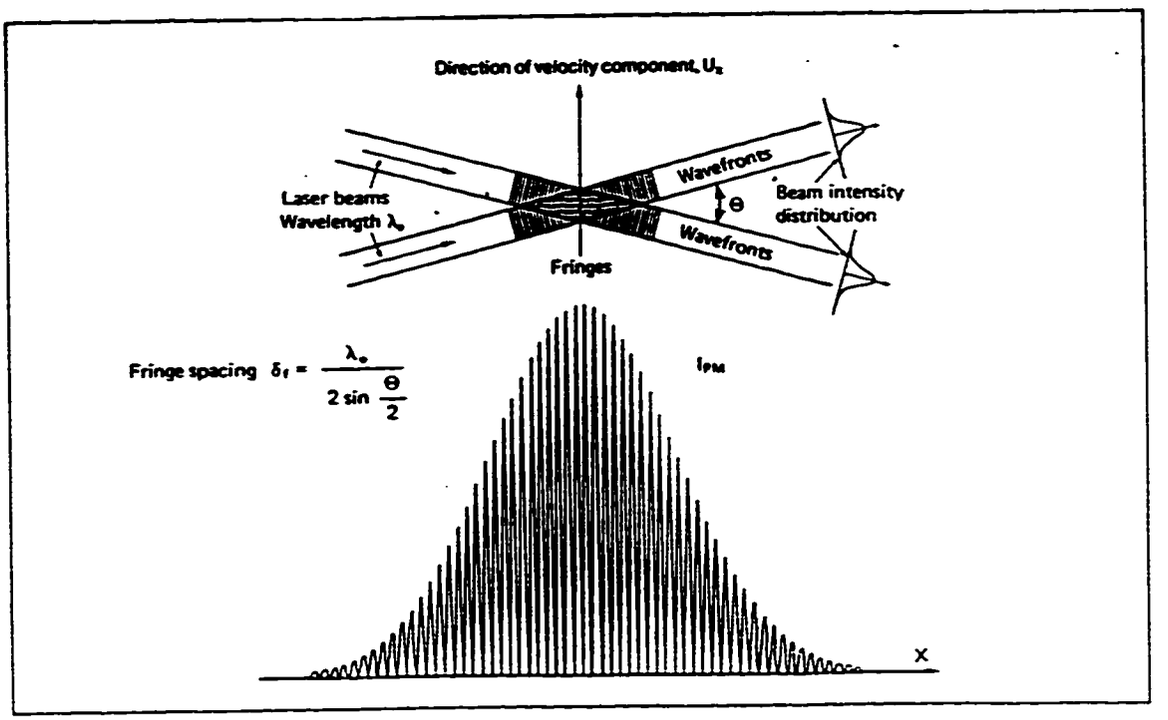

Figure 4-2 Optical orientations for the determination of three components of velocity as defined in cylindrical coordinates (from Kresta (1991)).

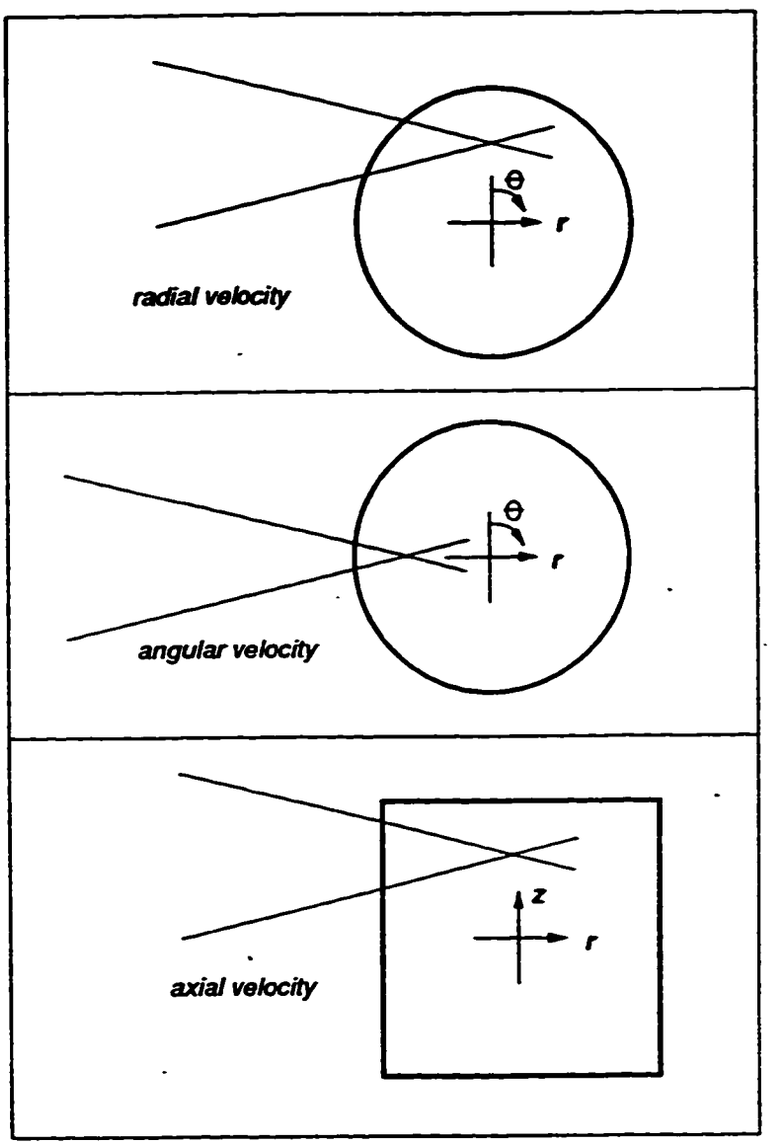

Figure 4-3 The importance of proper alignment of the laser beams (from Hanson, 1974).

a) crossing of the beams at the beam waist

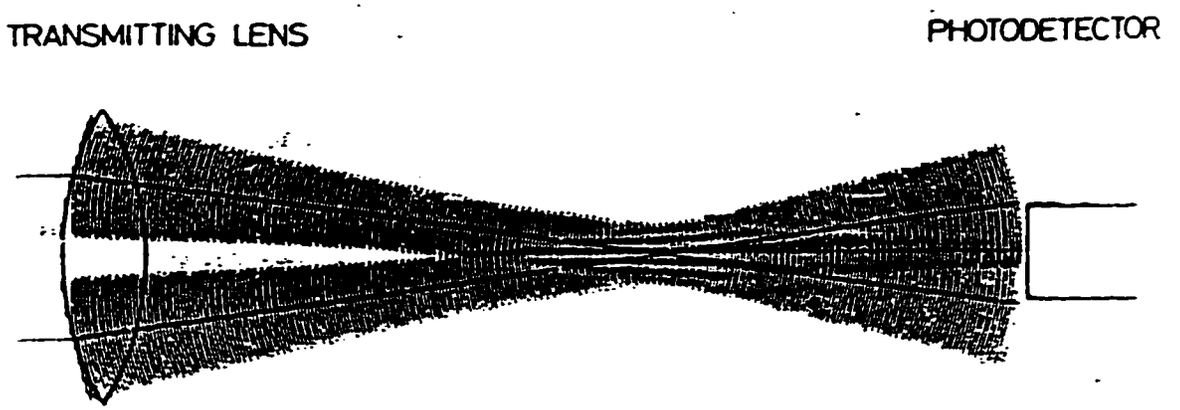

b) crossing of beams after the beam waist

Figure 4-4 "Thumb" diagram showing the velocity component (from Kresta (1991)).

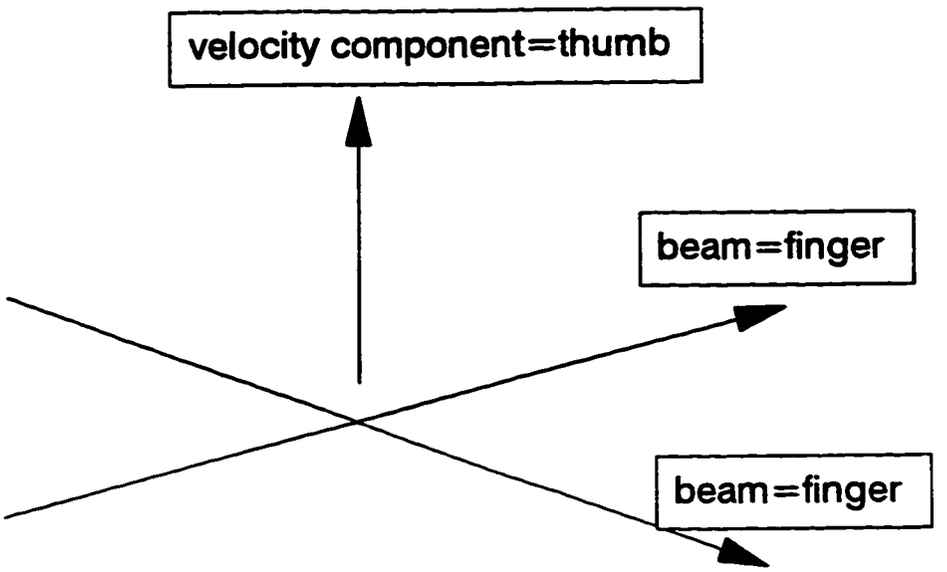

Figure 4-5 Arrangement of laser Doppler anemometer: 1-laser; 2-transmitting optics; 3-agitated tank; 4-tachometer; 5-receiving optics; 6-computerized X-Y traverses; 7-manual Z traverse; 8-Doppler signal analyzer; 9-traverse controller; 10-computer.

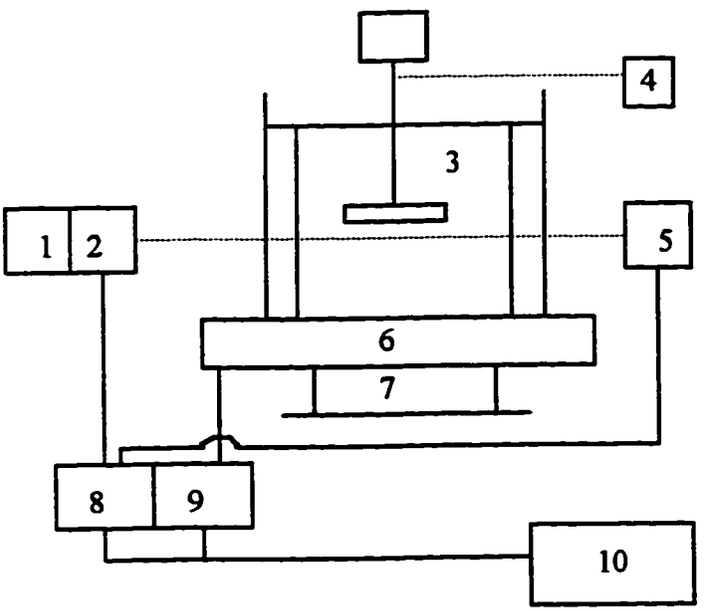

Figure 4-6 Axial velocity measurements using three tracks.

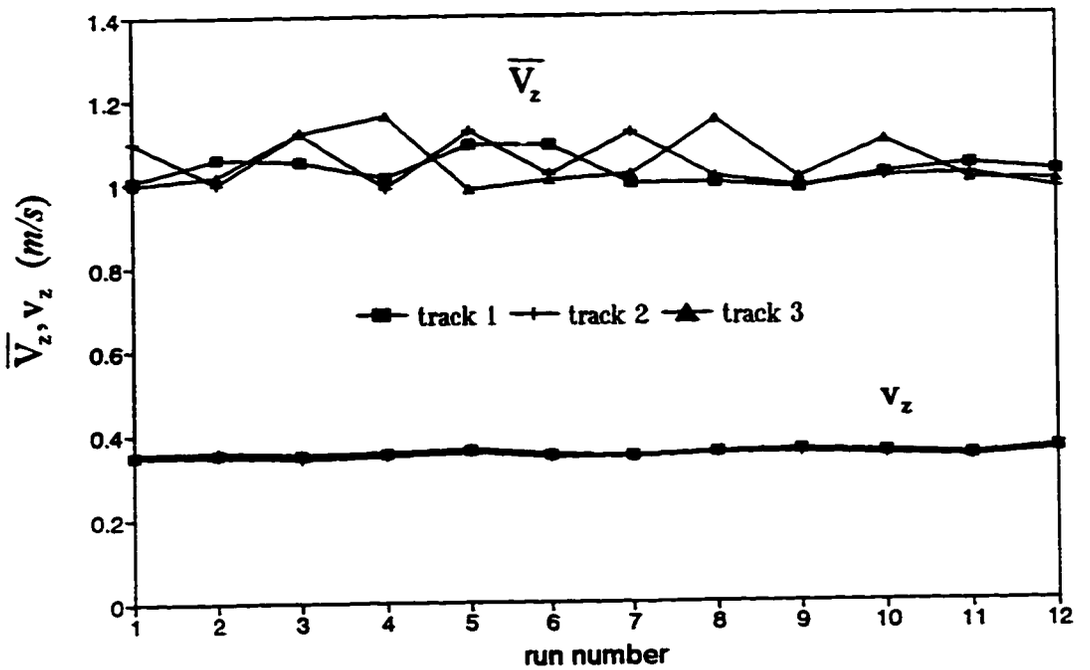

Figure 4-7 Axial velocity measurements with varying voltages. Each of the points in this figure was obtained by averaging values of 10 runs.

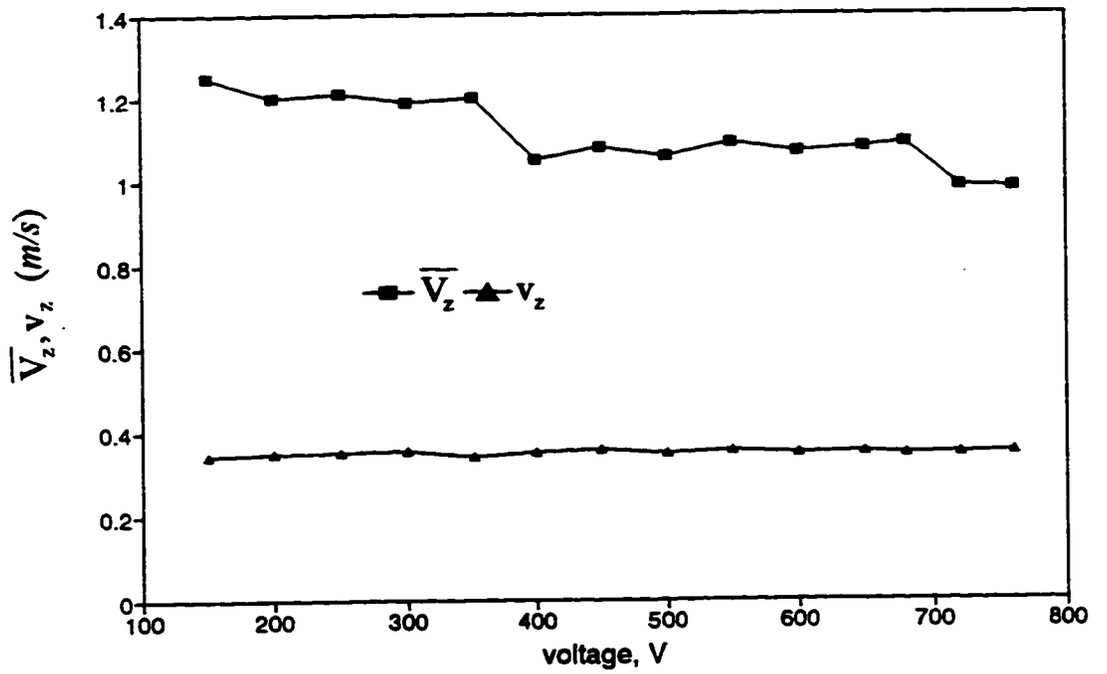

Figure 4-8 Axial velocity measurements with varying signal sampling frequencies. Each of the points in this figure was obtained by averaging values of 10 runs.

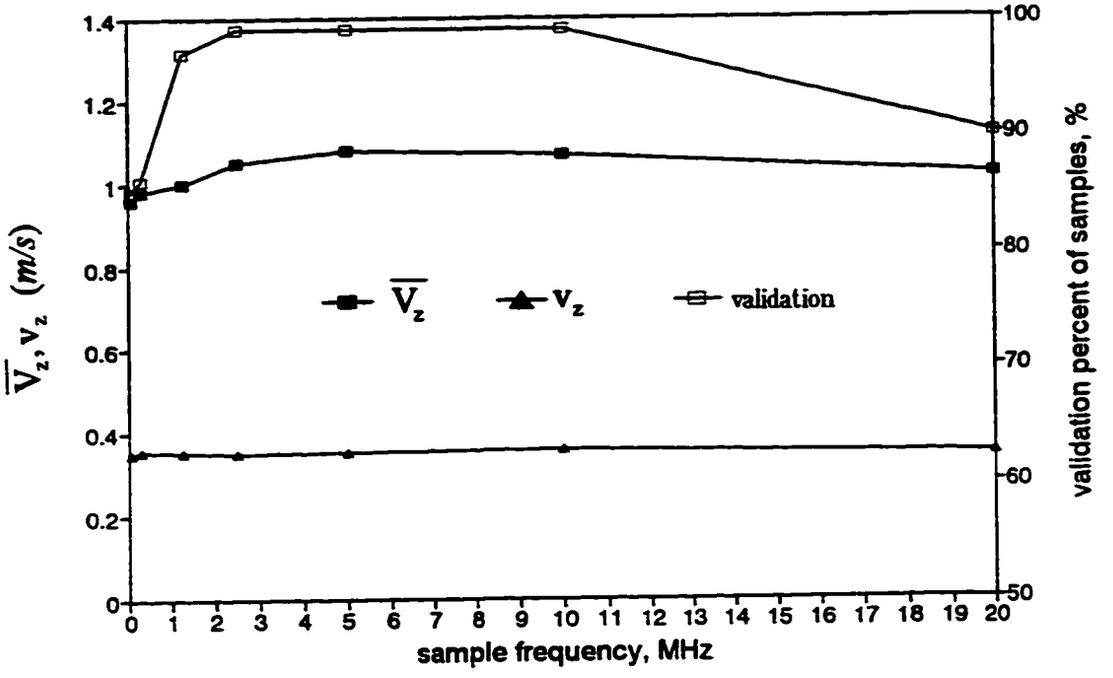

Figure 4-9 Axial velocity measurements with varying sample time. Sample size from 1800 to ~20,000. Each of the points in this figure was obtained by averaging values of 10 runs.

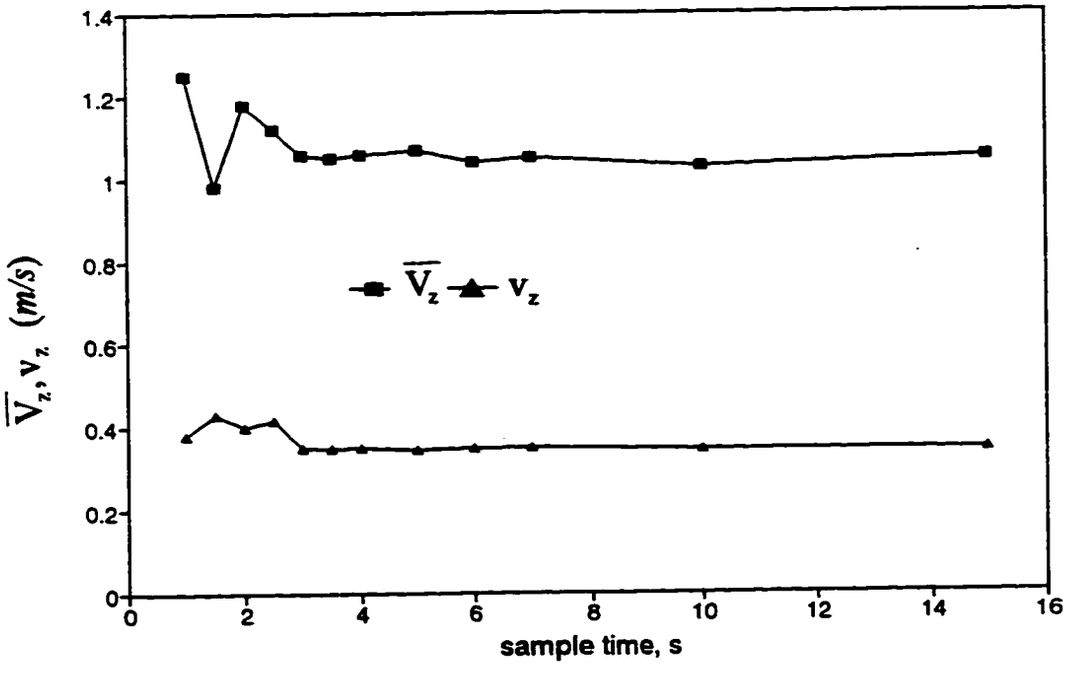

Figure 4-10 Axial velocity measurements with varying sampling size. Sample time≥3 s. Each of the points in this figure is obtained by averaging values of 10 runs.

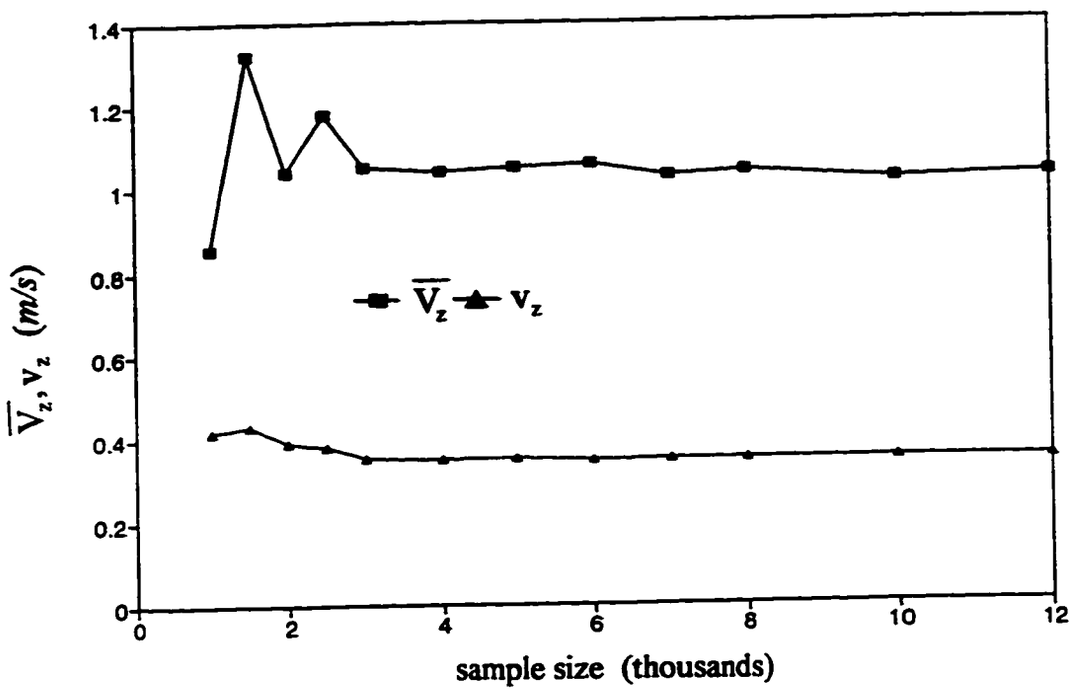

Figure 4-11 The measuring traverses and control volume for mass conservation (not to scale).

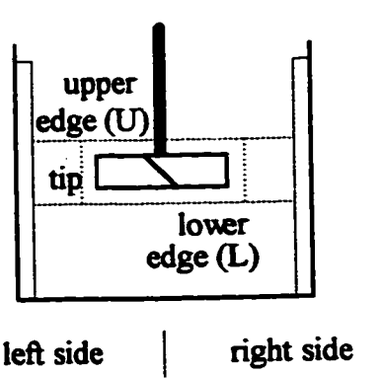

Figure 4-12 Reproducibility of the data (left side of upper edge).

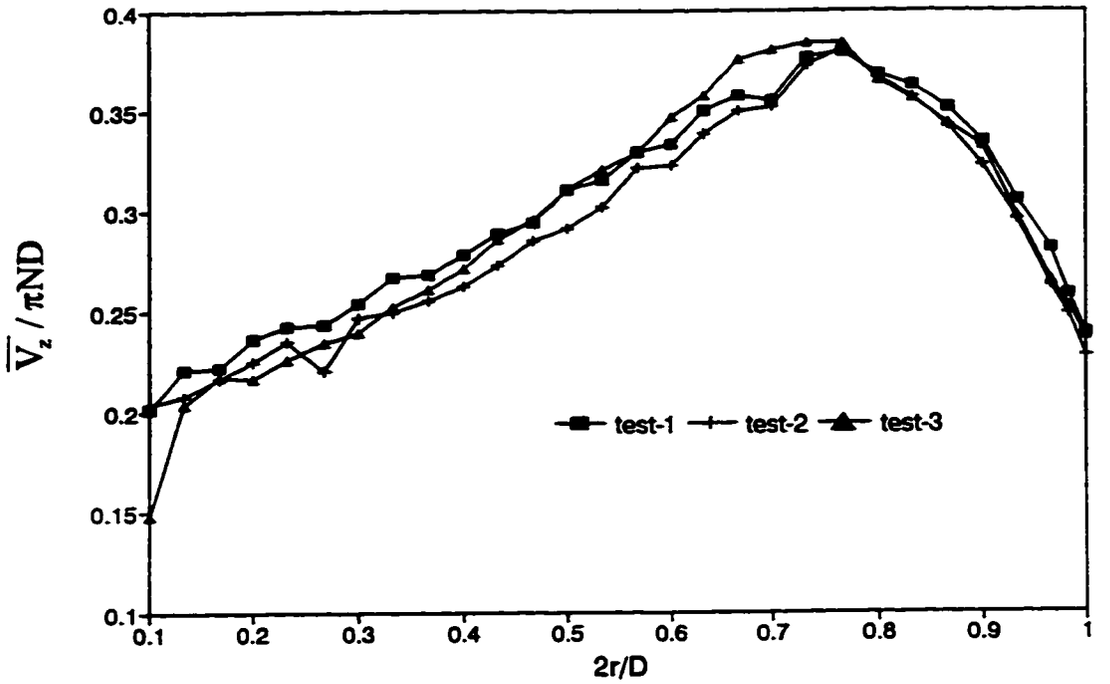

Figure 4-13 Reproducibility of the data (left side of lower edge).

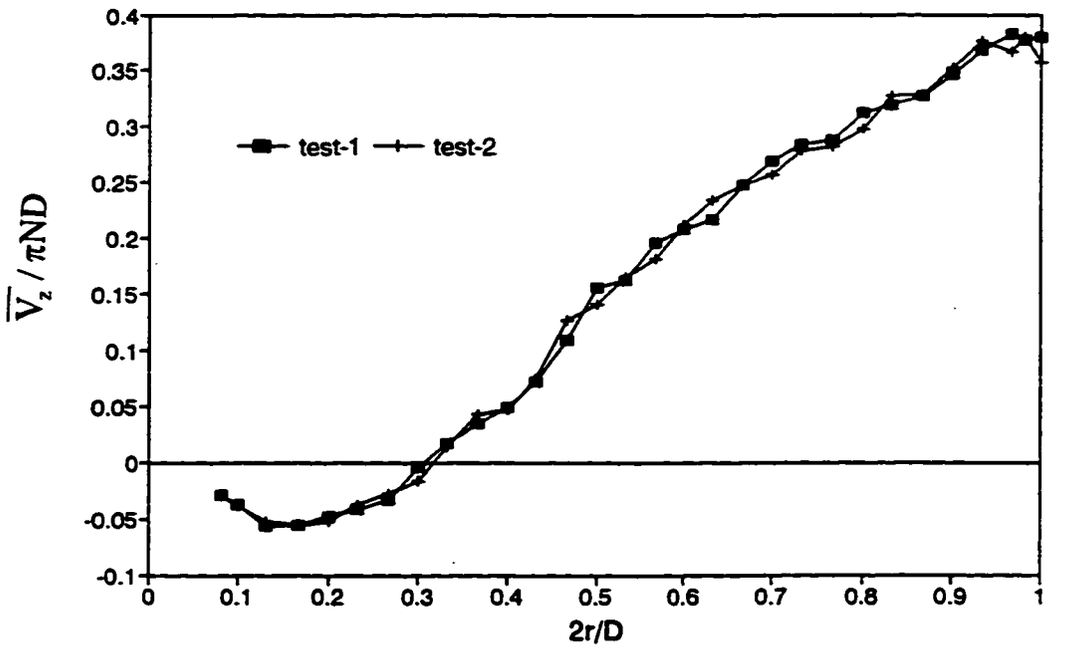

Figure 4-14 Symmetry of the flow at the upper edge of the impeller blades. z=-10.5 mm.

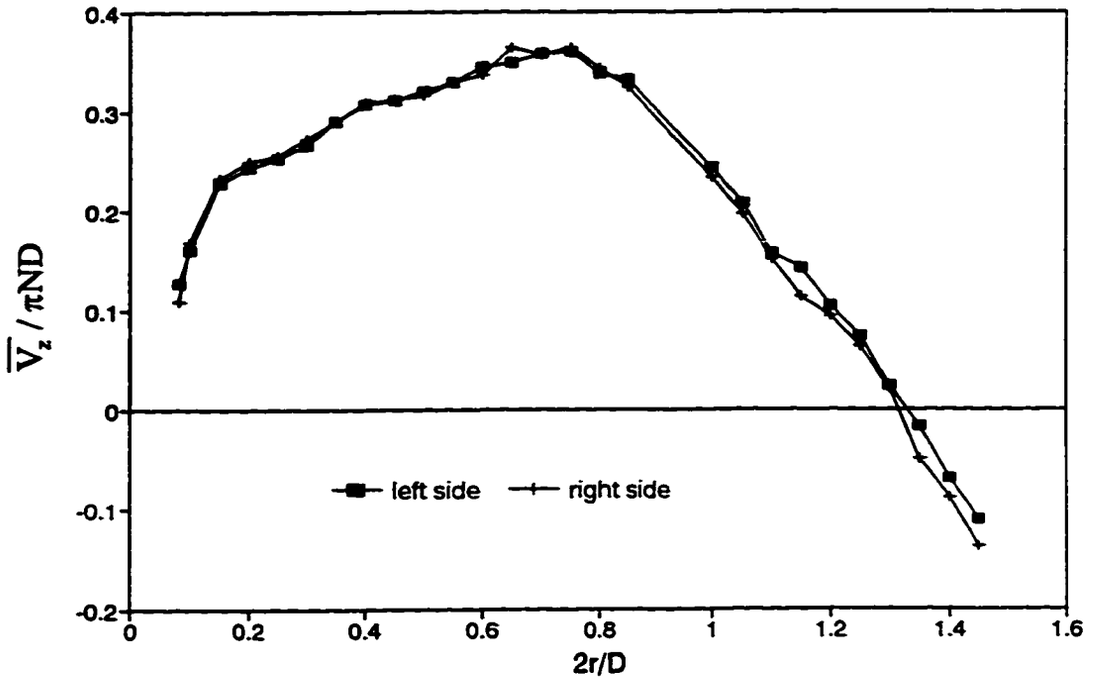

Figure 4-15 Symmetry of the flow at the lower edge of the impeller blades. z=10.5 mm.

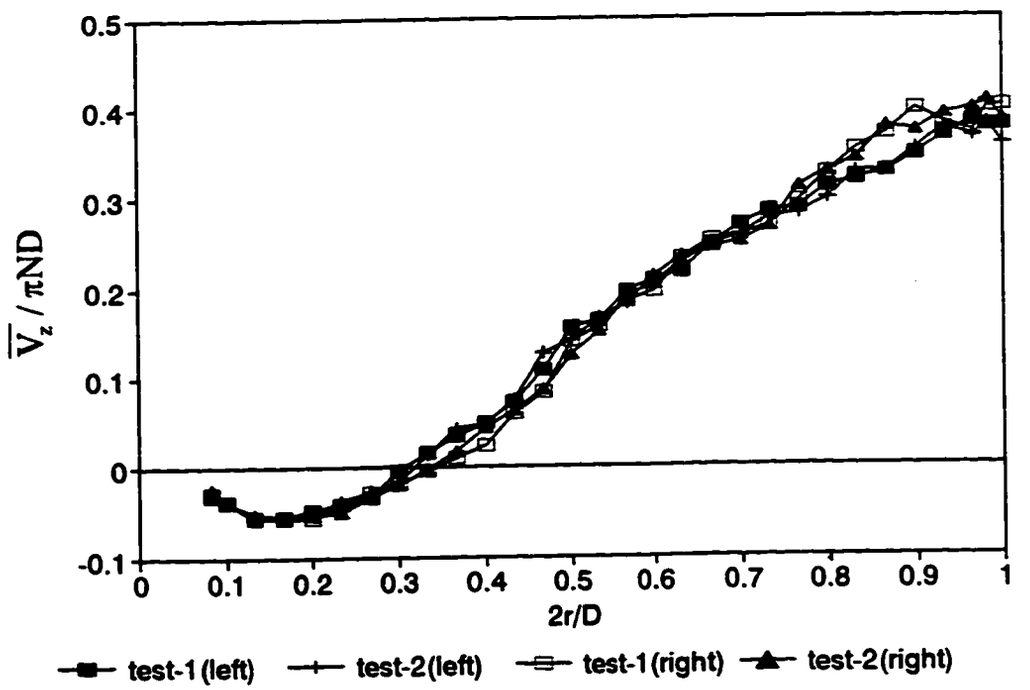

Figure 4-16 Symmetry of the flow at the tip of the impeller blades. r=63 mm.

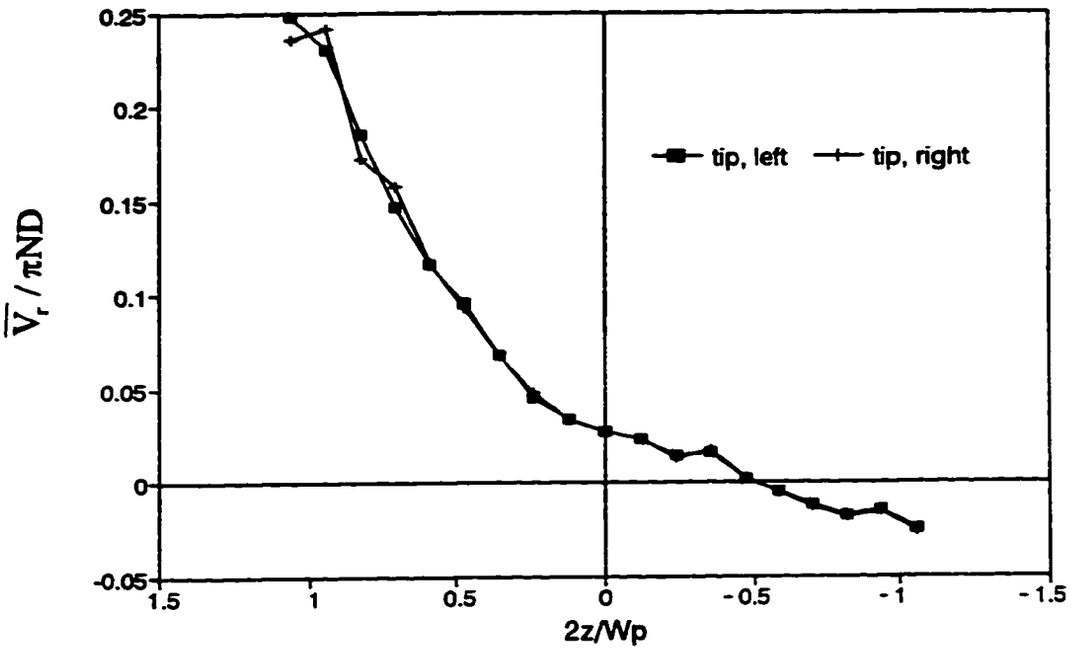

Figure 4-17 Comparison of experimental data with Kresta's data. D=T/2, C=T/2, N=407 rpm, PBT. Here clearance is defined as the distance from the lower edge of the impeller blades to the bottom of the tank.

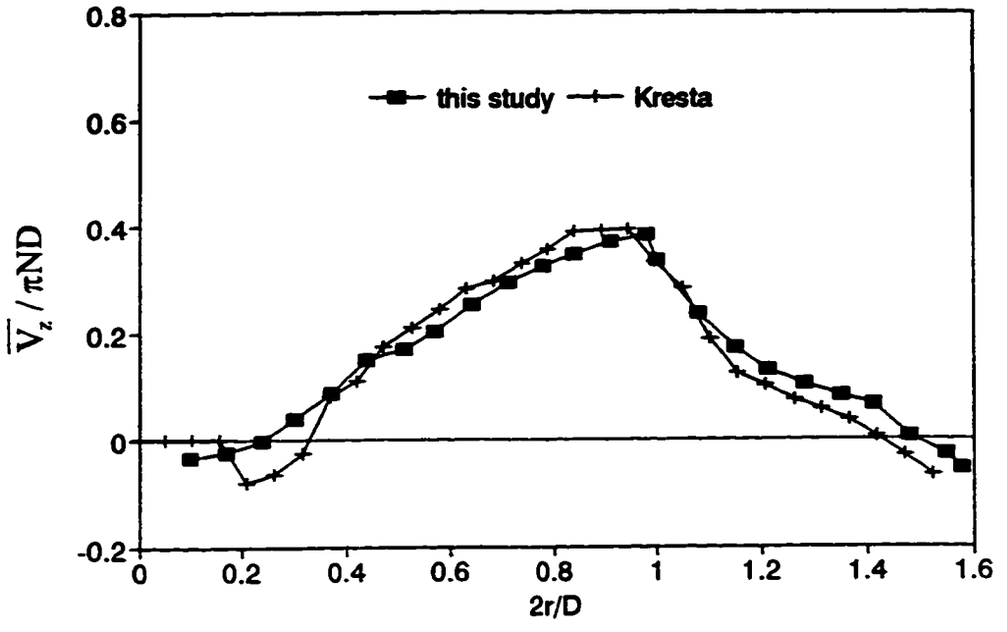

References

Bachalo W. D., Werthimer D., Raffanti R. and Hermes R. J., 1989, A high Speed Doppler Signal Processor for Frequency and Phase measurement. *Third Int. Conf. on Laser Anemometry, Advances and Applications*, Sept..

Bachalo W. D., Lecture on DSA Signal Processor, March, 1994.

Drain L. E., 1980, *The Laser Doppler Technique*, John Wiley and Sons, Toronto.

Encyclopedia of Chemical Technology, Volume 14, 3rd Ed., John Wiley & Sons, Toronto, 1981.

George, W. K., 1988, Quantitative measurement with the burst-mode laser Doppler anemometer. *Exptl. Thermal and Fluid Sci.***1**, 29-40.

Hanson, S., 1974, Coherent detection in laser Doppler velocimeters. *Opto-electronics* **6**, 263-269.

Ibrahim K. M., Werthimer G. D. and Bachalo W. D., 1990, Signal Processing Considerations for Laser Doppler and Phase Doppler Applications. *Fifth Int. Symp. on the Application of Laser Techniques of Fluid Mechanics*, Lisbon, Portugal, July 9-12.

Ibrahim K. M., Werthimer G. D. and Bachalo W. D., 1991, Signal Processing Considerations for Low Signal to Noise Ratio Laser Doppler and Phase Doppler Signals. *Fourth Int. Conf. on Laser Anemometry*, Cleveland, OH, August 5-9.

Kresta S. M., 1991, *Characterization, Measurement and Prediction of the Turbulent Flow in Stirred Tanks*, pp 51-60. Ph.D Thesis.

Chapter 5

Turbulence Energy Dissipation in the Impeller Regions*

5.1 The Derivation of the Macroscopic Mechanical Energy Balance Equation

5.1.1 Introduction

The characteristics of the turbulence energy dissipation in the impeller region and the impeller discharge region (these two regions are called the *impeller regions* below) is important to the understanding of liquid-liquid dispersion. As reviewed in **Chapter 2**, discrepancies exist among previous investigators on the turbulence energy dissipation in the impeller regions. In this chapter, a thoroughly theoretical treatment in the derivation of a macroscopic mechanical energy balance equation is first presented, then calculated results for the turbulence energy dissipation in the impeller regions for the three impellers (the RT, the PBT and the A310) are given.

5.1.2 Derivation

The macroscopic mechanical energy balance equation is derived starting with the stress equations of motion

$$\rho\left(\frac{\partial \bar{V}}{\partial t} + \bar{V} \bullet \bar{\nabla}\bar{V}\right) = \rho\bar{g} + \bar{\nabla} \bullet \hat{T} \tag{5-1}$$

where $\bar{V}$ is a velocity vector; $\bar{\nabla}$ is the divergence vector; $\hat{T}$ is the stress tensor. The material derivative is used to obtain:

$$\rho\frac{D\bar{V}}{Dt} = \rho\bar{g} + \bar{\nabla} \bullet \hat{T} \tag{5-2}$$

The scalar product of Eq.(5-2) with the velocity vector $\bar{V}$ is taken to form the mechanical energy balance:

$$\rho\bar{V} \bullet \frac{D\bar{V}}{Dt} = \bar{V} \bullet \rho\bar{g} + \bar{V} \bullet (\bar{\nabla} \bullet \hat{T}) \tag{5-3}$$

* *A modified version of this chapter was published in Trans. IChemE., vol. 74, pp. 379-389, 1996.*

A scalar ϕ=gz is introduced so that the gravity vector $\bar{g}$ may be expressed as:

$$\bar{g} = -\bar{\nabla}\phi \tag{5-4}$$

Substituting Eq.(5-4) into Eq.(5-3) and rearranging (Whitaker, 1981) gives:

Time rate of change of kinetic energy per unit volume ↓ | Rate of work done by surface forces per unit volume ↓

$$\frac{D}{Dt}\left(\frac{1}{2}\rho V^2\right) = -\bar{\nabla}\bullet(\rho\phi\bar{V}) + \bar{\nabla}\bullet(\bar{V}\bullet\hat{T}) - \Phi \tag{5-5}$$

↑ Rate of work done by gravity per unit volume | ↑ Rate of conversion to thermal energy per unit volume

Integrating Eq.(5-5) over a control volume V_a yields the macroscopic mechanical energy balance:

$$\frac{d}{dt}\int_{Q_a}\left(\frac{1}{2}\rho V^2\right)dQ + \int_{A_e}\frac{1}{2}\rho V^2(\bar{V}-\bar{W})\bullet\bar{n}dA = \int_{A_e}\bar{V}\bullet\bar{t}_{(n)}dA - \int_{A_a}\rho\phi\bar{V}\bullet\bar{n}dA + \dot{W} - \dot{E}_v \tag{5-6}$$

where Q_a- the control volume;

dQ - volumetric integration element;

A_a - the total area around the control volume;

A_e - the area of entrances and exits around the control volume;

dA - area integration element;

$\bar{W}$ - velocity of moving control volume surface;

$\bar{n}$ - unit normal vector of a surface;

$\bar{t}_{(n)}$ - stress vector, $\bar{t}_{(n)} = \bar{n}\bullet\hat{T}$;

$\dot{W}$ - rate of the shaft work input to the control volume;

$\dot{E}_V$ - total rate of viscous dissipation to internal energy, or the turbulence energy dissipation rate in the control volume. Since we are only interested in the turbulence energy dissipation in the impeller regions (around the impeller and in impeller discharge region), $\dot{E}_V$ can be directly converted into the turbulence energy dissipation per unit mass, $\bar{\varepsilon}_i$ defined in **Chapter 2** by dividing by the mass in a control volume.

For steady flow and a fixed control volume, Eq.(5-6) can be written as:

$$\underset{(I)}{\int_{A_c}\frac{1}{2}\rho V^2\bar{V}\bullet\bar{n}dA}=\underset{(II)}{\int_{A_c}\bar{V}\bullet\bar{\tau}_{(n)}dA}-\underset{(III)}{\int_{A_s}\rho\phi\bar{V}\bullet\bar{n}dA}+\underset{(IV)}{\dot{W}}-\underset{(V)}{\dot{E}_V} \qquad (5\text{-}7)$$

Considering a fixed control volume shown in **Figure 5-1** in an agitated tank enclosed with r from r_1 to r_2 and z from z_1 to z_2 in cylindrical coordinates, we analyze each term in Eq.(5-7) by assuming steady flow and radial symmetry of velocities in a horizontal surface.

First we notice that all surfaces are entrances or exits except r reaching the tank wall or z reaching the top cover or the bottom surface of the tank, and all surfaces have either $\bar{z}$ or $\bar{r}$ as their normal. For simplicity, z_1 is set to zero, regardless of the location of the control volume in the tank.

Term I on the left side of Eq.(5-7) can be expanded to:

$$\int_{A_c}\frac{1}{2}\rho V^2\bar{V}\bullet\bar{n}dA=\begin{array}{l}-\int_{r_1}^{r_2}\frac{1}{2}\rho[(V_z^2+V_r^2+V_\theta^2)(V_z)]_1\,2\pi r dr\\ +\int_{r_1}^{r_2}\frac{1}{2}\rho[(V_z^2+V_r^2+V_\theta^2)(V_z)]_2\,2\pi r dr\\ -\int_0^{z_2}\frac{1}{2}\rho[(V_z^2+V_r^2+V_\theta^2)(V_r)]_3\,2\pi r_1 dz\\ +\int_0^{z_2}\frac{1}{2}\rho[(V_z^2+V_r^2+V_\theta^2)(V_r)]_4\,2\pi r_2 dz\end{array} \qquad (5\text{-}8)$$

Where the subscripts 1, 2, 3, and 4 outside the square brackets in Eq.(5-8) stand for surfaces 1, 2, 3, and 4, respectively.

By expressing $\phi=gz$ and noticing that $z_1=0$, we can express term III in Eq.(5-7) as:

$$\int_{A_s}\rho\phi\bar{V}\bullet\bar{n}dA = \begin{matrix} +\int_{r_1}^{r_2}(\rho g z_2)[V_z]_2\,2\pi r dr \\ -\int_0^{z_2}\rho g[z V_r]_3\,2\pi r_1 dz \\ +\int_0^{z_2}\rho g[z V_r]_4\,2\pi r_2 dz \end{matrix} \qquad (5\text{-}9)$$

Term IV in Eq.(5-7) is the power input to the control volume by an impeller that can be measured directly by instruments or calculated by power number.

Term II in Eq.(5-7) must be treated with caution. As stated above, $\bar{t}_{(n)} = \bar{n}\bullet\hat{T}$. In cylindrical coordinates:

$$\bar{n} = \bar{r}\,n_r + \bar{\theta}\,n_\theta + \bar{z}\,n_z \qquad (5\text{-}10)$$

$$\bar{V} = \bar{r}\,V_r + \bar{\theta}\,V_\theta + \bar{z}\,V_z \qquad (5\text{-}11)$$

where $\bar{r}$, $\bar{\theta}$, $\bar{z}$ are unit vectors in r, θ, z directions, respectively;

n_r, n_θ, n_z are components of $\bar{n}$ in r, θ, z directions, respectively.

Using Eq.(5-10), $\bar{t}_{(n)}$ is expressed as:

$$\bar{t}_{(n)} = \begin{matrix} +\bar{r}[n_r T_{rr} + n_\theta T_{\theta r} + n_z T_{zr}] \\ +\bar{\theta}[n_r T_{r\theta} + n_\theta T_{\theta\theta} + n_z T_{z\theta}] \\ +\bar{z}[n_r T_{rz} + n_\theta T_{\theta z} + n_z T_{zz}] \end{matrix} \qquad (5\text{-}12)$$

Where T_{ij} (i,j=r, θ, z) in Eq.(5-12) are the nine components of the stress tensor $\hat{T}$.

For surface 1

$$\begin{matrix} n_r = 0 \\ n_\theta = 0 \\ n_z = -1 \end{matrix} \qquad (5\text{-}13)$$

For surface 2

$$\begin{matrix} n_r = 0 \\ n_\theta = 0 \\ n_z = 1 \end{matrix} \qquad (5\text{-}14)$$

For surface 3

$$\begin{matrix} n_r = -1 \\ n_\theta = 0 \\ n_z = 0 \end{matrix} \qquad (5\text{-}15)$$

For surface 4

$$n_r=1$$
$$n_\theta=0 \qquad (5\text{-}16)$$
$$n_z=0$$

Substituting Eq.(5-13) into Eq.(5-12), we obtain the stress vector on surface 1, denoting it by $\vec{t}_{(1)}$:

$$\vec{t}_{(1)} = -[\vec{r}\,T_{zr} + \vec{\theta}\,T_{z\theta} + \vec{z}\,T_{zz}] \qquad (5\text{-}17)$$

Substituting Eq.(5-14) into Eq.(5-12), we obtain the stress vector on surface 2, denoting it by $\vec{t}_{(2)}$:

$$\vec{t}_{(2)} = \vec{r}\,T_{zr} + \vec{\theta}\,T_{z\theta} + \vec{z}\,T_{zz} \qquad (5\text{-}18)$$

Substituting Eq.(5-15) into Eq.(5-12), we obtain the stress vector on surface 3, denoting it by $\vec{t}_{(3)}$:

$$\vec{t}_{(3)} = -[\vec{r}\,T_{rr} + \vec{\theta}\,T_{r\theta} + \vec{z}\,T_{rz}] \qquad (5\text{-}19)$$

Substituting Eq.(5-16) into Eq.(5-12), we obtain the stress vector on surface 4, denoting it by $\vec{t}_{(4)}$:

$$\vec{t}_{(4)} = \vec{r}\,T_{rr} + \vec{\theta}\,T_{r\theta} + \vec{z}\,T_{rz} \qquad (5\text{-}20)$$

Before substituting Eqs. (5-17), (5-18), (5-19) and (5-20) into the term II in Eq.(5-7), we expand $\hat{T}$ as:

$$\hat{T} = -p\hat{I} + \hat{\tau} \qquad (5\text{-}21)$$

Where p is pressure, $\hat{I}$ is a unit tensor, $\hat{\tau}$ is the viscous stress tensor. $\hat{T}$, $\hat{I}$ and $\hat{\tau}$ are all symmetric. In index notation, we have:

$$T_{ii} = -p + \tau_{ii}\ , \qquad i=r, \theta, z \qquad (5\text{-}22)$$

$$T_{ij} = \tau_{ij}\ , \qquad i\neq j,\ i,j=r, \theta, z \qquad (5\text{-}23)$$

By using Eq.(5-22) and Eq.(5-23), we can express Eqs. (5-17), (5-18), (5-19) and (5-20) as Eqs. (5-24), (5-25), (5-26), and (5-27), respectively:

$$\vec{t}_{(1)} = -[\vec{r}\,\tau_{zr} + \vec{\theta}\,\tau_{z\theta} + \vec{z}(-p+\tau_{zz})] \qquad (5\text{-}24)$$

$$\vec{t}_{(2)} = \vec{r}\,\tau_{zr} + \vec{\theta}\,\tau_{z\theta} + \vec{z}(-p+\tau_{zz}) \qquad (5\text{-}25)$$

$$\bar{t}_{(3)} = -[\bar{r}(-p+\tau_{rr}) + \bar{\theta}\tau_{r\theta} + \bar{z}\tau_{rz}] \tag{5-26}$$

$$\bar{t}_{(4)} = \bar{r}(-p+\tau_{rr}) + \bar{\theta}\tau_{r\theta} + \bar{z}\tau_{rz} \tag{5-27}$$

Substituting Eqs. (5-24), (5-25), (5-26), (5-27) and Eq.(5-11) into the term II in Eq.(5-7), we obtain:

$$\begin{aligned}\int_{A_e} \bar{V}\bullet\bar{t}_{(n)}dA = \; & -\int_{r_1}^{r_2} 2\pi[V_r\tau_{zr} + V_\theta\tau_{z\theta} + V_z(-p+\tau_{zz})]_1\, r dr \\ & +\int_{r_1}^{r_2} 2\pi[V_r\tau_{zr} + V_\theta\tau_{z\theta} + V_z(-p+\tau_{zz})]_2\, r dr \\ & -\int_0^{z_2}[V_r(-p+\tau_{rr}) + V_\theta\tau_{r\theta} + V_z\tau_{rz}]_3\, 2\pi r_1 dz \\ & +\int_0^{z_2}[V_r(-p+\tau_{rr}) + V_\theta\tau_{r\theta} + V_z\tau_{rz}]_4\, 2\pi r_2 dz\end{aligned} \tag{5-28}$$

For Newtonian fluid with constant density, ρ, the viscous stresses in Eq.(5-28) are:

$$\tau_{zr} = \tau_{rz} = \mu\left(\frac{\partial V_z}{\partial r} + \frac{\partial V_r}{\partial z}\right) \tag{5-29}$$

$$\tau_{z\theta} = \mu\left(\frac{\partial V_\theta}{\partial z} + \frac{1}{r}\frac{\partial V_z}{\partial \theta}\right) \tag{5-30}$$

$$\tau_{zz} = 2\mu\left(\frac{\partial V_z}{\partial z}\right) \tag{5-31}$$

$$\tau_{rr} = 2\mu\left(\frac{\partial V_r}{\partial r}\right) \tag{5-32}$$

$$\tau_{r\theta} = \mu\left[r\frac{\partial}{\partial r}\left(\frac{V_\theta}{r}\right) + \frac{1}{r}\frac{\partial V_r}{\partial \theta}\right] \tag{5-33}$$

Substituting Eqs.(5-29)-(5-33) into Eq.(5-28) and considering μ as a constant, we obtain:

$$\begin{aligned}&\int_{A_e} \bar{V}\bullet\bar{t}_{(n)}dA = \\ &-\mu\int_{r_1}^{r_2} 2\pi\left[V_r\left(\frac{\partial V_z}{\partial r} + \frac{\partial V_r}{\partial z}\right) + V_\theta\left(\frac{\partial V_\theta}{\partial z} + \frac{1}{r}\frac{\partial V_z}{\partial \theta}\right) + V_z\left(-\frac{p}{\mu} + 2\frac{\partial V_z}{\partial z}\right)\right]_1 r dr \\ &+\mu\int_{r_1}^{r_2} 2\pi\left[V_r\left(\frac{\partial V_z}{\partial r} + \frac{\partial V_r}{\partial z}\right) + V_\theta\left(\frac{\partial V_\theta}{\partial z} + \frac{1}{r}\frac{\partial V_z}{\partial \theta}\right) + V_z\left(-\frac{p}{\mu} + 2\frac{\partial V_z}{\partial z}\right)\right]_2 r dr \\ &-\mu\int_0^{z_2} 2\pi\left[V_r\left(-\frac{p}{\mu} + 2\frac{\partial V_r}{\partial r}\right) + \; + V_\theta\left(r\frac{\partial}{\partial r}\left(\frac{V_\theta}{r}\right) + \frac{1}{r}\frac{\partial V_r}{\partial \theta}\right) + V_z\left(\frac{\partial V_z}{\partial r} + \frac{\partial V_r}{\partial z}\right)\right]_3 r_1 dz \\ &+\mu\int_0^{z_2} 2\pi\left[V_r\left(-\frac{p}{\mu} + 2\frac{\partial V_r}{\partial r}\right) + \; V_\theta\left(r\frac{\partial}{\partial r}\left(\frac{V_\theta}{r}\right) + \frac{1}{r}\frac{\partial V_r}{\partial \theta}\right) + V_z\left(\frac{\partial V_z}{\partial r} + \frac{\partial V_r}{\partial z}\right)\right]_4 r_2 dz\end{aligned}$$

(5-34)

Eq.(5-34) is nearly impossible to apply to turbulent flow due to the first and second partial derivative terms. It may be simplified using order of magnitude analysis.

Considering the velocity field in the control volume shown in **Figure 5-1** in an agitated tank with a reasonable impeller rotational speed and fluids like water at about 20°C as working fluids, we know from experiments

$$V_i=0(1)\ m/s$$

$$p=0(10^5)\ kg/m.s^2$$

$$\mu=0(10^{-3})\ kg/m.s$$

$$\frac{\partial V_i}{\partial j}=0(10^1)\ s^{-1},\ i,j=r,\theta,z$$

Thus the terms with $\frac{\partial V_i}{\partial j}$ (i,j=r, θ, z) are much less than the terms with p. When all of these terms are neglected, Eq.(5-34) simplifies to:

$$\int_{A_c}\bar{V}\bullet\bar{t}_{(n)}dA=\int_{r_1}^{r_2}2\pi[V_zp]_1\,rdr-\int_{r_1}^{r_2}2\pi[V_zp]_2\,rdr+\int_0^{z_2}2\pi[V_rp]_3r_1\,dz-\int_0^{z_2}[V_rp]_4\,2\pi\,r_2\,dz \tag{5-35}$$

Substituting Eqs.(5-8), (5-9) and (5-35) into Eq.(5-7) and rearranging, we obtain:

$$\dot{W}-\dot{E}_V=$$

$$\int_{r_1}^{r_2}\left\{\left[\frac{\rho}{2}(V_z^2+V_r^2+V_\theta^2)V_z+V_zp+V_z\rho g\,z_2\right]_2-\left[\frac{\rho}{2}(V_z^2+V_r^2+V_\theta^2)V_z+V_zp\right]_1\right\}2\pi rdr$$

$$+\int_0^{z_2}\left[\frac{\rho}{2}(V_z^2+V_r^2+V_\theta^2)V_r+V_rp+V_r\rho gz\right]_4\,2\pi\,r_2\,dz$$

$$-\int_0^{z_2}\left[\frac{\rho}{2}(V_z^2+V_r^2+V_\theta^2)V_r+V_rp+V_r\rho gz\right]_3\,2\pi\,r_1\,dz \tag{5-36}$$

For steady turbulent flow, we express variables as the sum of a time-averaged value and a fluctuating component:

$$V=\overline{V}+v' \tag{5-37}$$

$$p=\overline{p}+p' \tag{5-38}$$

Substituting Eqs.(5-37) and (5-38) into Eq.(5-36) and taking the time average, we obtain the following equation by changing the order of the integration from area→time to time

→area and noting that the time average of a term including a single fluctuating variable is zero.

$$\dot{W} - \dot{E}_V =$$

$$\int_{r_1}^{r_2}\Big[\frac{\rho}{2}\Big\{\overline{V_z}^3 + 3\overline{V_z}\overline{(v'_z)^2} + \overline{(v'_z)^3} + (\overline{V_r})^2\overline{V_z} + \overline{V_z}\overline{(v'_r)^2} + 2\overline{V_r v'_r v'_z} + \overline{(v'_r)^2 v'_z}\Big\}$$

$$+\frac{\rho}{2}\Big\{(\overline{V_\theta})^2\overline{V_z} + \overline{V_z}\overline{(v'_\theta)^2} + 2\overline{V_\theta v'_\theta v'_z} + \overline{(v'_\theta)^2 v'_z}\Big\} + \overline{V_z p} + \overline{v'_z p'} + \rho g z_2 \overline{V_z}\Big]_2 2\pi r dr$$

$$-\int_{r_1}^{r_2}\Big[\frac{\rho}{2}\Big\{\overline{V_z}^3 + 3\overline{V_z}\overline{(v'_z)^2} + \overline{(v'_z)^3} + (\overline{V_r})^2\overline{V_z} + \overline{V_z}\overline{(v'_r)^2} + 2\overline{V_r v'_r v'_z} + \overline{(v'_r)^2 v'_z}\Big\}$$

$$+\frac{\rho}{2}\Big\{(\overline{V_\theta})^2\overline{V_z} + \overline{V_z}\overline{(v'_\theta)^2} + 2\overline{V_\theta v'_\theta v'_z} + \overline{(v'_\theta)^2 v'_z}\Big\} + \overline{v'_z p'} + \overline{V_z p}\Big]_1 2\pi r dr$$

$$+\int_{0}^{z_2}\Big[\frac{\rho}{2}\Big\{(\overline{V_z})^2\overline{V_r} + \overline{V_r}\overline{(v'_z)^2} + 2\overline{V_z v'_z v'_r} + \overline{(v'_z)^2 v'_r}\Big\} + \overline{V_r p} + \overline{v'_r p'} + \rho g z \overline{V_r}$$

$$+\frac{\rho}{2}\Big\{(\overline{V_r})^3 + 3\overline{V_r}\overline{(v'_r)^2} + \overline{(v'_r)^3} + (\overline{V_\theta})^2\overline{V_r} + \overline{V_r}\overline{(v'_\theta)^2} + 2\overline{V_\theta v'_\theta v'_r} + \overline{(v'_\theta)^2 v'_r}\Big\}\Big]_4 2\pi r_2 dz$$

$$-\int_{0}^{z_2}\Big[\frac{\rho}{2}\Big\{(\overline{V_z})^2\overline{V_r} + \overline{V_r}\overline{(v'_z)^2} + 2\overline{V_z v'_z v'_r} + \overline{(v'_z)^2 v'_r}\Big\} + \overline{V_r p} + \overline{v'_r p'} + \rho g z \overline{V_r}$$

$$+\frac{\rho}{2}\Big\{(\overline{V_r})^3 + 3\overline{V_r}\overline{(v'_r)^2} + \overline{(v'_r)^3} + (\overline{V_\theta})^2\overline{V_r} + \overline{V_r}\overline{(v'_\theta)^2} + 2\overline{V_\theta v'_\theta v'_r} + \overline{(v'_\theta)^2 v'_r}\Big\}\Big]_3 2\pi r_1 dz$$

(5-39)

Eq.(5-39) is the macroscopic mechanical energy equation obtained only by neglecting the contribution of viscous stresses. For practical use, it is not necessary, and is in fact nearly impossible to keep all terms of Eq.(5-39) to get the energy dissipation rate $\dot{E}_V$.

From the results of pressure measurements, we know that the magnitude of $\overline{p' v'_j}$, (j=r,z) is about two orders of magnitude less than $\frac{\rho}{2}\overline{V_j}\overline{(V_j)^2}$ or $\frac{\rho}{2}\overline{V_j}\overline{(v'_j)^2}$, (j=r,z), so $\overline{p' v'_j}$ can be neglected.

The values of the cross correlation terms and/or the cubed terms of the fluctuating velocities are randomly distributed and offset each other, so those terms are also neglected.

The average pressure $\bar{p}$ at surface 2 (namely, $\bar{p}_2$) can be expressed by the sum of the average pressure $\bar{p}$ at surface 1 (namely, $\bar{p}_1$) and $\rho g z_2$ due to the change of the axial coordinate, i.e. $\bar{p}_2=\bar{p}_1-\rho g z_2$.

Therefore the Eq.(5-39) can be simplified to

$$\begin{aligned}
&\dot{W}-\dot{E}_V = \\
&\int_{r_1}^{r_2}\rho\overline{V_z}[(\overline{V_z})^2+(\overline{V_r})^2+(\overline{V_\theta})^2+3\overline{(v'_z)^2}+\overline{(v'_r)^2}+\overline{(v'_\theta)^2}+\frac{2}{\rho}\bar{p}_1]_2\,\pi r dr \\
&-\int_{r_1}^{r_2}\rho\overline{V_z}[(\overline{V_z})^2+(\overline{V_r})^2+(\overline{V_\theta})^2+3\overline{(v'_z)^2}+\overline{(v'_r)^2}+\overline{(v'_\theta)^2}+\frac{2}{\rho}\bar{p}_1]_1\,\pi r dr \\
&+\int_0^{z_2}\rho\overline{V_r}[(\overline{V_z})^2+(\overline{V_r})^2+(\overline{V_\theta})^2+\overline{(v'_z)^2}+3\overline{(v'_r)^2}+\overline{(v'_\theta)^2}+\frac{2}{\rho}\bar{p}\ +2gz]_4\,\pi r_2 dz \\
&-\int_0^{z_2}\rho\overline{V_r}[(\overline{V_z})^2+(\overline{V_r})^2+(\overline{V_\theta})^2+\overline{(v'_z)^2}+3\overline{(v'_r)^2}+\overline{(v'_\theta)^2}+\frac{2}{\rho}\bar{p}\ +2gz]_3\,\pi r_1 dz
\end{aligned} \tag{5-40}$$

By taking $[\bar{p}+\rho g z]_3 \approx [\bar{p}+\rho g z]_4 \approx \bar{p}_1$, the pressure and gravity terms cancel by the continuity equation. Eq.(5-40) simplifies to:

$$\begin{aligned}
&\int_{r_1}^{r_2}\rho\overline{V_z}[(\overline{V_z})^2+(\overline{V_r})^2+(\overline{V_\theta})^2+3\overline{(v'_z)^2}+\overline{(v'_r)^2}+\overline{(v'_\theta)^2}]_2\,\pi r dr \\
&-\int_{r_1}^{r_2}\rho\overline{V_z}[(\overline{V_z})^2+(\overline{V_r})^2+(\overline{V_\theta})^2+3\overline{(v'_z)^2}+\overline{(v'_r)^2}+\overline{(v'_\theta)^2}]_1\,\pi r dr \\
&+\int_0^{z_2}\rho\overline{V_r}[(\overline{V_z})^2+(\overline{V_r})^2+(\overline{V_\theta})^2+\overline{(v'_z)^2}+3\overline{(v'_r)^2}+\overline{(v'_\theta)^2}]_4\,\pi r_2 dz \\
&-\int_0^{z_2}\rho\overline{V_r}[(\overline{V_z})^2+(\overline{V_r})^2+(\overline{V_\theta})^2+\overline{(v'_z)^2}+3\overline{(v'_r)^2}+\overline{(v'_\theta)^2}]_3\,\pi r_1 dz=\dot{W}-\dot{E}_V
\end{aligned} \tag{5-41}$$

In terms of RMS velocities, Eq.(5-41) will be written as Eq.(5-42):

$$\begin{aligned}
&\int_{r_1}^{r_2}\rho\overline{V_z}[(\overline{V_z})^2+(\overline{V_r})^2+(\overline{V_\theta})^2+3v_z^2+v_r^2+v_\theta^2]_2\,\pi r dr \\
&-\int_{r_1}^{r_2}\rho\overline{V_z}[(\overline{V_z})^2+(\overline{V_r})^2+(\overline{V_\theta})^2+3v_z^2+v_r^2+v_\theta^2]_1\,\pi r dr \\
&+\int_0^{z_2}\rho\overline{V_r}[(\overline{V_z})^2+(\overline{V_r})^2+(\overline{V_\theta})^2+v_z^2+3v_r^2+v_\theta^2]_4\,\pi r_2 dz \\
&-\int_0^{z_2}\rho\overline{V_r}[(\overline{V_z})^2+(\overline{V_r})^2+(\overline{V_\theta})^2+v_z^2+3v_r^2+v_\theta^2]_3\,\pi r_1 dz=\dot{W}-\dot{E}_V
\end{aligned} \tag{5-42}$$

Eq.(5-42) will be used to determine $\dot{E}_V$ using experimental data for V_z, V_r, V_θ, and v_z, v_r, v_θ.

5.2 Methods Used by Previous Investigators to Estimate Average and Local Dissipation Rate

Different types of impellers create different circulation patterns and different distributions of turbulence energy dissipation for the same tank geometry. The same average power input per unit mass (sometimes called the average energy dissipation, $P/\rho V_T$) can result in widely different distributions of turbulence energy dissipation when different impellers are used with the same tank geometry. The turbulence energy dissipation in agitated tanks, especially in the impeller region (the volume swept out by the impeller blades) and the impeller discharge region is needed to advance our understanding of mixing phenomena, such as the formation of liquid-liquid dispersions.

The average power input can be measured using torque transducers, or calculated using the power numbers of impellers. However, the local turbulence energy dissipation rate, ε, and the average turbulence energy dissipation rate for a specific control volume, $\bar{\varepsilon}_i$, are difficult to measure directly, since all three instantaneous velocities need to be measured simultaneously. Therefore, simplifying assumptions and/or semi-empirical equations must be used to estimate ε and $\bar{\varepsilon}_i$. Previous investigations into the average dissipation and the local dissipation in the impeller and impeller discharge region have used a variety of approaches which have been reviewed in **Chapter 2**. For clarity, the main results are summarized below.

5.2.1 Previous measurements of the average dissipation

Cutter (1966) started with a macroscopic energy balance and derived Eq. (2-36) to calculate the dissipation. He made the following assumptions in the derivation of Eq.(2-36):

a) the turbulence is steady;

b) the viscous forces are negligible;

c) the turbulence is isotropic, so $v_z^2 \approx v_r^2 \approx v_\theta^2$;

d) axial mean velocities are negligible compared with the radial and tangential components for an RT;

e) circular symmetry exists, i.e. $\partial/\partial\theta=0$.

With the exception of (d), the assumptions made by Cutter are reasonable, based on the data collected in our lab. The axial mean velocities measured for the RT are not small enough to be neglected.

Using radial and tangential velocity data measured by a photographic method in the flow produced by an RT, Cutter determined the average dissipation in the impeller region. He concluded that most of the energy supplied to the impeller is dissipated within the boundaries of the impeller (~20%) and in the impeller stream (~50%), with only about 30% being dissipated in the rest of the tank (which makes up approximately 90% of the tank volume).

Gunkel and Weber (1975) measured the distribution of dissipation for an RT using a hot-wire anemometer with air as the working fluid. They reported a totally different picture of the average dissipation. They found that most of the energy supplied to the impeller was dissipated outside the impeller stream, that is, in the bulk of the tank. This discrepancy may be caused by the different working fluid used, and by the difficulties of using hot wire anemometers in three dimensional, strongly recirculating flows.

Wu and Patterson (1989) measured the distribution of dissipation produced by an RT using LDA. They used Eqs (2-39a) and (2-39b) to calculate the kinetic energy flux in radial direction, KE_r and the kinetic energy flux in axial direction, KE_z. By performing an energy balance over a defined control volume, they concluded that about 30% of the total energy was dissipated in the impeller region, and about the same amount was dissipated in the impeller discharge region, leaving 40% to be dissipated in the bulk of the tank.

Jaworski and Fort (1991) investigated the average dissipation for pitched blade turbines of various sizes. They measured axial velocity and pressure profiles using a three-hole Pitot tube and calculated the average dissipation assuming that viscous stresses are negligible. They concluded that 54% of the input energy is dissipated in the region below the impeller, 32% in the impeller region, and 14% in the remaining volume of the tank.

Ranade and Joshi (1989), and Ranade et al. (1992) calculated the turbulence kinetic energy flux from LDA data for a PBT, using the same method as Wu and Patterson. The equations by Ranade et al., however, contain an erroneous factor of 2 which does not appear in the Wu and Patterson (1989) equations, or in the derived equation (5-42).

No previous investigations of the distribution of average dissipation for a fluidfoil impeller are available in the literature.

5.2.2 Previous estimates of the local dissipation, ε

The local dissipation can be defined in terms of the energy spectrum, E(k,t) by Eqs (2-13) and (2-14). Using Taylor's equation $\lambda^2 \propto \frac{Lv}{v}$, Batchelor (1953), simplified Eq.(2-14) to:

$$\varepsilon = A\frac{v^3}{L} \tag{2-41}$$

where A is an empirical constant, equal to 1 for isotropic turbulence, and L is the integral length scale. Using the basic definition of ε as the rate of change of turbulence kinetic energy (TKE), Tennekes and Lumley (1972) were also able to obtain Eq.(2-41). They used dimensional arguments to characterize the turbulence kinetic energy with v^2, and the characteristic time scale of the eddies with v/L.

Isotropic turbulence is assumed in both derivations of Eq.(2-41). This allows the turbulence kinetic energy to be calculated from a single component of the fluctuating velocities (v). In the more general case, all three fluctuating velocities are needed to find the turbulence kinetic energy. Thus the following equation is often used to estimate ε:

$$\varepsilon = A'\frac{q^{3/2}}{L} \tag{2-43}$$

where $q = \frac{1}{2}(v_z^2 + v_r^2 + v_\theta^2)$ and $A' = \left(\frac{2}{3}\right)^{3/2} A$.

The constant A in Eq.(2-41) or A' in Eq.(2-43) is determined by the choice of the integral length scale of turbulence L, and the choice of the velocity scale v or $q^{1/2}$. The

length scale can be obtained in two ways: one is to set it as some fraction of the impeller diameter (Brodkey, 1975), another is to calculate it from the integration of the autocorrelation function (Wu et al., 1989, Wu and Patterson, 1989, Kresta and Wood, 1993). Wu and Patterson obtained the macroscale length from the mean velocity and the Eulerian integral time scale (Eqs (2-44) to (2-46)). Wu and Patterson suggested that several corrections to these relations are necessary because the flow is three dimensional and the fluctuating velocity contains a periodic component. Kresta and Wood (1993) tested all of the proposed methods on one set of LDA data from the PBT and showed that the more complex corrections are not necessary. They recommended use of A=1, L=D/10, and a single component of RMS velocity in equation (2-41).

Schwartzberg and Treybal (1968) obtained an approximate value for L based on the scale of turbulence reported by Cutter (1966) for the energy-containing eddies in the impeller discharge stream of the tank. They presented the relation $\frac{1}{k_e} = L = 0.08D$ which is in excellent agreement with the value recommended by Kresta and Wood (1993).

This work was undertaken with two objectives in mind. The first was to put the value of the constant A on firmer ground by performing macroscopic energy balances on small control volumes, and comparing the results with the integral of the local dissipation over the same control volume. Laufhutte and Mersmann (1985) also attempted this approach; however, they only performed the macroscopic balance *over the whole tank.* Since it is known that the state of turbulence varies substantially over the tank, this choice of control volume incorporates a significant degree of uncertainty in the final results.

The second objective of the work was to determine where the power is consumed for the three impellers chosen. Since the power numbers vary from approximately 5 (RT) to 1.3 (PBT), to 0.3 (A310), it is important to understand where the additional energy is used: a) in generating stronger convection flows, or b) as higher maximum levels of turbulence. This question requires examination of both the distribution of dissipation throughout the tank (the final destination of *all* of the input power), and the various terms in the macroscopic balance equation close to the impeller.

5.3 Experimental Determination of the Turbulence Energy Dissipation Rates in the Impeller Regions

5.3.1 Apparatus

The LDA

The fundamentals and validation of laser Doppler anemometer (LDA) were described in **Chapter 4**. With the settings chosen in **Chapter 4** the data validation in all measurements was ≥99%. The average frequency of velocity determinations was 1.2 kHz.

Geometry of the baffled tank and the impellers

The baffled tank and the impellers are shown in **Figure 2-2** and **Figure 5-2**, respectively. Geometric variables are defined in **Chapter** 2 and **Chapter** 4. To prevent vortexing and the entry of air into the system, a lid was installed on top of the baffles, and covered with *5 cm of water to seal the tank.*

All three impellers were used in their standard configurations. The four-bladed PBT had blades inclined at 45° to the horizontal; the blade width of the PBT and RT was D/5; the blade length of the RT was D/4. The A310 was used as supplied by Lightnin'. The geometric and operating parameters for the three impellers are summarized in **Table 5-1**.

The control volumes

The traverses bounding the control volumes are shown in **Figure 5-3,** along with the additional traverses where the local dissipation was measured. The dashed lines enclose the control volumes used for the energy balances, and the dotted lines show the location of additional traverses where the local dissipation was measured. For the radial flow impeller RT, two volumes were chosen: one around the impeller and another from the tip of impeller blades nearly to the baffles (the impeller discharge stream). For each of the two axial flow impellers, the PBT and the A310, four volumes were chosen: one enclosing the impeller and three in the direction of the impeller discharge. Three control volumes were defined in the impeller discharge region since the flow fields generated by these two axial flow impellers are characterized by a combination of a strong downward

flow and less significant radial flow. The control volume with the highest $\bar{\varepsilon}_i$ of these three control volumes was designated the "impeller discharge stream". Four additional, evenly-spaced measuring traverses were used for determination of the local dissipation in this control volume.

5.3.2 Methods

The average dissipation, $\bar{\varepsilon}_i$

The macroscopic energy balance equation was derived as discussed in section **5.2**, using Cutter's assumptions (a, b, c and e); and an additional assumption that the change in potential energy exactly balances the mean pressure difference. It was then applied to each control volume shown in **Figure 5-3**. In order to clearly specify energy terms, equation (5-42) is rewritten as follows:

Power Dissipation Convective terms TKE terms

$$\begin{aligned}\dot{W} - \dot{E}_V = &\int_{r_1}^{r_2} \rho \overline{V_z}[(\overline{V_z})^2 + (\overline{V_r})^2 + (\overline{V_\theta})^2 + 3v_z^2 + v_r^2 + v_\theta^2]_2 \pi r dr \\ &- \int_{r_1}^{r_2} \rho \overline{V_z}[(\overline{V_z})^2 + (\overline{V_r})^2 + (\overline{V_\theta})^2 + 3v_z^2 + v_r^2 + v_\theta^2]_1 \pi r dr \\ &+ \int_0^{z_2} \rho \overline{V_r}[(\overline{V_z})^2 + (\overline{V_r})^2 + (\overline{V_\theta})^2 + v_z^2 + 3v_r^2 + v_\theta^2]_4 \pi r_2 dz \\ &- \int_0^{z_2} \rho \overline{V_r}[(\overline{V_z})^2 + (\overline{V_r})^2 + (\overline{V_\theta})^2 + v_z^2 + 3v_r^2 + v_\theta^2]_3 \pi r_1 dz\end{aligned} \tag{5-42}$$

The terms in the equation are as follows: $\dot{W}$ is the rate at which shaft work enters the control volume ($\dot{W}=N_p\rho N^3D^5$); $\dot{E}_v$ is the rate of viscous dissipation to internal energy ($\dot{E}_v = m_i\bar{\varepsilon}_i$); and the subscripts 1, 2, 3 and 4 outside the square brackets stand for surfaces 1, 2, 3 and 4, respectively, which are shown in the schematic drawing of a control volume (**Figure 5-1**). On the right hand side of equation, the mean velocity terms are grouped together as "convective" terms and the fluctuating velocity terms are grouped as "turbulence kinetic energy" (TKE) terms. Splitting the terms of the energy balance up in this way allows comparison of the three types of impellers.

The local dissipation, ε

Since it is practically impossible to measure ε directly, semi-empirical equations to estimate ε have to be chosen. Kresta and Wood (1993) gave an extensive review of the available methods. An experimental comparison of the methods as applied to the PBT showed that Eq.(2-41), i.e. $\varepsilon=Av^3/L$, provides a reasonable estimate of the dissipation close to the impeller where the flow can be approximated as locally isotropic.

Three things must be considered when Eq.(2-41) is used to estimate ε in flow fields generated by different turbines: the validity of the locally isotropic assumption, the value of the integral length scale L (as some fraction of impeller diameter, D), and the value of the constant A. The locally isotropic assumption was first checked in the control volumes for all the three impellers; values of L were obtained from the literature and from tuft visualization; then the assumption of A=1 was examined using a comparison of macroscopic energy balance results with the integration of the local dissipation (Eq. (5-43) below).

Local isotropy

All three components of the mean and fluctuating velocities were measured for each of the traverses shown in **Figure 5-3**. A representative set of profiles of the mean and fluctuating components for each impeller is shown in **Figures 5-4** (a to c). The traverse closest to the impeller blades was chosen since this is where the turbulence intensity is at a maximum. Examination of the other traverses showed that this traverse is neither the most closely isotropic, nor the worst case for a given impeller: the range of performance shown in **Figures 5-4** (a to c) is representative of the overall set of data.

Perfectly isotropic turbulence requires that all of the statistical features of the flow have no preference for any direction, so perfect disorder reigns. The most basic criterion is that the three fluctuating velocities are equal, so that the turbulence kinetic energy, $q=\frac{v_z^2+v_r^2+v_\theta^2}{2}$, can be calculated using a single component of the fluctuating velocity, i.e. $q=\frac{3v_i^2}{2}$, i=r, z, or θ. The single component of fluctuating velocity is often the

fluctuating velocity with the same direction as the main flow generated by an impeller. For the radial flow turbine, the radial fluctuating velocity is chosen, and for the axial flow turbines the axial fluctuating velocity is used. From **Figures 5-4** (a to c), this approximation is reasonable, i.e. the values of three fluctuating velocities are nearly equal. The quantitative verification of this is shown in **Figures 5-5** (a to c), where q is compared to $\frac{3v_i^2}{2}$ for all three impellers.

Determination of L using tuft visualization

Kresta and Wood (1993) argued that the theoretically based estimate of the integral length scale used in Eq.(2-41) is exactly equal to the length scale of the trailing vortices for both the RT and the PBT. Thus, by determining the length scale of the trailing vortices at the edge of the blade for the RT, PBT, and A310, the characteristic length L can be determined.

Flow visualization with tufts was used to determine the length scale of the trailing vortices for the RT, PBT, and A310. Fujicolor films (400 Super G) were used. The shutter speed was 1/500 sec. and focal length was set at f/3.5. The flow was in a fully turbulent state with $Re \geq 2.2 \times 10^4$. All photos were taken 40 minutes after the impeller started rotating.

For the RT, the tufts attached to the tip of impeller blades separate into two halves with the center line of the blade as their symmetry axis. Tuft visualization shows that the tufts of each half are wound together, stretching radially towards the tank wall. This gives the diameter of the vortices created by the RT equal to W/2, where W is the vertical width of the impeller blade. Since W=D/5, L=D/10. These results agree well with the results reported by Van't Riet and Smith (1975), by Yianneskis et al. (1987), and by Stoots and Calabrese (1995).

For the PBT and the A310, the tufts were attached to the lower edge of the impeller blades. Both the PBT and the A310 form a vortex which extends from the tip of the impeller to approximately D/10 from the tip. This is clearly shown in **Figure 5-2**,

where the tufts on either side of the mark at D/10 separate from each other. Tufts in the tip region of the PBT blades show clear winding, while no winding appears for tufts in the same region of the A310 blades; i.e. the PBT has a better defined vortex than the A310. These results support the use of L=D/10 for all three impellers.

5.4 Results

The average turbulence energy dissipation was calculated from equation (5-42) and the local turbulence energy dissipation was estimated from equation (2-41) with L=D/10 and A=1. To check the validity of equation (2-41) with L=D/10 and A=1, a comparison of the $\dot{E}_v$ calculated from integration of the local turbulence energy dissipation and the $\dot{E}_v$ from the macroscopic energy balance equation was carried out for the impeller discharge stream control volume. In this section, the three impellers are compared based on turbulence energy dissipation and the distribution of energy between convective and turbulent flows.

5.4.1 Comparison of the local and integral methods

The $\dot{E}_v$ calculated from Eq.(5-42) was compared with the integration of Eq.(2-41) for the impeller discharge stream control volume for each of the three impellers. For the RT, this control volume is enclosed by the four traverses - z_1=18 mm , z_2=-27 mm, r_1=63 mm and r_2=87 mm. For the PBT, the control volume is enclosed by the four traverses - z_1=40.5 mm, z_2=10.5 mm, r_1=63 and r_2=87 mm. For the A310, the control volume is enclosed by the four traverses - z_1=39.0 mm, z_2=9.0 mm, r_1=0 mm and r_2=63 mm. In order to obtain accurate integration results from Eq.(5-47), four radial traverses were added between z_1 and z_2 (see **Figure 5-3**). Again, the streamwise fluctuating velocity was used to estimate ε. The integration equation is:

$$\dot{E}_v = \sum_{i=1}^{5} \Delta z_i \int_{r_1}^{r_2} \varepsilon \rho 2\pi r dr \qquad (5\text{-}43)$$

where $\dot{E}_v$ is the energy dissipation rate in the control volume; i from 1 to 5 refers to the five subdivided volumes in the control volume for each of the three impellers; ε is the

average value of two local ε's on two adjoining traverses at the same r, where the local value of the dissipation is calculated by $A\frac{v^3}{L}$ with A=1 and L=D/10; Δz_i is the axial distance between two adjoining traverses; and ρ is 10^3 kg/m^3.

From the results given in **Table 5-2**, it is clear that the two methods are in very close agreement. That the local measurements give a consistently higher result may be caused by the use of the RMS velocity in the direction of the main flow for all the three impellers. Although the flow in the impeller and impeller discharge stream is approximately locally isotropic, the RMS velocity in the direction of the main flow is slightly larger than either of the other two RMS velocities at most of the points on the six radial traverses.

From the comparison of the two methods, it was concluded that: 1) the two equations agree well for the three impellers examined; 2) the local dissipation ε can be estimated from Eq.(2-41) with A=1 and L=D/10 close to the impeller; 3) comparison of $\dot{E}_v$ based on Eq.(5-42) with the integration of ε (Eq.(5-43)) will give the value of A. Efforts to extend this analysis to regions of the tank far removed from the impeller were not successful. This is due to the small velocities and large relative errors observed in the remaining tank volume.

5.4.2 Comparison of the three impellers

Values of the average dissipation, $\bar{\varepsilon}_i$

Figure 5-6 shows the percentage of the total energy dissipated and the average dissipation $\bar{\varepsilon}_i$ for each control volume. The percent of the total energy dissipated in a control volume was calculated from

$$\frac{\dot{E}_v}{P}\times 100\% \tag{5-44}$$

where P is the input power. The average dissipation $\bar{\varepsilon}_i$ was calculated from

$$\bar{\varepsilon}_i = \frac{\dot{E}_v}{m_i} \tag{5-45}$$

where m_i is the mass of fluid in the control volume. In order to make a direct comparison between the three impellers, the experimental $\bar{\varepsilon}_i$'s in **Figure 5-6** for the RT were multiplied by a factor of 1.54 (i.e. 10.3/6.71). Since both the mean ($\overline{V}$) and the fluctuating velocity (v) are proportional to ND, the terms $\overline{V}^3$ and $\overline{V}\,v^2$ in equation (5-42) are proportional to the power input $P=N_p\rho(N^3D^3)D^2$ for a given impeller. This adjustment allows comparison on the basis of equal power input per unit mass for all three impellers.

For the RT, the percent of the total energy dissipated in the two control volumes examined was 43.5%. By contrast, the fluid volume occupies only 10% of the volume of the tank. The average dissipation in the impeller discharge stream is twice that in the impeller region. This may be explained by the fact that vortices are formed in the impeller region, but are destroyed by the baffles which affect the flow in the impeller discharge stream. Comparison of the percent of the total energy dissipated in the impeller and impeller discharge stream with the data of Cutter (1966) and Wu and Patterson (1989) shows that the absolute values are close to Cutter's data in the impeller region, but smaller than Wu and Patterson's data. The equal distribution of dissipation between the impeller region and in the impeller discharge stream agrees well with Wu and Patterson. The difference in the percent of the total energy dissipated in the impeller region between this work and Wu and Patterson's can be partly explained by the difference in the ratio of D/T. Wu and Patterson used a ratio of D/T=0.344. In this work , D/T=0.5 was used. Sato et al. (1970) state that the dissipation becomes more uniform in stirred tanks when the impeller diameter increases. This means that if larger impeller diameters are used, less of the total energy will be dissipated in the impeller region. Nearly half of the total input energy is dissipated in the impeller and impeller discharge region for the RT.

For the PBT, the percent of the total input energy dissipated in the impeller control volume is 52%, although the fluid in the impeller region occupies only 3.45% of the tank volume. If all four control volumes are combined, the percent of the total input

energy dissipated in them is 75.1%. Unlike the RT, the maximum average dissipation for the PBT occurs in the impeller region. There is a 27.9 fold difference between the average dissipation existing in these four control volumes. Jaworski and Fort (1991) also found that most of the energy is dissipated in the impeller region and in the impeller discharge stream for a PBT.

For the A310, the characteristics of the turbulence energy dissipation are different from the PBT. The percent of the energy dissipated in the impeller region is just 18.0%. Again the fluid in the impeller region occupies only 3.45% of the tank volume. If all four control volumes are combined, the percent of the total input energy dissipated in them is 43.9% in 13.1% of the tank volume. Unlike the PBT, the average dissipation in the impeller region for the A310 is nearly the same as that in the impeller discharge stream. This can be explained by the homogeneity of the flow generated by the A310. Because of the slightly varying pitch and varying blade width of the A310, the turbulence energy dissipation is more homogenous in the impeller and impeller discharge stream. There is only a 11.0 fold difference between the average dissipation in the four control volumes.

Figure 5-6 shows that the average dissipation differs radically between impellers for the same total power input. To explain these differences, the various terms in the macroscopic energy balance were compared, again scaling the RT measurements to a basis of equal power input.

Distribution of power between convective and turbulent flow

A better understanding of the characteristics of turbulence energy dissipation in the impeller and impeller discharge stream for the three impellers can be reached if the distribution of power between convective terms, turbulence kinetic energy terms, and dissipation is analyzed. **Table 5-3** lists the contribution of each energy term in equation (5-42) for the impeller and the impeller discharge stream for all three impellers. The number in bold face is the largest term of the three impellers; the number in italics is the smallest.

From equation (5-42), the sign of an energy term is determined by the direction of the axial or radial mean velocity. At each point on the four traverses defining a control

volume, if the dot product of the mean velocity vector and the unit normal vector of a surface is negative, the associated terms are energy "in"; and if the dot product of the mean velocity vector and the unit normal vector of a surface is positive, the associated terms are energy "out". We begin the analysis of energy distribution with the impeller region.

Impeller region:

The PBT produces the most dissipation in the impeller region. This is because the PBT has the largest convective energy in and TKE in and the smallest convective energy out and TKE out. The axial flow generated by the PBT is very strong; from the upper edge, through the impeller and down to the lower edge of impeller blades. When compared with the other two impellers, it is clear that the PBT uses the returning flow to boost its performance.

Unlike the PBT, the RT has small values of the convective energy in and TKE in, and shows large values of TKE and convective energy out. The difference between the TKE out and TKE in (5.12-1.18=3.94) for the RT is about 40% of the power input, while the same difference for the PBT is only 15% of the power input. The RT transforms more of the power into turbulence kinetic energy. Note that for the RT the convective energy out and the TKE out are mainly due to the radial flow at the tip of the impeller blades; the flow from the top and the bottom of the impeller blades is weak.

For the A310, the dissipation in the impeller region is nearly the same as the RT, but with different features. The A310 has: 1) the smallest convective energy and TKE in; 2) the largest convective energy out. This is because correspondingly: 1) for the A310, the flow from the top region of the tank is much weaker than the flow generated by the PBT with the same power input; 2) the A310 generates a more axial flow than the PBT. The difference between the convective energy out and convective energy in (5.95-0.69=5.26) for the A310 is more than 50% of the power input, while the same difference for the PBT is around 30% of the power input. This means that the A310 is more efficient at generating downward convection.

Impeller discharge stream:

In the impeller discharge stream, the variation of dissipation between the three impellers is much less than that in the impeller region. The RT has the largest value of dissipation.

Because of the perfectly radial flow of the RT, the RT has both the largest TKE in and the largest TKE out. The TKE losses (TKE in-TKE out) are only 10% of the dissipation $\dot{E}_v$. The remaining 90% of the dissipation terms comes from the convective energy losses. The rapid decay of the main radial flow is the main source of dissipated energy.

The PBT has the smallest values of both convective energy in and convective energy out. The TKE losses (TKE in-TKE out) in this region for the PBT are nearly zero. This implies that the vortex cascade structure formed by the PBT is not destroyed in this region. The dissipation $\dot{E}_v$ is nearly totally due to the convective energy losses-the decay of the convective flow.

The A310 has both the largest convection in and the largest convection out, which again shows that the A310 is very efficient for convection. Experimental data show that the downward flow dominates even below the impeller discharge stream examined here, and that the downward flow decays much slower than the flow of the PBT. In contrast to the PBT, the dissipated energy for the A310 in this region is mainly due to the TKE losses.

5.5 Conclusions

The flow in the impeller and impeller discharge stream is approximately locally isotropic for the three impellers. The two equations for $\dot{E}_v$ (Eq.(5-42) and Eq.(5-43)) agree well for the three impellers. Eq.(2-41) with A=1 and L=D/10 gives a reliable estimation of the local turbulence energy dissipation. The constant A in Eq.(2-41) can be determined by comparison of the macroscopic energy balance (Eq.(5-42)) with the integrated local dissipation (Eq.(5-43)) for any impeller.

The dissipation was always very high in the impeller region and in the impeller discharge stream. The bulk of the energy is dissipated in the small volume occupied by the impeller and the impeller discharge for all three impellers: in order of increasing percentages 38.1% (A310), 43.5% (RT) and 70.5% (PBT). The dominant characteristics of energy distribution are different for each impeller. The A310 was most efficient at generating convective flow. The RT generated the most TKE, and the PBT derived a much larger portion of its energy from the return flow. These differences should be taken into account when selecting an impeller for a specific application.

Tables in Chapter 5

Table 5-1 Experimental conditions and selected results for the three impellers.

Variable	RT	PBT	A310
diameter, D	T/2	T/2	0.475T
off bottom clearance, C	T/2	T/2	T/2
number of baffles, N_f	4	4	4
rotational speed, N (rpm)	221	400	728
Reynolds number, Re	5.22×10^4	9.44×10^4	15.5×10^4
power number, N_p	5.4[a]	1.4[b]	0.30[c]
power input*, $P=N_p\rho N^3D^5$, ($kg\ m^2/s^3$)	6.71	10.3	10.3
power input per unit mass, $\bar{\varepsilon}$ (m^2/s^3)	0.618	0.950	0.950
input energy dissipated in all control volumes	43.5%	75.1%	43.9%
$\bar{\varepsilon}_{i,max} / \bar{\varepsilon}_{i,min}$ in control volumes	2.05	27.9	11.0

a averaged from 11 values in **Table 2-1**;

b averaged from 3 values and re-checked in this lab using a Torque Transducer;

c provided by Lightnin' and re-checked in this lab using a torque transducer;

* where $\rho=10^3$ (kg/m^3).

Table 5-2 Comparison of the two methods for the impeller discharge stream. All results are based on unscaled data.

Impeller	$\dot{E}_v$ from the macroscopic balance (Eq.(5-42)) ($kg\ m^2/s^3$)	$\dot{E}_v$ from the local dissipation (Eq.(5-43)) ($kg\ m^2/s^3$)	ratio of the two methods
RT	1.91	2.02	1.06
PBT	1.90	2.03	1.07
A310	2.07	2.15	1.04

Table 5-3 Distribution of power between convective terms, turbulent fluctuations and dissipation. Numbers in bold face are the largest, numbers in italics are the smallest. All terms have units of power (W). The RT results have been scaled to a basis of equal power input.

Impeller region						
Impeller	Convective energy in	TKE in	Power in $\dot{W}$	Convective energy out	TKE out	Dissipation $\dot{E}_v$
RT	1.08	1.18	10.3	5.88	**5.12**	*1.58*
PBT	**2.13**	**1.76**	10.3	*5.52*	*3.31*	**5.38**
A310	*0.69*	*0.92*	10.3	**5.95**	4.12	1.86
Impeller discharge stream						
Impeller	Convective energy in	TKE in	Power in $\dot{W}$	Convective energy out	TKE out	Dissipation $\dot{E}_v$
RT	5.90	**5.15**	0	3.29	**4.86**	**2.90**
PBT	*4.80*	*3.57*	0	*2.96*	3.51	*1.90*
A310	**6.10**	4.70	0	**5.41**	*3.32*	2.07

Figures in Chapter 5

Figure 5-1. A control volume in an agitated tank in cylindrical coordinates (r, θ, z).

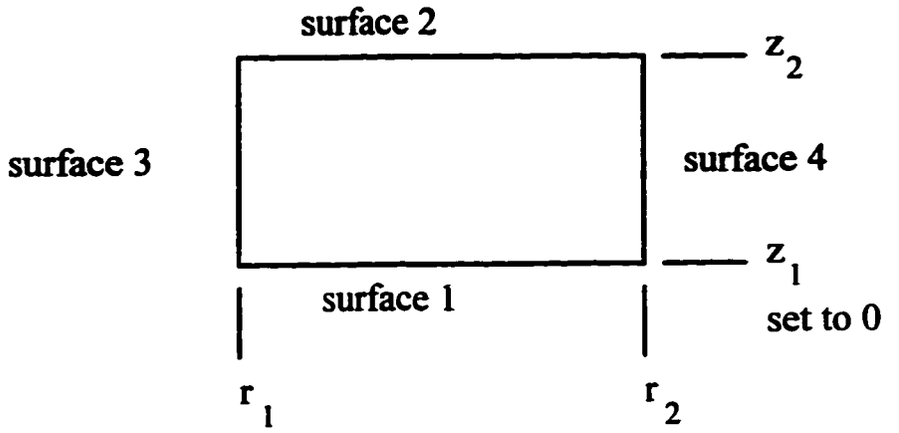

Figure 5-2 The three impellers studied, with tuft visualization of the trailing vortices at the blade tip.

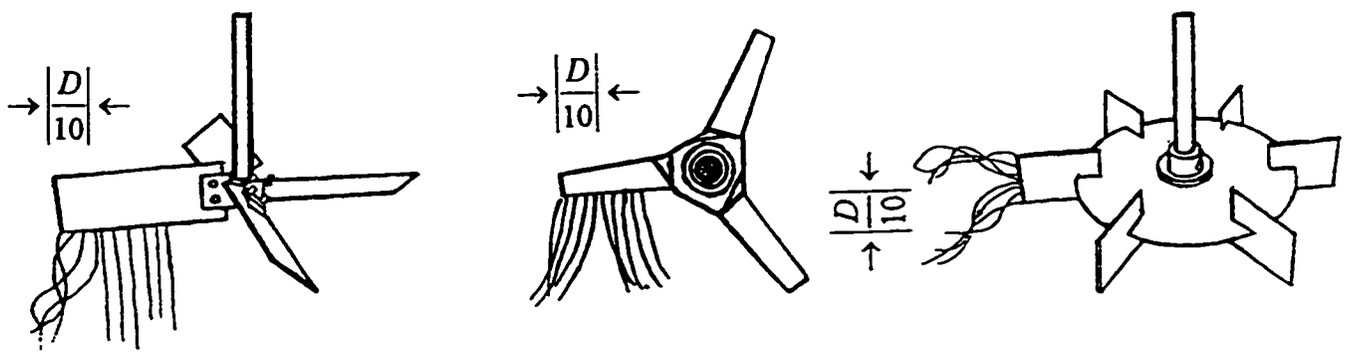

PBT A310 RT

Figure 5-3 The control volumes and local dissipation traverses for the three impellers. All numbers are in units of mm. The dashed lines enclosing the impellers define the impeller control volume. The lines enclosing the 6 evenly spaced traverses (e.g. dotted lines to the right of the RT) define the impeller discharge control volumes.

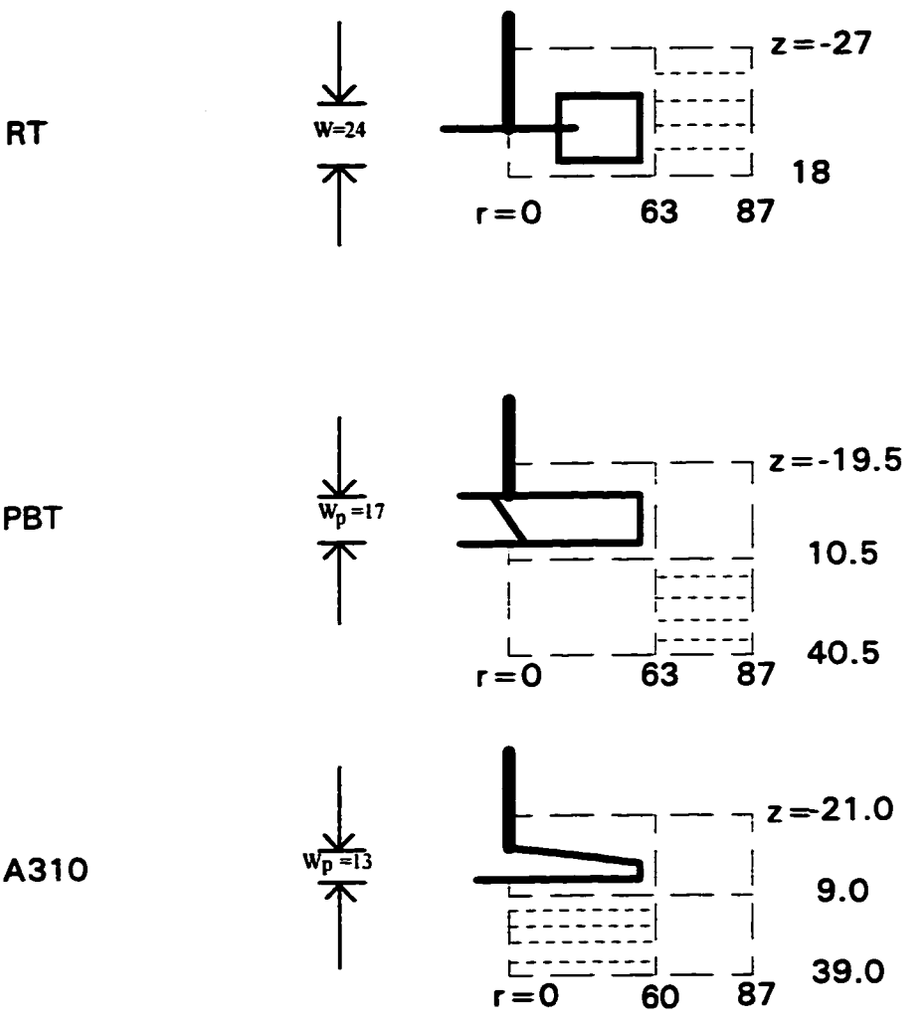

Figure 5-4a Axial profiles of mean and fluctuating velocities at r=63 mm for the RT.

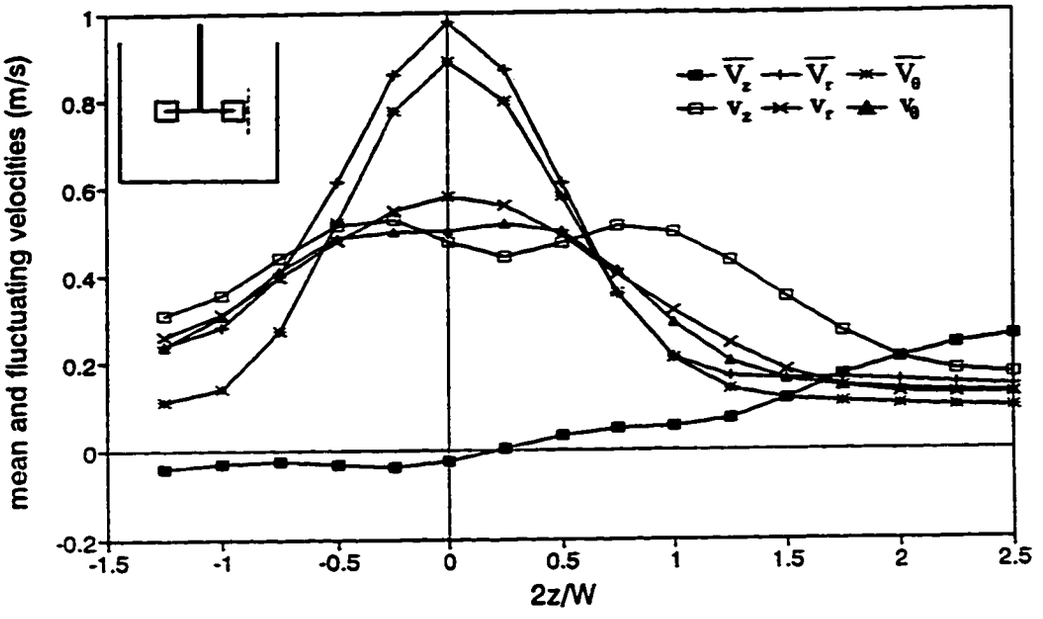

Figure 5-4b Radial profiles of mean and fluctuating velocities at z=10.5 mm for the PBT.

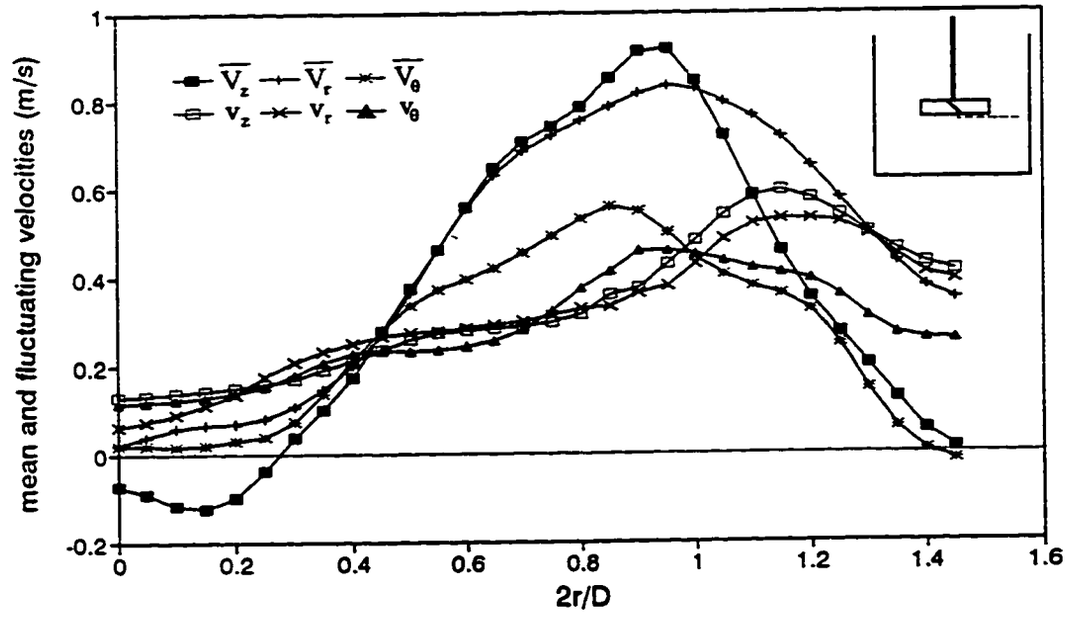

Figure 5-4c Radial profiles of mean and fluctuating velocities at z=9.0 mm for the A310.

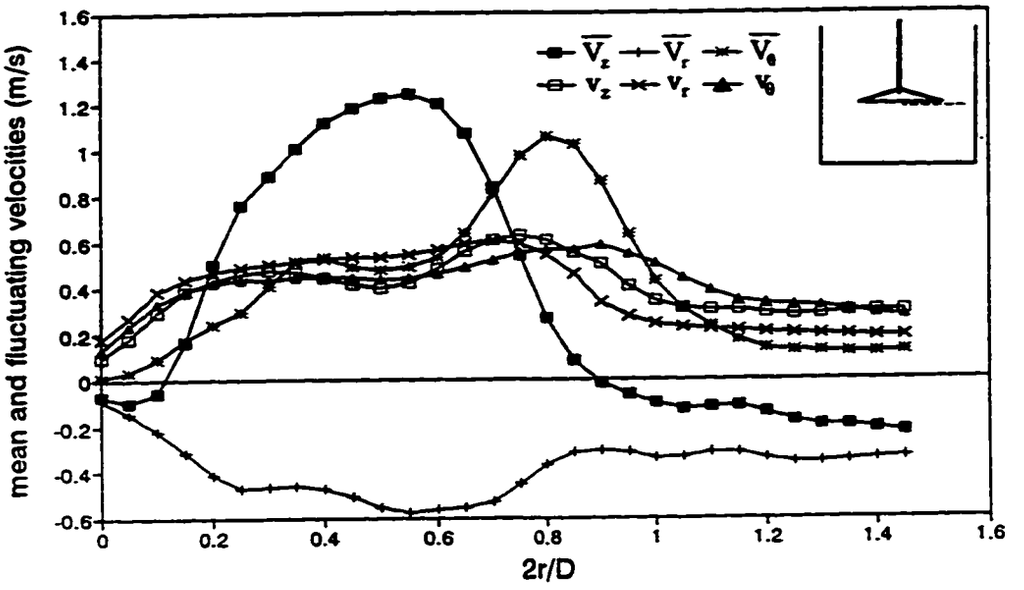

Figure 5-5a Comparison of the turbulence kinetic energy (q) calculated from 3 RMS velocities with q estimated from the radial RMS velocity, RT, tip of the impeller blades. D=T/2, C=T/2, N=221 rpm, at r=63 mm.

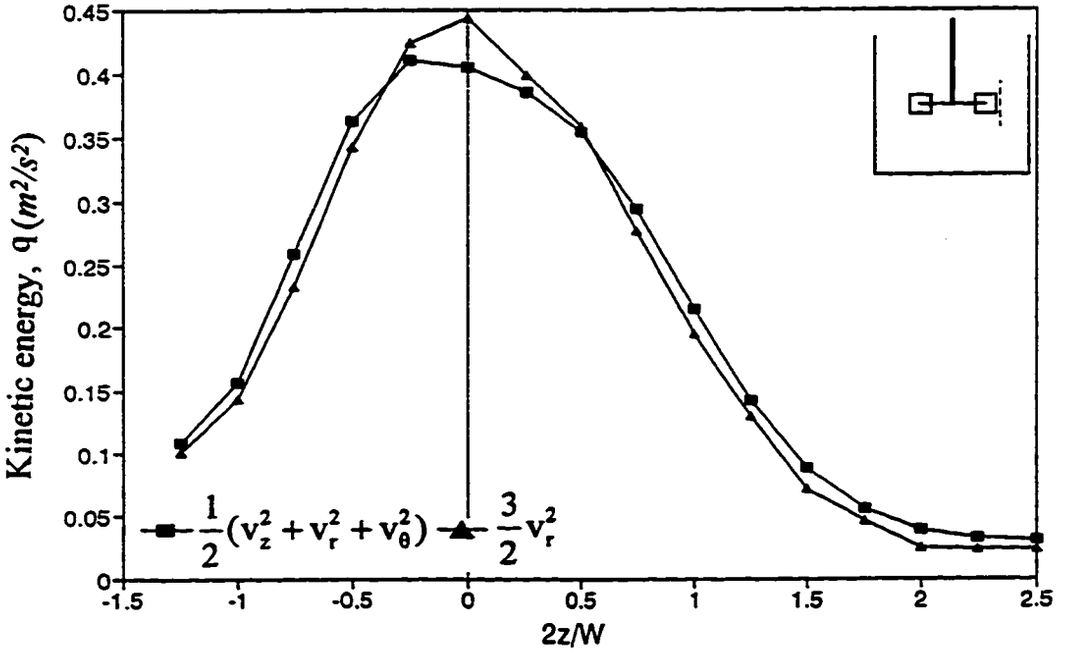

Figure 5-5b Comparison of the turbulence kinetic energy (q) calculated from 3 RMS velocities with q estimated from the axial RMS velocity, PBT, below the impeller blades. D=T/2, C=T/2, N=400 rpm, at z=10.5 mm.

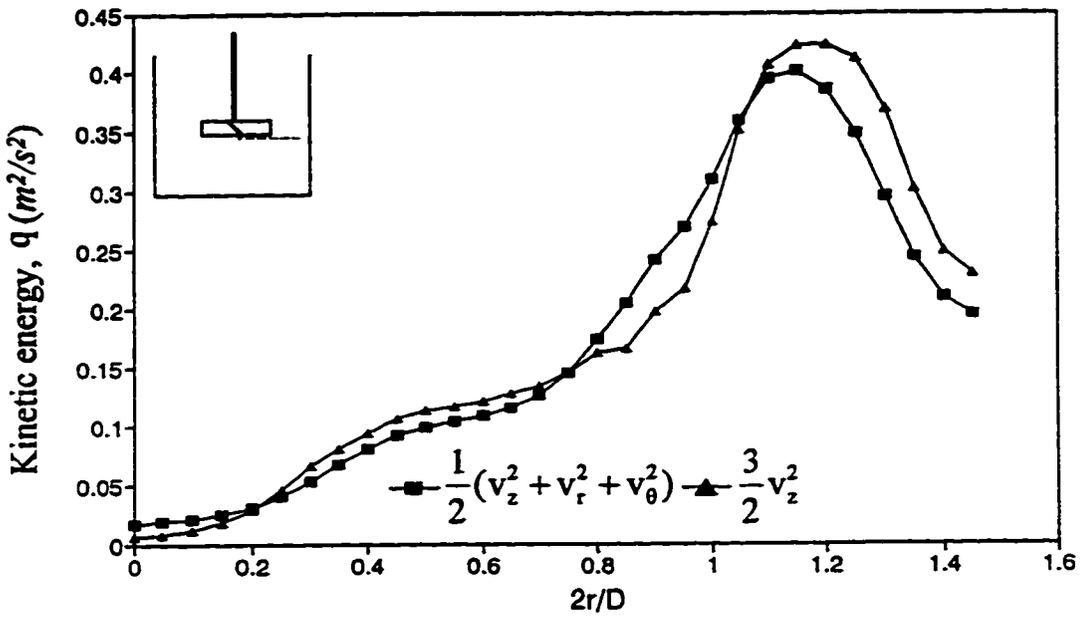

Figure 5-5c Comparison of the turbulence kinetic energy (q) calculated from 3 RMS velocities with q estimated from the axial RMS velocity, A310, below the impeller blades. D/T=0.475, C=T/2, N=728 rpm, at z=9.0 mm.

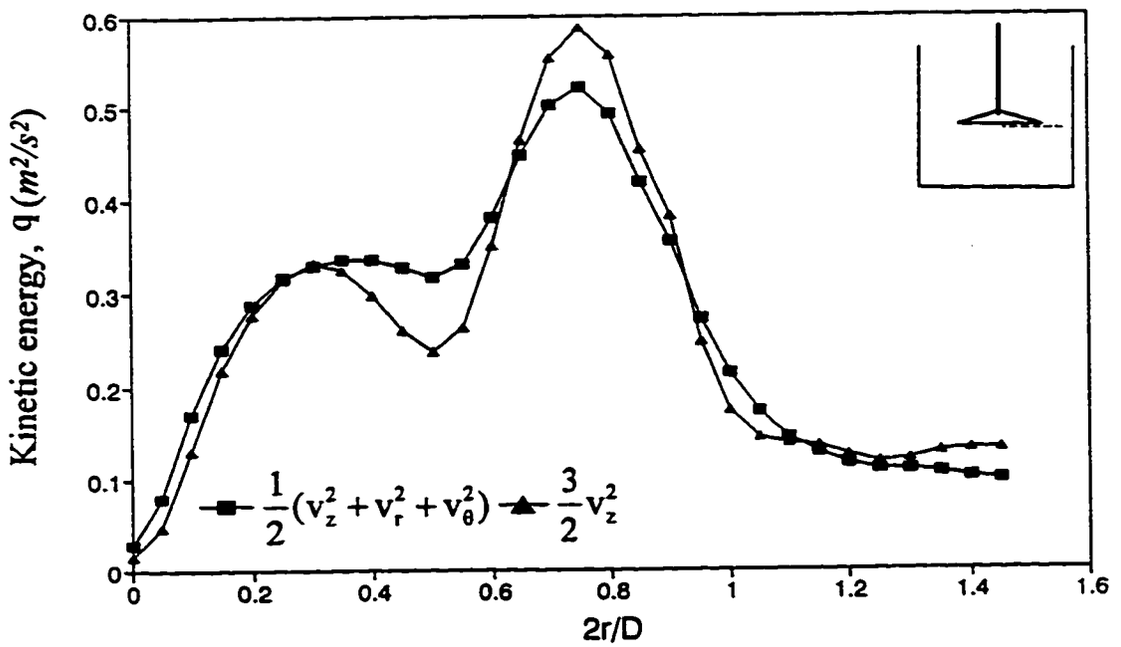

Figure 5-6 Percent of the power dissipated, and average dissipation $\overline{\varepsilon_i}$ (m^2/s^3) calculated from the macroscopic energy balance for all control volumes. Units of r and z are in mm. The results are based on equal power input.

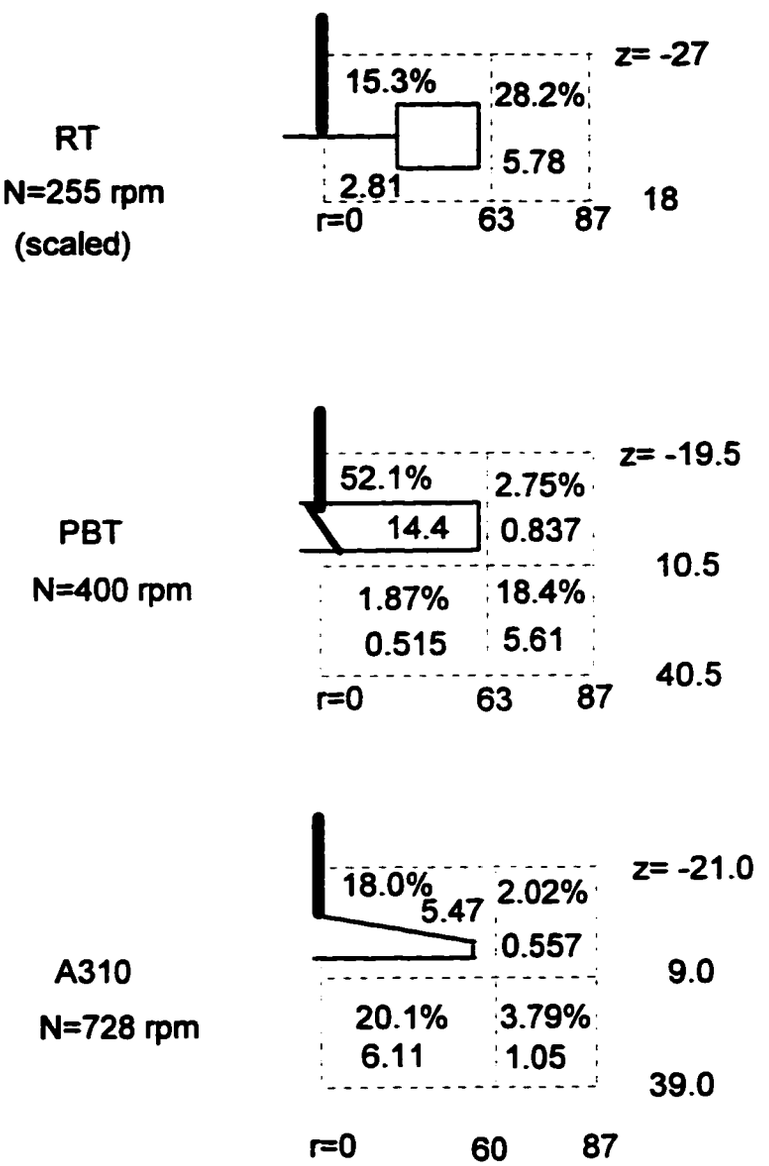

References

Batchelor, G.K., 1953, *The Theory of Homogeneous Turbulence*. Cambridge University Press, Cambridge.

Brodkey, R.S., 1975, *Turbulence in Mixing Operations*, Academic Press, New York.

Cutter, L.A., 1966, Flow and turbulence in a stirred tank. *A.I.Ch.E. J.* **12**, 35-45.

Gunkel, A.A. and Weber, M.E., 1975, Flow phenomena in stirred tanks: Part I. the impeller stream. *A.I.Ch.E. J.* **21**, 931-949.

Hinze, J.O., 1975, *Turbulence*. McGraw Hill, Toronto.

Jaworski, Z. and Fort, I., 1991, Energy dissipation rate in a baffled vessel with pitched blade turbine impeller. *Colln Czech. Chem. Commun.* **56**, 1856-1867.

Kresta, S.M. and Wood, P.E., 1993, The flow field produced by a pitched blade turbine: characterization of the turbulence and estimate of the dissipation rate. *Chem. Engng Sci.* **48**, 1761-1774.

Laufhutte, H.D. and Mersmann, A., 1985, Laser-Doppler velocimetry as a suitable measuring technique for the determination of flow behavior in stirred fluids. *Ger. Chem. Engng* **8**, 371-379.

Ranade, V.V. and Joshi, J.B., 1989, Flow generated by pitched blade turbines I: measurements using laser Doppler anemometer. *Chem. Engng. Commun.* **81**, 197-224.

Ranade, V.V., Mishra, V.P., Saraph, V.S., Deshpande, G.B. and Joshi, J.B., 1992. Comparison of axial flow impellers using a laser Doppler anemometer. *Ind. Engng. Chem. Res.* **31**, 2370-2379.

Rao, M.A. and Brodkey, R.S., 1972, Continuous flow stirred tank turbulence parameters in the impeller stream. *Chem. Engng Sci.* **27**, 137-156.

Sato, Y., Kamiwano, M. and Yamamoto, K., 1970, Turbulent flow in a stirred vessel-effects of impeller types. *Kagaku Kogaku* **34**, 104-106.

Schwartzberg, H.G. and Treybal, R.E., 1968, Fluid and particle motion in turbulent stirred tanks-fluid motion. *Ind. Engng Chem. Fundam.* **7**, 1-6.

Stoots, C.M. and Calabrese, R.V., 1995, Mean velocity field relative to a Rushton turbine blade. *A.I.Ch.E. J.* **41**, 1-11.

Tennekes, H. and Lumley, J.L., 1972, *A First Course in Turbulence*, MIT Press, Cambridge, **MA**.

Van't Riet, K. and Smith, J.M., 1975, The trailing vortex system produced by Rushton turbine agitators. *Chem. Eng. Sci.* **30**, 1093-1105.

Whitaker, S., 1981, *Introduction to Fluid Mechanics*, pp.211-230. Robert E. Krieger Publishing Company, Malabar, Florida.

Wu, H. and Patterson, G. K., 1989, Laser Doppler measurements of turbulent-flow parameters in a stirred mixer. *Chem. Eng. Sci.* **44**, 2207-2221.

Wu, H., Patterson, G. K. and Van Doorn, M., 1989, Distribution of turbulence energy dissipation rates in a Rushton turbine stirred mixer, *Expts Fluids* **8**, 153-160.

Yianneskis, M., Popiolek, Z. and Whitelaw, J.H., 1987, An experimental study of the steady and unsteady flow characteristics of stirred reactors. *J. Fluid Mech.* **175**, 537-555.

Chapter 6

Impact of Tank Geometry on the Maximum Turbulence Energy Dissipation Rate*

6.1 Introduction

The power input per unit mass of fluid in an agitated tank ($P/\rho V_T$) is not sufficient to completely define the characteristics of the turbulence energy dissipation. According to the length scale defined by Kolmogoroff, $\eta = (\nu^3 / \varepsilon)^{1/4}$, the minimum length scale in a dispersion is determined by the maximum turbulence energy dissipation rate per unit mass, ε_{max} *if* the Kolmogoroff length scale expresses the real relationship between drop size and the turbulence energy dissipation rate, so the *local* turbulence energy dissipation rate is critical. Since all the particles in the dispersion have a finite probability of passing through the position where ε_{max} occurs, the minimum drop size in a dispersion of gas or liquid will be determined by ε_{max}. Most investigations of drop breakup and gas dispersion, however, characterize ε_{max} by the power input per unit mass ($P/\rho V_T$), and examine only one tank geometry. Thus, the investigation of the effect of geometry on ε_{max} is important for both improved fundamental understanding and for practical applications.

In **Chapter 2** and **Chapter 5**, the methods to estimate local turbulence energy dissipation rate ε were reviewed. In **Chapter 5**, Eq. (2-41) with L=D/10 and A=1 as an estimation of local turbulence energy dissipation rate was verified by a combination of tuft visualization experiment and comparison with the macroscopic mechanical energy balance.

Prior to this thesis, no work had been published to investigate the effect of tank geometry on the *maximum* turbulence energy dissipation rate in stirred tanks. Research on the effect of tank geometry on the *local* dissipation rate is limited to some very specific correlations reported by Okamoto et al. (1981). They reported Eqs. (2-38) and (2-39) to

* *A modified version of this chapter was published in the AIChE J., vol.42, pp. 2476-2490 (1996).*

correlate the local turbulence energy dissipation rates in the impeller stream ε_i and in the circulation region ε_c to the ratio of D/T. These equations account for the effect of impeller diameter and of impeller blade width on ε. In fact, Eqs. (2-38) and (2-39) can only be used to correlate the effect of the width of impeller blades or impeller diameter on ε for a single point, since the locations of ε_i and ε_c were fixed. Measurements have shown that ε varies from point to point, especially in the region around the impeller blades, so that any single measurement of ε can not reliably represent the maximum, minimum, or the average dissipation rate in a region. For example, if D/T=1/2, Eq. (2-37) gives $\varepsilon_i = 5.93\bar{\varepsilon}$, which is well below the maximum dissipation ($11.3\,\bar{\varepsilon}$) reported by the same authors, and $\varepsilon_c = 0.42\bar{\varepsilon}$, which is well above the minimum dissipation ($0.16\,\bar{\varepsilon}$) in the upper region of the tank.

This investigation focuses on the effects of one operating variable (rotational speed N) and three geometric variables (impeller diameter D, off bottom clearance C and number of baffles N_f) on the local rate of turbulence energy dissipation per unit mass, ε, close to the impeller. The dissipation was estimated using Eq. (2-41), i.e. $\varepsilon = A\frac{v^3}{L}$ with A=1 and L=D/10, where v is the streamwise component of fluctuating velocity. For the RT, v is the radial RMS velocity in the impeller discharge stream at the tip of impeller blades, while for the PBT, A310 and HE3, v is the axial RMS velocity below the blades.

The effect of tank geometry on the maximum dissipation was investigated using factorial designs of experiments. Factorial designs are ideally suited to initial investigations such as this one, where it is not initially clear which variables will be important. They are based on the premise that not one single variable may be important, but variables may interact to produce magnified, or opposite, effects. Thus, an experimental block based on a factorial design can give a more general picture of the phenomenon of interest with a limited number of experiments. However, because the data are limited, a very careful analysis of the results is required. The variables must be chosen carefully if they are to reflect the underlying physics, and the initial experimental design must often be modified and expanded to check conclusions, and to test hypotheses

obtained from the initial results. For this study, three different 2-level factorial designs were planned, and the results were analyzed using a combination of 95% confidence intervals, normal probability plots, and a detailed examination of the data.

6.2 Experimental

6.2.1 The LDA

The validation of the one dimensional laser Doppler anemometer (LDA) was detailed in **Chapter 4.** The main parameters are summarized here: beam separation=0.01691 m; focal length of both the transmitter and the receiver=500 mm; high voltage=500V; sample size=6000; signal sampling frequency=2.5 MHz; the average frequency of velocity measurement was 1.2 kHz. Comparison of the velocity measurements from two separate detectors, based on this signal sampling rate, gave a data validation rate $\geq$ 99%.

6.2.2 Geometry of the Baffled Tank and the Impellers

The baffled tank is shown in **Figure 2-2.** Vertical baffles (width=T/10) were equally spaced around the periphery of the tank. The liquid depth, H, was equal to the tank diameter (H=T). To prevent vortexing and the entry of air into the system, a lid was installed on top of the baffles, and covered with *5 cm of water to seal the tank.*

All four impellers were used in their standard configurations. The four-bladed PBT had blades inclined at 45° to the horizontal; the blade width of the PBT and RT was D/5; the blade length of the RT was D/4 and the disc diameter of the RT was 2/3D. The A310 was used as supplied by Lightnin' Inc. and the HE3 was used as supplied by Chemineer.

6.2.3 Experimental Designs

All of the experimental runs and experimental results are summarized in **Tables 6-1** to **6-4.** For each impeller, three sets of experiments were run. The first was used to verify the scaling of ε with N^3. The second was a factorial design in N_f, D and C. The

third was a modified factorial design using the dimensionless off bottom clearance C/D. instead of C.

6.2.3.1 Rotational Speed

To test the effect of rotational speed on ε_{max}, five different N's (N1 to N5 in **Tables 6-1** to **6-4**) were used in the same tank geometry for each of the four impellers. One rotational speed (bold and italic in **Tables 6-1** to **6-4**) was chosen to match the power input used in the factorial designs.

6.2.3.2 Factorial Design in N_f, D and C

To examine the effects of the three geometric variables on ε_{max}, factorial designs with three variables at two levels (designated +1 and -1) were applied.

The number of baffles, N_f, and impeller diameter, D, are two of the most important geometric variables in the study of mixing. Two alternatives are used in the literature for the off bottom clearance: C or C/D. For the first factorial design, C was chosen as a geometric variable. Thus the first set of experiments used the three geometric variables N_f, D and C (Runs 1 to 8 in **Tables 6-1** to **6-4**). N_f is either 4 (+1) or 2 (-1); D is either T/2 (+1) or T/4 (-1); and C is either T/2 (+1) or T/4 (-1).

6.2.3.3 Factorial design in N_f, D and C/D

Analysis of the experimental data in the first factorial design indicated that a modified design was needed. This modified design was then carried out with the variables N_f, D and C/D (Runs 3 to 10 in **Tables 6-1** to **6-4**). When C/D was chosen as a geometric variable, C/D was either 1 (+1) or 1/2 (-1).

In summary, there are two sets of experiments for factorial designs: the first is based on N_f, D, and C; and the second on N_f, D and C/D. Each has three variables at two levels. The number of experimental runs for each factorial design is 8, i.e. 2×2×2. In the third factorial design, the second set of data was rescaled from constant power input (N^3D^5=constant), to constant dissipation (N^3D^2=constant) and reanalyzed.

For each of the experimental runs, **Tables 6-1** to **6-4** list the combinations of variables, the values of the Reynolds number, the power input per unit mass $\bar{\varepsilon}(=P/\rho V_T)$, ε_{max}, and ε_{max} made dimensionless with N^3D^2. Scaling of the local dissipation with N^3D^2 is based on the fact that ε is proportional to v^3/D (from reduction of the time averaged equations of turbulence (Kresta and Wood (1991)) and $v \propto ND$, so ε is proportional to N^3D^2.

The power input used for calculating $\bar{\varepsilon}$ was computed using the power number (N_p) for each impeller. For the tank geometries used in this study, the power numbers for the four impellers are: 5.4 for the RT; 1.35 for the PBT; 0.30 for the A310; 0.25 for the HE3 with D/T=1/2 and 0.30 for the HE3 with D/T=1/4. The power numbers for the HE3 were supplied by Chemineer Inc.; the power number for the A310 was supplied by Lightnin'; and the power numbers for the PBT was measured using a Torque Transducer in this lab, and the RT were averaged from data published by previous investigators (**Table 2-1**).

6.3 Results

6.3.1 Determination of the Location of the Maximum Dissipation

According to Eq. (2-41), ε_{max} appears at the same position as the maximum fluctuating velocity. In order to avoid locating the position of ε_{max} arbitrarily, all three fluctuating velocities were measured on traverses in both the impeller regions and the bulk of the tank (see **Figure 6-1**). The radial traverse just below the impeller blades and the radial traverse just above the impeller blades are 2 mm away from the impeller blades. The axial traverse near the tip of impeller blades is 3 mm away from the impeller tip. From these measurements, several conclusions were drawn.

The maximum fluctuating velocity is v_z for the three axial flow impellers (the PBT, A310 and HE3), and it always occurs just below the impeller blades. **Figures 6-2** (a and b) show radial profiles of v_z for the PBT and A310, respectively. The line with z=10.5 mm in **Figure 6-2a** represents the radial traverse 2 mm below the impeller blades (the projected blade width, W_p, is 17.0 mm, half of W_p is 8.5 mm) and the maximum v_z

always appears on this traverse. The same is true for the A310, but note that two clear peaks occur on the traverse where the maximum v_z appears. Experimental results showed that for axial flow impellers the maximum fluctuating velocity is the axial fluctuating velocity for all 15 runs examined, although in the impeller region, the radial and tangential fluctuating velocities are nearly the same as the axial fluctuating velocity (see isotropic check in **Chapter** 5).

For the radial flow impeller (RT), the maximum v_r always appears at the tip of impeller blades, and the maximum fluctuating velocity is v_r (with the exception of run 3 where the maximum v_z is 4.5% larger than the maximum v_r). In this thesis only the effects of geometric variables on the maximum dissipation calculated with the radial fluctuating velocity are considered. **Figure 6-2c** shows the axial profiles of v_r for the RT at the two radii of 63 mm and 87 mm. From **Figure 6-2c**, the maximum v_r appears at r=63 mm, but the profiles of v_r decay slowly in the impeller discharge stream. Thus the maximum turbulence energy dissipation is approximately constant in this region.

As stated above, the work reported in this chapter is primarily an investigation of the effect of geometry on ε_{max}. To be sure that the location of the traverse containing ε_{max} is independent of geometry, the effect of geometry on the location of this traverse was investigated. It was found that the traverse on which ε_{max} is found is independent of clearance, impeller diameter, and number of baffles.

With the locations of the maximum fluctuating velocities and thus ε_{max} determined, streamwise velocity measurements were performed on a single traverse to find ε_{max}. For the PBT, A310 and HE3, the axial fluctuating velocity was measured on a radial traverse 2 mm below the impeller blades; for the RT, the radial fluctuating velocity was measured on an axial traverse 3 mm away from the tip of the RT blades. The velocity was measured at 3 mm intervals. In the figures which follow, the dimensionless variables (2r/D and 2z/W) are used.

6.3.2 Effect of Rotational Speed on ε_{max}

If the flow is fully turbulent, the fluctuating velocities scale exactly with the tip speed of an impeller for a constant tank geometry. Thus, from Eq. (2-41), ε should be proportional to N^3. This is supported by the experimental results of this work. Profiles of the scaled ε for five different values of N are shown in **Figures 6-3** (a to d) for the PBT, A310, HE3 and RT, respectively. The five profiles of the scaled ε overlap in all four figures, as do the five scaled ε_{max}'s. Note that this close agreement appears even though the experimental error in the velocity measurements has been cubed. These results confirm that ε_{max} is proportional to N^3 *when the geometry and scale are constant.* Two peaks are clearly shown for the A310. Experimental results show that this double peak appears consistently for the A310, regardless of the geometry used.

6.3.3 Range of Variation in Scaled ε_{max}

Different impellers create different flow fields. It is important to know how the impeller style and tank geometry affect ε_{max} because of its importance in determining process results. **Figure 6-4** compares the scaled ε_{max}'s for all 60 experiments. The RT runs were arranged in order of increasing values of the scaled ε_{max}. Runs for the PBT, A310 and HE3 were arranged to match the RT geometry. Serial numbers 2-6 on each of the four lines represent the five runs with different rotational speeds and the same geometry.

The values of the scaled ε_{max} for the RT, ranging from 9.75 to 19.9, are much larger than for the three axial flow impellers, none of which exceed 4. The values of the scaled ε_{max} for the A310 and the HE3 follow each other closely over changes in tank geometry. The magnitude of the scaled ε_{max} shows the same trend as the power number: the impellers with larger power numbers generate larger scaled ε_{max}'s. This is to be expected, since N was set for each run based on a constant power input.

6.3.4 Effect of Tank Geometry on ε_{max}

The experimental runs designed to study the effect of tank geometry on ε_{max} were based on three factorial designs for each of the four impellers. These experiments were done in a random order and the results are summarized in **Tables 6-1** to **6-4**. For each set of experiments, there are three main variables (N_f, D, and C or C/D) and four possible interactions between these variables (N_f-D, N_f-C, D-C and N_f-D-C; or N_f-D, N_f-C/D, D-C/D and N_f-D-C/D); therefore there are seven possible geometric effects.

The effects of these geometric variables on ε_{max} are estimated using the method given by Box et al. (1978, pp.306-373). Factorial designs will not be reviewed in detail here, but the method of calculating the effects of variables is explained. By denoting two levels of each variable with +1 representing the higher level and -1 representing the lower level, the effect of a variable on ε_{max} scaled with N^3D^2 (namely, $\varepsilon_{max.scaled}$ in the equation below) can be calculated using the following expression:

$$e_i = \frac{\sum l_i \varepsilon_{max.scaled}}{4} \qquad (6\text{-}1)$$

where $\sum$ means to take the sum of all eight runs, and l_i is the product of the levels for variable or interaction *i*. For example, in run 1 for the first factorial design in **Tables 6-1** to **6-4**, the number of baffles, N_f (variable 1), and the off bottom clearance, C (variable 3), were both at the +1 level; the impeller diameter, D (variable 2), was at the -1 level. Thus the levels of the main effects for N_f, C and D are +1, +1 and -1, respectively; the level of the interaction between N_f-C, l_{13}, is +1. Similarly, l_{12}, l_{23} and l_{123} are all -1. $\varepsilon_{max.scaled}$ is the scaled ε_{max} of the corresponding run. In this way, the three main effects and the four interactions were calculated one by one. The method used to calculate the geometric effects on ε_{max} was similar. The results are summarized in **Tables 6-5, 6-6** and **6-7**.

Note that all experiments in the three factorial designs have a constant power input per unit mass. $\bar{\varepsilon}$ was 0.652 m^2/s^3 for the PBT, A310 and RT, while $\bar{\varepsilon}$ was 0.484 m^2/s^3 for the HE3. The HE3 $\bar{\varepsilon}$ was lower than the $\bar{\varepsilon}$ used for the PBT, A310 and RT due to limitations on the rotational speed set by operational stability and prevention of the

suction of air bubbles. Because the scaling with N^3 was shown to be exact, this difference in experimental conditions did not preclude comparisons between impellers.

6.3.4.1 Criteria Used to Evaluate the Statistical Significance of the Effects

The effect of a variable on ε_{max} can either be a true effect resulting from the variable, or can be caused by chance occurrences. It is necessary to analyze the statistical significance of the geometric effects on ε_{max} to distinguish whether the effects are caused by chance occurrences or are real effects. Three criteria were used to assess the significance of effects: the 95% confidence interval (or estimated experimental error), normal probability plots, and a detailed evaluation of the data.

95% confidence interval, or estimated experimental error

The effects of geometric variables on ε_{max} may be partly attributed to experimental errors in the velocity measurements. Separation of the real effects from the experimental errors is critical to accurate statistical analysis. The experimental errors were quantified by a 95% confidence interval using the data at 5 different rotational speeds and the same geometry (runs N1 to N5). Given that the 5 scaled ε_{max}'s for 5 different rotational speeds with the same geometry should be equal, the differences between them may be attributed to experimental errors. Thus the mean value of the 5 scaled ε_{max}'s and the sample standard deviation can be computed for each of the four impellers. The 95% confidence interval (95% C.I.) for each of the impellers was determined by assuming a *t*-distribution with 4 degrees of freedom. The calculated results are listed in **Table 6-8a**. Effects which fall outside the 95% C.I. cannot be attributed entirely to experimental error. Note that the A310 impeller produces a more stable flow field and its velocity measurement has a correspondingly good reproducibility. This is reflected by an extremely small standard deviation.

Normal probability plots

When the calculated effects given in **Tables 6-5** and **6-6** are plotted on normal probability plots, the effects which are randomly distributed are expected to fall on a straight line. Box et al (1978, pp.306-373) state that if the seven effects (main effects and interactions) occur simply as the result of random variation about a fixed mean, and the changes in levels of the variables have no real effect on the scaled ε_{max}, *then the seven effects are roughly normal and distributed about zero.* Thus, when normal probability plots are used, effects which do not fall on a straight line may be considered significant.

Detailed evaluation of experimental data

Using the 95% C.I. and normal probability plots as guides, the differences between experimental runs were evaluated in detail. This last step is crucial for determining the physical meaning behind the statistical analysis, and for evaluating the validity of the experimental design.

In the final analysis, only effects which meet all three criteria can be considered significant.

6.3.4.2 Discussion of Significant Effects

Three factorial designs are discussed here: the first is based on the variables N_f, D and C with constant power input or $\bar{\varepsilon}$; the second on N_f, D and C/D, again with constant power input; and the third on the N_f, D and C/D design rescaled to a basis of constant ε_{max}. While some significant differences are apparent between the first and second factorial designs, none appear between the second and third when the results are rescaled. The conclusions drawn are based not only on the statistical analysis, but on the overall behavior of the flow field, and on the combined results of the three factorial designs.

First factorial design: N_f, D and C, scaling based on constant $P/\rho V_T$

The 95% confidence intervals and normal probability plots for the first factorial design are shown in **Figures 6-5** (a to d). **Figures 6-6** (a to d) show the full details of all

eight experimental traverses for each of the four impellers. To aid the interpretation of these figures, the runs are grouped into two sets of four based on impeller diameter. Symbols of the same shape are used for the same off bottom clearance, with the filled symbols used for runs with 4 baffles and the open symbols used for runs with 2 baffles. Combining analysis of the two sets of figures, the following observations are made:

1) For the PBT, the 95% confidence interval, normal probability plot, and details of the data all lead to the same conclusion; the impeller diameter is the only variable which has a significant effect on the magnitude of ε_{max}. While the off bottom clearance effect is slightly greater than the 95% confidence interval, it falls close to the regression line, and has a very small effect on the experimental traverses.
2) For the A310 and the HE3, the variability is much smaller, and conclusions drawn from the 95% confidence interval and the normal probability plot are less definitive. They must be combined with the experimental data before conclusions are drawn. The A310 shows a dependence on D and C (ε_{max} decreases with decreasing C for both impeller diameters). The HE3 data shows similar overall trends to the A310, but the significant variables are C and the interaction between C and D. Note that the ε_{max} values for the D=T/4 impeller are much larger for the HE3 (thus the lack of dependence on D), and that ε_{max} decreases with decreasing C only for the D=T/2 impeller (leading to both the dependence on C and on the interaction between C and D).
3) Although the variation in ε_{max} is very large for the RT, no conclusions can be drawn from the results of this factorial design. The 95% confidence interval indicates that *all* variables are significant (with the exception of the interaction 13, between N_f and C) while the normal probability plot indicates that *none* are significant, and the experimental data show no clear trends. This observation led to a reevaluation of the experimental design.
4) An overall examination of the experimental data shows clear shifts in the D=T/2 traverses with changes in C (particularly for the A310 and HE3 impellers), while the D=T/4 traverses are almost identical for all three axial impellers. Kresta and Wood

(1993b) reported that the flow field generated by the PBT depends on the *dimensionless* off-bottom clearance, C/D; not on the absolute value of C. A transition between two flow patterns occurs at C/D=0.6. The C/D values for the D=T/2 impeller (1.0 and 0.5) bracket this value, while the C/D values for the D=T/4 impeller (2.0 and 1.0) are both well above the transition point. A new factorial design was implemented, which uses C/D instead of C, with values of 1.0 and 0.5 for all impellers. This required only 2 additional runs for each impeller (see **Tables 6-1** to **6-4**).

Second factorial design: N_J, D and C/D, scaling based on constant $P/\rho V_T$

The 95% confidence intervals and normal probability plots for the second factorial design are shown in **Figures 6-7** (a to d). Combining these figures with the full experimental traverses shown in **Figures 6-8** (a to d), the following observations are made:

1) Based on an examination of the D=T/4 traverses in **Figure 6-8**, the change in design was justified. Distinct shifts in the position and magnitude of ε_{max} are now evident for the PBT, A310, and RT. For the HE3 impeller, the order and magnitude of ε_{max} values has changed; the decrease in ε_{max} with decreasing C/D is roughly 4 times that observed with the variable C.
2) Returning to the analysis of individual effects, the PBT again shows the impeller diameter as the most significant effect, with the addition of the interaction between D and C/D (due to the additional experimental information). All three evaluation criteria (95% confidence interval, normal probability plot, and experimental traverses) are met.
3) The A310 and HE3 again show the smallest variability. Combining information from all three criteria, the impeller diameter remains the most important variable for the A310. The effect of C/D is large for the D=T/2 impeller, but much smaller for the D=T/4 impeller. This gives rise to the two smaller effects of C/D, and the interaction of D with C/D, both of which fall outside the 95% confidence interval,

but on the regression line. Similarly, the HE3 maintains the off bottom clearance, now in the form of C/D, as the largest effect. The interaction between D and C/D can now be neglected due to the reordering of the D=T/4 data as discussed in (1) above.

4) The RT results now offer some clear conclusions. The diameter is the most important variable, followed by the interaction between D and C/D. Although the effect of C/D alone falls off the regression line and is somewhat larger than the 95% confidence limit, the experimental data show that it interacts strongly with D rather than providing a consistent effect when it is the only variable which is changed.

5) Both the first and second factorial designs indicate a dependence on D beyond the dependence on D^2 predicted by theory. This observed dependence may be due to either real interactions between the impeller and the tank walls, or due to the scaling of N to maintain a constant power input ($\bar{\varepsilon}$), as opposed to scaling to maintain a constant ε.

Third factorial design: N_j, D and C/D, scaling based on constant ε

For the first two factorial designs, all rotational speeds were scaled to maintain the same power input per unit mass. Thus when the impeller diameter D changed from D_1=T/2 to D_2=T/4, the rotational speed N was changed according to the formula:

$$N_2^3 = N_1^3\left(\frac{D_1}{D_2}\right)^5 \qquad (6\text{-}2)$$

When N is scaled based on constant ε, however, the rotational speed N is adjusted according to:

$$N_2^3 = N_1^3\left(\frac{D_1}{D_2}\right)^2 \qquad (6\text{-}3)$$

Since $\varepsilon_{max} \propto N^3$ for a given impeller diameter D, the difference between the two methods of scaling is exactly $(D_1/D_2)^3$. In our case, $(D_1/D_2)^3$ is 8 for the PBT, HE3 and RT, and 3.88 for the A310. Dividing the D=T/4 results by these factors changes the scaling to a basis of constant ε, or more specifically, ε_{max}.

In order to compare the unscaled ε_{max}'s between the four impellers directly, the HE3 results were multiplied by a factor of 1.35 (i.e. 0.652/0.484) to correct for the smaller power input used for this impeller.

The two scaling methods are compared in **Figure 6-9**. The eight cases for each impeller are grouped into two sets of four based on impeller diameter. Runs for the RT were arranged in order of increasing ε_{max}, and runs for the PBT, A310 and HE3 were arranged to match the RT geometry. On the right half of **Figure 6-9**, the four upper lines (solid symbols) represent the four runs scaled based on constant power input; the four lower lines (open symbols) represent the same four runs scaled for constant ε. Scaling for constant ε gives much less variability in the results.

Since scaling with constant ε gives more constant absolute values of ε_{max}, the factorial analysis of the effects of geometry on ε_{max} was repeated for scaling with constant ε. All results were adjusted as for **Figure 6-9**, and the effects recalculated.

The experimental errors were again quantified by a 95% confidence interval using the data at 5 different rotational speeds and the same geometry (runs N1 to N5). Because the absolute values of ε_{max} are used here, the ε_{max} values with 5 different rotational speeds cannot be used directly to calculate the 95% confidence interval. For the third factorial design, the ε_{max}'s at 5 different rotational speeds were first scaled with the appropriate value of N^3D^2, then multiplied by $N_i^3 D_i^2$ to adjust the 5 ε_{max}'s to the case of D_i=T/2 for the PBT, HE3 and RT or D_i=0.550T for the A310. The calculated 95% confidence intervals for the four impellers are listed in **Table 6-8b**.

The resulting normal probability plots are shown in **Figures 6-10** (a to d). From these figures, the following observations are made:

1) Comparison of **Figures 6-10** (a to d) with **Figures 6-7** (a to d) shows no change in the results for the PBT, A310 and RT. For these three impellers, D is the dominant effect. Thus the statistical analysis of the geometric effects on the scaled ε_{max} for the PBT, A310 and RT based on constant power input is also true if the scaling of N is based on holding ε constant. The effect of D is due to interactions between the impeller and the tank walls; not due to the choice of scaling.

2) For the HE3, C/D dominated the variation in scaled ε_{max} for the first two factorial designs. The normal probability plot for the HE3 shows a larger effect of D and of the interaction between D and C/D with the rescaled data. This makes the observations for the HE3 more consistent with the observations for the other three impellers. Note that the HE3 was the only impeller for which the off bottom clearance was the dominant effect in the first two factorial designs.

Summary

Three forms of factorial design have been used to evaluate the effect of tank geometry on the maximum dissipation, ε_{max}. The first design used the variables N_f, D and C, but gave unclear results for the RT. Since previous investigations showed that the flow field depends on the ratio C/D for the PBT, the experimental design was modified to use the variables N_f, D and C/D. This second factorial design provided better results for all four impellers. Finally, in the third factorial design, the results were rescaled to a basis of constant ε_{max} (instead of constant power input) to verify the conclusions. Three criteria were used throughout to evaluate the significance of each geometric variable: the 95% confidence interval, a normal probability plot, and detailed examination of the experimental profiles. Taking the results of all three factorial designs together, several important conclusions can be drawn about the effect of tank geometry on ε_{max}:

1) The effect of impeller diameter on ε_{max} is larger than the scaling with D^2 predicted by theory. This can only be due to interactions between the impeller and the tank walls; put another way, significant changes in the turbulent flow field occur when the D/T ratio is changed.
2) The off bottom clearance is also an important variable, which is best quantified by its *dimensionless* form, C/D. It may appear as an independent variable, or in the form of interactions with the impeller diameter, depending on the impeller used. This means that *the off bottom clearance and impeller diameter cannot be independently considered.*

3) The number of baffles, N_f, has no significant effect on ε_{max}, either as an independent variable, or in the form of interactions with other geometric variables. This is true for all four impellers, and all three factorial designs.

4) To maintain a roughly constant ε_{max}, scale up which is not geometrically exact should be based on D^2, not on D^5. This is the scaling predicted from theory, rather than the constant $P/\rho V_T$ (equivalently constant power per unit mass, or average dissipation) which is commonly used in the literature.

6.4 Conclusions

This work represents the first extensive analysis of the effect of tank geometry on the maximum rate of dissipation of turbulence kinetic energy, ε_{max}. Three axial impellers (the PBT, A310 and HE3) and one radial impeller (the RT) were studied. These impellers represent the full spectrum of impellers currently used for turbulent mixing in industry. Three geometric variables were considered: the number of baffles, the impeller diameter, and the impeller off bottom clearance.

The local dissipation was estimated from the streamwise RMS velocity fluctuations using $\varepsilon=Av^3/L$ where A=1.0 and L=D/10 for all four impellers. The dissipation was shown to scale exactly with N^3 for the case where the tank geometry is held constant. The maximum dissipation was located on the traverse immediately below the impeller for the three axial impellers, and on the traverse at the tip of the impeller blades for the RT.

Comparison of the scaled ε_{max} values for all geometries considered shows significant variation between the results both when constant power input per unit mass ($P/\rho V_T$) is used as the scaling criterion, and when ε_{max} is scaled with N^3D^2. The dominant variable was shown to be the impeller diameter. This effect is in addition to the expected scaling with D^2. Substantial dependence on the off bottom clearance was also demonstrated. This dependence can be most accurately observed when the dimensionless clearance, C/D, is used as the experimental variable. The off bottom clearance often interacts strongly with the impeller diameter, and thus should not be considered as an

independent variable. The number of baffles had no significant effect on the ε_{max}, either as an independent variable, or in interactions with other geometric variables. The same effects of geometric variables were observed when the results were rescaled based on maintaining a constant dissipation.

The results of this work show that the maximum local dissipation is larger for impellers with a larger power number. In addition to the dependence on power number, there is a substantial effect of tank geometry on the value of ε_{max}. In future, experimental work which depends on ε_{max} should be designed to examine the effects of D/T, C/D, and interactions between the two variables on the results. Scale up of stirred tanks should consider ε_{max} as well as $P/\rho V_T$, particularly in cases where the type of impeller and/or the tank geometry are to be changed. The results contained in this work provide some guidance as to when these effects will be most important, and what values of ε_{max} can be expected for some standard impellers and tank configurations.

Tables in Chapter 6

Table 6-1 Experimental Design and Results-PBT

Run	N_f + 4 - 2	D + T/2 0 T/3 - T/4	C + T/2 0 T/3 - T/4	C/D + 1 - 1/2	N (rpm)	Re $*10^{-4}$	$\bar{\varepsilon}$ (m^2/s^3)	ε_{max} (m^2/s^3)	$\frac{\varepsilon_{max}}{N^3D^2}$
1	+	-	+		1133	6.69	0.652	51.5	2.13
2	-	-	+		1133	6.69	0.652	56.2	2.32
3	+	-	-	+	1133	6.69	0.652	43.2	1.78
4	-	-	-	+	1133	6.69	0.652	48.2	1.99
5	+	+	+	+	357	8.43	0.652	12.0	3.94
6	-	+	+	+	357	8.43	0.652	10.5	3.47
7	+	+	-	-	357	8.43	0.652	10.1	3.32
8	-	+	-	-	357	8.43	0.652	9.46	3.12
9	+	-		-	1133	6.69	0.652	77.6	3.20
10	-	-		-	1133	6.69	0.652	69.1	2.85
Varying rotational speed									
N-1	+	0	0		357	3.75	0.086	3.34	2.47
N-2	+	0	0		480	5.04	0.209	7.71	2.36
N-3	+	0	0		580	6.09	0.368	15.1	2.62
N-4	+	***0***	***0***		***701***	***7.36***	***0.652***	***23.8***	***2.33***
N-5	+	0	0		800	8.40	0.966	37.1	2.44

Table 6-2 Experimental Design and Results-A310.

Run	N_f + 4 - 2	D + 0.550T 0 0.475T - 0.350T	C + T/2 0 T/3 - T4	C/D + 1 - 1/2	N (rpm)	Re $*10^{-4}$	$\bar{\varepsilon}$ (m^2/s^3)	ε_{max} (m^2/s^3)	$\frac{\varepsilon_{max}}{N^3D^2}$
1	+	-	+		1068	12.4	0.652	30.2	0.758
2	-	-	+		1068	12.4	0.652	28.1	0.706
3	+	-	-	+	1068	12.4	0.652	25.9	0.652
4	-	-	-	+	1068	12.4	0.652	20.9	0.526
5	+	+	+	+	503	14.4	0.652	12.5	1.22
6	-	+	+	+	503	14.4	0.652	11.6	1.13
7	+	+	-	-	503	14.4	0.652	8.43	0.821
8	-	+	-	-	503	14.4	0.652	8.16	0.795
9	+	-		-	1068	12.4	0.652	26.1	0.655
10	-	-		-	1068	12.4	0.652	18.6	0.467
Varying rotational speed									
N-1	+	0	0		430	9.17	0.196	4.69	0.979
N-2	+	0	0		503	10.7	0.313	7.36	0.961
N-3	+	0	0		570	12.2	0.456	10.9	0.976
N-4	+	***0***	***0***		***642***	***13.7***	***0.652***	***15.2***	***0.952***
N-5	+	0	0		720	15.3	0.919	21.7	0.967

Table 6-3 Experimental Design and Results-HE3.

Run	N_f + 4 - 2	D + T/2 0 T/3 - T/4	C + T/2 0 T/3 - T/4	C/D + 1 - 1/2	N (rpm)	Re $*10^{-4}$	$\bar{\varepsilon}$ (m^2/s^3)	ε_{max} (m^2/s^3)	$\frac{\varepsilon_{max}}{N^3D^2}$
1	+	-	+		1694	10.0	0.484	70.6	0.871
2	-	-	+		1694	10.0	0.484	86.8	1.07
3	+	-	-	+	1694	10.0	0.484	65.6	0.810
4	-	-	-	+	1694	10.0	0.484	80.7	0.996
5	+	+	+	+	567	13.4	0.484	13.1	1.08
6	-	+	+	+	567	13.4	0.484	15.1	1.24
7	+	+	-	-	567	13.4	0.484	6.73	0.554
8	-	+	-	-	567	13.4	0.484	7.53	0.620
9	+	-		-	1694	10.0	0.484	59.2	0.731
10	-	-		-	1694	10.0	0.484	53.8	0.664
Varying rotational speed									
N-1	+	0	0		861	9.04	0.259	24.4	1.29
N-2	+	0	0		961	10.1	0.360	35.2	1.34
N-3	**+**	***0***	***0***		***1061***	***11.1***	***0.484***	***48.1***	***1.36***
N-4	+	0	0		1161	12.2	0.634	58.7	1.27
N-5	+	0	0		1261	13.2	0.812	74.3	1.25

Table 6-4 Experimental Design and Results-RT.

Run	N_f + 4 - 2	D + T/2 0 T/3 - T/4	C + T/2 0 T/3 - T/4	C/D + 1 - 1/2	N (rpm)	Re $*10^{-4}$	$\bar{\varepsilon}$ (m^2/s^3)	ε_{max} (m^2/s^3)	$\frac{\varepsilon_{max}}{N^3D^2}$
1	+	-	+		714	4.22	0.652	59.1	9.75
2	-	-	+		714	4.22	0.652	81.7	13.5
3	+	-	-	+	714	4.22	0.652	89.8	14.8
4	-	-	-	+	714	4.22	0.652	84.3	13.9
5	+	+	+	+	225	5.31	0.652	13.5	17.1
6	-	+	+	+	225	5.31	0.652	9.42	12.4
7	+	+	-	-	225	5.31	0.652	15.1	19.9
8	-	+	-	-	225	5.31	0.652	13.8	18.1
9	+	-		-	714	4.22	0.652	74.6	12.3
10	-	-		-	714	4.22	0.652	74.6	12.3
Varying rotational speed									
N-1	+	0	0		225	2.36	0.086	4.10	12.1
N-2	+	0	0		300	3.15	0.204	9.73	12.2
N-3	+	0	0		370	3.88	0.382	17.8	11.8
N-4	+	***0***	***0***		***442***	***4.64***	***0.652***	***31.4***	***12.3***
N-5	+	0	0		510	5.35	1.00	48.4	12.3

Table 6-5 Calculated effects of geometric variables and interactions on ε_{max}/N^3D^2 for the factorial design based on N_f, D and C. Scaling of N for constant power input.

Variable or Interaction	Effect on the scaled ε_{max}			
impeller	PBT	A310	HE3	RT
N_p	1.35	0.30	0.25~0.30	5.4
power input per unit mass	0.652	0.652	0.484	0.652
average of $\varepsilon_{max} / N^3D^2$	2.78	0.826	0.906	14.9
main effects				
number of baffles, N_f	0.0670	0.0735	-0.154	0.963
impeller diameter, D	1.41	0.331	-0.0623	3.84
clearance, C	0.413	0.255	0.321	-3.54
two-factor interactions				
N_f×D	0.268	-0.0155	0.0383	2.39
N_f×C	0.0725	-0.00250	-0.0283	-0.388
D×C	0.0725	0.112	0.254	-0.813
three-factor interaction				
N_f×D×C	0.0625	0.0345	-0.0218	**1.94**

Table 6-6 Calculated effects of geometric variables and interactions on ε_{max}/N^3D^2 for the factorial design based on N_f, D and C/D. Scaling of N for constant power input.

Variable or Interaction	Effect on the scaled ε_{max}			
impeller	PBT	A310	HE3	RT
N_p	1.35	0.30	0.25~0.30	5.4
power input per unit mass	0.652	0.652	0.484	0.652
average of $\varepsilon_{max} / N^3D^2$	2.96	0.783	0.837	15.1
main effects				
number of baffles, N_f	0.202	0.108	-0.088	1.87
impeller diameter, D	1.01	0.417	0.074	3.58
ratio of clearance to diameter, C/D	-0.328	0.198	0.390	-1.08
two-factor interactions				
N_f×D	0.133	-0.050	-0.028	1.38
N_f ×C/D	-0.072	0.001	-0.087	0.925
D×C/D	0.813	0.170	0.185	-3.18
three-factor interaction				
N_f ×D×C/D	0.208	0.032	0.038	0.525

Table 6-7 Calculated effects of geometric variables and interactions on ε_{max} for the factorial design based on N_f, D and C/D. ε_{max}'s for the 16 cases with small D were divided by $(D_1/D_2)^3$ to give scaling for constant ε_{max}.

Variable or Interaction	Effect on ε_{max}			
impeller	PBT	A310	HE3	RT
N_p	1.35	0.30	0.25~0.30	5.4
power input per unit mass	0.652	0.652	0.652	0.652
average of ε_{max}	8.97	8.04	12.6	11.4
main effects				
number of baffles, N_f	0.614	1.10	-1.36	1.42
impeller diameter, D	3.06	4.28	3.40	2.73
ratio of clearance to diameter, C/D	-0.992	2.03	6.11	-0.817
two-factor interactions				
$N_f \times D$	0.402	-0.507	-0.544	1.04
$N_f \times C/D$	-0.219	0.005	-1.27	0.702
$D \times C/D$	2.463	1.74	3.31	-2.41
three-factor interaction				
$N_f \times D \times C/D$	0.629	0.323	0.454	0.399

Table 6-8a 95% confidence intervals calculated from ε_{max}/N^3D^2 values for the 5 runs with varying N.

impeller	mean	standard deviation	95% C.I.
PBT	2.44	0.114	0.316
A310	0.967	0.011	0.031
HE3	1.30	0.047	0.133
RT	12.1	0.207	0.575

Table 6-8b 95% confidence intervals calculated from ε_{max} values for the 5 runs with varying N.

impeller	mean	standard deviation	95% C.I.
PBT	7.41	0.345	0.957
A310	9.93	0.113	0.314
HE3	15.8	0.577	1.60
RT	9.22	0.157	0.437

Figures in Chapter 6

Figure 6-1 Schematic drawing of the stirred tank and the measuring traverses (- - - - -) used to locate ε_{max} for each of the four impellers.

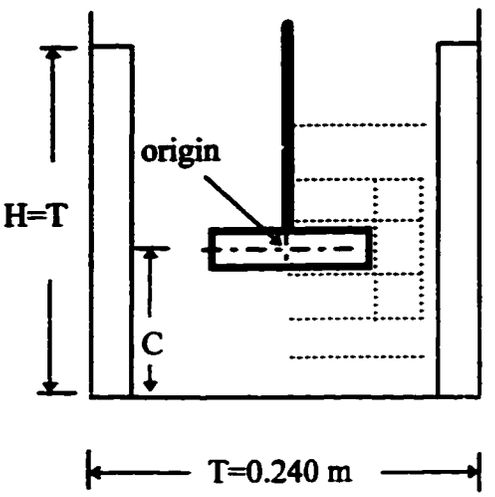

Figure 6-2 (a to c) Velocity profiles used to locate ε_{max}:

2a) **PBT**; radial profiles of v_z; N_f=4, D/T=1/2, C/T=1/3, N=400 rpm.

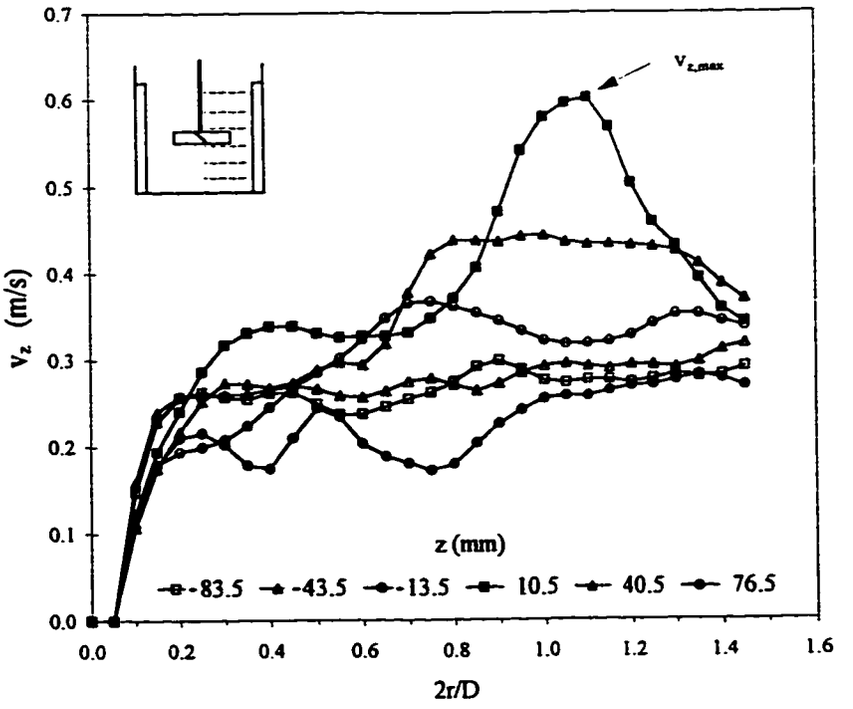

2b) **A310**; radial profiles of v_z; N_f=4, D/T=0.550, C/T=1/3, N=652 rpm.

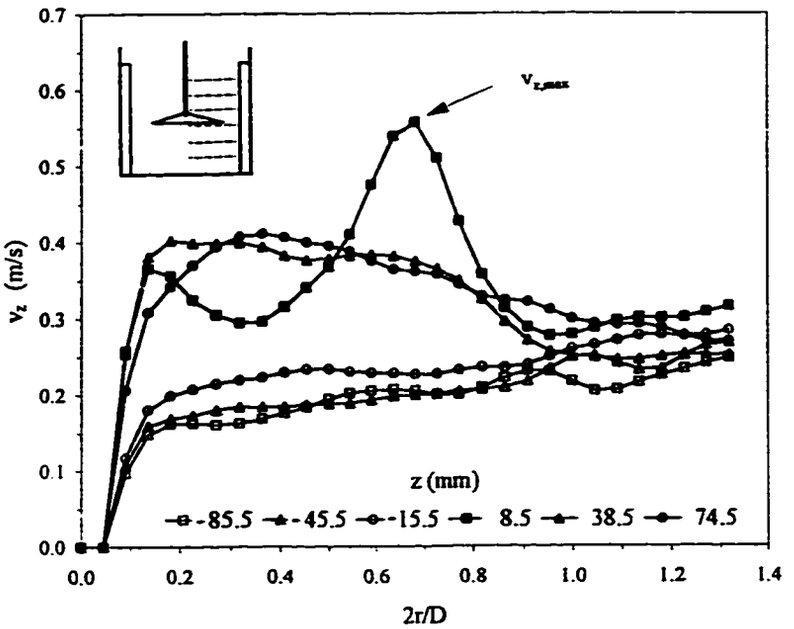

2c) **RT**; axial profiles of v_r; N_f=4, D/T=1/2, C/T=1/3, N=221 rpm.

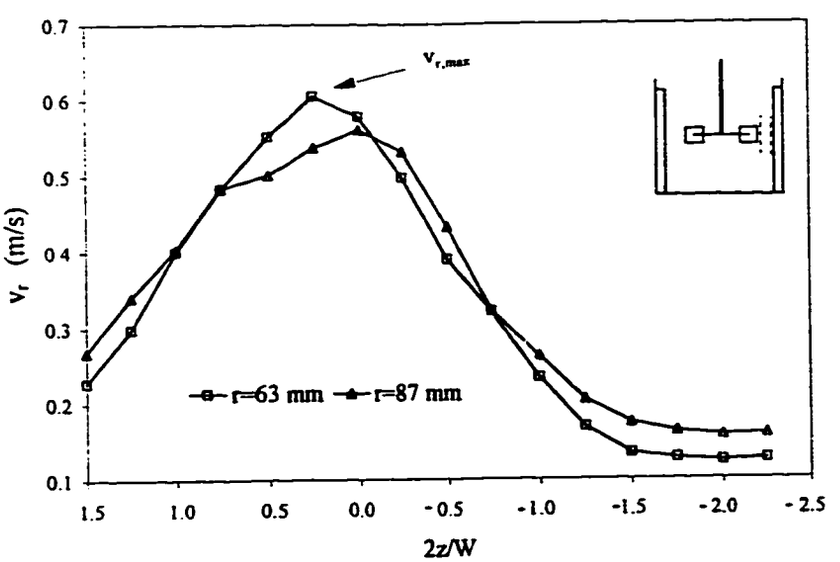

Figure 6-3 (a to d) Validation of the scaling of ε with N^3; N_f=4, C=T/3.

3a) **PBT**; D/T=1/3, $2z/W_p$=1.35.

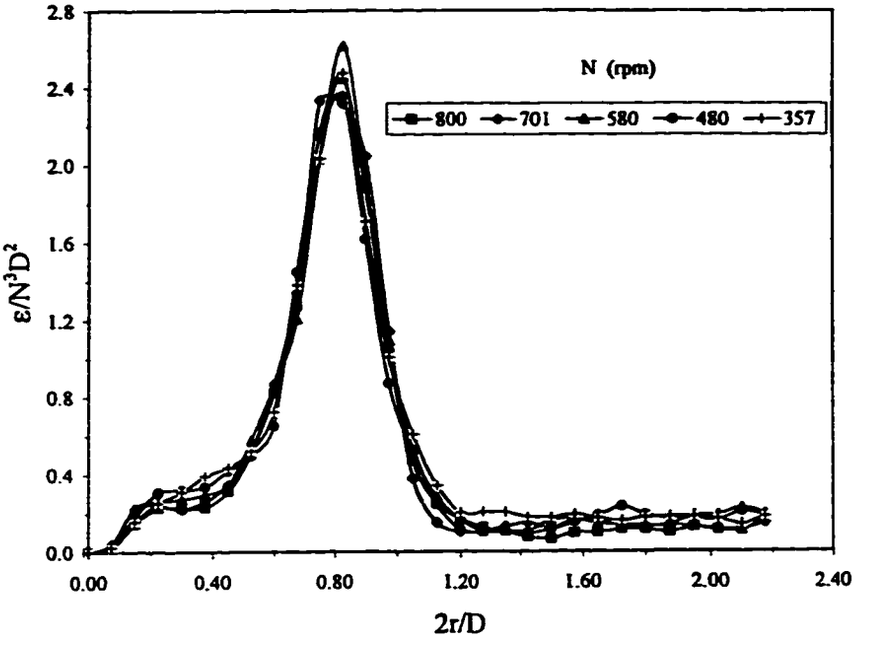

3b) **A310**; D/T=0.475, $2z/W_p$=1.30.

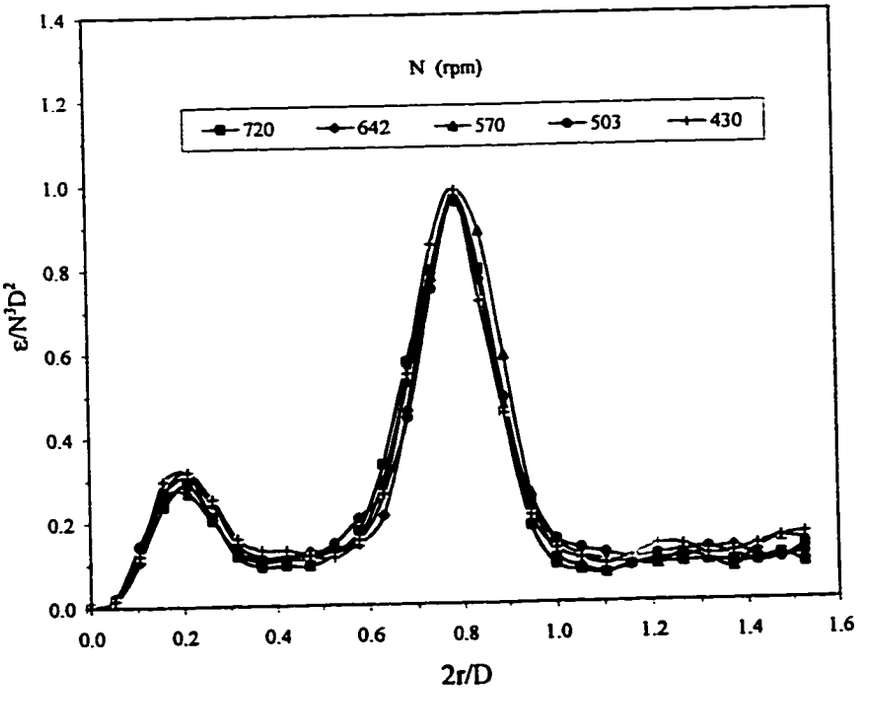

3c) **HE3**; D/T=1/3, $2z/W_p$=1.46.

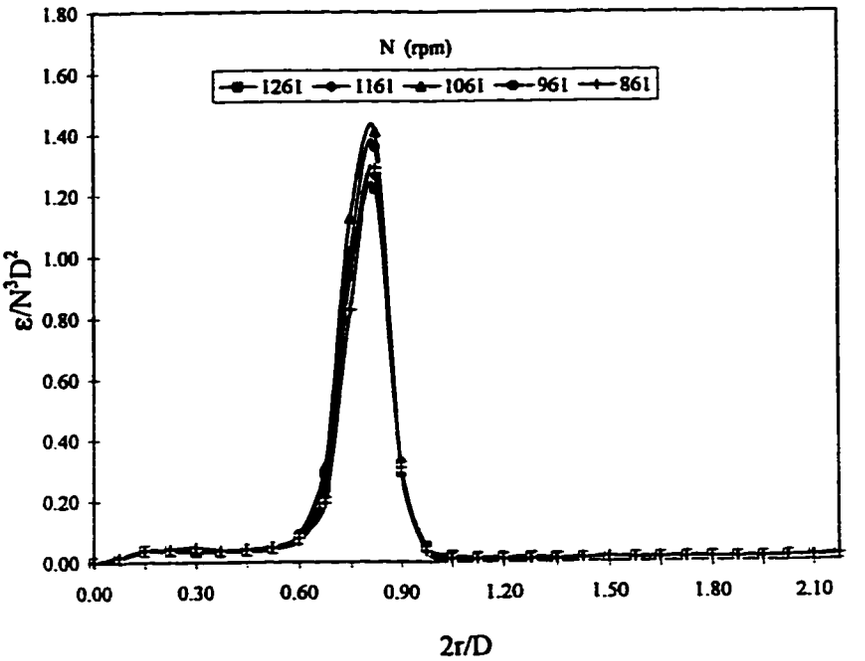

3d) **RT**; D/T=1/3, 2r/D=1.08.

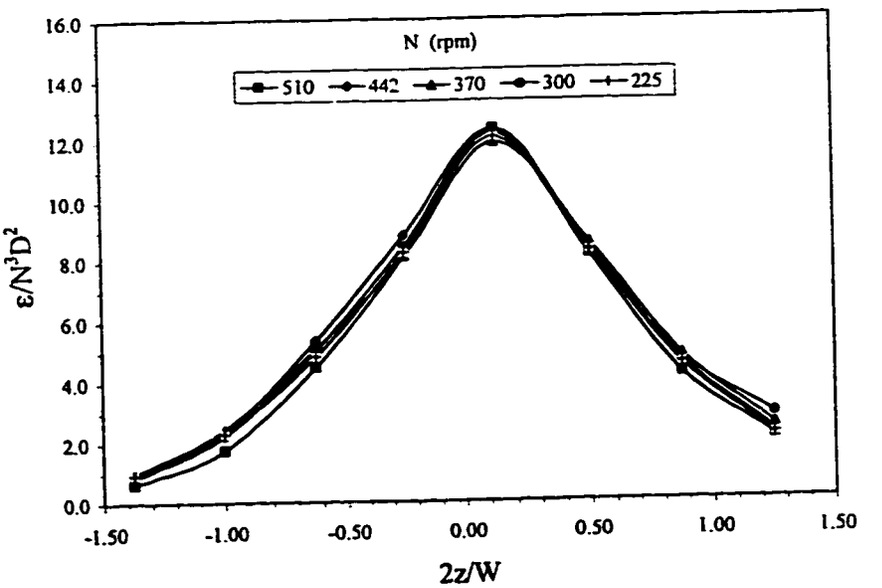

Figure 6-4 Comparison of the scaled ε_{max}'s for all experiments. The RT data was arranged in order of increasing ε_{max}/N^3D^2. Runs for the PBT, A310 and HE3 were arranged to match the RT geometry with the same serial number.

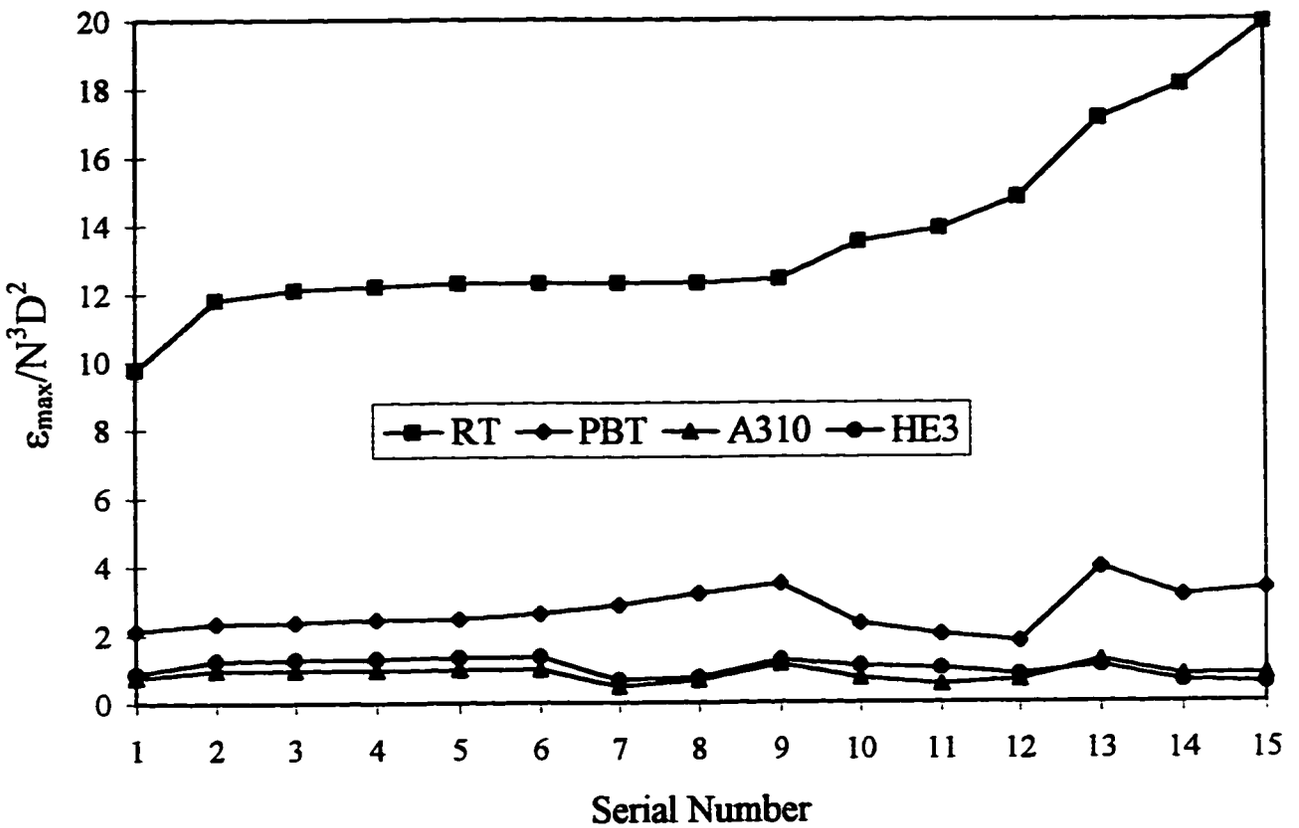

Figure 6-5 (a to d) Normal probability plots of the effects of geometric variables on ε_{max}/N^3D^2 showing the 95% confidence interval around zero effect for the factorial design based on N_f, D and C.

5a) **PBT**

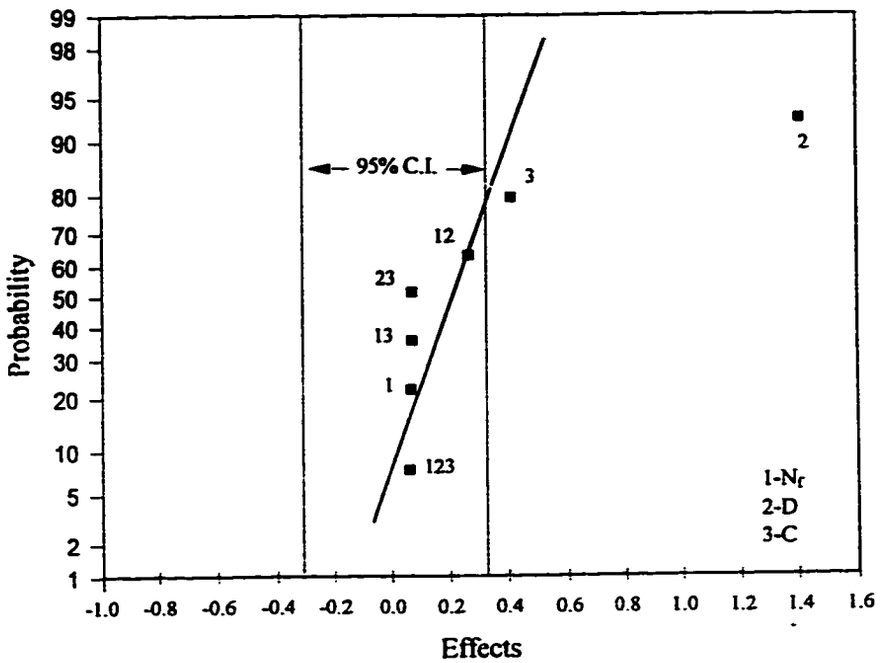

5b) **A310**

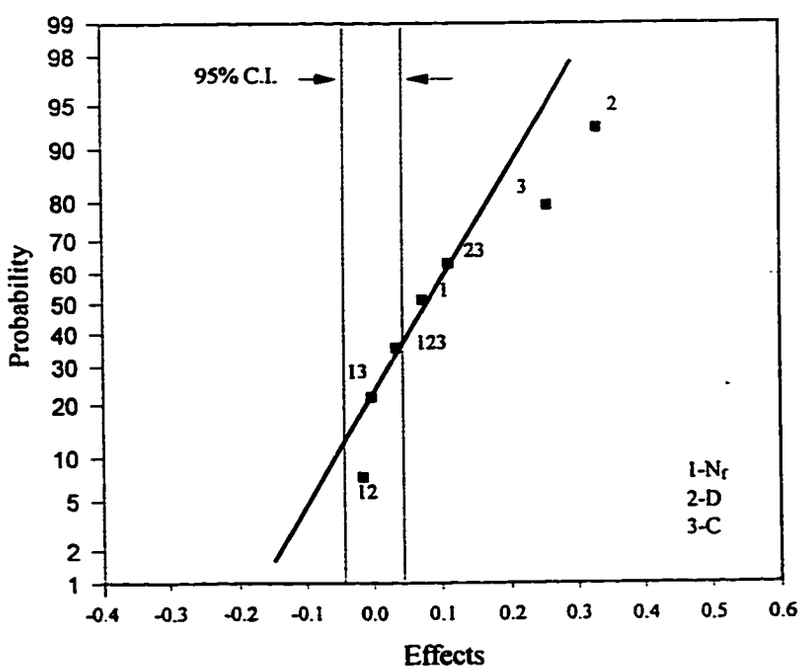

5c) **HE3**

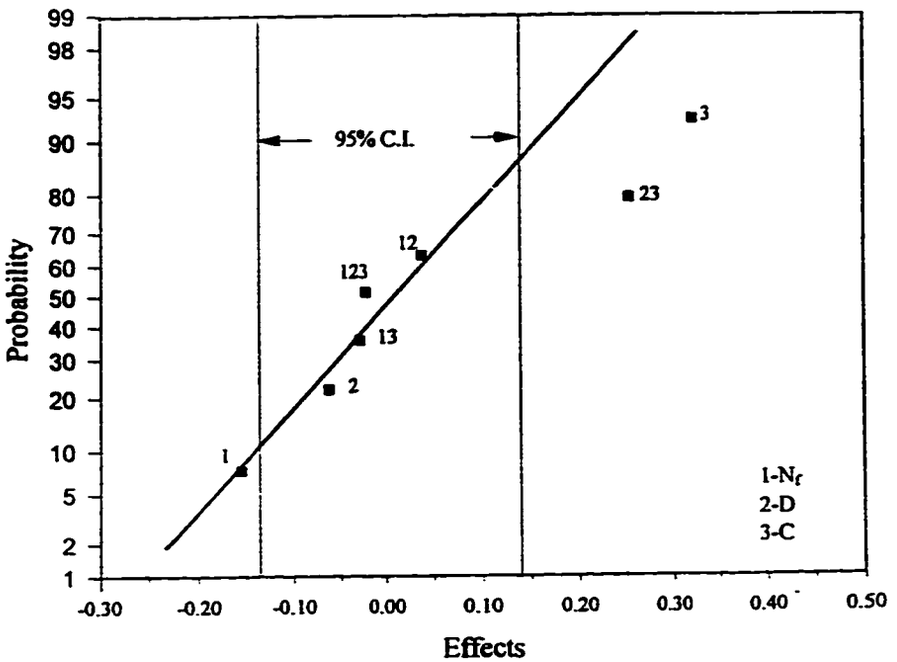
Probability
99
98
95
90
80
70
60
50
40
30
20
10
5
2
1
95% C.I.
3
23
12
123
13
2
1
1-Nf
2-D
3-C
-0.30
-0.20
-0.10
0.00
0.10
0.20
0.30
0.40
0.50
Effects

5d) **RT**

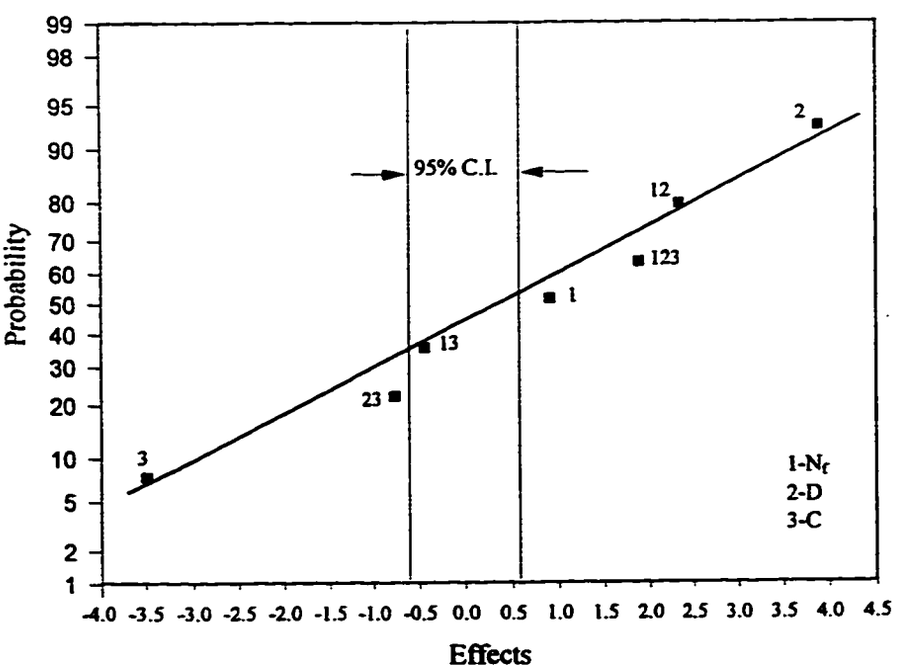
Probability
99
98
95
90
80
70
60
50
40
30
20
10
5
2
1
95% C.I.
2
12
123
1
13
23
3
1-Nf
2-D
3-C
-4.0
-3.5
-3.0
-2.5
-2.0
-1.5
-1.0
-0.5
0.0
0.5
1.0
1.5
2.0
2.5
3.0
3.5
4.0
4.5
Effects

Figure 6-6 (a to d) Profiles of ε/N^3D^2 showing the details of the experimental results for the factorial design based on N_f, D and C.

6a) **PBT**

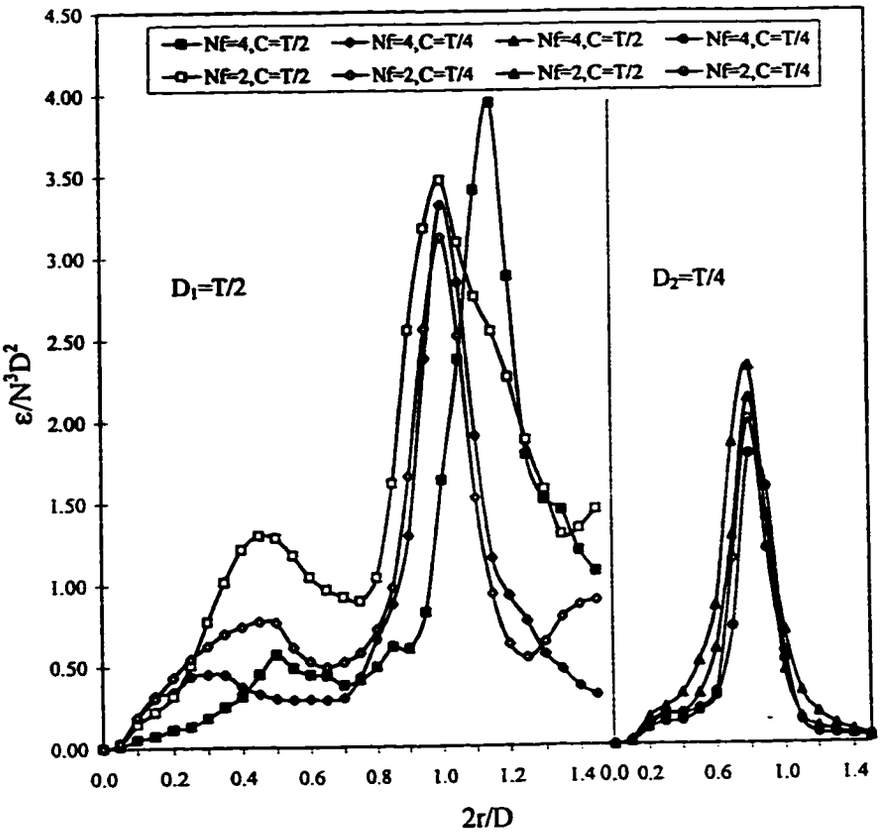

6b) **A310**

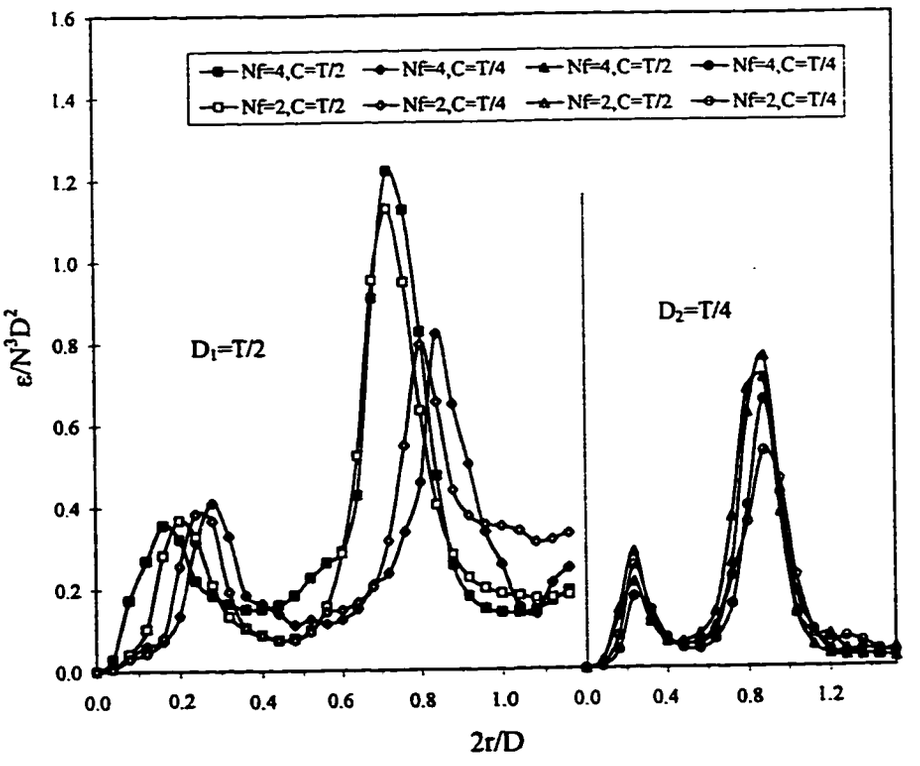

6c) **HE3**

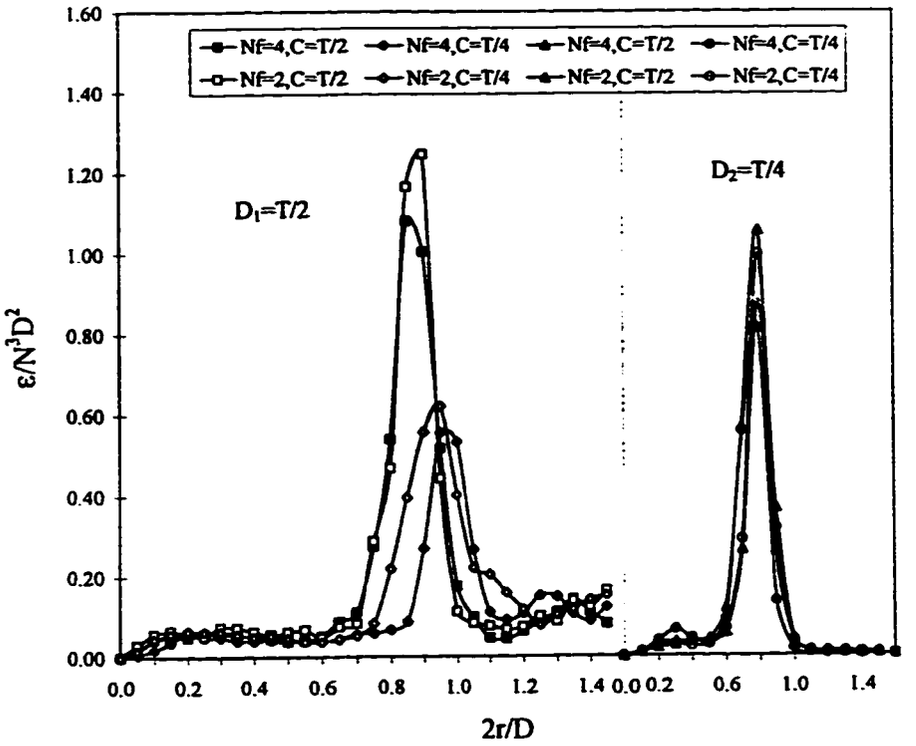
Nf=4,C=T/2
Nf=4,C=T/4
Nf=4,C=T/2
Nf=4,C=T/4
Nf=2,C=T/2
Nf=2,C=T/4
Nf=2,C=T/2
Nf=2,C=T/4
D1=T/2
D2=T/4
ε/N3D2
2r/D

6d) **RT**

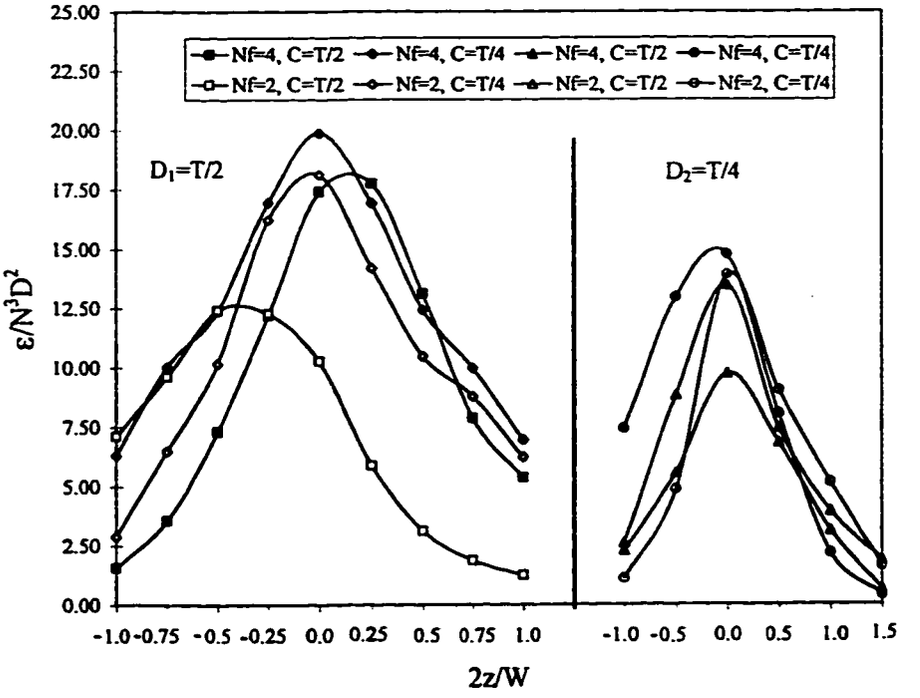
Nf=4, C=T/2
Nf=4, C=T/4
Nf=4, C=T/2
Nf=4, C=T/4
Nf=2, C=T/2
Nf=2, C=T/4
Nf=2, C=T/2
Nf=2, C=T/4
D1=T/2
D2=T/4
ε/N3D2
2z/W

Figure 6-7 (a to d) Normal probability plots of the effects of geometric variables on ε_{max}/N^3D^2 showing the 95% confidence interval around zero effect for the factorial design based on N_f, D and C/D.

7a) **PBT**

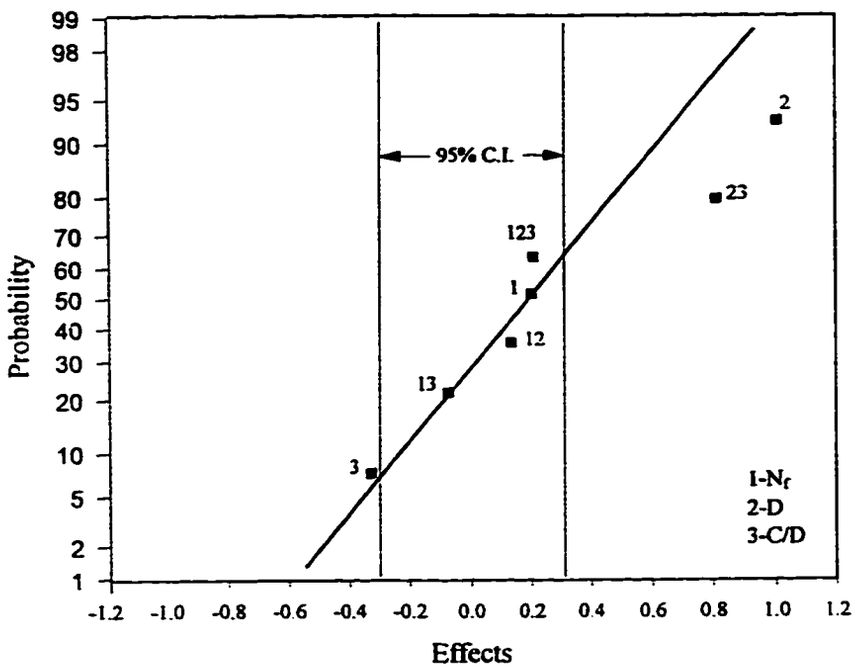

7b) **A310**

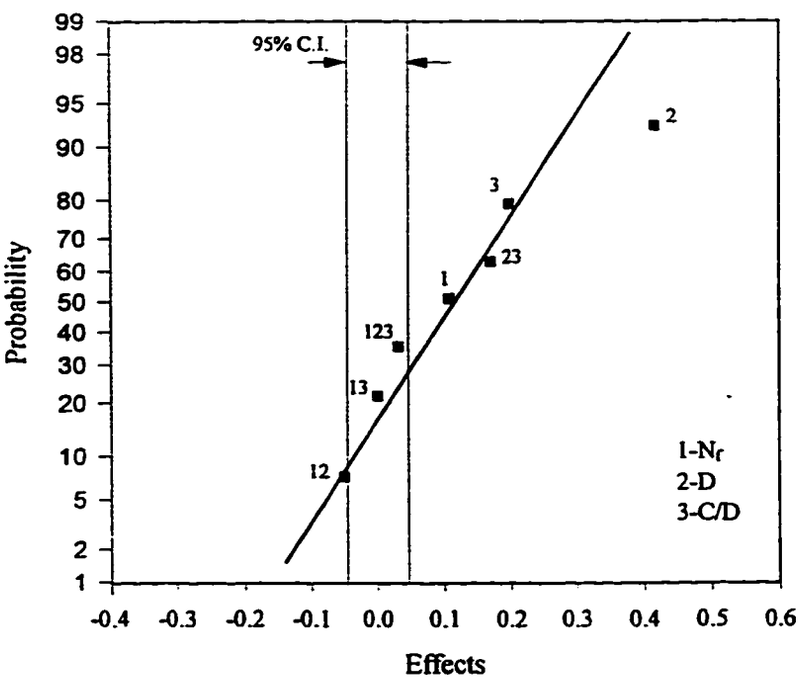

7c) **HE3**

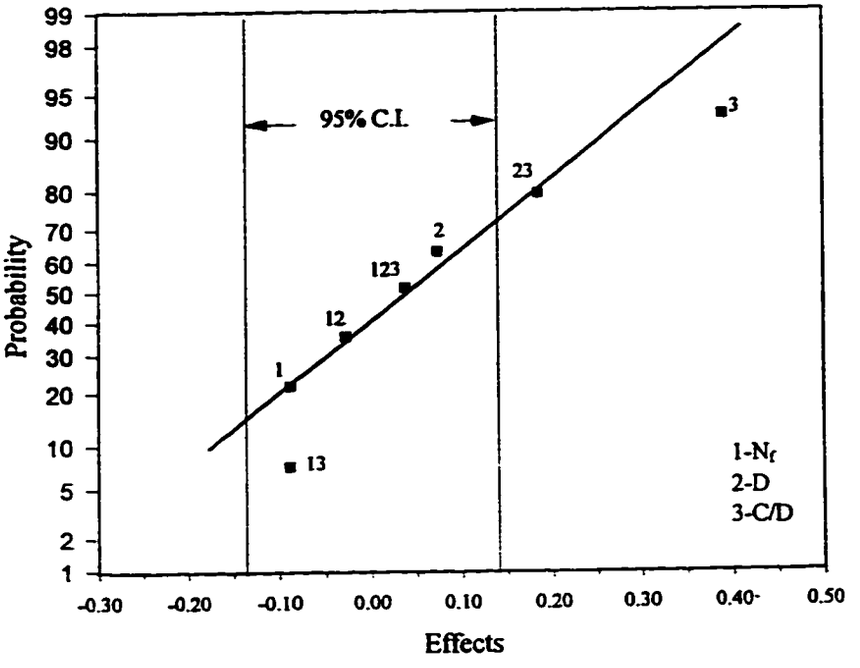
99
98
95
90
80
70
60
50
40
30
20
10
5
2
1
Probability
95% C.I.
3
23
2
123
12
1
13
1-N_f
2-D
3-C/D
-0.30
-0.20
-0.10
0.00
0.10
0.20
0.30
0.40
0.50
Effects

7d) **RT**

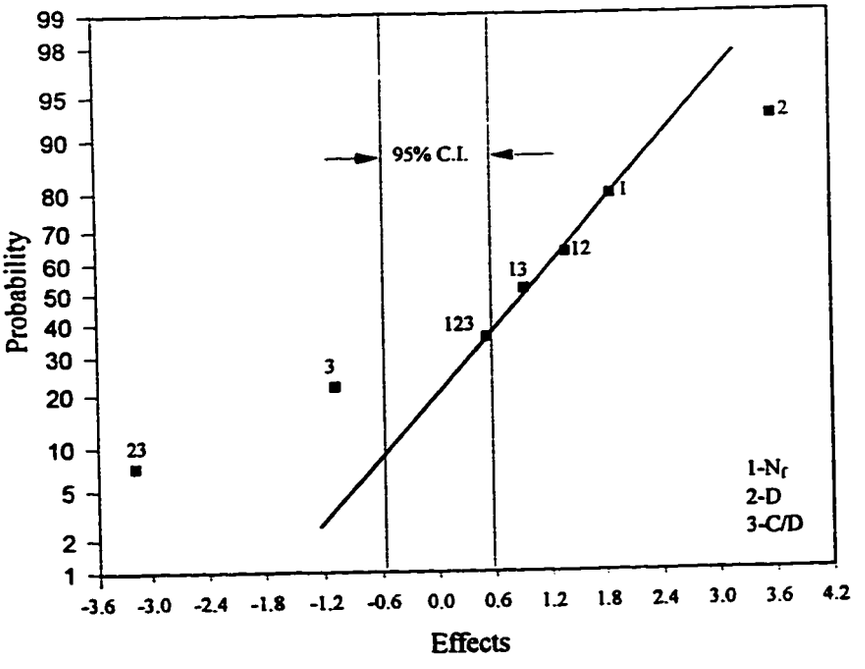
99
98
95
90
80
70
60
50
40
30
20
10
5
2
1
Probability
95% C.I.
2
1
12
13
123
3
23
1-N_f
2-D
3-C/D
-3.6
-3.0
-2.4
-1.8
-1.2
-0.6
0.0
0.6
1.2
1.8
2.4
3.0
3.6
4.2
Effects

Figure 6-8 (a to d) Profiles of ε/N^3D^2 showing the details of the experimental results for the factorial design based on N_f, D and C/D.

8a) **PBT**

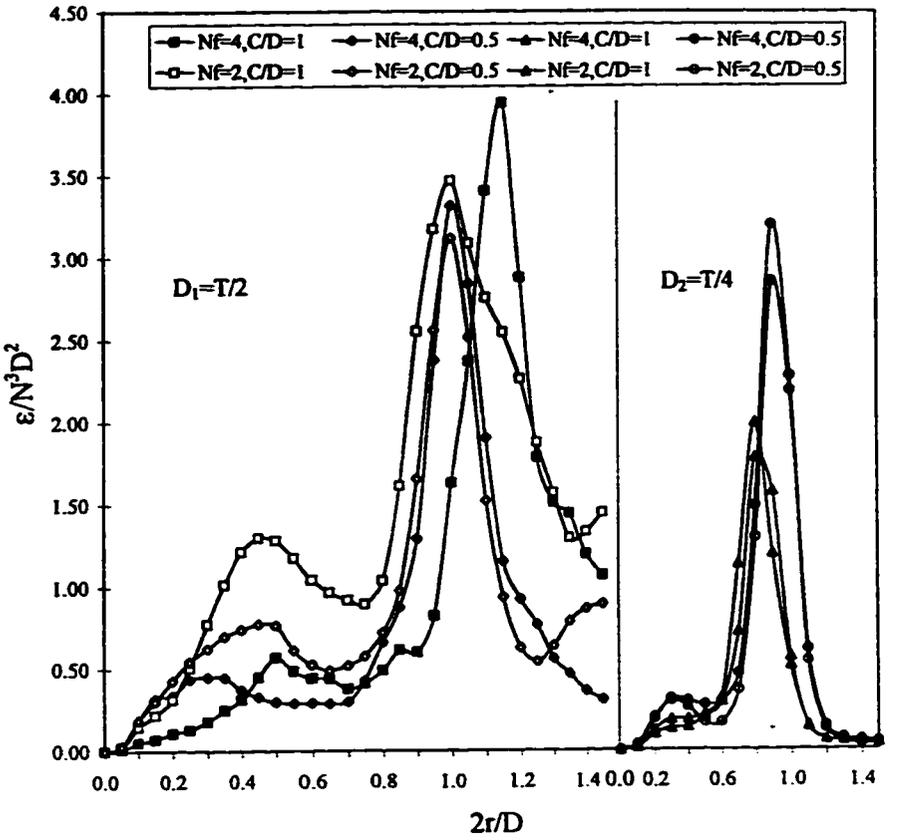

8b) **A310**

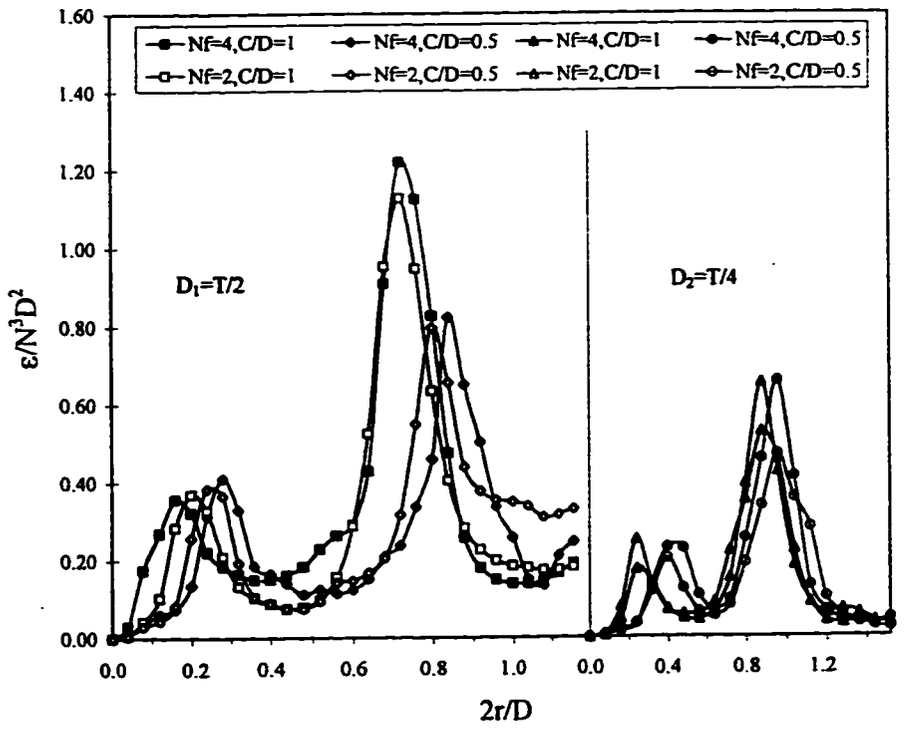

8c) **HE3**

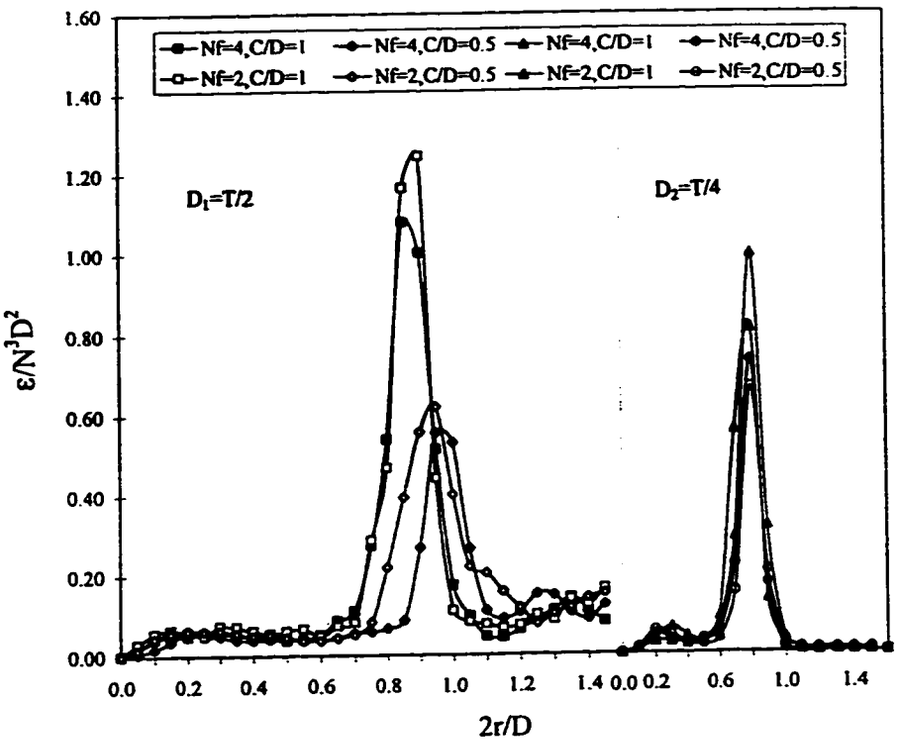
Nf=4,C/D=1
Nf=4,C/D=0.5
Nf=4,C/D=1
Nf=4,C/D=0.5
Nf=2,C/D=1
Nf=2,C/D=0.5
Nf=2,C/D=1
Nf=2,C/D=0.5
D1=T/2
D2=T/4
ε/N³D²
2r/D

8d) **RT**

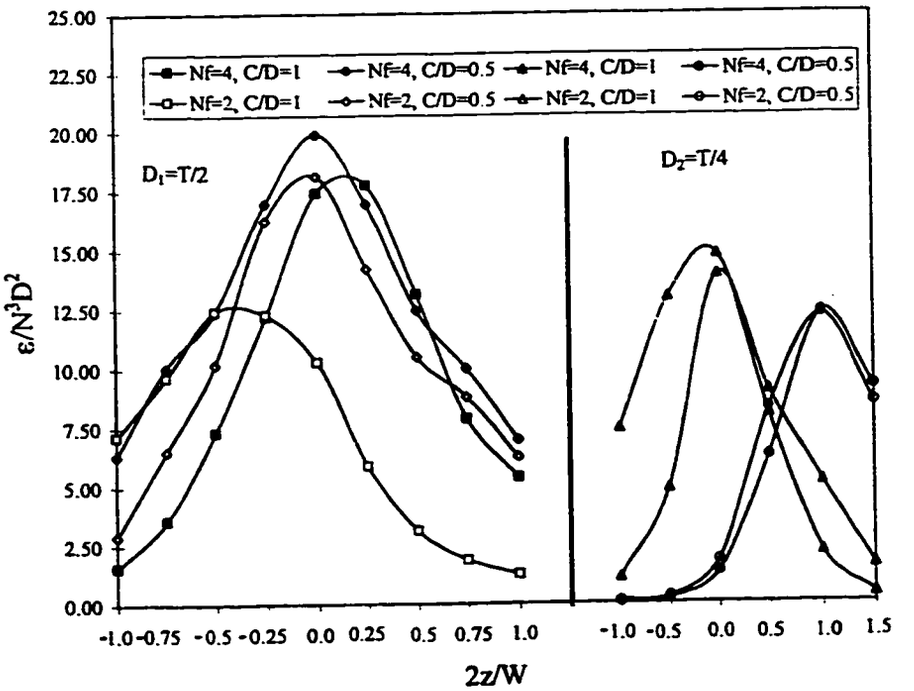
Nf=4, C/D=1
Nf=4, C/D=0.5
Nf=4, C/D=1
Nf=4, C/D=0.5
Nf=2, C/D=1
Nf=2, C/D=0.5
Nf=2, C/D=1
Nf=2, C/D=0.5
D1=T/2
D2=T/4
ε/N³D²
2z/W

Figure 6-9 Comparison of scaling based on constant power (closed symbols) vs. scaling based on constant ε_{max} (open symbols) when the impeller diameter is changed from D=T/2 to D=T/4.

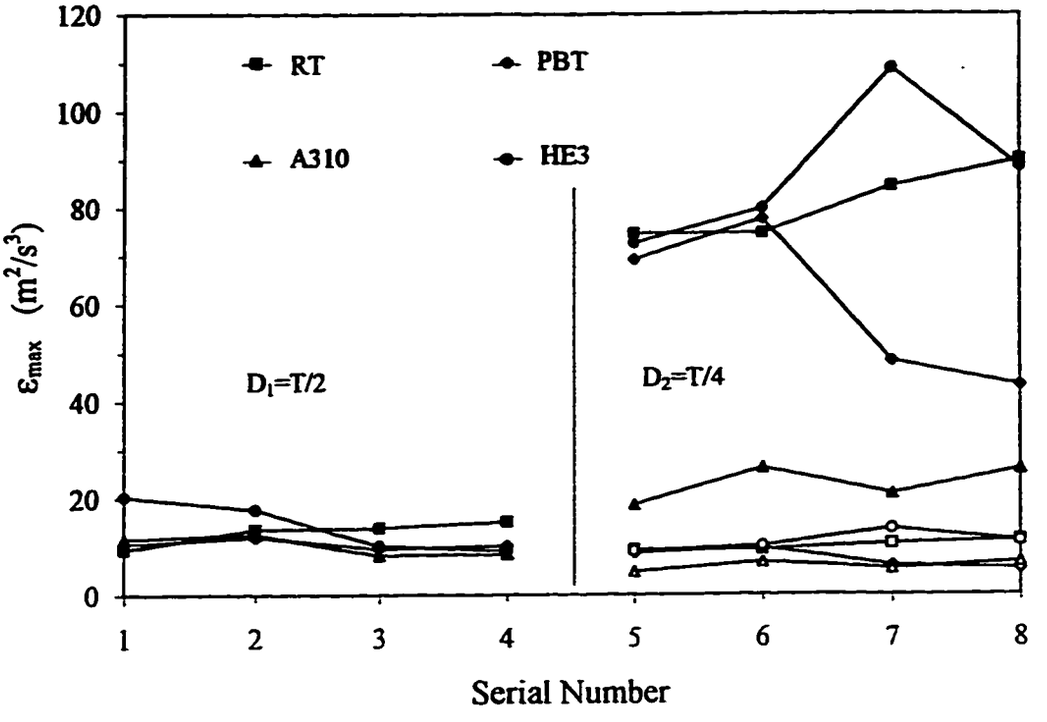

Figure 6-10 (a to d) Normal probability plots of the effects of geometric variables on ε_{max} showing the 95% confidence interval around zero effect for the factorial design based on N_f, D and C/D.

10a) **PBT**; ε_{max}'s for the four cases with D=T/4 were divided by 8.

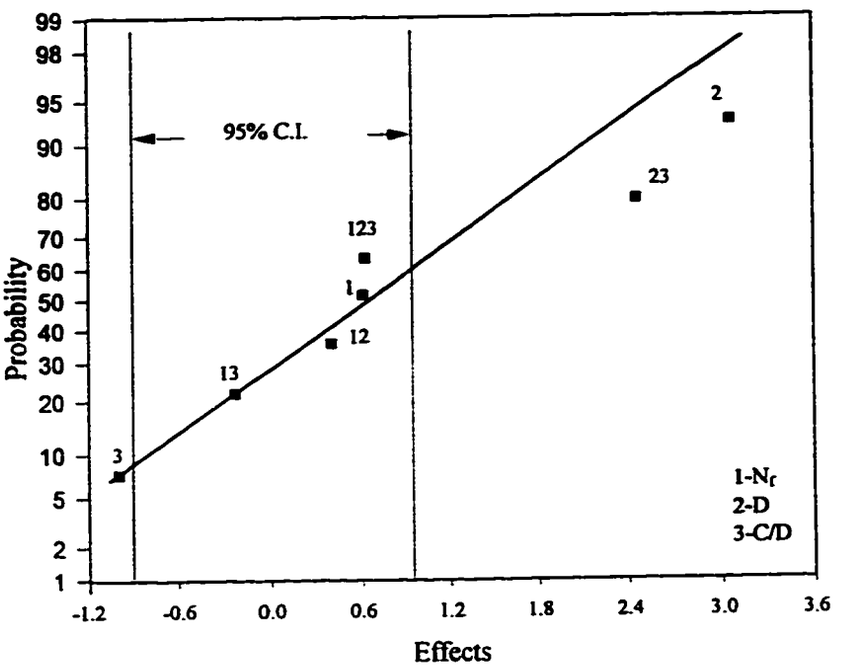

10b) **A310**; ε_{max}'s for the four cases with D=0.375 were divided by 3.88.

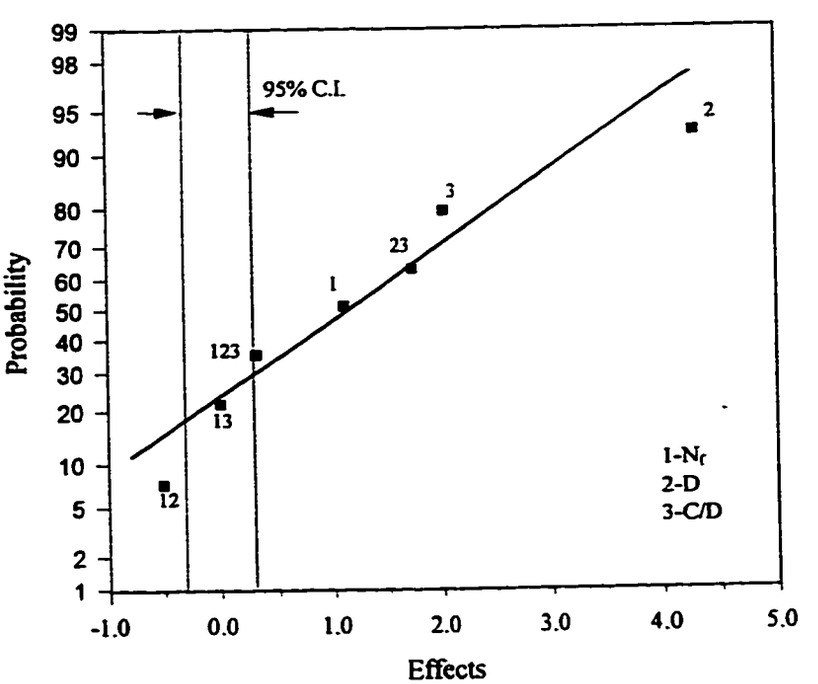

10c) **HE3**; ε_{max}'s for the four cases with D=T/4 were divided by 8.

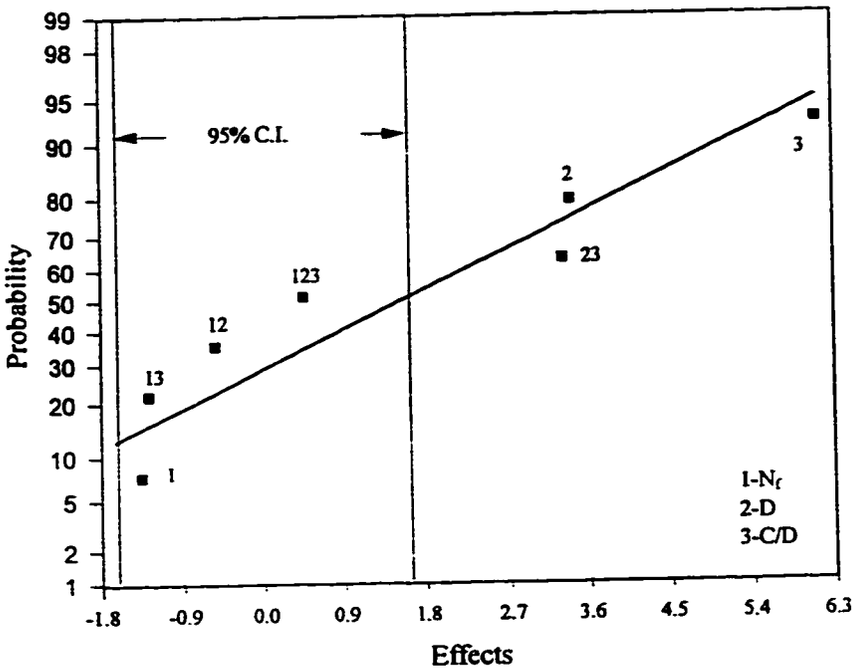

10d) **RT**; ε_{max}'s for the four cases with D=T/4 were divided by 8.

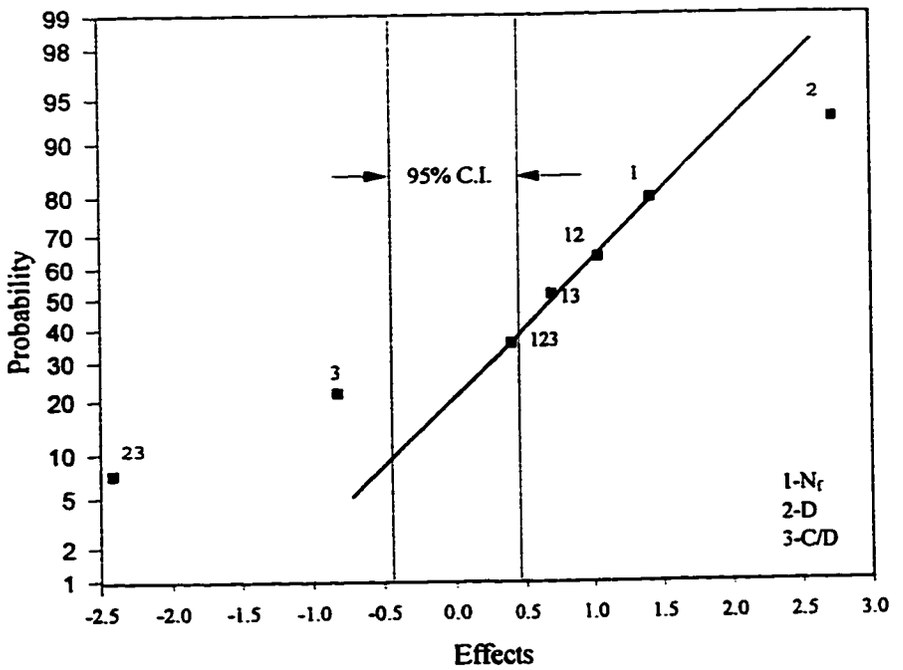

References

Box, G. E. P., Hunter, W. G. and Hunter, J. S., 1978, *Statistics for experimenters, An introduction to design, data analysis, and model building,* pp.306-379. John Wiley & Sons, New York.

Costes, J. and Couderc, J. P., 1988, Influence of the size of the units-II. spectral analysis and scales of turbulence. *Chem. Eng. Sci.* **43**, 2765-2772.

Cutter, L. A., 1966, Flow and turbulence in a stirred tank. *AIChE J.* 12, 35-45.

Jaworski, Z., Nienow, A. W., Koutsakos, E., Dyster, K. and Bujalski, W., 1991, An LDA study of turbulent flow in a baffled vessel agitated by a pitched blade turbine. *Trans. IChemE.* **69**, Part A, 313-320.

Kresta, S. M., and Wood, P. E., 1991, Prediction of the three-dimensional turbulent flow in stirred tank. *AIChE J.* **37**, 448.

Kresta, S. M., and Wood, P. E., 1993a, The flow field produced by a pitched blade turbine: characterization of the turbulence and estimation of the dissipation rate. *Chem. Eng. Sci.* **48**, 1761-1774.

Kresta, S. M., and Wood ,P. E., 1993b, The mean flow field produced by a 45-degree pitched blade turbine: changes in the circulation pattern due to off bottom clearance. *Can. J. Chem. Eng.* **71**, 42-53.

Kresta, S. M., 1991, *Characterization, measurement and prediction of the turbulent flow in stirred tanks,* Ph.D. Thesis.

Okamoto, Y., Nishikawa, M. and Hashimoto, K., 1981, Energy dissipation rate distribution in mixing vessels and its effects on liquid-liquid dispersion and solid-liquid mass transfer. *Int. Chem. Eng.***21**, 88-94.

Ranade, V. V. and Joshi, J. B., 1989, Flow generated by pitched blade turbines I: measurements using laser Doppler anemometer. *Chem. Eng. Commun.* **81**, 197-224.

Van't Riet, K. and Smith, J. M., 1975, The trailing vortex system produced by Rushton turbine agitators. *Chem. Eng. Sci.* **30**, 1093-1105.

Wu, H. and Patterson, G. K., 1989, Laser Doppler measurements of turbulent-flow parameters in a stirred mixer. *Chem. Eng. Sci.* **44**, 2207-2221.

Yianneskis, M., Popiolek, Z. and Whitelaw, J.H., 1987, An experimental study of the steady and unsteady flow characteristics of stirred reactors. *J. Fluid Mech.* **175**, 537-555.

Chapter 7

Particle Size Measurement Using the Phase Doppler Particle Analyzer

7.1 Introduction

The mean drop size and drop size distribution characterize a liquid-liquid dispersion and determine the transfer rates (mass, heat and/or chemical reaction) in the dispersion. To improve our understanding of the fundamentals of drop dispersion, the relationship of the drop size distribution to the flow field was investigated for several stirred tank configurations, specifically, the effect of dissipation and geometry on the distribution was investigated. The energy distribution in impeller regions produced by one radial impeller (the RT) and two axial impellers (the PBT and the A310) was reported in **Chapter 5**. The effect of geometric variables on the maximum dissipation for the four impellers (the RT, PBT, A310 and HE3) was investigated in detail in **Chapter 6**. The validation of the phase Doppler particle analyzer (PDPA) experimental method is presented in this chapter. Experimental measurements of the Sauter mean diameter (d_{32}), the minimum drop size and drop size distribution with changing rotational speeds (i.e. different power input per unit mass and different local dissipation rates) for the four impellers (the RT, PBT, A310 and HE3) are presented in the following chapter. Some considerations about the scale-up of liquid-liquid dispersion system are also analyzed there.

7.2 Phase Doppler Particle Analyzer

As stated in **Chapter 4**, a phase Doppler particle analyzer (PDPA) measures one component of velocity and the droplet diameter simultaneously. The velocity is measured using the principle of LDA as presented in **Chapter 4**. The PDPA mode uses phase shift to determine drop size, and there are considerations in PDPA mode in addition to those associated with an LDA mode. Thus, before the details of our drop size measurements are considered, the fundamentals of PDPA are explained in some detail.

7.2.1 Interference Behavior of a Droplet

When a light beam is incident upon a liquid droplet, the light beam is scattered and a specific scattering interference is formed due to the unique scattering characteristics (reflections, diffractions and refractions) of the droplet. Different scattering interferences are formed by liquid droplets with different refractive indices. The scattering interference formed by a droplet with a refractive index higher than that of its surroundings is shown in **Figure 7-1**, in which only two internal reflections (i.e. the second order internal reflection) are included, and diffraction due to the deviation of light passing in the forward direction is not shown.

7.2.2 Geometric Optics Approach

A relationship between the signal phase shift and the drop diameter can be obtained using either of two theoretical tools: (i) Lorenz-Mie theory or (ii) geometric optics approach.

Lorenz-Mie theory is based on general and exact laws for electromagnetic waves. The scattering interference is described exactly by Lorenz-Mie theory, however, even with large computers, the computation time required to calculate the scattering coefficients for a range of drop sizes using Lorenz-Mie theory can be prohibitive (Bachalo and Houser, 1984).

Geometric optics is an asymptotic approximation to the laws for electromagnetic waves. For spheres very much larger than the wavelength of the incident light (i.e., $\pi d/\lambda >> 1$), it is possible to approximate Lorenz-Mie scattering by the interference of diffracted, refracted, and reflected rays according to van de Hulst (1957). Van de Hulst demonstrated that for $\pi d/\lambda > 10$, the scattering of electromagnetic radiation is separable into the simplified theories of diffraction, refraction, and reflection. When the spheres have refractive indices sufficiently different from the surroundings, the amplitude functions derived from the geometric optics are, in the asymptotic limit, equal to the Mie amplitude functions. In such a scattering interference, regions are found with one of the three scattering patterns (reflection, diffraction and refraction) dominating. A linear

relationship between phase shift and drop diameter can be used for refractive and reflective scatter, with different slopes for different scattering patterns and orders. The order of scatter classifies the same scattering pattern experiencing different times of internal reflections. If several scattering orders are present, each type of scattered light will interfere and the resulting phase vs diameter relationship may be highly nonlinear and not useful for measurements. To prevent this being the case, scattering angles must be chosen where a single scattering order is dominant and diffraction is minimized (Sellens, 1989, Sankar and Bachalo, 1991).

Diffractive scatter is concentrated in a lobe in the forward direction. Diffraction effects can be neglected when the off-axis collection angle is greater than ~20° (Sankar and Bachalo, 1991). Reflective scatter dominates when a PDPA is used in backward scatter. This is shown in **Figure 7-1**. For a forward scatter PDPA with a off-axis collection angle of 30°, refractive scatter dominates. **Figure 7-2** shows a sketch of the dominant scattering lobes when silicone oil with a refractive index of 1.495 is dispersed in water.

7.2.3 Optical Configuration of a PDPA

In **Chapter 4**, the operating principles of an LDA were explained using a simple fringe model. The operating principles of a PDPA can be similarly understood. As a droplet moves through the measurement volume the projected fringes are swept through space. A LDA uses one photomultiplier (detector) to measure the frequency shift of the scattered light, while a PDPA uses two or more (often three for a one-component system) photomultipliers (PMT's) placed at different angles to measure the same frequency shift but with a relative *phase shift* between each pair of PMT's which is proportional to the *PMT spacing* divided by the projected *fringe spacing*. The projected fringe spacing is inversely proportional to the droplet diameter, so the measured *phase shift is proportional to the droplet diameter*. **Figure 7-3** shows the schematic of an Aerometrics PDPA optical configuration.

7.2.4 Experimental Parameters

Instrument Parameters

In **Chapter 4**, the instrument parameters for the LDA mode were described. Parameters related to the PDPA mode are listed below:

wavelength λ=0.5145 μm

transmitter: beam diameter d_{beam}=1.17 mm

clear aperture=72 mm

receiver: clear aperture=106 mm

collection angle and sizing slope

The rule to choose a proper collection angle is to place the receiver in a region where refraction dominates to obtain a linear relationship between drop diameter and phase difference. Based on the above instrument parameters and the dispersion of silicone oil with refractive index of 1.4950 in water, the optimum collection angle can be determined using the software LSAP offered by Aerometrics, Inc.. A collection angle of ***22.5°*** is in the middle of the region where refraction dominates. The real angle of the receiver from the center line of two beams is 22.5°x 1.33 (refractive index of water), i.e. 30°, and a sizing slope of ***1.186*** is determined accordingly by optical geometry and the ratio of refractive indices of the dispersed phase and the continuous phase. Thus the collection angle of 22.5° and the sizing slope of 1.186 are chosen.

Drop Size Measurement Ranges

The measurement range of velocity is well beyond the flow in an agitated tank. It can be as high as 10^3 m/s (see **Table 7-1**), while the velocity in the tank is just 1 m/s, so velocity measurement puts no limitations on PDPA parameters.

The PDPA used in this work has three sets of beam separations (called tracks in PDPA) for a fixed focal length (500 mm) of the transmitter. A large beam separation forms a large intersection angle (γ) at the probe (measuring) volume.

For drop size measurement, the larger the intersection angle is, the smaller the drop size which can be measured for a fixed focal length of both the transmitter and the receiver. When the beam separation (track) is fixed, a larger focal length of the transmitter (or the receiver) enables larger drop sizes to be measured. Thus, choosing a smaller beam separation and larger focal length of the transmitter (or the receiver) allows out of drop sizes in the upper measuring limit of the PDPA; while choosing a larger beam separation and smaller focal length of the transmitter (or the receiver) allows measurement of drop sizes in the lower measuring limit of the PDPA. Nevertheless, changing the focal length of the transmitter requires readjustment of the position of the receiver, which is both inconvenient, and may affect the repeatability of the experimental method. Thus, it is better to use one fixed focal length of the transmitter. For the same reason, the focal length of the receiver is also better left fixed.

Calculation of diameter measurement ranges with the tracks and lens focal lengths (f) available in this PDPA was based on personal communication with Gregory Payne (Aerometrics, Inc.). The diameter measurement ranges and related parameters are listed in **Table 7-1**. For drop size measurements, only two factory settings were chosen which are in bold face in **Table 7-1**. They cover both the largest and the smallest drop size measured using this PDPA. Using these two settings avoids readjusting the receiver. For completeness, and for possible reference by other users of this PDPA, the diameter ranges with focal lengths and tracks other than those chosen are also listed in **Table 7-1**.

Two points need to be mentioned:

1) The diameter measurement range for each set of parameters listed in **Table 7-1** only means that the minimum and maximum diameters can be measured with that set of parameters, it does not mean that the measurement for both the minimum and maximum diameters can be achieved simultaneously. Within the range the maximum diameter can be chosen arbitrarily. In most cases, setting the maximum diameter is possible to adjust the diameter measurement range to cover the whole range of the drop size distribution.

2) The minimum drop size is 0.5 μm.

In the following experiments, the focal length of both transmitter and receiver lens was 500 mm; track 1 was used when the mean drop size was larger than 50 μm and track 3 was used when the mean drop size was smaller than 50 μm (see numbers in bold face in **Table 7-1**).

7.3 Choice of Fluids and Tank Materials

Choice of fluids

Measurement of drop sizes using the PDPA mode is more complex than measurement of velocity using the LDA mode due to the introduction of the dispersed phase and the more difficult signal processing needed to obtain the phase shift. To obtain good signal quality, the dispersed phase must be a transparent liquid with a refractive index different from that of the continuous phase. It must have physical properties which enable the formation and equilibration of a dispersion dominated by flow conditions determined by the agitation and the tank and impeller geometry in a mixing system, rather than by undetermined factors, such as: possible floating or sinking of the dispersed phase due to large density differences between the dispersed phase and the continuous phase; sticking of the dispersed phase to tank walls due to the strong bonding between the dispersed phase and the tank material; poor visibility and signal quality due to an improper ratio of refractive indices between the dispersed phase and the continuous phase; or due to an improper volume fraction of the dispersed phase. **Table 7-2** summarizes the fluids used by previous investigators with their physical properties and operating parameters. Only the cases where water was used as the continuous phase are summarized here.

Accurate measurement of drop size must avoid the above conditions. After reviewing the systems used by other authors, and considering the properties of transparency, density and refractive index, silicone oil was chosen as the most favorable. The reasons for this choice are as follows.

1) The density of the dispersed phase is critical to the measurement of drop size and drop size distribution. If the density of the dispersed phase is *much larger* than the density of the continuous phase (water), the oil drops will tend to sink to the bottom of the tank, especially when the rotational speed of an impeller is low; if the density of the dispersed phase is *much smaller* than the density of the continuous phase, oil drops will tend to float to the top of the fluid in the tank: thus the smaller the difference between the density of the dispersed phase and that of the continuous phase is, the better. Paraffin oils with reasonable viscosity seldom have densities near the density of water. Silicone oils can be chosen with a wide range of densities.

2) The refractive index of the dispersed phase is important to the signal quality of the PDPA. A suitable ratio of the refractive indices between the dispersed phase (n_d) and the continuous phase (n_c=1.33 for water) is needed. A large ratio of refractive indices reduces the received signal strength; while a low ratio of refractive indices reduces the signal quality. Again, silicone oils can have refractive indices around 1.5, giving a ratio of refractive index about 1.1 which is well suited to the PDPA measurement.

Fluid Properties

To determine the linear relationship between drop size and phase difference, one needs to know the ratio of refractive indices between the dispersed phase and the continuous phase; while to define Weber number and Reynolds number, one needs to know the viscosity, density of the continuous phase and the surface tension of the two fluids. All of these properties depend on temperature. Over the course of these experiments, the temperature remained constant at 20 ± 1°C.

From **Table 7-2**, when water was used as the continuous phase, it was always deionized to avoid a possible introducing of external forces other than the surface tension and gravity force. To avoid impurities possibly existing in deionized water and affecting measurements, deionized *ultra-filtered* (DIUF) water was used as the *continuous phase* in drop size measurements. The DIUF water was supplied by FisherScientific (Catalog No.

W2-20). Its density and viscosity at 20±1 C° are 998 Kg/m^3 and $1.00x10^{-3}$ Kg/s.m., respectively (Gerhart et al. 1992).

As stated in **Chapter** 5, vortices are formed in agitated tanks. Air bubbles are inevitably entrained by the vortices in an open system. To get reliable data of drop size measurement, one must be sure that no particles or air bubbles are measured with oil droplets when oil is added. Experimental results showed that negligible particles were found in DIUF water. **Figures 7-4 (a and b)** show the experimental results of particle size measurement for DIUF water with no oil. The collection angle of the receiver and sizing slope value were the same as drop size measurements with silicone oil which are given in section **7.2.4**. In the experiment with only DIUF water, because nearly no measurable particles exist, it was difficult to get any signal at a *high voltage* of 450 V which was used in the experiments when silicone oil was added, so 700 V of *high voltage* was used. From **Figure 7-4a**, over more than 18 seconds only 23 particles were measured when the largest diameter was set at 170 μm. The ratio of sample to time is 1.3 s^{-1}. From **Figure 7-4b**, when the largest diameter was set at 50 μm only 10 particles were measured within 50 seconds. The ratio of sample to time is only 0.2 s^{-1}. Both figures show that there are nearly no particles with diameter of <50 μm in DIUF water and particles with diameter >50 μm are negligible, and air bubbles entrained by vortices are not measured when the collection angle of the receiver and sizing slope value are set for drop size measurements with silicone oil. To check the size distribution of air bubbles, the collection angle of the receiver and sizing slope value was changed according to the ratio of refractive indices (water to air), and air bubbles were measured. **Figure 7-4c** shows the results. It was found that most of air bubbles measured are with diameters larger than 250 μm, and air bubbles with diameters <250 μm are negligible.

When the experimental results for DIUF water with no silicone oil are compared with those in which silicone oil was added, particles in DIUF water are negligible considering such low ratios of sample to time and so high *high voltage* in the DIUF water measurement. **Figure 7-5** shows a typical experimental result with silicone oil. At 450 V of high voltage, 6000 samples were measured within less than 16 seconds. The ratio of

sample to time is 375 s^{-1}. Even through the effect of high voltage on the ratio of sample to time is *not* considered, a maximum of 3 particles in DIUF water may be measured in a sample of 1000 oil drops.

The *dispersed phase* was silicone oil with refractive index of 1.4950 and density of 1050 kg/m^3 (supplied by Aldrich Chemical Company, Inc., Catalog No. 17,563-3). The ratio of refractive indices between the dispersed phase and the continuous phase is 1.124. The density of this type of silicone oil is perfect for our purpose. This is justified in **Figure 8-2**. The RMS velocities between the two cases with and without silicone oil agree with each other which means oil droplets move with the continuous phase with no slip.

The viscosity of the silicone oil was measured using a co-axial cylinder viscometer (Contraves Rheomat 115) in this department. The gap width of the measuring head was 500 μm. The length of the rotating bob was 114.3 mm. The bottom clearance between the bob and the cup was 330 μm. A mean value of 173.2×10^{-3} kg/m·s with a standard deviation of 1.212 was obtained for the viscosity of the silicone oil from 8 repeated experiments at 20°C (raw data is given in **Appendix-4**).

The interfacial tension of the silicone oil/water was measured using a FISHER Surface Tensiomat, Model 21 (du Nouy method) in this department. The surface tension of water at 20°C was first measured. Results showed that data obtained with this Tensiomat agreed with the published surface tension of water at 20°C (72.8 dyne/cm, Gerhart et al., 1992): the relative error between them is less than 2%. The interfacial tension of silicone oil/water was measured seven times. The apparent values had a good reproducibility (45.3, 45.1, 44.8, 44.6, 45.0, 45.3, 45.1 dyne/cm) with a mean value of 45.0 and standard deviation 0f 0.196. The value of 45.0 dyne/cm is used as the interfacial tension of silicone oil/water.

Choice of Tank Material

Although data for the contact angle between perspex and silicone oil in air is rare in literature, a simple experiment done in our lab shows that perspex is a very strong hydrophobic material: a drop of silicone oil spread quickly on the surface of perspex

plate; while a drop of water did not. If a tank made of perspex is used, some oil in the dispersed phase will possibly stick to walls of the tank. This will certainly affect the accuracy and the reliability of measurements of drop size in the dispersion, especially for a dispersion with a low volume fraction of the dispersed phase. Two choices are available to prevent the adherence of oil drops to the walls of the tank. One is to add some surfactant to the dispersion, which inevitably changes the properties of the dispersion. The second is to rebuild the inner tank using hydrophilic materials. To avoid any unknown effects caused by surfactants, the cylinder of inner tank was rebuilt using glass, with the top and bottom plates contacting directly with fluids in the dispersion made of stainless steel which is also hydrophilic. In order to keep the same tank geometry as was used for the velocity measurements, the glass tank has the same diameter and the same height as the perspex tank used for the velocity measurements. To avoid the introduction of any surfactants, the connection between the stainless steel bottom plate and the glass tank is free of any kind of glue or sealing agent. The outer square tank was left unchanged.

7.4 Validation of PDPA Size Measurement

Validation of the drop size measurements was performed in three stages:

1) PDPA size measurements using standard particles;

2) repeatability of the instrument and of the experimental method;

3) feasibility of using step-change in N to combine several experiments in one.

These three issues are explained in detail in the following sections.

7.4.1 PDPA Size Measurements Using Standard Particles

In **Chapter 4**, it was explained that increasing the high voltage on the photomultipliers increases the sampling speed of velocity measurement. The voltage applied to the photomultipliers affects not only the sampling speed but also the *accuracy* of drop size measurement. Higher voltages give preference of measurement to drops with large diameters, so a lower voltage is suggested by the PDPA manufacturers, but the sampling rate prevents lowering the voltage without limit. By balancing the sampling speed with measurement accuracy, a voltage of 450 V was chosen for all of the size

measurements for both standard particles/water dispersion and oil/water dispersion. The suitability of this voltage was verified by the accuracy check of PDPA measurements using standard particles.

Standard polystyrene particles (in solution state) with a mean diameter of 14.6±0.4 μm (supplied by Duke Scientific Corp., Catalog No. 241) were used. The ratio of refractive indices is 1.195, so the collection angle and the sizing slope are 22° and 1.046, respectively. As an impeller agitates the fluid in the tank, air is entrained into the fluid by vortices formed in the flow and is then broken to form air bubbles. More air bubbles are created when a large impeller diameter is used. In order to determine if the air bubbles affected the accuracy of the PDPA measurement, standard particle measurements both with and without sealing water on the top of the tank cover were performed. The experimental conditions were: A310, C/D=1/2, N=8.33 1/s, D=0.550T which is the largest impeller diameter used in drop size measurement. A sample size of 1500 was used. Experimental results showed that measurements using PDPA give results in good agreement with the known size range of the standard particles: results of all 11 runs are within the given size range of the standard particles. **Table 7-3** lists the results. The typical particle size histogram is shown in **Figure 7-6**.

From **Table 7-3**, though it is not possible to define the experimental error of this technique because the mean diameter of the standard particles is given as a range (14.2 to 15.0 μm), the feasibility of PDPA technique was verified. Again, the results are shown in **Table 7-3**, and it is clear that the effect of air bubbles is negligible. This is because air bubbles have totally different light scattering interference. By choosing a proper collection angle and sizing slope the effect of air bubbles was eliminated.

7.4.2 Repeatability of the Instrument and of the Experimental Method

The transparency requirement of the PDPA makes it necessary to determine the maximum volume fraction of the dispersed phase before performing drop size measurements in the oil/water dispersion. After a proper volume fraction was determined, the same volume fraction was used to check the repeatability of the instrument and the experimental method.

7.4.2.1 Volume Fraction, ϕ, of Silicone Oil

The number density of drops in a dispersion increases with the increase of volume fraction, ϕ, of a dispersed phase. There is a limit on ϕ for the proper performance of a PDPA. When ϕ increases to a value which produces a number density of drops high enough to block the incident light, no signal can be collected by the receiver. The volume fraction of silicone oil was first set at 0.01%, and drop sizes were measured at four points: one at r=0 and the other at r=87 mm (near baffles) with $2z/W_p$=2.0 to give a spatial flexibility of measurements as large as possible. Since the limit of ϕ is also determined by the type of an impeller and by the turbulent strength (rotational speed of the impeller), the A310 with D=0.550T and D=0.350T and the RT with D=0.500T and D=0.250T were chosen operating at their highest possible rotational speeds. ϕ was gradually increased until no good signal could be obtained. Experimental results showed that ϕ=0.03% is the maximum value which is suitable for all the operating conditions to be investigated. although the PDPA can measure drop sizes with ϕ as high as 1.5% at r=87 mm in some cases. ϕ=0.03% was chosen to enable the use of a large impeller diameter, variation in wide rotational speeds and arbitrary sampling positions. In all of the following experiments in which silicone oil was used, the volume fraction of silicone oil is **0.03%**.

7.4.2.2 Repeatability of the Instrument and Sample Size

The results in **Table 7-3** show that the reproducibility of drop size measurements is good when standard particles are used. To be sure that this is true for a silicone oil/water dispersion, the repeatability of the instrument with silicone oil was checked. The instrument repeatability was tested by repeating drop size measurements at one point 11 times. The first 7 measurements had a sample size of 4000, and the other four had a sample size of 6000. A large sample size was used because the drop size distribution in silicone oil/water dispersion is much wider than that of the standard particles. Experimental conditions were: A310, D=0.550T, C/D=1/2, N=8.22 1/s. The results are listed in **Table 7-4**.

The data in **Table 7-4** show that a good repeatability can be obtained using the PDPA. The maximum difference of d_{32} among the first 7 runs is 2.3 μm (see the two numbers in bold in **Table 7-4**). The repeatability with the sample size of 6000 was similar to that with the sample size of 4000. This means that the sample size of 4000 is high enough to achieve a good repeatability. A sample size of 4000 was used for the drop size measurements below.

7.4.2.3 Rinse Procedure and Repeatability of the Experiment

Because of the strong sensitivity of a dispersion to clearness of mixing equipment (tank, impellers), a proper rinse procedure for the tank and impellers is a prerequisite to obtain reliable data.

There are two main rinse procedures used by the previous investigators listed in **Table 7-2**:

i) acetone-twice distilled water.

ii) nitric acid-distilled water-acetone-distilled water.

The efficiency of a rinse procedure can be tested by checking the repeatability of the experiment. In this work, the repeatability of the experiment was checked by repeating one case 4 times on 4 different days. The chosen case was: the A310; D=0.550T; C/D=1/2; N=8.22 1/s. The examination of repeatability was intended to justify the rinse procedure of the tank, baffle and impeller. The rinse procedure was as follows:

i) tap water with detergent;

ii) immersed in running tap water for more than 20 minutes;

iii) nitric acid (0.001 mol/l);

iv) immersed in running tap water for more than 20 minutes;

v) deionized ultra-filtered water (at least three times).

The results in **Table 7-5** show that although the repeatability of the experiment is not as good as the repeatability of the instrument (the maximum difference of d_{32} among the four runs is 3.3 μm (see the two numbers in italic in **Table 7-5**)), it is still in the range

of the random error shown by the data in **Table 7-4.** **Figure 7-7** shows the drop size distributions at 2r/D=0.55 measured on the four days. They are similar to each other. The repeatability of the mean drop diameter and size distribution means that the rinse of mixing equipment is sufficient to ensure experimental repeatability.

7.4.3 Feasibility of Using a Step-Change in N

To find the relationship between Sauter mean drop size (d_{32}) and energy dissipation, or turbulence strength (local maximum and/or the average power input per unit mass, or the tip speed of an impeller), we need to know how d_{32} changes with the rotational speed of the impeller. Thus experiments of drop size measurement could be designed as: fix a rotational speed and obtain a d_{32} after the equilibrium state of the dispersion is reached; then increase the rotational speed and obtain another equilibrium d_{32}. Here d_{32} is chosen because it is directly used in the calculation of transfer process via the *total surface area per unit volume*, a, by the equation $a=6\phi/d_{32}$.

Two things need to be considered:

1) How long will it take the dispersion to achieve its equilibrium state?

2) Is it possible to directly change from a low rotational speed to a higher rotational speed without rinsing and restarting (*step-change measurement*)? Is there a difference between a step-change measurement and a new experiment with rinse and refill of the water and oil before changing to the next rotational speed (*rinse-and-change measurement*)? If there is no significant difference between the step-change and the rinse-and-change measurement, how long will it take the dispersion to achieve a new equilibrium state at the new rotational speed?

7.4.3.1 Equilibrium Time of Silicone Oil/Water Dispersion

From the velocity measurement experiments, it was found that after 10 to 15 minutes a stable flow is established. Experiments showed that the time needed for a dispersion in an agitated tank to reach its equilibrium state is much longer than that needed for a flow field. The data show that the equilibrium state is not attained until at

least 3 hours after the oil is added. **Table 7-6** lists the data. Each entry in this table represents the average values from 14 spatial points ($2z/W_p$=1.4 and r from 6 to 84 mm with Δr=6 mm) for that time. The total measuring time for all 14 points was less than 2 minutes. The time in **Table 7-6** is the time when the first point was measured. **Figure 7-8** shows the plot of d_{32} changing with time from the data in **Table 7-6**. Here two lines are included: one of them shows the effect of surfactant on liquid-liquid dispersion. The experimental procedure was the same for both cases:

Experimental conditions were: A310, D=0.350T, C/D=1, N=*17.8* s^{-1}.

The inner cylindrical glass tank was first filled with deionized ultra-filtered water; then the outer square tank was filled with distilled water.

The rotational speed of the impeller was adjusted to the desired value. After 20 minutes, silicone oil was injected into the DIUF water below impeller blades near the impeller tip. When surfactant was used, 0.0004 mol/l of surfactant-*sodium dodecyl sulfate* (SDS) was added first and silicone oil was injected 5 minutes after the SDS was added. Injecting oil after a stable flow field is created prevents large oil drops from being trapped in *dead-zones* of the flow field. This is specially necessary when the rotational speed is low.

Measurement of the drop size was taken at 14 spatial points in both the impeller region and the bulk of the tank every 15 minutes after silicone oil was added.

It is clear from **Figure 7-8** that the dispersion of silicone oil both with and without surfactant does not reach its stable state until 3 hours after the oil is added (the beginning of the dispersion). Addition of surfactant shows a complex effect on d_{32}: in the first 60 minutes it slows down drop breakup; then it decreases d_{32} sharply in the next 45 minutes; after these two stages the dispersion with surfactant shows the same trend as that without surfactant. Both dispersions achieve their equilibrium state at about 180 minutes, which is longer than the time reported by Calabrese et al. (1986). They found that after more than one hour, a silicone oil/water dispersion reaches an equilibrium state.

7.4.3.2 Effect of a Step-Change in N

To check the feasibility of a step-change measurement, mean drop size data were collected by changing N step by step. For comparison with the data in section **7.4.3.1**, an A310 with D=0.350T and C/D=1 was chosen. A series of 5 rotational speeds was collected. **Table 7-7** lists the results. **Figure 7-9** is the plot of d_{32} vs time for each N using the data in **Table 7-7**. The initial time for N=15.5 s^{-1} started from when silicone oil was added, and the initial time for the other four N's started from when each of them was changed. The first data was collected 3 hours after silicone oil was added, and the other four were collected 2 hours after the N was changed. The data without SDS in **Table 7-6** can be compared directly with the data with N=17.8 s^{-1} in **Table 7-7**. The only difference is that the latter was measured after a step-change in N and experienced a longer time in the tank. The difference between the step-change and the rinse-and-change measurement is 1.06 (74.68-73.62) μm at 120 minutes and 1.02 (74.42-73.40) μm at 150 minutes (see numbers in bold face in **Tables 7-6** and **7-7**), both with less than 1.5% relative error and within the difference (2.3 μm) shown in experiments to measure the instrument repeatability. As long as enough time is given, a new equilibrium state is established responding to the new rotational speed, no matter what lower rotational speed was used before. This may not be true for dispersions which involve strong coalescence or interactions between the dispersed phase and the continuous phase. Experiments showed that this was also not true when N was changed from high to low instead of low to high since the minimum drop size created by a high N can not be coalesced at a lower N. Excepting the first rotational speed, the equilibrium time is about 120 minutes. The longer time required for the first equilibrium is easily explained since the dispersion at the first N evolves beginning with the initial oil injection, and the others evolve from an established distribution.

7.5 Conclusions

The PDPA used in this work is suitable for the measurement of drop diameters in the silicone oil/DIUF water dispersion. The repeatability of the PDPA equipment and of the experiment is good, which verifies the suitability of the sampling size of 4000 and the

rinse procedure. A wide impeller diameter and rotational speed range with no limitation on sampling positions can be achieved when the volume fraction of the dispersed phase is 0.03%. As long as enough time is given, a new equilibrium state is established responding to a step increase in rotational speed, and the *step-change* measurements give good agreement with the *rinse-and-change* measurements when the rotational speed is increased.

Tables in Chapter 7

Table 7-1 Diameter measurement ranges

track	transmitter lens focal length (f) (mm) *	beam expander ratio *	beam waist dia. d_w (μm) **	beam separation s (mm) *	fringe spacing δ_f (μm) **	nominal fringe count **	velocity range (m/s)	diameter measurement ranges (μm)			
								receiver lens focal length (mm) *			
								238		500	
								min.	max.	min.	max.
1	300	1.0	168	16.9	9.1	18	-319~1004	0.5	96.6	0.7	203
	500	1.0	280	16.9	15.2	18	-532~1673	0.5	161	**1.1**	**338**
2	300	2.0	84	33.8	4.6	18	-160~502	0.5	48.5	0.5	102
	500	2.0	140	33.8	7.6	18	-266~837	0.5	80.4	0.5	169
3	300	3.8	45	63.4	2.4	18	-85~268	0.5	26.0	0.5	54.7
	500	3.8	75	63.4	4.1	18	-142~446	0.5	43.4	**0.5**	**91.1**

* Factory settings; ** The probe volume characteristics (beam waist diameter, fringe spacing and fringe count) are computed as follows: beam waist diameter: $d_W = \frac{4\lambda f}{\pi d_{beam}}$; fringe spacing: $\delta_f = \frac{\lambda}{2\sin(\gamma/2)} \approx \frac{\lambda f}{s}$ where γ is the beam angle: $\gamma = 2\tan^{-1}\left(\frac{s}{2f}\right)$;

Nominal fringe count= $\frac{d_W}{\delta_f}$.

Table 7-2 Physical properties and operating parameters of the dispersion systems used by previous investigators

Author(s)	Continuous phase			Dispersed phase				σ dyne /cm	Temp. °C	Remark
	Fluid	μ_c cp	ρ g/cm^3	Fluid	ϕ	μ_d cp	ρ g/cm^3			
Arai et al., 1977	water with polyvinyl alcohol[a] (PVA) (0.1g/l)/glass, stainless steel	0.97	1.00	polystyrene-*o*-xylene solution with polystyrene at 0 to 25 wt%	<0.003	0.78 to 1500	0.879 to 0.922	22±0.4	22±1	photo-graphy
Brown and Pitt, 1972	water/glass pipe	1.00	0.998	kerosene	0.05, 0.10, 0.20[b]	1.62	0.783	50.0	20	photo-graphy
Berkman and Calabrese, 1988	water/static mixer			silicone oil		19.4 to 204	0.946 to 0.967	37.4	20 to 23	photo-graphy
				paraffin oil	0.00057 to 0.001	43 to 161	0.853 to 0.876	41.6	23 to 25	
				p-xylene		0.63, 0.64	0.856, 0.857	31.8	21, 22	
Chen and Middleman, 1967	water[c]	1.27	1.001	benzyl alcohol	0.001 to 0.005	5.30	1.042	4.75	25	photo-graphy
Coulaloglou and Tavlarides, 1976	water/glass, stainless steel, teflon			63% kerosene and 37% dichlorobenzene	0.025 to 0.15	1.30	0.972	43	-	photomi-crography
Calabrese et al., 1986	water/glass	0.893	0.997	silicone oils	≤0.0015	96.0 to 10510	0.960 to 0.975	37.8	25	photo-graphy

continued **Table 7-2** Physical properties and operating parameters of the dispersion systems used by previous investigators

Author(s)	Continuous phase			Dispersed phase				σ	Temp.	Remark
	Fluid	μ_c cp	ρ g/cm^3	Fluid	ϕ	μ_d cp	ρ g/cm^3	dyne /cm	°C	
Chatzi et al., 1989	water with 0.5g/l PVA /glass,	0.915	0.997	styrene	0.01 to 0.03	0.730	0.901	11.5	25	sampling photo-
	stainless steel	0.550	0.988			0.459	0.879	7.4	50	graphy
Godfrey and Grilc, 1977	water	0.89	0.997	kerosene	0.05 to 0.5	2.05	0.783	34.5		sampling
		0.90	0.996	n-octanol		8.6	0.829	8.4	25	photo-
		1.19	0.986	n-butanol		3.17	0.824	1.9		graphy
Hatzikiriakos et al., 1990	water/ perspex			linseed oil (85 vol.%)+TCE (15 vol.%)		17	1.000	6.2	-	photo- graphy
				cottonseed oil (83 vol.%) +TCE (17 vol.%)		19	1.000	23.6		
				castor oil (90 vol.%)+TCE (10 vol.%)		180	1.010	34.3		
				dibenzyl ether		5	1.040	5.0		
Godfrey and Grilc, 1977	water	0.89	0.997	kerosene	0.05 to 0.5	2.05	0.783	34.5		sampling
		0.90	0.996	n-octanol		8.6	0.829	8.4	25	photo-
		1.19	0.986	n-butanol		3.17	0.824	1.9		graphy
Hatzikiriakos et al., 1990	water/ perspex			linseed oil (85 vol.%)+TCE (15 vol.%)		17	1.000	6.2	-	photo- graphy
				cottonseed oil (83 vol.%)+TCE (17 vol.%)		19	1.000	23.6		
				castor oil (90 vol.%)+TCE (10 vol.%)		180	1.010	34.3		
				dibenzyl ether		5	1.040	5.0		

continued **Table 7-2** Physical properties and operating parameters of the dispersion systems used by previous investigators

Author	Continuous phase			Dispersed phase				σ	Temp.	Remark
	Fluid	μ_c cp	ρ g/cm^3	Fluid	ϕ	μ_d cp	ρ g/cm^3	dyne /cm	°C	
Konno et al., 1980	water + 0.002 mol/l Na_3PO_4[d] /glass, stainless steel	0.88	0.998	*o*-xylene (64 wt.%) + carbon tetrachloride (36 wt.%)	<0.002	0.74	1.04	34.3	25± 0.5	photo-graphy
Laso et al., 1987	water/pyrex[e], stainless steel	1.002	0.998	34.7 vol.% CCl_4+ 65.3 vol.% n-heptane	~0.09	0.627	1.001	48.3	20	sampling photo-graph
				22.6 vol.% CCl_4+ 77.4 vol.% 1-octanol		0.844	0.999	16.7		
				25.1 vol.% CCl_4+ 74.9 vol.% MIBK		0.684	1.001	18.5		
Mlynek and Resnick, 1972	water/pyrex			isooctane+CCl_4	0.025 to 0.34		1.005	~41		sampling, photomi-crography
Park and Blair, 1975	water/pyrex	0.89	0.997	methylisobutyl-ketone (MIBK)	0.005	0.59	0.795	10.5	25	photo-graphy probe photo-graphy
					0.10					
Ross et al., 1978	water[e] with 0.001N Na_3PO_4	1.9	1.0+	39.1 vol.% Dowtherm-E[f] + 61.9 vol.% Shell No.3747 base oil	0.025, 0.05, 0.1, 0.2	3.5	<1.0	35	22	

continued **Table 7-2** Physical properties and operating parameters of the dispersion systems used by previous investigators

Author	Continuous phase			Dispersed phase				σ dyne /cm	Temp. °C	Remark
	Fluid	μ_c cp	ρ g/cm^3	Fluid	ϕ	μ_d cp	ρ g/cm^3			
Skelland and Kanel, 1992	water/glass	0.87	0.9971	chlorobenzene	0.03, 0.07	0.73	1.083	33.5	25	photo-graphy
Tobin et al., 1990	water/glass baffles fused to the vessel wall[g]	0.90	1.00	hexane-CCl_4 (0.564/0.436 mol)	0.05	0.44	1.000	~21		sampling photo-graphy
				heptane-CCl_4 (0.553/0.447 mol)		0.54	1.000	~23		
				benzene-CCl_4 (0.839/0.161 mol)		0.67	1.000	28.14		
Vermeulen et al., 1955	water[h]/stainless steel	0.998	1.00	CCl_4	0.2	0.980	1.595	39.9	20	light trans-mittance
Zhang et al., 1989	water	0.997	0.875	kerosene + CCl_4	0.2 to 0.4	1.22	1.024	34.5	25	sampling photomi-crography

a Polyvinyl alcohol was added to prevent adhesion of drops to the wall of the tank; Water was saturated with *o*-xylene prior to each experimental run.
b Assuming non-coalescence even at this volume fraction.
c Various dispersed phases were used.
d Na_3PO_4 was added to prevent adhesion of drops to the wall of the tank.
e Wall mixing effect was mentioned: Clumps of dispersed phase became attached to the baffles, grew in size, became unstable, and broke off.
f Primarily orthochlorobenzene.
g Closed system.
h Various dispersed phases were used.

Table 7-3 Experimental results with standard polystyrene particles

Run	Mean diameter, d_{10} (μm)	Average $\overline{d_{10}}$ (μm)	Standard deviation	Sealed with water
1	14.5	14.8	0.167	yes
2	14.9			
3	14.8			
4	14.7			
5	14.9			
1	14.7	14.6	0.117	no
2	14.7			
3	14.5			
4	14.6			
5	14.4			
6	14.6			

Table 7-4 Repeatability of the PDPA instrument

Run	1	2	3	4	5	6	7
Sample size	4000						
Mean diameter, d_{32} (μm)	104.4	105.2	**103.8**	104.7	**106.1**	104.9	105.5
Average $\overline{d_{32}}$ (μm)	104.9						
Standard deviation	0.750						
Run	8	9	10	11			
Sample size	6000						
Mean diameter, d_{32} (μm)	105.8	104.8	104.3	103.6			

Table 7-5 Repeatability of the experiment

Run	1	2	3	4
Mean diameter, d_{32} (μm)	104.9*	*103.4*	*106.7*	105.9
Average $\overline{d_{32}}$ (μm)	105.2			
Standard deviation	1.42			

* from the case in **Table 7-4**.

Table 7-6. Time evolution of mean drop size, d_{32}.

Time (minutes)	d_{32} (SDS=0) (μm)	d_{32} (SDS=0.0004 mol/l) (μm)
15	92.73	96.16
30	87.51	94.10
45	83.79	92.07
60	80.88	88.59
75	78.61	82.92
90	76.93	77.75
105	75.85	73.28
120	74.68	71.63
135	74.44	71.08
150	74.42	70.51
165	73.72	69.81
180	73.24	68.99
195	73.22	68.97

Table 7-7 Step-change measurement of mean drop size, d_{32}

Time (minutes)	d_{32} (μm)				
	N=15.5 (1/s)	N=16.3 (1/s)	N=16.9 (1/s)	N=17.8 (1/s)	N=21.8 (1/s)
30	120.0	92.51	87.31	82.11	72.71
60	99.01	90.00	84.50	79.00	68.00
90	95.03	89.03	83.20	75.02	64.02
120	93.92	87.72	82.50	73.62	62.10
150	93.01	87.56	82.37	73.40	61.81
180	92.73				

Figures in Chapter 7

Figure 7-1 Ray trace for light incident on a spherical, transparent particle with an index of refraction higher than that of its surroundings as is the case for a silicone oil droplet in water.

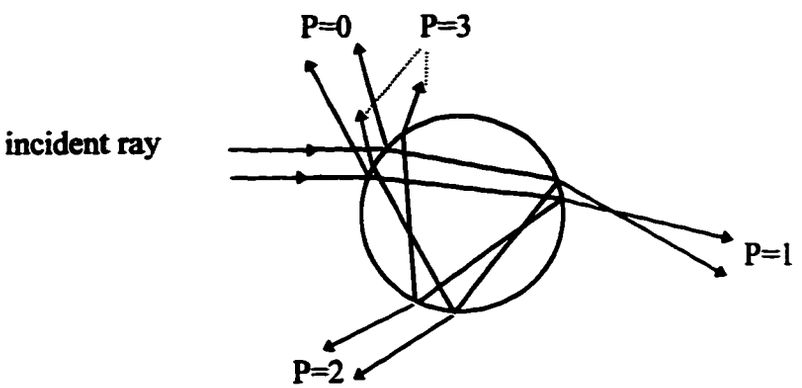

0 Reflection
1 Refraction
2 One internal reflection
3 Two internal reflections

Figure 7-2 Schematic of the scattering lobes for a spherical, transparent silicone oil droplet with a refractive index of 1.495. Numbers are in units of degrees (not to scale).

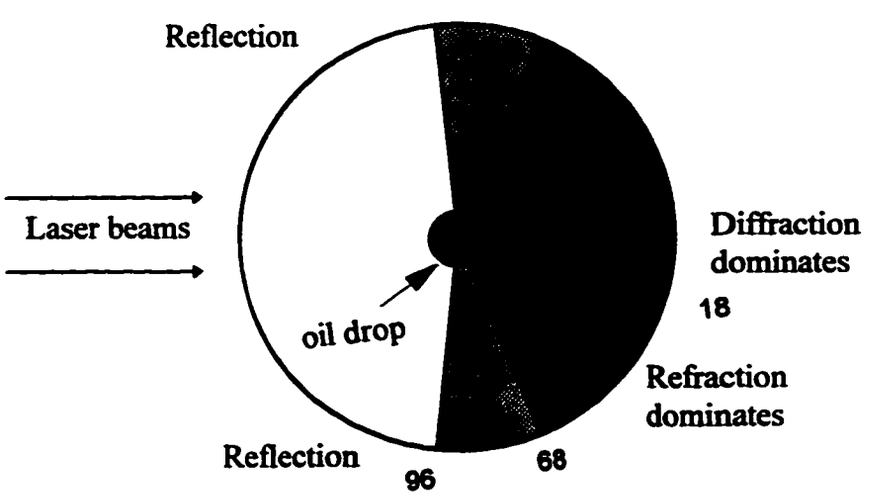

Figure 7-3 Schematic of an Aerometrics PDPA optical configuration.

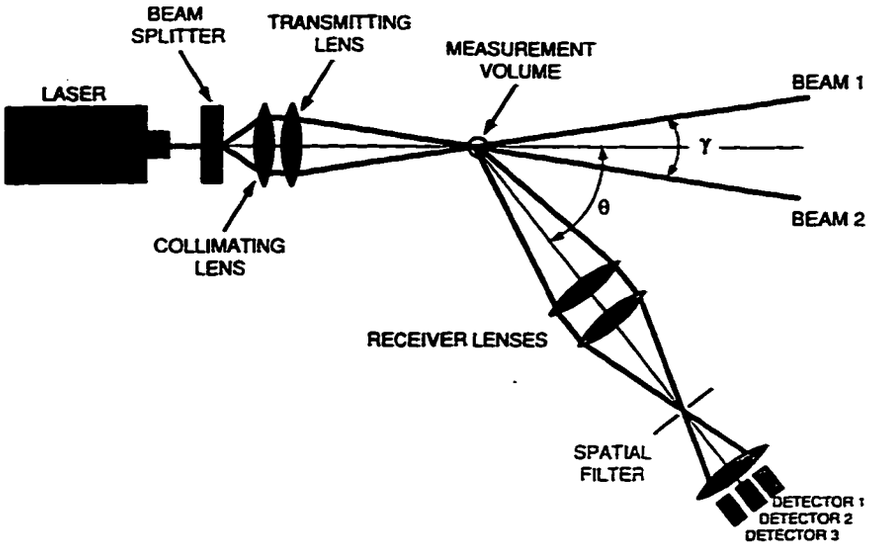

Figure 7-4 Particle and air bubble measurement in deionized ultra-filtered water.

4a) particle measurement with largest diameter set at 170 μm.

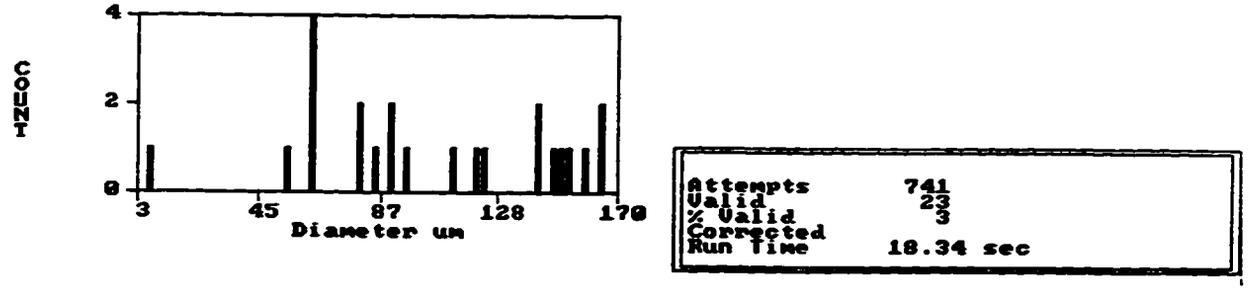

4b) particle measurement with largest diameter set at 50 μm.

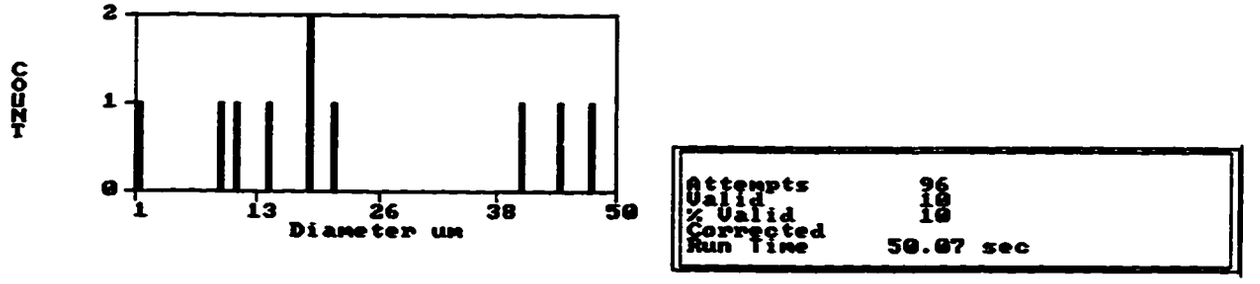

4c) air bubble measurement in deionized ultra-filtered water.

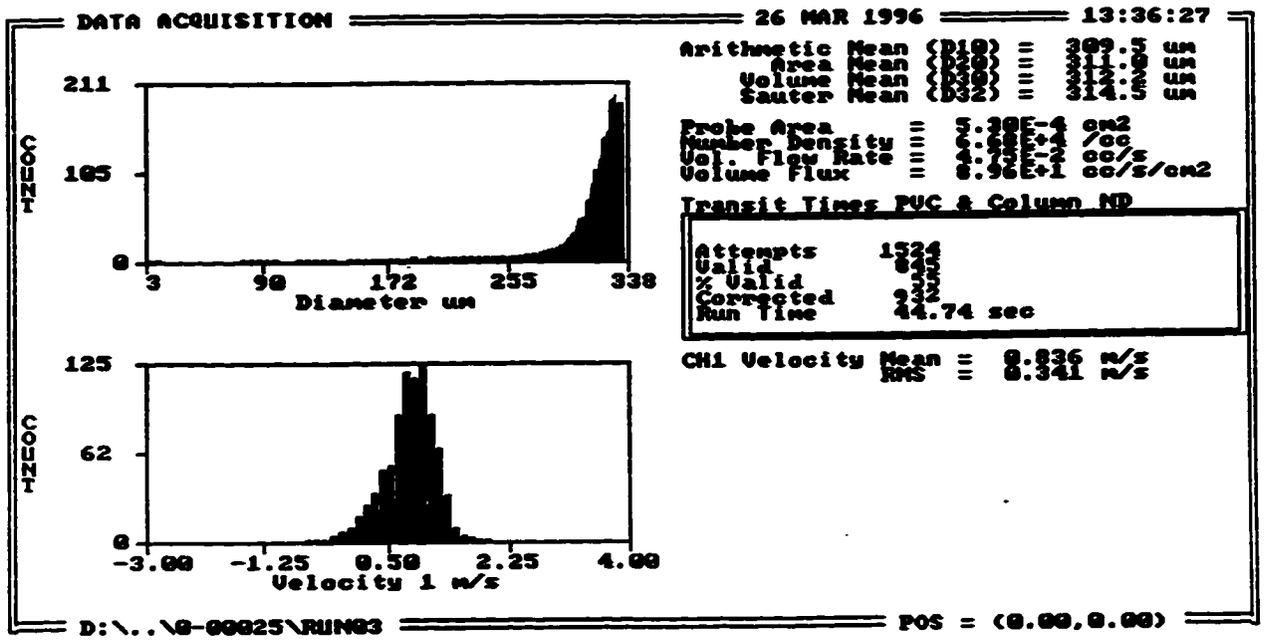

Figure 7-5 Size histogram measured in silicone oil/DIUF water dispersion.

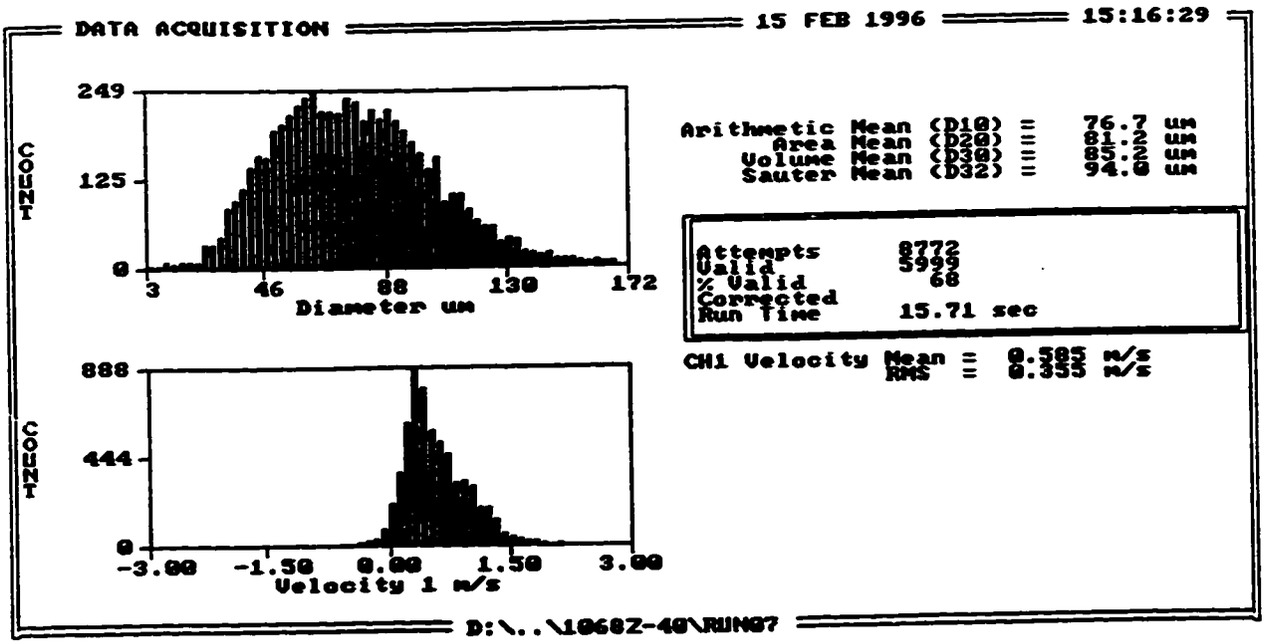

Figure 7-6 Typical size histogram of standard particles.

6a) Particle size histogram (without sealing water)

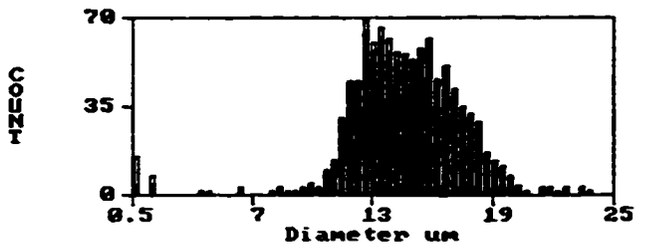


```
Arithmetic Mean (D10) =    14.4 um
     Area Mean (D20) =    14.8 um
   Volume Mean (D30) =    15.0 um
   Sauter Mean (D32) =    15.5 um

Probe Area      =  7.45E-4 cm2
Number Density  =  2.64E+2 /cc
Vol. Flow Rate  =  1.81E-8 cc/s
Volume Flux     =  2.43E-5 cc/s/cm2

Transit Times PUC & Column ND

Attempts      3981
Valid          960
% Valid         24
Corrected     1024
Run Time    100.41 sec
```

6b) Particle size histogram (with sealing water)

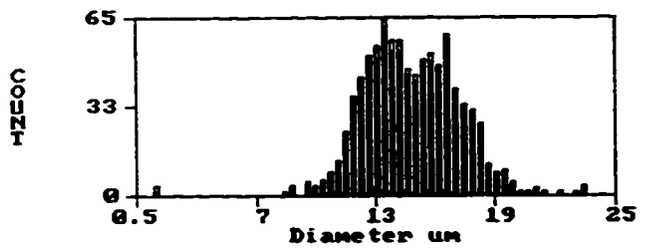


```
Arithmetic Mean (D10) =    14.7 um
     Area Mean (D20) =    14.9 um
   Volume Mean (D30) =    15.1 um
   Sauter Mean (D32) =    15.5 um

Probe Area      =  7.32E-4 cm2
Number Density  =  2.03E+2 /cc
Vol. Flow Rate  =  1.61E-8 cc/s
Volume Flux     =  2.20E-5 cc/s/cm2

Transit Times PUC & Column ND

Attempts      1241
Valid          854
% Valid         69
Corrected      896
Run Time    100.15 sec
```

Figure 7-7 Drop size distribution for the 4 runs with the same tank geometry and N measured on 4 consecutive days. The Sauter mean diameters are listed in **Table 7-5.**

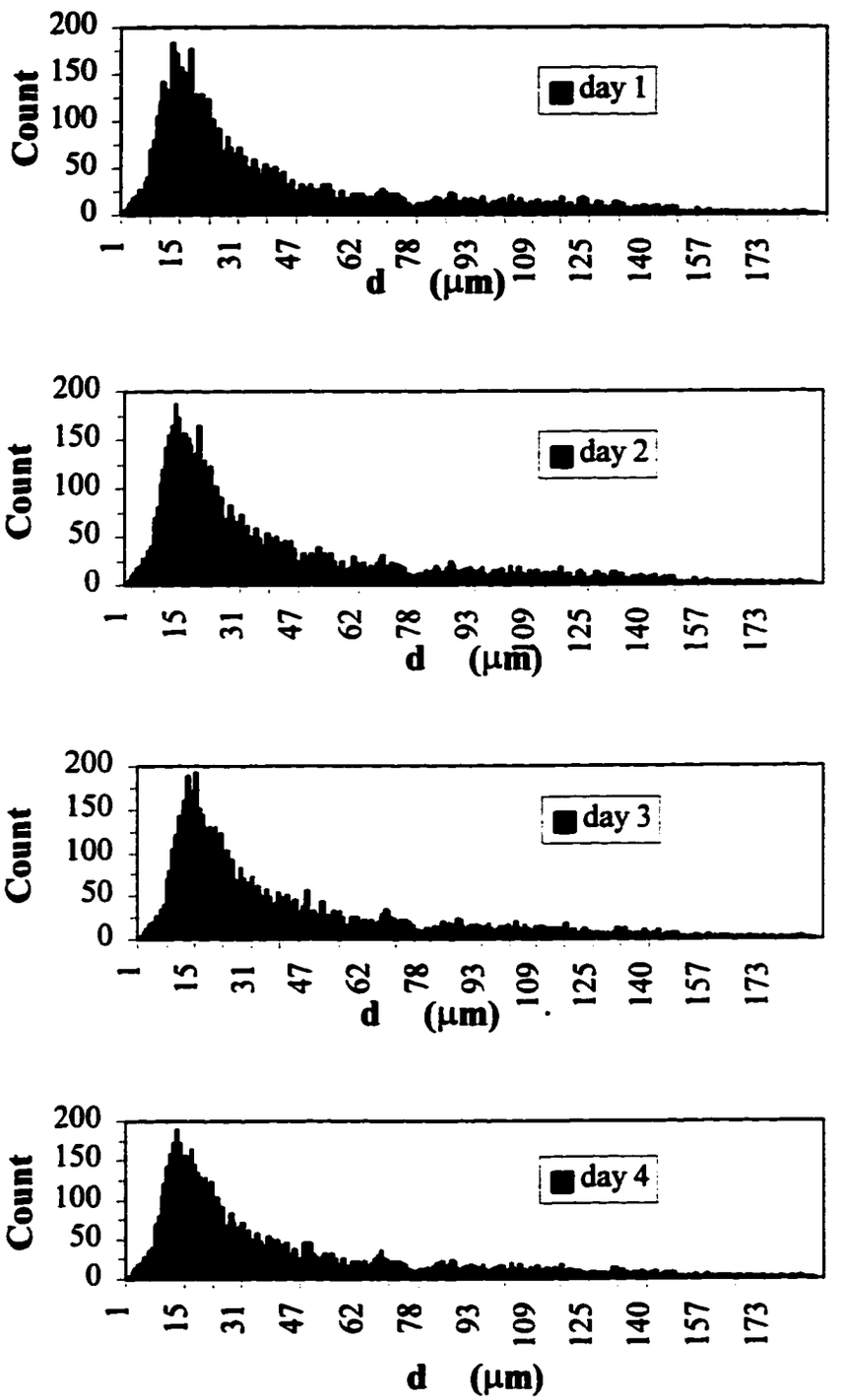

Figure 7-8 Equilibrium time for silicone oil/DIUF water dispersion.

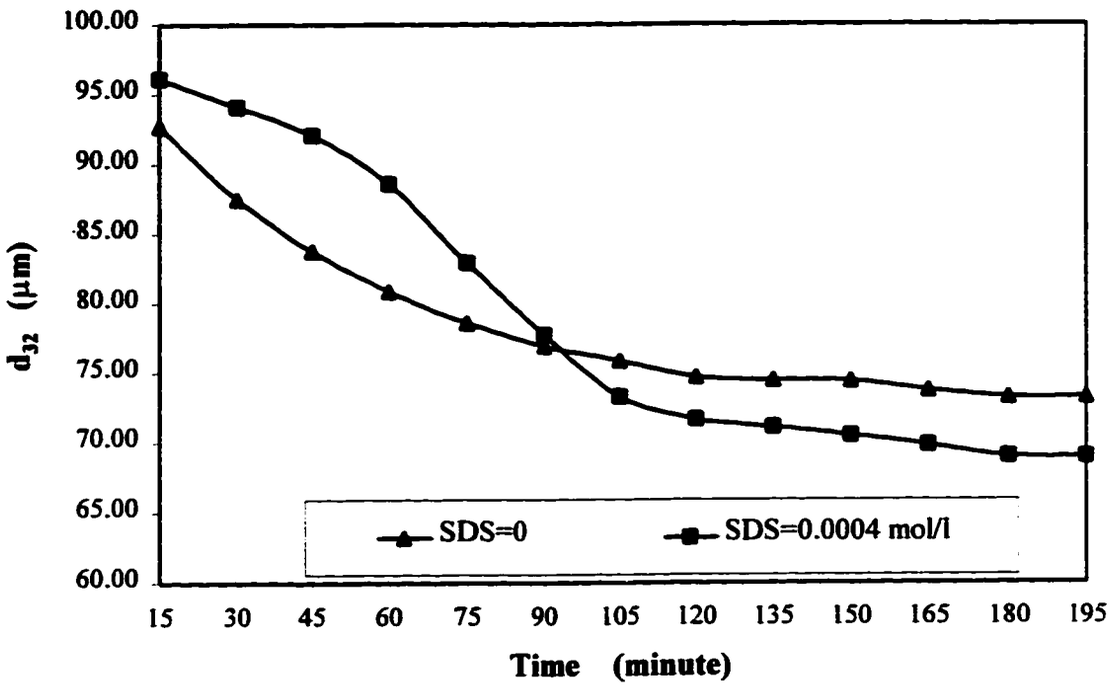

Figure 7-9 Step-change measurement: d_{32} vs time at varying N's.

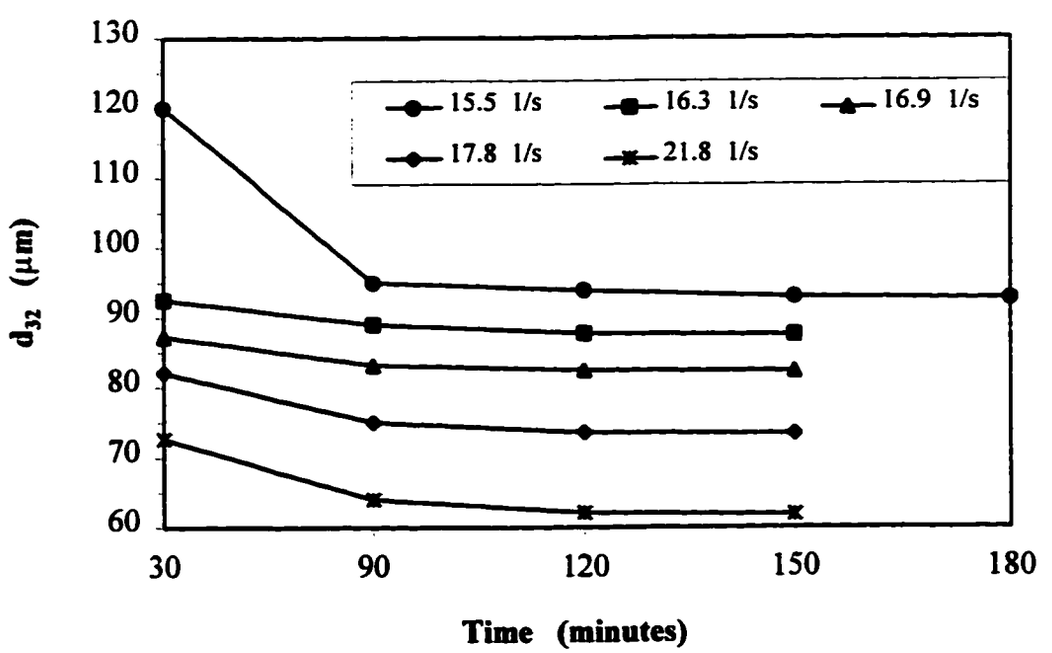

References

Bachalo, W.D. and Houser, M.J., 1984, Phase/Doppler spray analyzer for simultaneous measurements of drop size and velocity distributions. *Optical Eng.* **23**, 583-590.

Calabrese, R. V., Chang, T. P. K. and Dang, P. T., 1986, Drop breakup in turbulent stirred-tank contactors, Part I: Effect of dispersed-phase viscosity. *AIChE J.* **32**, 657-666.

Gerhart, P. M., Gross, R. J. and Hochstein, J. I., 1992, *Fundamentals of Fluid Mechanics*, 2nd edition, Addison-Wesley, New York.

Sankar, S.V. and Bachalo, W.D., 1991, Response characteristics of the phase Doppler particle analyzer for sizing spherical particles larger than the light wavelength. *Applied Optics* **30**, 1487-1496.

Sellens, R.W., 1989, A derivation of the phase Doppler measurement relations for an arbitrary geometry. *Expts Fluids* **8**, 165-168.

Van de Hulst, H.C., 1957, *Light scattering by small particles.* Wiley, New York.

Chapter 8

Characterization of Liquid-Liquid Dispersions

In **Chapter 7**, the validation of the PDPA used in this work was presented. In this chapter, the experimental results for drop size distributions are analyzed.

As stated in **Chapters 5** and **6**, in the experiments to investigate turbulence energy dissipation in impeller regions and the geometric effect on ε_{max}, a 50 mm layer of extra water layer was added on the tank cover to prevent entrained air bubbles forming vortices, in order to separate the effect of air bubbles from that of tank geometry on the flow field. The introduction of the dispersed phase prevents the use of the extra water layer on the tank cover because oil droplets may be driven up to the surface over the tank cover by the flow. Preliminary experiments were carried out to investigate the effect of the extra water layer on the flow field and to measure the mean and fluctuating velocities without the extra water layer to estimate the maximum turbulence energy dissipation rate. Preliminary experiments also included the investigation of the effect of oil addition on the flow field.

Four impellers (the A310, the HE3, the PBT and the RT) were used in drop size measurements with varying geometries. Drop sizes were measured over a wide range of rotational speeds using the validated PDPA. The emphasis was on the drop size distribution, on the minimum drop size in oil/water dispersions and on the Sauter mean diameter. Correlations of d_{32} with ND (equal tip speed), with $P/\rho V_T$ (equal power input per unit mass) and with ε_{max} (a new approach) were compared to determine which is the best.

First, the experimental procedure and preliminary experiments are presented.

8.1 Experimental Design

8.1.1 Impellers and Tank Geometry

Four impellers were used: the A310; the PBT; the HE3 and the RT. All the impellers followed the standard geometries described in section **6.2.2**. The seven tank geometries used for investigating the oil/water dispersion and the flow field are listed in **Table 8-1**. These seven cases were chosen based on the experimental results presented in **Chapter 6** (refer to **Figures 6-7** (a to d) and **Figures 6-10** (a to d)):

a) The number of baffles, N_f, has no effect on ε_{max}, so four baffles were used in all seven cases.

b) The impeller diameter has a significant effect on ε_{max} for the A310, the PBT and the RT, so two A310 diameters were used to investigate the effect of impeller diameter on Sauter mean drop size and drop size distribution. The reason for choosing the A310 to check the effect of impeller diameter on drop size distribution is that the A310 has a more stable flow field and entrains few air bubbles. Because fewer air bubbles are entrained, a larger impeller diameter can be used.

c) The effect of C/D and the interaction of D and C/D on ε_{max} is the strongest for the RT from the analysis in **Chapter 6**, so two ratios of C/D were used for the RT.

d) Since the effect of C/D and the interaction of D and C/D on ε_{max} is not significant for the A310, the relationship between the mean drop size and the flow field should be characterized in a similar way when C/D changes *if* ε_{max} dominates drop breakup process. Thus, two ratios of C/D were used for the A310. The other reason to use two C/D's for the A310 is because the A310 is an axial flow impeller, so the effect of C/D on d_{32} can be investigated using both one radial flow impeller (the RT) and one axial flow impeller (the A310).

8.1.2 Measurement Locations

Because of the non-homogeneous nature of the local turbulence energy dissipation rates in the tank, the mean drop size and drop size distribution may be non-homogeneous in the tank. Obtaining a reliable mean drop size to represent the dispersion depends on the choice of sampling positions. For this thesis, a traverse-average mean drop size was calculated by taking the arithmetic average of the *mean drop sizes* on all sampling points on *a traverse*. An overall mean drop size was calculated by taking the arithmetic average of the *mean drop sizes* on all sampling points for *a run*, i.e. over all traverses.

For the low holdup dispersion (ϕ=0.03%) used in this work, it was found that when the Reynolds number (=ND^2/ν) is larger than $5x10^4$ the traverse-averages are the same throughout the tank. **Table 8-2** lists the mean drop sizes measured over four radial traverses each having 5 sampling points - 2 located inside the impeller blades; one near the tip of the impeller and two beyond the impeller blades. The experimental conditions were: A310, D=0.350T, C/D=1, N=17.5 s^{-1}, Re=12.3×10^4. From **Table 8-2**, the mean drop sizes are different from point to point on a radial traverse (the maximum difference of mean drop sizes is 8.11 μm, but the maximum difference among the traverse-average mean drop sizes is only 2.49 μm (from the two numbers in bold in **Table 7-9**). One should note that the traverse-average value of d_{32} cannot be exactly calculated by dividing the sum of the 5 d_{32}'s by 5 because d_{32} is not an arithmetic average. However, the experimental results showed a similar shape of the drop size distribution at the 5 sampling points on each traverse when the equilibrium state was achieved. Calculation of d_{32} using the raw data (drop diameter vs number) for all 5 points on the traverse 2z/W=1.40 and the Eq. (3-17) returned a value of 76.32 for d_{32}. The relative error between these two methods was only 2%, so the arithmetic average of d_{32}'s was used for the rest of the data.

The sampling positions were chosen as follows: when Reynolds number was $<5x10^4$, four radial traverses were measured to evaluate the non-homogeneity of the drop size distribution in the tank: two of them were located above the impeller, one just below the impeller blades and one half-way from the tank bottom to the impeller blades; when

the Reynolds number was >$5x10^4$, only one radial traverse just below the impeller blades was measured since the dispersion is homogeneous above this limit. Each radial traverse had 5 or 6 sampling points. **Table 8-3** lists the locations all of the radial traverses, and the points on each traverse.

8.1.3 Experimental Parameters and Procedure

The PDPA parameters, experimental conditions and experimental procedures were presented in **Chapter 7**, and are summarized below.

Fluids and their properties at 20°C:*

continuous phase: deionized ultra-filtered water.

dispersed phase: silicone oil with a density of 998 kg/m^3 and a refractive index of 1.495; volume fraction of silicone oil, ϕ, 0.03% (vol. of oil/vol. of water).

interfacial tension: $45x10^{-3}$ kg/s^2.

* Temperature was kept at 20±1°C.

PDPA parameters:

1) voltage applied to photomultipliers=450 V.
2) collection angle=22.5°; sizing slope=1.186.
3) sample size=4000.
4) focal length of both the transmitter and the receiver=500 mm.
5) track 1 was used when $d_{32} > 50$ μm; track 3 was used when $d_{32} < 50$ μm.

rinse procedure:

1) tap water with detergent;
2) immersed in running tap water for more than 20 minutes;
3) nitric acid (0.001 mol/l);
4) immersed in running tap water for more than 20 minutes;
5) Deionized ultra-filtered water (at least three times).

Experimental procedure:

1) Fill inner cylindrical tank with DIUF water; then fill outer square tank with distilled water.

2) Set the lowest rotational speed (the first N). Add 3.24 ml silicone oil into the DIUF water below impeller blades using a pipette (precision=±0.01 ml) after the impeller has operated 20 minutes (the volume of the inner tank is 10.8 l, so the oil volume added is 3.24 ml for ϕ=0.03%).

3) Equilibration time for the first N is 180 minutes and 120 minutes for each following N.

4) Perform drop size measurements on four radial traverses (two above and two below the impeller) when $Re<5x10^4$ and on one radial traverse below the impeller when $Re>5x10^4$. Each traverse has 5 points for the A310 (2 inside impeller blades, one at impeller tip and two beyond impeller); each traverse has 6 sampling points for the HE3, the PBT and the RT (2 inside impeller blades, one at impeller tip and three beyond impeller).

5) Increase N step by step to the maximum value, when the entrained air bubbles strongly weaken the signal. Stop the impeller and thoroughly wash and rinse the mixing equipment for the next case.

8.2 Preliminary Experiments to Investigate the Effect of the Extra Water Layer and Oil Addition on the Flow Field

8.2.1 Effect of the Extra Water Layer on the Flow Field

As explained in **Chapter 5** and **Chapter 6**, the maximum turbulence energy dissipation rate can be estimated using Eq. (2-41) from the maximum RMS velocities in a flow field. The effect of geometry on the maximum turbulence energy dissipation rate was analyzed in **Chapter 6**. As stated in that chapter, in order to prevent other factors from interfering with the geometric effect on ε_{max}, a 50 mm of water (*extra water layer*)

was added on the top of tank cover to prevent entrained air bubbles forming vortices. Experiments with silicone oil cannot use the extra water layer because the oil droplets are driven up onto the tank cover through the hole for the impeller shaft. Thus, when no extra water layer is added, the maximum RMS velocities in flow fields without silicone oil need to be measured separately with the same tank geometries as cases with silicone oil. In order to compare the effects of tank geometry on ε_{max} with and without an extra water layer, a factorial design was used with two D's and two C/D's for the four impellers. Since the number of baffles has no significant effect on ε_{max}, the number of baffles was not changed and four baffles were used throughout. The experimental results and tank geometries are shown in **Table 8-4**. Comparing the data in **Table 8-4** with the results listed in **Tables 6-1** to **6-4** where the extra water layer was used shows that when no extra water layer is used the ε_{max}'s decrease by about 10%, but the effect of tank geometry on ε_{max} shows no significant change. **Figure 8-1 (a and b)** compares the typical experimental results for RMS velocities with and without an extra water layer and without an extra water layer when no silicone oil is present. The entrained air bubbles damp the turbulence intensity, but do not significantly change the behavior of the flow field close to the impeller.

8.2.2 Effect of Oil Addition on the Flow Field

As discussed in **Chapter 3**, drop breakup in liquid-liquid dispersions may occur by two main mechanisms, namely ligament stretching and turbulent fragmentation. Ligament stretching breakup dominates when the dispersed phase is viscous and/or the Reynolds number is low; while turbulent fragmentation dominates when the viscosity of the dispersed phase is low and/or the Reynolds number is very high. For a less viscous dispersed phase, the turbulent fragmentation of droplets is caused by turbulent pressure fluctuations, often estimated using $\rho_c\overline{V^2(d)}$. Note that $\rho_c\overline{V^2(d)}$ is the *external* or *deforming* force in a continuous phase experienced by a drop with a diameter of d. If the size and the velocity of the *drop* are measured simultaneously, the drop velocity may not represent the velocity of the continuous phase as experienced by the drop and thus could

not be used to express the turbulent pressure fluctuations. Thus it is necessary to measure the velocity of the continuous phase and the drop diameter separately. The validity of this method and the possibility of relating the drop size to the separately measured flow relies on the assumption that the dispersed phase has a very low volume fraction. In this case, introduction of the dispersed phase creates a negligible difference in the flow field and because the drops are small, they closely follow fluctuations in the flow. In this work, the volume fraction of the dispersed phase is 0.03%. Both the flow without the dispersed phase (water velocity) and with the dispersed phase (drop velocity) were measured without the extra water layer. Comparison of the RMS velocities between the two cases shows that 0.03% (vol.) of silicone oil has a negligible effect on the flow field and that the oil droplets closely follow the water flow. **Figure 8-2** (**a** and **b**) shows typical results. However, since $\varepsilon \propto v^3$, the error in the RMS velocity is cubed when ε is estimated, so the RMS velocities were measured separately with no extra water layer. The experimental results are listed in **Table 8-4**.

8.3 Drop Size Distributions

The mean drop size can not fully characterize a dispersion because the same Sauter mean drop diameter can be obtained for dispersions with different drop size distributions. To describe a dispersion, both the mean drop size and the drop size distribution are needed.

8.3.1 Drop Size Distributions Proposed by Previous researchers

A lot of work has been done to characterize the drop size distributions of various dispersions, and several functions have been proposed. There are two main types of drop size distribution, normal and log-normal. Because of improving methods of drop size measurement and coverage of wider operational conditions of more dispersion systems, several other distributions have been suggested.

a) *Normal Distribution*

The volumetric probability distribution function can be represented by a normal distribution function. Chen and Middleman (1967) used a normal distribution function normalized with respect to d_{32} to represent the drop size distribution of a xylene/water dispersion agitated by Rushton turbines (Eq. (3-21)). They found that the drop size distribution *depends only upon* d_{32}.

Brown and Pitt (1972) used an equation similar to Eq.(3-21) to represent the drop size distribution of a kerosene/water dispersion agitated by Rushton turbines. By a detailed examination, they noticed that a bimodal form of the distribution exists. They found that *no effect of impeller speed on the distribution was evident.* Photographic measurements were used in their work. They assumed that no coalescence existed in the kerosene/water dispersion even with a volume fraction of the dispersed phase as high 0.20, so pictures were taken near the bottom of the tank. Because of the sampling location, large drops were truncated and no data beyond 1.7 times the standard deviation ($1.7\sigma(d/d_{32})$) were obtained.

Nishikawa et al. (1991) used a combination of normal distributions to express both the number density distribution and the volumetric probability distribution in order to fit a whole range of drop sizes. They found that a combination of three normal distributions gives a good fit for the volumetric drop size distribution and that a combination of two normal distributions can fit the number density distribution.

b) *Log-normal Distribution*

Several investigators found that the number probability distribution function of drops is a log-normal distribution (Keey and Glen, 1969, Nagata and Yamaguchi, 1960, Yamaguchi et al., 1963, cited from Tavlarides and Stamatoudis, 1981):

$$f_n(d) = \frac{1}{\sqrt{2\pi}\log\sigma}\exp\left[-\frac{(\log d - \log d_{10})^2}{2(\log\sigma)^2}\right]$$

where d_{10} is the arithmetic mean drop diameter, σ is the standard deviation.

Parthasarathy and Ahmad (1994) used a sampling/photography method to investigate the bubble size distribution of an air/water dispersion in a gas-sparged tank agitated by a Rushton turbine. 50 ppm of methylisobutyl-carbino was added to prevent coalescence. They found that with increasing agitation, the drop size distribution changes from unimodal to bimodal, and again to unimodal, as the bubble population moves progressively down the size scale. They summed two log-normal distributions, each with its distinct statistical parameters, to deal with the bimodal distribution.

c) *Other Distributions*

Several other distributions have been proposed, such as the Erlang distribution, the Weibull distribution, and the Gamma distribution for bubble size distribution, but they are less common in liquid-liquid dispersions. The distribution given by Schwarz-Bezemer was found to fit the drop size distribution very well (Sprow, 1967a):

$$\ln V\% = \ln 100 + d_c / d_{max} - d_c / d$$

where V% is the cumulative volume percent of drops below diameter d, d_c is a characteristic diameter related to the maximum of the distribution function, and d_{max} is the largest drop diameter in the dispersion. Another distribution function worth mentioning is that proposed by Gal-Or and Hoelscher (1966, cited from Tavlarides and Stamatoudis, 1981) which directly relates drop size distribution with the rotational speed and holdup fraction

$$f(d) = 4\left(\frac{\alpha^2}{\pi}\right)^{1/2} d^2 \exp(-\alpha d^2)$$

in which

$$\alpha = (16\pi^{1/2} N / 3\phi)^{2/3} > 0$$

Many investigators have found that a single distribution function is not able to describe the whole range of drop sizes, especially the small or large drop sizes, so the current trend is to use a combination of distribution functions of the same form to express

the drop size distribution (see Nishikawa et al. (1991) and Parthasarathy and Ahmad (1994)).

8.3.2 Changes in the Drop Size Distribution with Increasing Rotational Speed

In some industrial processes (e.g. processes involving selective chemical reactions or separations) a well defined size distribution is ideal for achieving a better process result. Knowledge of drop size distributions as they evolve with turbulence intensity and/or rotational speed is important to understand the fundamentals of mixing as they relate to industrial applications.

In this work efforts were made to measure drop sizes with varying impellers and with as wide a range of operational conditions as possible to cover a broad range of possible evolution patterns. The experimental results: changes on the drop size distribution with changing rotational speed, are shown in **Figure 8-3** and in **Appendix-1**. In general, four distributions appear in the evolution of the drop size distribution with rotational speeds for the four impellers studied:

a) At low rotational speeds, the drop size distribution has a *high peak* on the low diameter side and a long tail on large diameter side. This distribution was named a *long tail distribution*. The distribution on the lower diameter side can be simply represented by a normal distribution.

b) As N increases, the large drops are broken by the enhanced flow and a second peak appears in the middle of the distribution. This distribution was named a *double peak distribution*. The double peak distribution can be represented by superimposing two normal distributions with their unique mean drop sizes and standard deviations.

c) As N increases further, the distribution on the large diameter side continuously shrinks and the whole distribution changes back to mono-modal, but with a wider and skewed peak. This distribution was named a *skew distribution*. A skew distribution can not be simply represented by a single normal distribution. A skew distribution such as a Poisson distribution, an exponential distribution, a Γ–distribution, or two superimposed normal distributions need to be used.

d) Finally, N reaches a value at which both the small diameter side and the large diameter side shrink and the distribution becomes more symmetric. This distribution was named a *skew-normal distribution* to distinguish it as a distribution close to a normal distribution. A normal distribution can represent this mono-modal distribution. The symmetry of the distribution is due to the coalescence of small droplets and breakup of large drops. Both of these occur due to increased energy in the flow.

By checking the evolution of drop size distribution with N, a more symmetric size distribution can be expected when N is larger than 22.7 s^{-1}.

Although all four distributions were not present in all seven cases studied, the trends described were followed in each case. The only exception is the RT with C/D=1, for which no clear second peak forms when N increases, which may be because it has a narrower drop size distribution and the newly-formed drops (from continuous breakup of large drops due to the enhanced flow as N increases) have diameters in the range of the first peak.

A quantitative description of the evolution of drop size distribution with rotational speed, based on the fitting parameters for two normal distributions would provide no new physical insights: however, it would be useful to have a single descriptive variable which tracks the drop size distribution. Several possibilities were examined.

Following d_{10} as it changes with N shows the evolution of the drop size distributions. Thus, instead of deriving distribution functions for all impellers and rotational speeds, the arithmetic mean diameters and their deviations at different rotational speeds for all seven cases were plotted to show the evolution of the drop size distributions. The case - A310 with D=0.350T and C/D=1 (which clearly shows the four distributions) is analyzed in detail.

The arithmetic mean drop size was calculated using Eq.(3-14):

$$d_{10} = \frac{\sum_{min.d}^{max.d} d_i n_i}{\sum_{min.d}^{max.d} n_i} \qquad (3\text{-}14)$$

and the standard deviation $\sigma(d)$ was calculated using:

$$\sigma(d) = \sqrt{\frac{\sum_{min.d}^{max.d} (d_i - d_{10})^2 n_i}{\sum_{min.d}^{max.d} n_i - 1}} \qquad (8\text{-}1)$$

The area mean and volume mean diameters, d_{20} and d_{30} were defined in **Chapter 3**. The values of d_{10}, $\sigma(d)$, d_{20} and d_{30} with N, Re, $P/\rho V_T$ and ε_{max} are listed in **Table 8-5**. d_{10}, $\sigma(d)$, d_{20} and d_{30} are all *overall* mean values (defined in section **8.1.2**). From **Table 8-5**, $\sigma(d)$ shows a consistent decrease with an increase in rotational speed. The volume mean diameter, d_{30}, also shows a consistent decrease with the increase in rotational speed, excepting the case of the A310 with D=0.350T and C/D=1. The arithmetic and area means show a similar pattern of change with rotational speed, but d_{10} tracks changes in the drop size distribution more closely. Because d_{32} can characterize the drop size changes with rotational speed as effectively as d_{30} and is analyzed in detail in section **8.5**, d_{10} and $\sigma(d)$ were chosen to characterize the evolution of the drop size distribution with rotational speed.

Figures 8-4 (**a** to **g**) are the plots of d_{10} and $\sigma(d)$ versus rotational speed for all seven cases. From **Figures 8-4** (**a** to **g**), it is found that the standard deviation decreases consistently with increasing N because the drop size distribution become more symmetric and narrower as N increases; the arithmetic mean drop size showed no consistent behavior with increasing N because of the appearance of the second peak and/or the movement of peak towards the large diameter side.

For the A310 with D=0.350T at both C/D=1 and 1/2 (**Figures 8-4a** and **b**), the arithmetic mean drop size first increases with increasing N as the second peak is formed due to the breakup of large drops; then the arithmetic mean drop size decreases as N increases because of the continuous breakup of large drops; finally, when N reaches a value at which coalescence becomes significant the arithmetic mean drop size increases with increasing N. For the A310 with D=0.550T (**Figure 8-4c**), the range of rotational speeds is limited by air bubble entrainment, so the highest value of N is 10.5 s^{-1} - at

which the ε_{max} was only 18.1 m^2/s^3. In general however, the arithmetic mean drop size decreases with increasing N in the range of N measured.

For the HE3 (**Figure 8-4d**) and the PBT (**Figure 8-4e**), the arithmetic mean drop size shows similar trends to the A310 as N increases. That is: an increase in d_{10} with the formation of the second peak, a decrease with the continuous breakup of large drops, and an increase with the coalescence of small droplets. When N increases further, the arithmetic mean drop size decreases again; this effect may be caused by further breakup of large drops at high ε_{max}'s.

For the RT, no clear second peak is found in the range of N investigated. When C/D=1 the drop size distribution is characterized by quick movement of the peak towards the larger diameter and quick shrinkage of the largest drops, so the arithmetic mean drop size *increases* with increasing N. When C/D=1/2 the arithmetic mean drop size decreases slowly with increasing N. Note that ε_{max} is much smaller for large for C/D=1/2 than for C/D=1. **Figures 8-4f** and **g** show the plot of d_{10} and $\sigma(d)$ vs N for the RT with C/D=1 and C/D=1/2, respectively.

From **Figures 8-4a** through **g**, it is clear that the arithmetic mean diameter can not consistently be used as a characteristic mean to depict the relationship between the mean drop size and the turbulent flow; however, the changes in d_{10} with N can be clearly explained if the evolution of the drop size distribution is also considered.

From the experimental results and analysis above, it is clear that the drop size distribution changes with the rotational speed. The evolution of the drop size distribution with N is expected to become more complex when high volume fractions of the dispersed phase are used, due to increased coalescence. From this work, we can conclude that some distribution functions proposed by previous investigators may only represent the dispersion at the rotational speed range they chose. The evolution of the drop size distribution with rotational speed investigated in this work illustrates why so many different drop size distributions have been reported in the literature.

8.3.3 Characterization of the Drop Size Distribution Using Two Superimposed Normal Distributions

In the section above, the evolution of the drop size distribution with rotational speed was analyzed qualitatively. Four types of distribution were presented. Although a general description of the distribution was not attempted, fitting the experimental distribution using distribution functions is sometimes useful for predicting the drop size distribution in varying flow conditions. In this section, the experimental distributions are fit with distribution functions.

It is clear from the seven cases investigated that a single distribution function cannot characterize the evolution of the drop size distribution with N. The long tail distribution can be represented by a normal distribution on the small diameter side and an equal-probability distribution on the large diameter side; the double peak distribution can be represented by superimposing two normal distributions; the skew distribution is a kind of distribution which should be represented either by a Poisson distribution, a χ^2 distribution, or a Γ–distribution. Alternately, the drop size distribution (from the double peak distribution to the skew distribution and finally to the skew-normal distribution) may be represented by combining two normal distributions. No further explanation is needed for the double peak distribution and the skew-normal distribution. For the skew distribution, one can superimpose two normal distributions with overlapping two sub-ranges of diameter - a *main* normal distribution on low diameter side and a secondary normal distribution on large diameter side to characterize skewness. When N is large, the two predicted normal distributions become one.

The following explains how two superimposed normal distributions are used to fit the double peak distribution, the skew distribution, and finally the skew-normal distribution. The normal number probability density is given by the following equation:

$$P_n(d_i) = \frac{n_i}{\sum_{\min.d}^{\max.d} n_i} \frac{1}{\Delta d_i} = \frac{1}{\sigma\sqrt{2\pi}} \exp[-\frac{1}{2\sigma^2}(d_i - d_{10})^2] \qquad (8\text{-}2)$$

and the cumulative number probability density is calculated by:

$$F_n(d_i) = \sum_{\text{min.d}}^{d_i} p_n(d_i) \qquad (8\text{-}3)$$

Double Peak Distribution

When N=15.5 s^{-1} in **Figure 8-3**, the second peak appears clearly in the drop size distribution. Two normal distributions can represent this distribution well. The range of drop diameters is divided into two sub-ranges. The drop size distribution in each of the two sub-ranges is represented by Eq. (8-2) with different d_{10}'s and σ's. d_{10} and σ are in units of μm. **Figure 8-5a** shows the comparison of experimental drop size distribution (plotted as $F_n(d)$ vs d) and the distribution fit using two superimposed normal distributions with two sets of (d_{10}, σ): (27.4, 13.1) and (88.3, 25.0). Two line segments represent the predicted cumulative density for each normal distribution. The fit distribution agrees well with the experimental distribution.

Skew Distribution

As large drops break further with increasing N, the second peak in the drop size distribution gradually disappears. A skewed distribution forms with an increase of mid-size diameter drops. This is shown for N=18.8 s^{-1} in the case of A310 with D=0.350T and C/D=1. **Figure 8-5b** shows the comparison of the experimental drop size distribution (plotted as $F_n(d)$ vs d) and the distribution fit using two superimposed normal distributions with two sets of (d_{10}, σ): (23.4, 10.4) and (65.3, 18.7). The distribution is again in good agreement with the experimental distribution.

Skew-Normal Distribution

As N increases, the drop size distribution becomes more symmetric and finally a single nearly normal distribution appears. This is shown for N=22.7 s^{-1} in the case of A310 with D=0.350T and C/D=1. This distribution can be represented by a single normal distribution, but the use of two superimposed normal distributions can better

represent the experimental distribution. **Figure 8-5c** shows the comparison of the experimental drop size distribution (plotted as $F_n(d)$ vs d) and the distribution fit using two superimposed normal distributions with two sets of (d_{10}, σ): (21.7, 8.39) and (59.3, 15.7). The predicted distribution is in good agreement with the experimental distribution.

If measurements of the drop size distribution were taken at small intervals of N in the range from the double peak distribution (after the long tail distribution) to the skew-normal distribution, a relationship between the rotational speed and the parameters (d_{10}, σ), as well as the division of the two diameter sub-ranges could be obtained. This approach may result in an unique distribution function which generates the experimental distribution from the double peak distribution. The data collected here are not complete enough to generate a model.

8.3.4 Conclusions about the Drop Size Distribution

Four types of drop size distribution were found in the evolution of the drop size distribution with N: the long tail distribution; the double peak distribution; the skew distribution and the skew-normal distribution. The arithmetic mean diameter (d_{10}) can not be used as a characteristic mean to depict the relationship between the mean drop size and the turbulent flow as all the impellers are considered, but its changes with N track the evolution of the drop size distribution with N for each impeller. Excepting the long tail distribution, the drop size distributions can be fit using two normal distributions with two different diameter sub-ranges. It may be possible to derive an unique distribution function to represent the drop size distribution from the double peak distribution using the parameters (d_{10}, $\sigma(d)$) and the break between the two distributions as functions of N.

8.4 Minimum Drop Size

8.4.1 Kolmogoroff length scale

Kolmogoroff used dimensional analysis and derived a length scale η ($=(\nu^3/\varepsilon)^{1/4}$). This Kolmogoroff length scale has frequently been used as an estimate of the minimum drop size for dispersions in agitated tanks. The relationship between η and the turbulence energy dissipation rate ε described by Kolmogoroff's equation is shown in **Figure 8-6**. When ε is low, η decreases rapidly with increasing ε. For example, when ε increases from 10 to 25 m^2/s^3, η decreases by 3.64 μm; but when ε increases from 400 to 1000 m^2/s^3, η decreases only 1.45 μm (taking water at 20 °C as the continuous phase). For the flow in an agitated tank, the reported values of the ratio $\varepsilon/\bar{\varepsilon}$ are of the magnitude of 100 m^2/s^3. The highest ratio of $\varepsilon/\bar{\varepsilon}$ reported by previous investigators is 270 (Cutter, 1966). Most reported values of $\varepsilon/\bar{\varepsilon}$ are smaller than 100 (Okamoto et al., 1981, Costes and Couderc, 1988, Wu and Patterson, 1989(see **Chapter 2**), this work(see **Chapter 5**)). The value of $\bar{\varepsilon}$ for the flow in an agitated tank is ~1 m^2/s^3. The maximum possible value of ε_{max} is 1000 m^2/s^3. Even for ε_{max}=1000 m^2/s^3, η can not be smaller than 5 μm if Kolmogoroff's equation holds. The experimental drop size distributions consistently include drops much smaller than this.

Chen and Middleman (1967) once predicted that "*under conditions of extremely high energy input it is possible to produce drops smaller than* η. *Such drops would be in a dynamic regime known as the viscous subrange.*" The turbulence in agitated tanks, however, shows behavior characteristic of the *inertial subrange* (Cutter, 1966, Kim and Manning, 1964, Komasawa et al., 1974, Nishikawa et al., 1976, Gunkel and Weber, 1975, Kresta and Wood, 1991, Hinze, 1987), not the viscous subrange. Thus the power input cannot be considered *extremely* high.

Unlike the maximum stable drop size in a dispersion, which has been investigated extensively, no published articles question the suitability of the Kolmogoroff length scale for dispersions with varying turbulence energy dissipation levels. There are four possible reasons for this scarcity:

a) the local turbulence energy dissipation rate ε can not be determined simultaneously with drop size measurement when traditional measuring methods, such as sampling/photography and drop encapsulation are used.

b) lack of a suitable measuring method to detect droplets smaller than 10 μm. In a recent paper of Pacek and Nienow (1995), the video and capillary technique are compared. They found that the video technique allows droplets from 25 μm upwards to be measured and that both the minimum and maximum drop diameters measured with the capillary technique are limited by the design of the capillary (funnel diameter and tube diameter and length).

c) strong coalescence coexists in dispersions (the minimum volume fraction of the dispersed phase used by previous investigators is 0.057% (Berkman and Calabrese, 1988, see **Table 7-2**).

d) the non-arbitrary sampling always over-estimates drop size (e.g. sampling near tank wall in in-situ photography method; smallest droplets undetected by capillary tube; difficult to access the strongest turbulent energy dissipation region using sampling/photography method).

Contradicting the scarcity of the investigation of the minimum drop size in dispersions, the relationship between the minimum drop size and the agitation in mixing equipment is very important to some industrial processes. This research on the minimum drop size in an oil/water dispersion is based on requirements at Syncrude Canada Inc.. In the bitumen extraction process, fine water droplets of 1 μm diameter are found after the separation of bitumen from oil sand in a tumbler. The fine water droplets contain dissolved minerals which are harmful to the following processes. Knowing the relationship between the minimum drop size and turbulent flow may be helpful to efforts to prevent generation of the fine water droplets.

As stated in **Chapter 7**, with this PDPA, the minimum drop diameter measured can be as small as 0.5 μm if a proper diameter range and settings are chosen. Thus the PDPA makes it possible to measure the minimum drop sizes in dispersions agitated by different impellers with varying tank geometries. This is the first effort ever made to

experimentally test the suitability of the Kolmogoroff length scale as an estimate of the minimum drop size in liquid-liquid dispersions in agitated tanks.

8.4.2 Experimental Results for the Minimum Drop Size

The minimum drop sizes are presented in terms of:

a) *number probability density, $P(d_i)$*

$$P_n(d_i) = \frac{n_i}{\sum_{min.d}^{max.d} n_i} \frac{1}{\Delta d}$$

where n_i is the number of droplets with diameters between d_i and d_{i+1}; and

b) *Cumulative number probability density, $F_n(d_i)$*

$$F_n(d_i) = \sum_{min.d}^{d_i} P_n(d_i)$$

When $d_i=\eta$, $F_n(d_i)$ is expressed as $F(\eta)$ which determines the number percentage of drops with diameters $\leq\eta$. If the Kolmogoroff length is the smallest drop size, $F(\eta)$ should be zero.

The experimental results which follow show that the minimum drop sizes are well below what Kolmogoroff's equation predicts. These smallest droplets are formed purely by *agitation*, not by other factors because no such droplets exist in DIUF water. **Figure 7-3b** shows that in 50 seconds, only 3 droplets smaller than 13 μm were measured in DIUF water. When silicone oil was dispersed in the DIUF water, 4000 drops were measured in 10 seconds. Effectively, all of the droplets smaller than η in the dispersion are oil drops created by the flow.

The experimental $F(\eta)$'s at different N's are listed in **Table 8-5**. The ε_{max}'s in **Table 8-5** are calculated using $\varepsilon_{max,2} = \varepsilon_{max,1} \cdot (N_2/N_1)^3$. N_1 and $\varepsilon_{max,1}$ are taken from **Table 8-4**. Each $F(\eta)$ at a rotational speed in **Table 8-5** was from one of the sampling points in each case, not a traverse-average mean value or overall mean value. The measurements were taken inside the impeller blades ($2r/D<1$) to avoid selecting the region where ε_{max}

appears since $F(\eta)$ may be larger in the region which contains ε_{max}. In fact, the dispersion is homogeneous in the tank when $Re>5x10^4$ (see section **8.1.2**).

The measured drop size distributions show that in some cases as many as 35% of drops have diameters smaller than η, particularly when N is low. With an increase in N, $F(\eta)$ decreases for six cases out of the seven listed in **Table 8-1**. One case (A310 with D=0.350T and C/D=1) shows a *jump* in $F(\eta)$ after a consistent decrease with N. The higher number percentage of drops with diameters $<\eta$ when N is low is an indication that drop breakup in this system may be mainly due to the turbulent fragmentation mechanism and that drop breakup dominates when N is low. Droplets smaller than η are created continuously by the turbulent fragmentation and can survive at low N's. Only 3 values of $F(\eta)$ are less than 1% (see numbers in bold and italic in **Table 8-5**). They are: the A310 with D=0.350T and C/D=1 at $N=20.7\ s^{-1}$; the PBT with D=T/4 and C/D=1 at $N=30.0\ s^{-1}$ and the RT with D=T/4 and C/D=1 at $N=20.3\ s^{-1}$. All three values of $F(\eta)$ less than 1% resulted from the highest N used. This means that even with a low volume fraction of dispersed phase, coalescence occurs when N is high.

Figure 8-7 shows the evolution of the cumulative number probability density as well as $F(\eta)$ for various rotational speeds for the PBT with D=T/4 at C/D=1 and 2r/D=0.30. The figures in **Appendix-B** show the evolution of the cumulative number probability density as well as $F(\eta)$ for various rotational speeds for the six other cases summarized in **Table 8-1**. The slope of the line on the low diameter side with increasing N as the peak of the drop size distributions moves to larger diameters, possibly due to a) enhanced flow and b) increased collision efficiency due to increased energies of collision.

There are two arguments for why the Kolmogoroff length scale does not predict the size of the smallest drops in dispersions in agitated tanks: a) the Kolmogoroff's equation is incorrect; b) ε_{max} is incorrect, c) Kolmogoroff's equation *does* predict the smallest drop which can be *broken*, but does *not* predict the smallest drops *resulting from* the breakup of mother drops into *multiple* smaller drops, The author of this thesis considers that argument (a) may be the real reason why Kolmogoroff length fails to predict minimum drop sizes in dispersions in agitated tanks. The reason is simple: using

Kolmogoroff's equation to obtain 1 μm drops requires that the ε_{max}, or the ratio of $\varepsilon/\bar{\varepsilon}$, is of a magnitude of 10^6, which is unimaginable for the flow in agitated tanks.

From the data presented above, it is reasonable to question the applicability of Kolmogoroff length as an estimation of minimum drop size in dispersions in agitated tanks, especially when no coalescence exists. It is also clear that the Kolmogoroff length as an estimate of the *length scale* of drops in agitated tanks is in agreement with the data obtained in this work: the Kolmogoroff length is of a magnitude of 10 μm (6 to 20 μm using the estimated ε_{max}'s in **Table 8-4**). The diameters for most droplets measured are also of a magnitude of 10 μm.

8.4.3 Correlation of F(η) with Flow Field and with Drop Size Distribution

From the data listed in **Table 8-5**, **Figure 8-7**, and the analysis above, it is clear that the minimum drop size (F(η)) is related to the flow field and to the drop size distribution. At low rotational speeds, F(η) is large, corresponding to the distribution with a peak on small diameter side. When N increases, F(η) decreases as the peak moves to larger diameters.

Turbulent fragmentation appears to dominate drop breakup when N is low since a lot of droplets are formed with diameters smaller than the Kolmogoroff length; coalescence coexists with drop breakup when N is high since the drop size distribution shrinks in the low diameter side. Both the turbulent fragmentation and the coalescence produced by the enhanced flow are related to the turbulence energy dissipation, so F(η) should be related to ε_{max}. Plots of F(η) versus N, ND, Re, ε_{max} and $P/\rho V_T$ (**Figures 8-8**) show that ε_{max} gives the closest correlation with F(η). Excepting the plot of F(η) vs ε_{max}, the data are more scattered when all seven cases and four impellers are considered together. Although $P/\rho V_T$ shows nearly as good a correlation with F(η) as ε_{max} (based on the R-square value), the data for the A310 with D=0.550T fall off the curve in **Figure 8-8e**, while only single points are bad in **Figure 8-8d**. When each of the seven cases is considered separately, F(η) shows a somewhat defined relationship with any of the

variables considered. Only when a wide range of D/T, C/D, ε_{max} and impeller geometries are combined does the underlying physics begin to emerge.

An effort was also made to correlate $F(\eta)$ to the drop size. **Figures 8-9 (a to c)** are the plots of $F(\eta)$ with d_{10}, d_{30} and d_{32}, respectively. The d_{32}'s at different N's for each of the seven cases are listed in **Table 8-9**. From **Figures 8-9 (a to c)**, the data on each plot are scattered. No clear relationship between $F(\eta)$ and d_{10} or d_{30} or d_{32} can be drawn when the seven cases of the four impellers are considered together. This is because $F(\eta)$ is related to the whole distribution of the drop size, not just the drops with small diameters or large diameters, whereas d_{10}, d_{30} and d_{32} are mean diameters which over-estimate either drops with small diameters or drops with large diameters. Thus, $F(\eta)$ is replotted with d_{30}/d_{10} and with d_{32}/d_{10}. **Figures 8-10 (a and b)** are the plots of $F(\eta)$ vs d_{30}/d_{10} and $F(\eta)$ vs d_{32}/d_{10}, respectively. The data on both figures are included in a fan-shaped region which can be closed by two dashed straight lines, and the intercepts of the two lines on each abscissa are crossed at a point on the abscissa. If all the data of $F(\eta)$ vs d_{30}/d_{10} or $F(\eta)$ vs d_{32}/d_{10} are correlated using a straight line, two equations are obtained:

$$F(\eta)=41.6(d_{30}/d_{10})-48.7$$

$$F(\eta)=14.8(d_{32}/d_{10})-17.6 \qquad (8\text{-}4)$$

The two R-square values are 0.672 and 0.632, respectively. If $F(\eta)$) in each equation is set to zero, the intercept on each abscissa is obtained which turns out 1.19 for $F(\eta)$ vs d_{30}/d_{10} and 1.17 for $F(\eta)$ vs d_{32}/d_{10}. This means that if $d_{30}/d_{10}\leq 1.19$ or $d_{32}/d_{10}\leq 1.17$, $F(\eta)=0$ ($F(\eta)$ cannot be less than 0), and the minimum drop size is estimated by Kolmogoroff length scale. It is not clear whether these two values (1.19 and 1.17) are generally true for different liquid-liquid dispersions.

8.4.4 Conclusions about the Minimum Drop Size

A significant number of drops smaller than the Kolmogoroff length scale were measured in the seven tank geometries investigated. The Kolmogoroff length scale is generally suitable as an estimate of the order of *magnitude* of the mean drop size in the

dispersion in an agitated tank, but it cannot be used as an estimate of the *minimum drop size* in the dispersion.

When N is low, the number percentage of drops smaller than the Kolmogoroff length scale ($F(\eta)$), is high due to drop breakup dominating in the dispersion; $F(\eta)$ decreases with an increase in N since coalescence increases with an increase in N. $F(\eta)$ approaches zero only at very high N.

$F(\eta)$ is clearly related to ε_{max}. When *all* of the data are considered at once, the correlation $F(\eta)=-7.77\ln(\varepsilon_{max})+46.1$ is obtained with an R-square value of 0.665. $F(\eta)$ is also clearly related to the drop size distribution. When $d_{30}/d_{10}\leq 1.19$, the minimum drop size can be estimated using the Kolmogoroff length scale.

Returning to the Syncrude problem, increasing the coalescence of water droplets may be useful for removing the fine water droplets. To achieve this, some chemical processes may be better than the physical one (high rotational speeds and increased ε_{max}) since the latter is not easily obtained for such a large process.

8.5 Sauter Mean Diameter

The drop size distributions and minimum drop sizes were presented and analyzed above. Although it was found that the drop size distribution changed with rotational speed; the arithmetic and area mean drop sizes showed no consistent pattern with an increase of rotational speed because of the movement of the drop size distribution towards the large diameter side and possible coalescence at high rotational speeds (high turbulence energy dissipation rates); however, the Sauter mean diameter decreases consistently as the rotational speed increases.

Many investigators have related the Sauter mean diameter to the physical properties of fluids in dispersions and/or the turbulence in agitated tanks. Diverse correlations have been presented. Some of them were summarized in **Table 3-1**, in chronological order. In these correlations, two main scale-up principles are recommended: one is based on constant power input per unit mass, $P/\rho V_T$, which is proportional to N^3D^2 *when the ratio of D/T is kept the same for the same impeller*; the

other is based on constant tip speed of an impeller (ND). One of the objectives of this work was to compare these two scale-up principles with a new scale-up approach: constant maximum turbulence energy dissipation rate, ε_{max}, and to test their compatibility under various operating conditions and tank geometries by measuring drop sizes over a wider range of rotational speeds and using four different impellers and various tank geometries, and possibly to propose a new scale-up rule.

Since the relationship between the Sauter mean diameter and the physical properties of fluids in dispersions has been investigated extensively and verified by many researchers, only one dispersed phase was studied in this work. The relationship between the Sauter mean diameter and the turbulent flow was examined in detail. More general fluid dynamic considerations for scaling up dispersions in agitated tanks are the result.

8.5.1 Maximum Stable Drop Diameter in the Turbulent Flow in Agitated Tanks

The maximum stable drop diameter, d_{max} is determined by the balance between the external deforming forces and the restoring forces experienced by droplets. The main restoring force on a droplet is the interfacial tension, σ/d. The dynamic pressure due to the deformation of the droplet defined by Eq. (3-1) can be included in the interfacial tension. As for the viscous stresses, which are of the order of $\mu_d \cdot (\tau/\rho_d)^{-1/2}/d$ (Hinze, 1955), they can be neglected when μ_d is not extremely high. The main external deforming force is determined by the intensity of the turbulence in agitated tanks. There are three possible cases:

a) Mean velocity gradients dominate drop breakup. In this case, drop breakup happens mainly around the edges of the impeller blades. This is especially true when the rotational speed is very low. The deforming force in this case is of magnitude $\mu_c \cdot N$.

b) Macroscale eddies dominate drop breakup when d is of magnitude D. In this case the deforming force is of magnitude $\rho_c \cdot \overline{V}^2$ with $\overline{V}^2 \propto (ND)^2$, so the deforming force is estimated by $\rho_c \cdot (ND)^2$.

c) Turbulent pressure fluctuations dominate drop breakup when the turbulence is in the inertial subrange, which is the case most frequently occurred in agitated tanks. The

deforming force is of magnitude $\rho_c \cdot \overline{V^2(d)}$ with $\overline{V^2(d)} \propto (\varepsilon d)^{2/3}$ and $\varepsilon \propto N^3 D^2$, so the deforming force can be estimated by $\rho_c \cdot N^2 D^{4/3} d^{2/3}$.

The maximum stable drop diameter for the three cases above is determined by the balance between the deforming force and the interfacial tension. By replacing d with d_{max} and taking the ratio of the deforming forces to the interfacial tension, the following expressions of d_{max} are obtained (Blount and Calabrese, 1995):

i) Mean velocity gradients vs interfacial tension

$$\frac{d_{max}}{D} \propto \frac{\sigma}{\mu_c}(ND)^{-1} \tag{8-5}$$

ii) Macroscale eddies vs interfacial tension

$$\frac{d_{max}}{D} \propto \frac{\sigma}{\rho_c} N^{-2} D^{-3} = (W_{e,T})^{-1} \tag{8-6}$$

iii) Turbulent pressure fluctuations vs interfacial tension

$$\frac{d_{max}}{D} \propto \left(\frac{\sigma}{\rho_c} N^{-2} D^{-3}\right)^{3/5} = (W_{e,T})^{-3/5} \propto \left(\frac{\sigma}{\rho_c}\right)^{3/5} \frac{1}{D} (\bar{\varepsilon})^{-2/5} \tag{8-7}$$

Note that $(W_{e,T})^{-3/5} \propto \left(\frac{\sigma}{\rho_c}\right)^{3/5} \frac{1}{D} (\bar{\varepsilon})^{-2/5}$ *is only true when D/T is kept the same.*

8.5.2 Relationship between the Sauter Mean Diameter and the Maximum Stable Drop Diameter

The arithmetic-mean, area-mean, volume-mean and Sauter mean diameters were defined in **Chapter 3**. Among them, the Sauter mean diameter d_{32} is the most useful since it is directly related to the interfacial area per unit volume, a which is one of process parameters needed to determine process results (heat, energy, mass transfer and/or chemical reaction rate). The relationship between the Sauter mean diameter d_{32} and the interfacial area per unit volume, a, is $6\phi/d_{32}$. Directly relating the Sauter mean diameter to fluid properties, operating conditions and tank geometry through a force or energy analysis (as in the case of the maximum stable drop diameter) involves many uncertainties related to the statistics of varying drop sizes. Nevertheless, in most cases

the Sauter mean diameter is proportional to the maximum stable drop diameter which is determined by the balance between the deforming and restoring force acting on droplets in the flow. It was Sprow (1967b) who first assumed that $d_{32}=c \cdot d_{max}$ and then verified this relation with his experimental data. His assumption was confirmed by many subsequent investigators. **Table 8-6** summarizes some values of the constant c obtained by previous researchers. The cases in **Table 8-6** cover batch and continuous processes, breakup and coalescence regions, agitated tanks and a static mixer with various impellers. This means that the form of the relationship between the Sauter mean diameter and the maximum stable drop diameter is independent of the geometry of tanks and impellers, and of the nature of the mixing process (i.e. batch or continuous).

Experimental results from this work show that the constant c is not actually a constant, though it does not change significantly over a limited range of N. **Table 8-7** lists c at different N's for the seven cases listed in **Table 8-1**. The value of c decreases with increasing N. When N is very high, c approaches a constant value. The range of values for c from this work is 0.42 to 0.69, which agrees with previous investigations. The relationship between c and the turbulent flow was checked using 5 plots: c vs N; c vs ND; c vs Re (i.e. ND^2 because ν is constant); c vs ε_{max} and c vs $P/\rho V_T$. All plots include the data for all seven cases. The plots are shown in **Figures 8-11 (a to e)**. Comparison of these five figures shows that c is most closely related to the Reynolds number. From **Figure 8-11c**, one can see a clear linear relation between c and ND^2 although the data are divided into two groups: one group includes the data for the A310 with two different clearances and two different impeller diameters; the other group includes all other impellers: the HE3; the PBT and the RT (two different clearances for the RT). The linear regression equations are: $c=-0.020Re+0.806$ with $R^2=0.750$ for the A310 and $c=-0.027Re+0.739$ with $R^2=0.596$ for the HE3, PBT and RT group. When d_{32} is related to d_{max} using $d_{32}=c\ d_{max}$, the effect of the Reynolds number on the value of c should be considered.

To summarize, all correlations between d_{max} and the physical properties of fluids, operating conditions and tank geometries are also valid for d_{32} except that a different

constant needs to be used and the effect of the Reynolds number on the value of c needs to be considered.

8.5.3 Scale-up of Geometrically Similar Dispersion Systems

The scaleup of geometrically similar dispersion systems for the three cases above can be derived from Eqs (8-5) to (8-7). For case a), $d_{max} \propto \sigma/(\mu_c N)$, so the scale-up for d_{32} is based on constant impeller rotational speed (N); for case b), $d_{max} \propto (\sigma/\rho_c)N^{-2}D^{-2}$, so the scale-up is based on constant tip speed (ND); for case c), $d_{max} \propto (\sigma/\rho_c)^{3/5}(\bar{\varepsilon})^{-2/5}$, so the scale-up is based on constant power input per unit mass ($\bar{\varepsilon}$) if *D/T is kept the same.* Of course, these scale-up rules for d_{32} are based on the assumption that $d_{32}=c \cdot d_{max}$. Most of the correlations summarized in **Table 3-1** are in the form of Eq. (8-7) and arrive at the scale-up based on constant power input per unit mass.

Okufi et al. (1990) measured drop sizes in two dispersion systems (n-heptane/water and n-heptane containing different concentrations of di-(2-ethylhexyl) phosphoric acid dispersed in an aqueous solution) with capillary and photography methods. They used three different diameters of tanks and the same D/T ratio (D/T=1/3, RT impeller). They found that equal impeller tip speed provides the best scale-up criterion for equal interfacial areas per unit volume (i. e. for equal d_{32} when ϕ is constant).

Brown and Pitt (1974) suggested using the following equation to correlate d_{32}:

$$d_{32}^{5/3}\frac{\rho}{\sigma}\bar{\varepsilon}\frac{t_c}{T^{2/3}} = \text{constant} \tag{8-8}$$

They used the equation

$$d_{32} \propto \left(\frac{\sigma}{\rho \bar{\varepsilon} t_c}\right)^{3/5} \tag{8-9}$$

to correlate their data. In their paper, they also presented an equation to correlate the circulation time t_c with N and tank geometry:

$$0.122N^{-1}\left(\frac{W}{T}\right)^{-2/3}\left(\frac{D}{T}\right)^{-8/3} = t_c \tag{8-10}$$

(a value of 0.0122 was given in their paper, but from the data for N, t_c, W/T and D/T given in Tables 1 and 2 in their paper, the constant should be 0.122). Substituting Eq.(8-10) into Eqs (8-8), one obtains $d_{32} \propto D^{2/5}$, which implies that d_{32} increases with an increase of impeller diameter if T and W are kept the same. This contradicts physical principles and other investigators' work. **Table 8-8** lists values of the exponent of D in the correlations of d_{32} summarized in **Table 3-1** when D is considered as an independent variable. From **Table 8-8,** these correlations show that an increase in the impeller diameter reduces d_{32}. The exponent of D varies from -0.326 to -0.8 in **Table 8-8**. In the breakup region, the exponent on D is -0.8, in the coalescence region, the exponent on D is -0.5. The conclusion obtained by Brown and Pitt resulted mainly from an unsuitable measuring method: the large drops in their distributions were not measured. Because of this, the enhanced drop breakup which occurs with an increase in the impeller diameter could not be captured in their data. It is not necessary to test the scale-up rule (Eq.(8-8)) they proposed.

Although the presented scale-up rules are used satisfactorily for some dispersion systems, their suitability is limited to specific operating conditions and tank geometries. The reasons for the lack of a more general scale-up rule include:

i) Confusion of the local turbulence energy dissipation rate with the power input per unit mass ("average dissipation rate"). Drop breakup mainly occurs in the strongest turbulence energy dissipation region, so ε_{max} dominates the deformation of droplets. Using equal power input per unit mass to scale up dispersions fails to fully characterize the real physics involved in dispersions.

ii) Previous investigations focus mainly on the effect of physical properties of fluids on dispersions. Much less thought has been devoted to the effect of the interaction of ε_{max} and the mean flow on dispersions. It is reasonable to assume that a dispersion with a stronger mean flow may have a smaller d_{32} than a dispersion with the same ε_{max} and a weaker mean flow since in the latter droplets visit the impeller region less frequently, and stay longer in the more quiescent regions of the tank.

iii) The assumption that c in $d_{32}=c \cdot d_{max}$ is independent of scale and valid for all cases is questionable. From this work, the value of c can only be considered a constant over a limited range of operating conditions.

In this work, the local maximum turbulence energy dissipation rate was chosen to characterize the deforming force. Correlations of d_{32} to the mean flow (ND), ε_{max}, and the average power input per unit mass ($P/\rho V_T$) are compared. To improve the correlations of d_{32}, the interaction of ε_{max} with the mean flow ($\varepsilon_{max} \cdot ND$) is compared to the correction of the non-constant effect of c ($\varepsilon_{max} \cdot ND^2$). This effort was also made for $P/\rho V_T$.

When ND is used as the scaling criterion (**Figure 8-12a**), two groups of data appear: one for the RT, and one for the axial impellers. From **Table 8-4**, these two groups could also be divided according ε_{max}, with the exception of the PBT.

When ε_{max} is used as the scaling criterion (**Figure 8-12b**), two groups of data also appear: one for the PBT and the RT, and one for the HE3 and the A310. This means that when d_{32} is related to ε_{max}, the impellers with high power numbers (the PBT and the RT) are grouped and the impellers with low power numbers (the HE3 and the A310) are grouped.

Finally, when d_{32} is related to $P/\rho V_T$, the data are scattered and no unique characteristics can be defined.

Using this data, the correlation suggested by Brown and Pitt can be re-examined. From **Figure 8-12b**, it is clear that the increase of impeller diameter reduces d_{32} rather than increases d_{32}. The A310 with D=0.550T has a smaller d_{32} than the A310 with D=0.350T at the same ε_{max}. If the effect of impeller diameter on d_{32} is accounted for using $\varepsilon_{max} \cdot (D/D_0)^2$ with D_0= 0.350T, the three cases for the A310 fall in a single line on the plot of d_{32} vs $\varepsilon_{max} \cdot (D/D_0)^2$. **Figure 8-13** shows the plot. If one uses $d_{32} \propto 1/(\varepsilon_{max} \cdot t_c)$ and $t_c \propto D^{-8/3}$ as Brown and Pitt suggested, the plot of d_{32} vs $\varepsilon_{max} \cdot (D/D_0)^{-8/3}$ gives the opposite picture. **Figure 8-14** shows the result. The data for the A310 become more scattered.

It is clear from **Figures 8-12 (a to c)** that the scale-up rule based equal tip speed is not suitable to scale up this dispersion. It is also clear that the interaction of energy dissipation and mean flow needs to be considered. Thus d_{32} vs $\varepsilon_{max}\cdot ND$, $\varepsilon_{max}\cdot ND^2$ and $\varepsilon_{max}\cdot (ND)^2$ are plotted to determine which of these characteristics may collapse the data. To double check the suitability of $P/\rho V_T$, d_{32} vs $P/\rho V_T\cdot ND$, $P/\rho V_T\cdot ND^2$ and $P/\rho V_T\cdot (ND)^2$ are also plotted. **Figures 8-15 (a to c)** and **Figures 8-16 (a to c)** show the plots and regression results for ε_{max} and $P/\rho V_T$, respectively. The correlation with $\varepsilon_{max}\cdot ND^2$ is suggested by the fact that the constant c changes with rotational speed; and the correlation with $\varepsilon_{max}\cdot (ND)^2$ or $\varepsilon_{max}\cdot ND$ is suggested by the fact that there is an interaction between ε_{max} and the mean flow. To include the effect of physical properties - density of the continuous phase and interfacial tension, in $\varepsilon_{max}\cdot ND$, or $\varepsilon_{max}\cdot ND^2$, or $\varepsilon_{max}\cdot (ND)^2$ to form $\sigma/(\rho_c\varepsilon_{max}\cdot ND)$, or $\sigma/(\rho_c\varepsilon_{max}\cdot ND^2)$, or $\sigma/(\rho_c\varepsilon_{max}\cdot (ND)^2)$ just changes the value and units of the constant in each regression equation and does not change the exponents. This is also true for $P/\rho V_T$. Comparison of these six figures shows that correlation for impeller diameter is better when the second power of D is used. Regression of d_{32} against $\varepsilon_{max}\cdot ND^2$ gives the best result. This agrees with both theoretical and experimental scale-up considerations: drop breakup should be determined by ε_{max} rather than by $P/\rho V_T$; the constant c changes with N and can be correlated with ND^2. The regression equation for d_{32} with $\varepsilon_{max}\cdot ND^2$ is:

$$d_{32} = 118.6(\varepsilon_{max} ND^2)^{-0.270} \qquad (8\text{-}11)$$

with an R-square of 0.809, which is good for a correlation for all seven cases and four impellers. The correlation can be rewritten in another form using the Reynolds number (ND^2/ν_c) since ν_c is constant ($1.00\text{x}10^{-6}$ m^2/s):

$$d_{32} = 4944(\varepsilon_{max} Re)^{-0.270} \qquad (8\text{-}12)$$

The PBT falls apart from the other three impellers in **Figure 8-15b**. The reason is not clear from the existing data, but may be due the secondary circulation loop formed in the flow when C/D is larger than 0.6 (Kresta and Wood, 1993).

Complete correlation results for d_{32} versus ND, ε_{max} and $P/\rho V_T$ for each of seven tank geometries are listed in **Appendix-3**.

8.5.4 Conclusions about the Sauter Mean Diameter

Drop sizes were measured using four different impellers with varying diameters and clearances. The assumption that d_{32} can be directly related to the maximum stable drop diameter through a single, unvarying constant is not valid when the operating conditions change dramatically. To relate d_{32} to the flow, one must consider the interaction between ε_{max}, the mean flow and drop breakup and coalescence. The correlation given in Eq. (8-12) is suggested from this work.

8.6 Summary

Drop sizes were measured over a wide range of rotational speeds using four different impellers with varying diameters and clearances. Three sets of conclusions can be drawn from the experimental results:

Drop size distribution

The drop size distributions (normal or log-normal, mono-modal, or bimodal) proposed by previous investigators are only true under the specific operating conditions used. By checking a wide range of rotational speeds for the four different impellers, four types of drop size distribution were found in the evolution of the drop size distribution with N: the long tail distribution; the double peak distribution; the skew distribution and the skew-normal distribution. Excepting the long tail distribution, the drop size distribution can be predicted using two superimposed normal distributions and two diameter sub-ranges

Minimum drop size

Using the Kolmogoroff length scale as an estimate of the minimum drop size in dispersions in agitated tanks in which the flow is in an inertial subrange is questionable. The Kolmogoroff length scale is generally suitable as an order of magnitude estimate of the mean size of drops in dispersions in agitated tanks, but it can not be used as an estimate of the ***minimum drop size*** in the dispersions. A significant number of drops smaller than the Kolmogoroff length scale were measured in the dispersions for all seven tank geometries investigated. When N is low, the number percentage of drops smaller than the Kolmogoroff length scale, $F(\eta)$, is high because drop breakup dominates in the dispersion; $F(\eta)$ decreases with an increase in N since coalescence coexists in the enhanced flow. Only at very high N, does $F(\eta)$ approach zero. $F(\eta)$ is clearly related to ε_{max} and the shape of the drop size distribution. When $d_{30}/d_{10} \leq 1.19$, $F(\eta)=0$ and the minimum drop size may be estimated using the Kolmogoroff length scale.

Sauter mean diameter

The assumption that d_{32} is directly proportional to the maximum stable drop diameter is not valid when the operating conditions change dramatically. Relating d_{32} to the flow requires consideration of the effect of the flow on the constant c in the equation $d_{32}=c \cdot d_{max}$ or consideration of the effects of the interaction between ε_{max} and the mean flow on drop breakup in agitated tanks. The correlation given in Eq. (8-12) is suggested from this work, and the value of the constant in Eq. (8-12), the effects of σ and ρ_c on d_{32} need to be verified, when different dispersions are used.

Tables in Chapter 8

Table 8-1 Cases investigated

Impeller	C/D=1	C/D=1/2	
A310	D=0.350T	D=0.550T	D=0.350T
	√	√	√
	D=T/4	D=T/4	
RT	√	√	
PBT	√		
HE3	√		

Table 8-2 Mean drop size at different radial traverses

Radial position 2r/D	Mean drop size, d_{32} (μm)			
	2z/W=-1.40	2z/W=-5.50	2z/W=9.10	2z/W=20.0
0.50	76.36	76.12	74.96	76.32
0.79	76.36	79.79	74.98	78.05
1.07	74.31	71.68	75.58	80.25
1.36	73.26	71.90	72.61	74.61
1.64	73.73	73.17	72.46	73.80
Traverse-average	74.80	74.53	**74.12**	**76.61**
overall mean*	75.02			
Standard deviation for traverse-average values	1.10			
Standard deviation for all 20 values	2.40			

* overall mean is the arithmetic average value of all 20 d_{32}'s (5x4) on the four traverses.

Table 8-3 Sampling points for mean drop size measurements

Impeller	Radial traverse 2z/W (numbers in italic)					
	Re<5x10^4			Re>5x10^4		
	D=0.550T	D=T/4*		D=0.550T	D=T/4*	
	C/D=1/2	C/D=1	C/D=1/2	C/D=1/2	C/D=1	C/D=1/2
A310	*4.40* *1.26* *-8.80* *-17.9*	*7.60* *1.36* *-10.5* *-21.1*	*1.36* *-9.64* *-19.3* *-28.7*	*1.26*	*1.36*	*1.36*
r (mm)	39, 51, 63,75,87	18, 30, 42, 54, 66		39, 51, 63,75,87	18, 30, 42, 54, 66	
PBT	*no data*	*7.08* *1.47* *-16.5* *-33.0*	*1.47* *-13.4* *-26.9* *-40.1*	*no data*	*1.47*	*1.47*
r (mm)		9, 21, 33, 45, 57, 69			9, 21, 33, 45, 57, 69	
HE3	*no data*	*11.1* *1.74* *-25.9* *-51.9*	*1.74* *-21.1* *-42.2* *-63.0*	*no data*	*1.74*	*1.74*
r (mm)		9, 21, 33, 45, 57, 69			9, 21, 33, 45, 57, 69	
RT	*no data*	*5.00* *1.33* *-11.7* *-23.3*	*1.33* *-9.50* *-19.0* *-28.3*	*no data*	*1.33*	*1.33*
r (mm)		9, 21, 33, 45, 57, 69			9, 21, 33, 45, 57, 69	

* For A310, D=0.350T instead of D=T/4.

Table 8-4 Maximum turbulence energy dissipation rates (no extra water layer)

Impeller	Case	D† + T/2 - T/4	C/D + 1 - 1/2	N (rpm)	Re $x10^{-4}$	$P/\rho V_T$ (m^2/s^3)	ε_{max} (m^2/s^3)	$\frac{\varepsilon_{max}}{N^3D^2}$	Same geometry as (Table, run)
A310	**A-1**	+	+	503	14.4	0.652	14.2	1.38	6-2, 5
	A-2	+	-	503	14.4	0.652	9.16	0.89	6-2, 7
	A-3	-	+	1068	12.4	0.652	36.9	0.93	6-2, 3
	A-4	-	-	1068	12.4	0.652	35.7	0.90	6-2, 9
HE3	H-1	+	+	567	13.4	0.484	15.5	1.28	6-3, 5
	H-2	+	-	567	13.4	0.484	7.22	0.59	6-3, 7
	H-3	-	+	1694	10.0	0.484	74.2	0.92	6-3, 3
	H-4	-	-	1694	10.0	0.484	61.5	0.76	6-3, 9
PBT	P-1	+	+	357	8.43	0.652	16.1	5.31	6-1, 5
	P-2	+	-	357	8.43	0.652	12.5	4.12	6-1, 7
	P-3	-	+	1133	6.69	0.652	83.7	3.45	6-1, 3
	P-4	-	-	1133	6.69	0.652	94.3	3.89	6-1, 9
RT	R-1	+	+	225	5.31	0.652	15.4	20.3	6-4, 5
	R-2	+	-	225	5.31	0.652	17.1	22.6	6-4, 7
	R-3	-	+	714	4.22	0.652	106	17.5	6-4, 3
	R-4	-	-	714	4.22	0.652	93.0	15.3	6-4, 9

† Values for the A310 in this column are: "+" for 0.550T; "-" for 0.350T.

Table 8-5 List of d_{10}, $\sigma(d)$, d_{20}, d_{30}, η and $F(\eta)$ at different rotational speeds (ε_{max} were obtained by using $\varepsilon_{max,2} = \varepsilon_{max,1} \cdot (N_2/N_1)^3$. N_1 and $\varepsilon_{max,1}$ were from (**Table 8-4**).

Impeller/ Geometry	N (s^{-1})	Re $x10^{-4}$	$P/\rho V_T$ (m^2/s^3)	ε_{max} (m^2/s^3)	d_{10} (μm)	$\sigma(d)$ (μm)	d_{20} (μm)	d_{30} (μm)	η (μm)	$F(\eta)$ x100
	11.3	7.94	0.165	9.31	46.0	45.2	64.7	82.2	18.1	27.8
	13.3	9.41	0.274	15.5	52.1	36.1	75.4	89.5	15.9	13.4
A310/	15.5	10.9	0.430	24.3	52.3	36.1	63.7	72.9	14.2	10.7
N_f=4	16.3	11.5	0.497	28.1	46.1	32.3	56.6	65.2	13.7	10.5
D=0.350T	16.9	11.9	0.558	31.6	38.9	30.4	49.5	58.3	13.3	18.5
C/D=1	17.8	12.6	0.652	36.9	38.1	26.9	46.9	54.5	12.8	12.8
	18.8	13.3	0.772	43.7	35.4	23.8	43.0	49.8	12.3	12.7
F(η) at	20.7	14.6	1.030	58.3	43.4	25.7	49.4	55.3	11.5	7.15
2r/D=0.50	22.7	16.0	1.346	76.1	44.9	19.7	49.3	53.0	***10.7***	***0.46***
A310/	11.3	7.94	0.165	9.00	40.4	43.5	59.7	77.7	18.3	38.3
N_f=4	13.4	9.46	0.278	15.2	42.4	42.0	60.2	75.5	16.0	29.6
D=0.350T	15.0	10.6	0.393	21.5	41.2	35.7	55.0	66.4	14.7	22.2
C/D=1/2	16.8	11.8	0.545	27.8	38.5	30.4	49.3	58.5	13.5	18.9
	18.8	13.2	0.764	41.8	32.6	23.2	40.2	47.2	12.4	14.6
F(η) at	20.5	14.5	1.000	54.7	30.1	20.0	36.4	42.1	11.6	15.0
2r/D=0.50	22.6	15.9	1.325	72.5	35.4	17.5	39.9	43.8	10.8	3.01
A310/	7.67	13.4	0.499	7.01	46.9	44.1	65.3	80.0	19.4	35.8
N_f=4	8.22	14.3	0.614	8.62	42.6	38.2	57.8	70.6	18.5	34.0
D=0.550T	8.78	15.3	0.750	10.5	42.8	34.1	55.0	65.8	17.6	24.5
C/D=1/2	9.43	16.4	0.930	13.1	38.4	29.5	48.8	58.4	16.6	22.5
F(η) at	10.5	18.3	1.288	18.1	34.6	20.9	40.6	47.0	15.3	12.4
2r/D=0.55										

Table 8-5 Cont'd

Impeller/ Geometry	N (s^{-1})	Re $x10^{-4}$	$P/\rho V_T$ (m^2/s^3)	ε_{max} (m^2/s^3)	d_{10} (μm)	σ(d) (μm)	d_{20} (μm)	d_{30} (μm)	η (μm)	F(η) x100
HE3/	14.0	5.04	0.059	9.05	46.3	51.3	69.7	89.6	18.2	38.6
N_f=4	16.0	5.76	0.088	13.5	48.2	45.7	65.8	80.3	16.5	27.3
D=T/4	19.1	6.88	0.150	23.0	32.5	31.0	45.3	58.1	14.4	25.4
C/D=1	21.6	7.79	0.218	33.4	25.1	22.2	33.7	43.9	13.2	25.2
	25.6	9.21	0.360	55.2	26.9	23.5	32.4	41.2	11.6	17.6
F(η) at	28.3	10.2	0.487	74.7	24.9	18.5	31.1	38.1	10.8	13.5
2r/D=0.30	29.9	10.8	0.575	88.3	23.2	17.4	29.2	35.9	10.3	15.4
	16.4	5.90	0.425	54.7	48.5	44.7	67.0	80.5	11.6	16.6
PBT/	17.2	6.18	0.489	62.9	49.0	42.6	65.2	77.5	11.2	12.6
N_f=4	18.4	6.61	0.599	77.0	46.0	37.5	59.8	70.7	10.7	8.80
D=T/4	20.0	7.20	0.773	99.4	42.0	33.5	53.8	64.1	10.0	7.80
C/D=1	22.4	8.07	1.089	140	35.1	25.7	43.8	51.7	9.19	5.93
	24.1	8.67	1.351	174	33.6	23.2	41.0	47.8	8.71	6.20
F(η) at	26.4	9.51	1.782	229	34.3	20.5	40.1	45.3	8.13	3.95
2r/D=0.30	30.0	10.8	2.611	336	37.5	16.0	40.9	44.1	***7.39***	***0.31***
RT/	11.1	3.98	0.522	85.2	28.7	28.8	40.0	52.0	10.4	15.5
N_f=4	12.1	4.36	0.685	112	28.7	26.7	39.5	50.3	9.72	10.6
D=T/4	13.5	4.86	0.952	155	30.9	25.2	38.3	46.7	8.96	7.80
C/D=1	15.2	5.46	1.349	220	33.7	21.7	39.7	45.1	8.21	4.96
F(η) at	17.1	6.17	1.945	318	36.5	17.8	40.8	44.6	7.49	1.45
2r/D=0.30	20.3	7.31	3.235	528	52.2	12.2	39.5	43.8	***6.60***	***0.01***
RT/	8.62	3.10	0.247	35.3	31.0	34.9	46.9	62.4	13.0	34.3
N_f=4	9.92	3.57	0.377	53.8	34.2	33.9	49.6	62.5	11.7	20.0
D=T/4	11.4	4.10	0.570	81.4	32.8	31.0	45.4	56.3	10.5	20.5
C/D=1/2	13.4	4.82	0.931	133	30.5	26.1	40.4	49.1	9.32	12.4
	15.5	5.57	1.436	205	29.2	22.8	37.3	44.4	8.36	8.91
F(η) at	17.6	6.32	2.096	299	26.9	18.3	32.6	37.9	7.60	6.10
2r/D=0.70	19.2	6.91	2.730	389	25.1	15.2	29.4	33.7	7.12	4.05

Table 8-6 Constant (c) values in the equation $d_{32}=c \cdot d_{max}$ obtained by previous investigators

Investigators	value of c	Remarks
Sprow, 1967b	0.380	non-coalescing dispersion
Brown and Pitt, 1972	0.70	
Coulaloglou and Tavlarides, 1976	0.67	continuous process
Calabrese et al., 1986	0.48~0.60 0.64	μ_d from 0.0960 to 10.51 Pa.s from the data of Chen and Middleman,1967
Nishikawa et al., 1987	0.50 0.45	breakup region coalescence region
Berkman and Calabrese, 1988	0.67	dispersion in a static mixer
This work	0.42~0.69	c decreases with an increase in N

Table 8-7 Constant (c) values in the equation $d_{32}=c \cdot d_{max}$

Impeller	Geometry		Rotational speed (s^{-1}) (N)									
			c									
A310	D=0.350T	C/D=1	N	11.3	13.3	15.5	16.3	16.9	17.8	18.8	20.7	22.7
			c	0.69	0.63	0.57	0.54	0.54	0.54	0.54	0.54	0.54
	D=0.350T	C/D=1/2	N	11.3	13.4	15.0	16.8	18.8	20.5	22.6		
			c	0.67	0.60	0.59	0.57	0.51	0.48	0.47		
	D=0.550T	C/D=1/2	N	7.67	8.22	8.78	9.43	10.5				
			c	0.61	0.57	0.53	0.50	0.42				
HE3	D=T/4	C/D=1	N	14.0	16.0	19.1	21.6	25.6	28.3	29.9		
			c	0.62	0.59	0.55	0.50	0.49	0.48	0.47		
PBT	D=T/4	C/D=1	N	14.0	16.4	17.2	18.4	20.0	22.5	24.1	26.4	
			c	0.69	0.68	0.67	0.55	0.50	0.49	0.47	0.46	
RT	D=T/4	C/D=1	N	11.1	12.1	13.5	15.2	17.1	20.3			
			c	0.66	0.65	0.56	0.54	0.53	0.50			
		C/D=1/2	N	8.62	9.92	11.4	13.4	15.5	17.6	19.2		
			c	0.65	0.64	0.62	0.60	0.56	0.51	0.46		

Table 8-8 Values of the exponent of D in typical correlations of d_{32} if D is considered as an independent variable.

Investigators	Correlation	Values of the exponent of D	Remarks
Chen and Middleman, 1967	$\frac{d_{32}}{D} = 0.053(W_{e,T})^{-0.6}$	$d_{32} \propto D^{-0.8}$	$W_{e,T}=\rho N^2 D^3/\sigma$
Roger et al., 1956	$\frac{d_{32}}{D} = B(D/T)^{-b}(W_{e,T})^{-0.36}$	$d_{32} \propto D^{-(0.08+b)}$	
Calderbank, 1958	$\frac{d_{32}}{D} = 0.06(1+9\phi)(W_{e,T})^{-0.6}$	$d_{32} \propto D^{-0.8}$	
Shinnar, 1961	$\frac{d_{32}}{D} = B(\sigma D)^{-3/8}(W_{e,T})^{-3/8}$	$d_{32} \propto D^{-1/2}$	coalescence control
Weinstein and Treybal, 1973	$d_{32} = 10^{(-2.316+0.672\bar{\phi})}\nu_c^{0.0722}$ $\varepsilon^{-0.194}(\sigma g_c/\rho_c)^{0.196}$	$d_{32} \propto D^{-0.388}$	for batch process $\varepsilon \propto N^3 D^2$
	$d_{32} = 10^{(-2.066+0.732\bar{\phi})}\nu_c^{0.047}$ $\varepsilon^{-0.204}(\sigma g_c/\rho_c)^{0.274}$	$d_{32} \propto D^{-0.416}$	for continuous process
Godfrey and Grilc, 1977	$d_{32} = 10^{(-3.18+0.74\bar{\phi})}\bar{\varepsilon}^{-0.2755}$ $(\sigma/\rho_c)^{0.1787}$	$d_{32} \propto D^{-0.551}$	$\bar{\varepsilon} \propto N^3 D^2$
Wang and Calabrese, 1986	$\frac{d_{32}}{D} = 0.053(W_{e,T})^{-0.6}$ $(1+0.97\,Vi^{0.79})^{3/5}$	two terms: 1st term $d_{32} \propto D^{-0.8}$; 2nd term $d_{32} \propto D^{-0.326}$	$Vi = \frac{\mu_d ND}{\sigma}(\frac{\rho_c}{\rho_d})^{1/2}$
Nishikawa et al., 1987	$\frac{d_{32}}{D} = 0.095N_p^{-2/5}(W_{e,T})^{-0.6}$ $(1+2.5\phi^{2/3})(\mu_d/\mu_c)_d^{1/5}(\mu_d/\mu_c)_c^{1/8}$	$d_{32} \propto D^{-0.8}$	(breakup region)
	$\frac{d_{32}}{D} = 0.035N_p^{-1/4}(W_{e,T})^{-3/8}D^{-3/8}$ $(1+3.5\phi^{3/4})(\mu_d/\mu_c)_d^{1/5}(\mu_d/\mu_c)_c^{1/8}$	$d_{32} \propto D^{-1/2}$	(coalescence region)

Table 8-9 Sauter mean drop sizes at different rotational speeds for the four impellers

impeller	Geometry		Rotational speed (s^{-1}) / d_{32} (μm)									
A310	D=0.350T	C/D=1	N	11.3	13.3	15.5	16.3	16.9	17.8	18.8	20.7	22.7
			d_{32}	149.0	125.0	94.90	87.40	81.80	72.81	68.21	64.70	58.91
	D=0.350T	C/D=1/2	N	11.3	13.4	15.0	16.8	18.8	20.5	22.6		
			d_{32}	138.4	117.6	97.01	81.72	63.12	54.03	50.91		
	D=0.550T	C/D=1/2	N	7.67	8.22	8.78	9.43	10.5				
			d_{32}	117.5	104.7	93.10	81.20	60.20				
HE3	D=T/4	C/D=1	N	14.0	16.0	19.1	21.6	25.6	28.3	29.9		
			d_{32}	148.5	122.2	93.40	76.52	61.03	55.21	54.72		
PBT	D=T/4	C/D=1	N	14.0	16.4	17.2	18.4	20.0	22.5	24.1	26.4	30.0
			d_{32}	141.4	117.8	109.6	100.0	89.51	73.42	62.32	55.91	50.72
RT	D=T/4	C/D=1	N	7.50	8.88	9.83	11.1	12.1	13.5	15.2	17.1	20.3
			d_{32}	125.0	105.7	97.82	90.12	82.09	71.01	58.89	53.78	51.72
		C/D=1/2	N	8.62	9.92	11.4	13.4	15.5	17.6	19.2		
			d_{32}	111.0	96.61	86.02	73.49	61.39	51.02	44.53		

Figures in Chapter 8

Figure 8-1 Comparison of RMS velocities between the two cases with and without an extra water layer when no silicone oil was added. Open symbols with water layer, closed symbols without.

1a) HE3

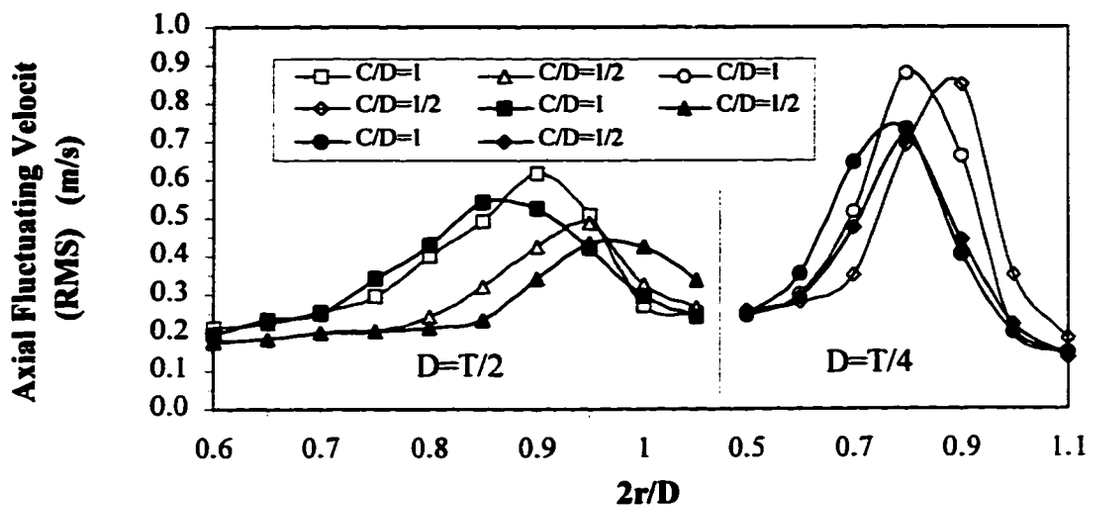

1b) PBT

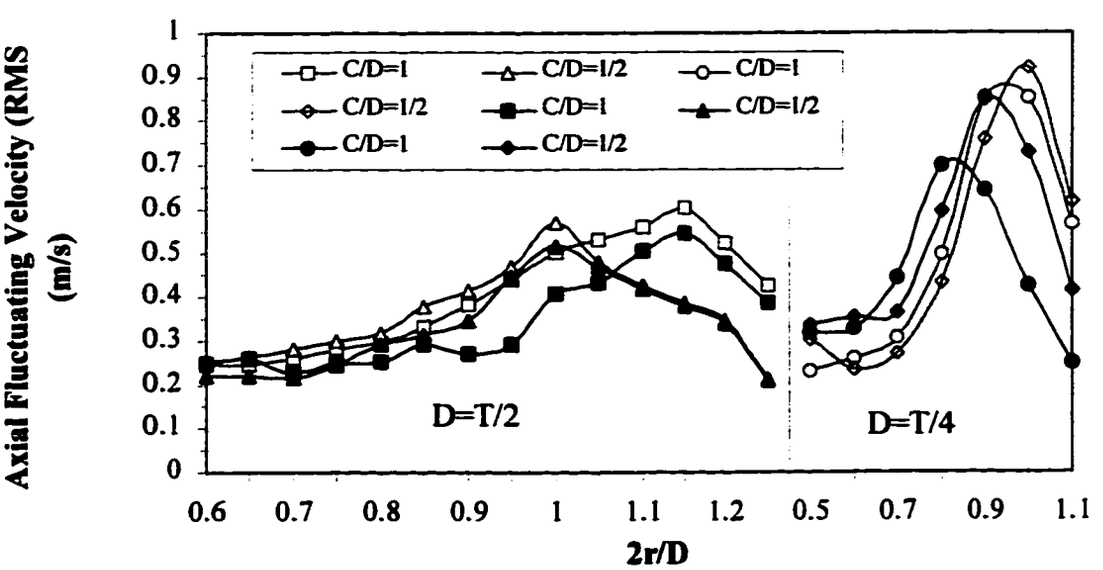

Figure 8-2 Comparison of RMS velocities between the two cases with and without silicone oil when no extra water layer was added.

2a) HE3

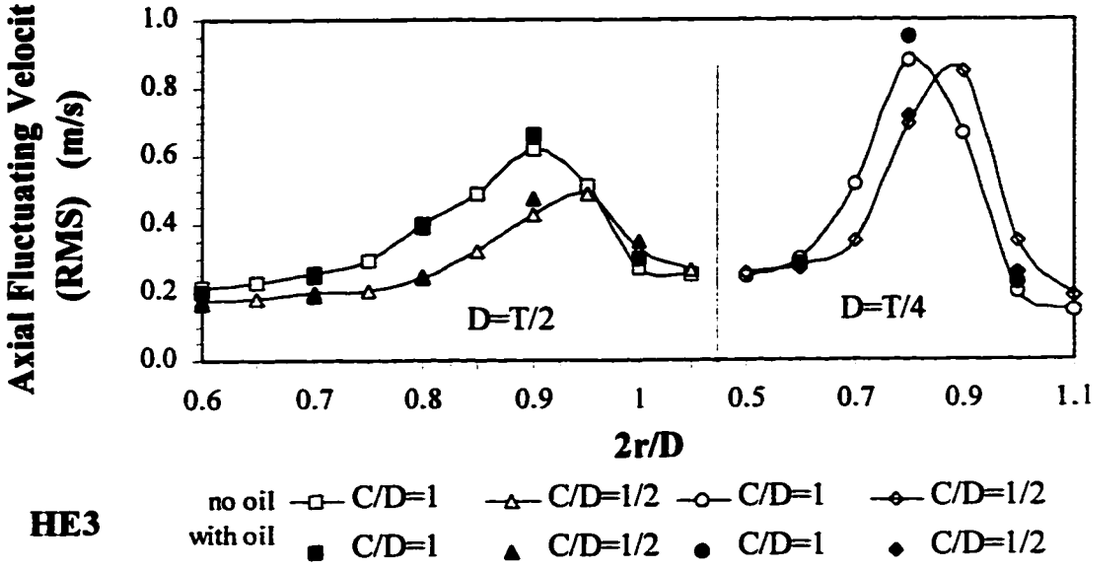

2b) PBT

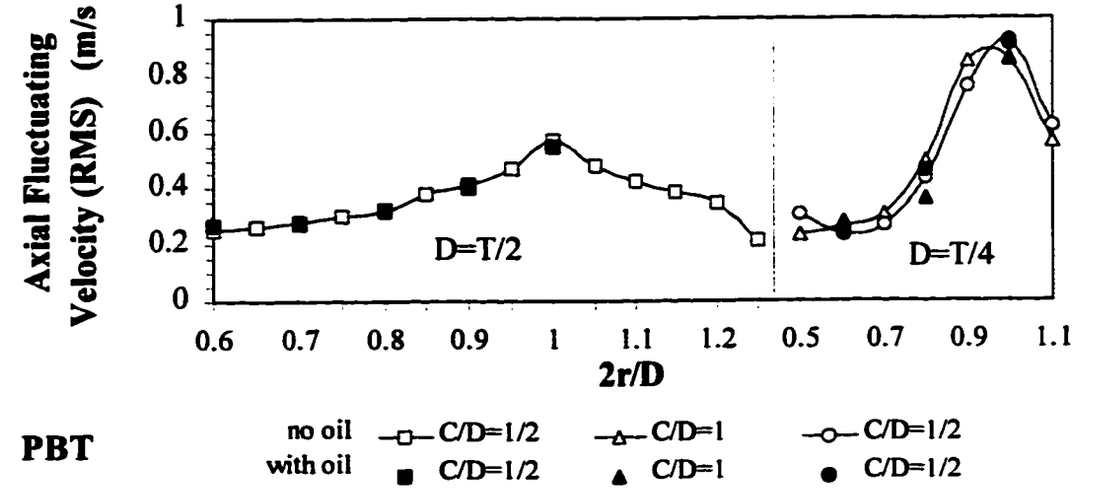

Figure 8-3 Plots of drop size distributions at different rotational speeds for case: A310: D=0.350T, C/D=1, 2r/D=0.50.

a)

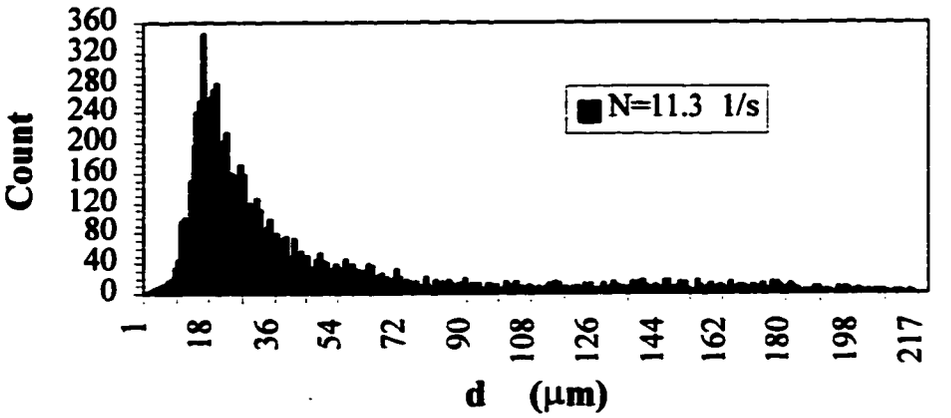

b)

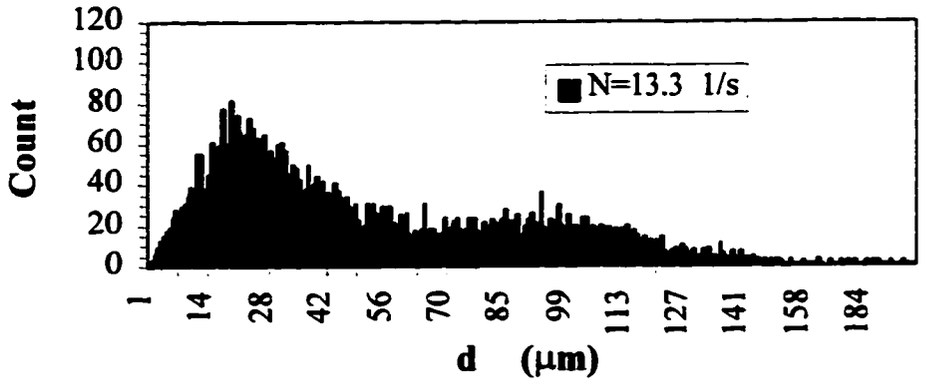

c)

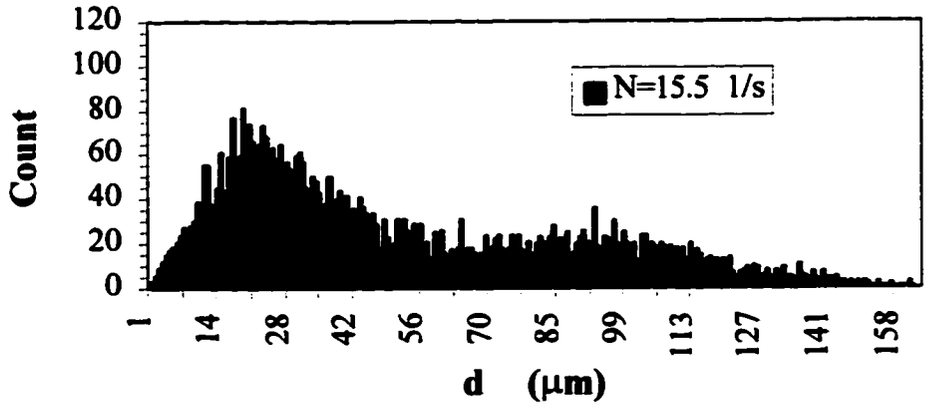

Cont'd **Figure 8-3**

d)

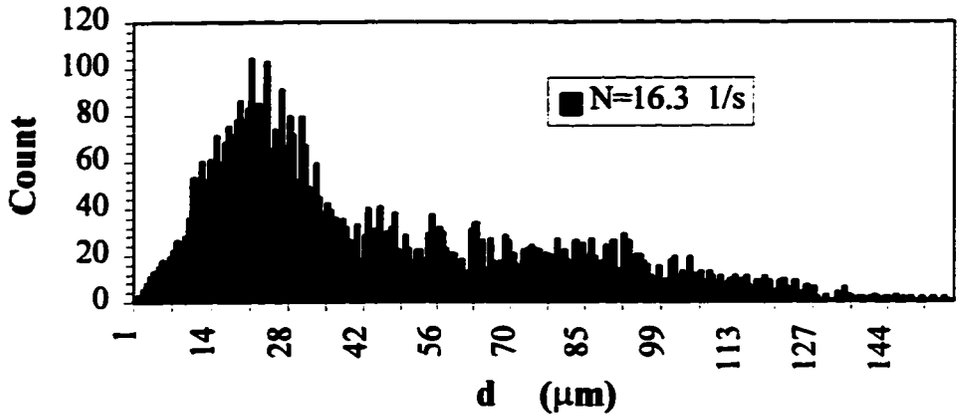

e)

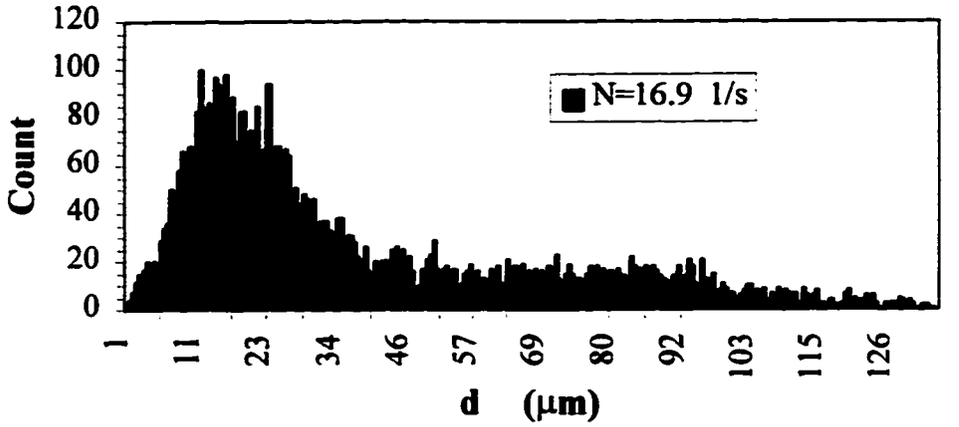

f)

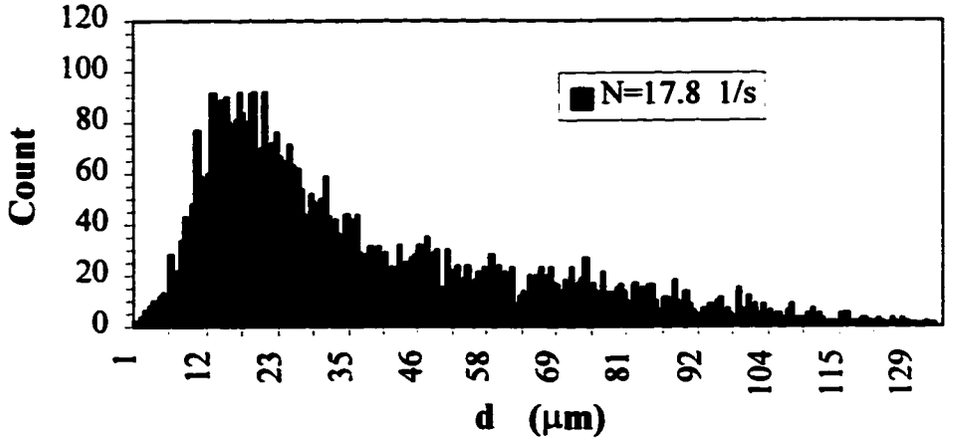

Cont'd **Figure 8-3**

g)

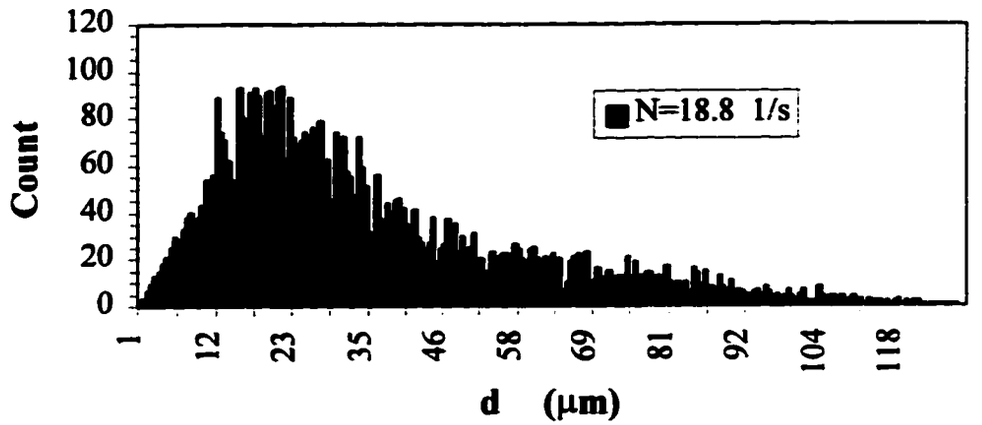

h)

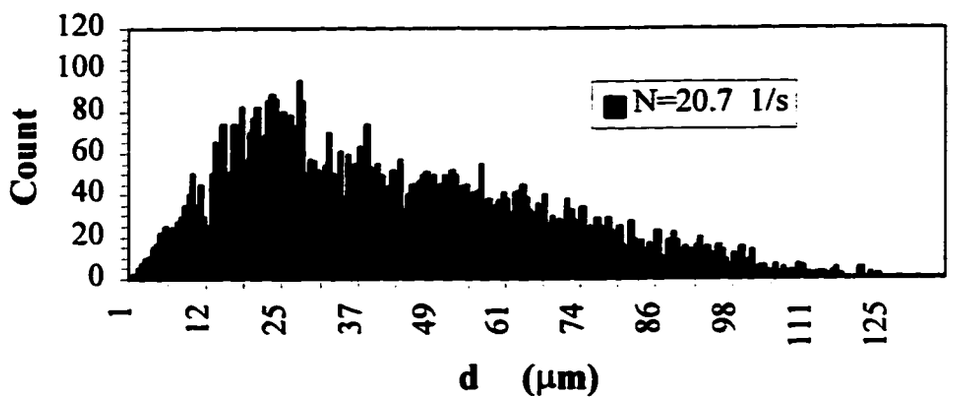

i)

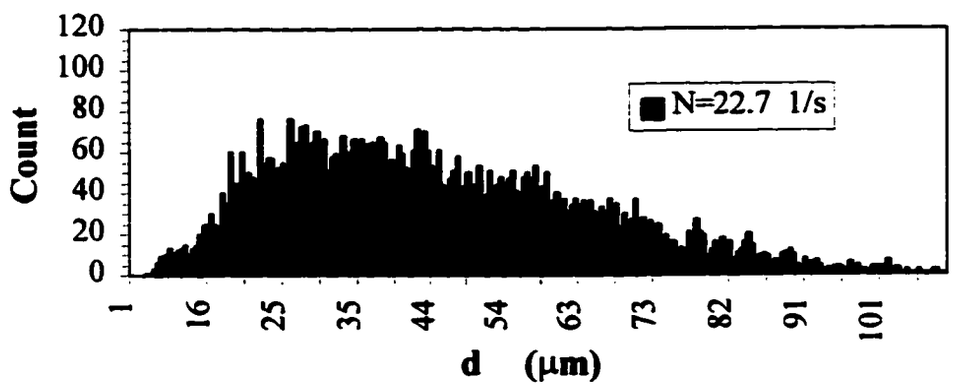

Figure 8-4 Plots of arithmetic mean drop sizes and standard deviations vs N

4a) A310: D=0.350T, C/D=1.

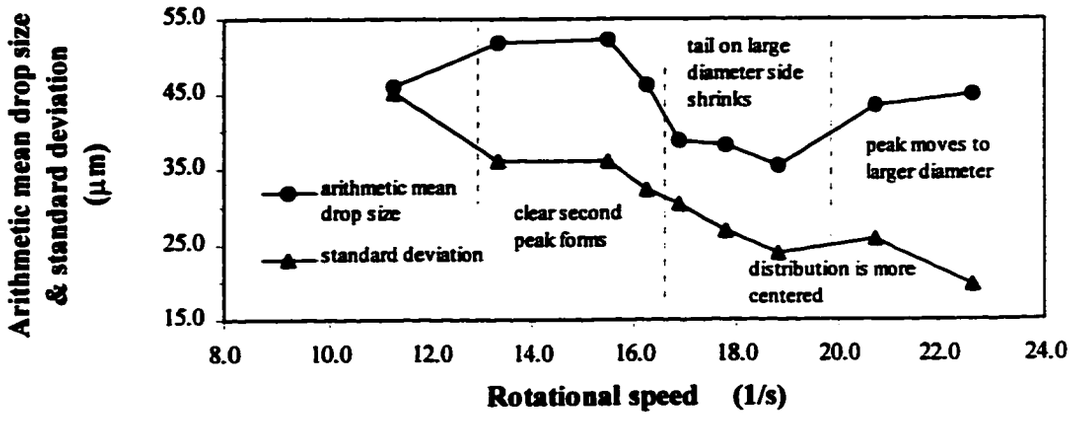

4b) A310: D=0.350T, C/D=1/2.

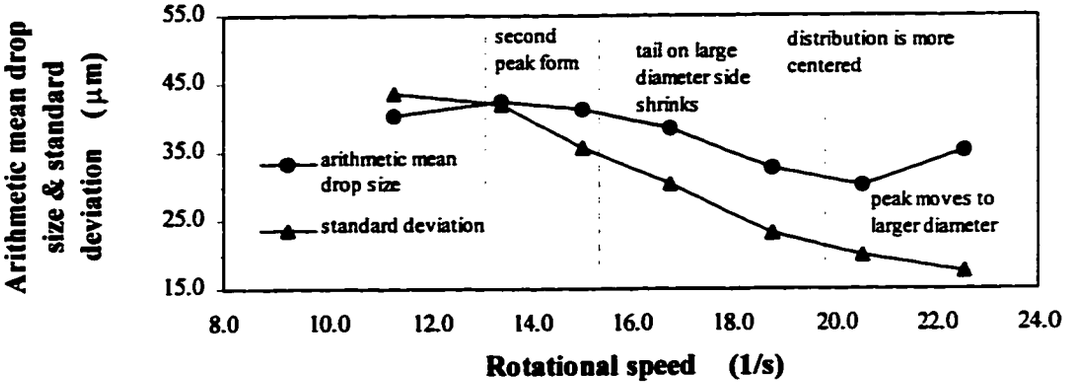

4c) A310: D=0.550T, C/D=1/2.

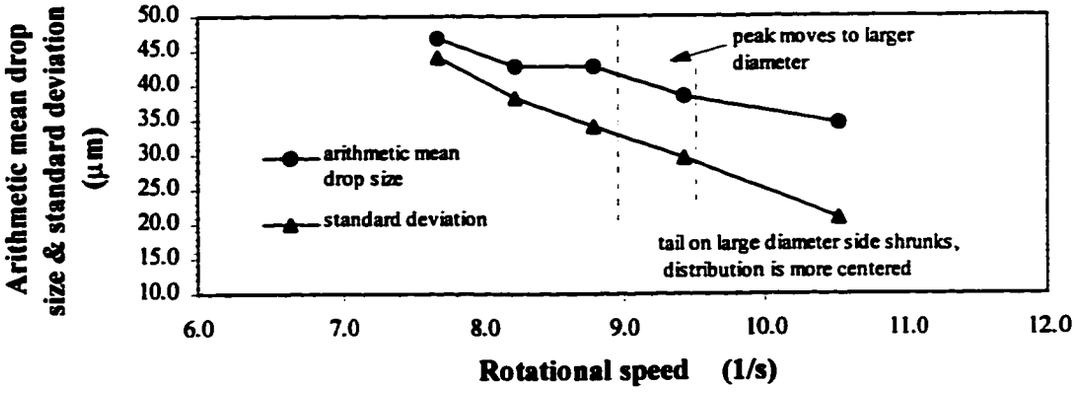

4d) HE3: D=T/4, C/D=1.

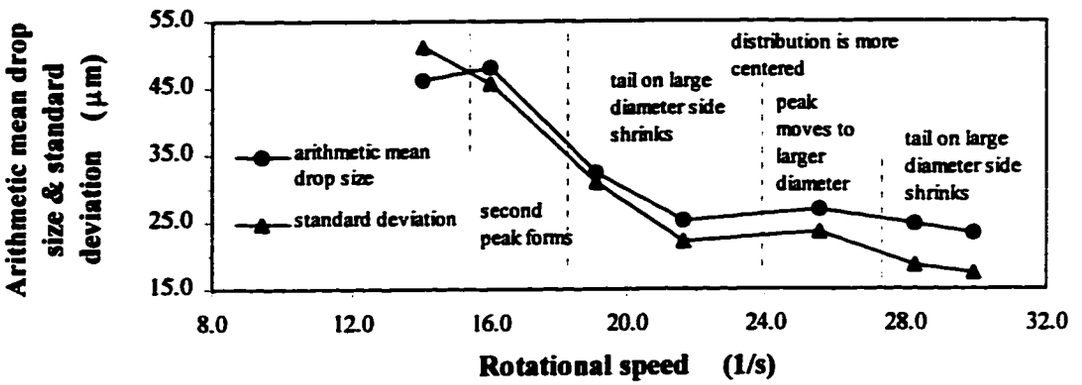

4e) PBT: D=T/4, C/D=1.

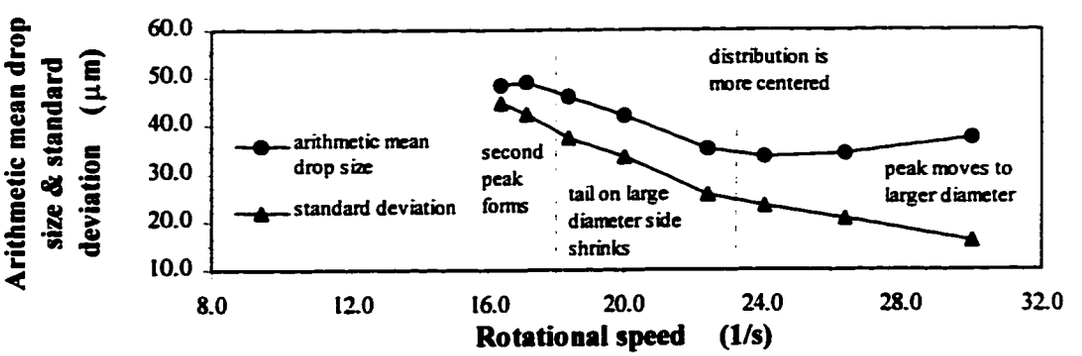

4f) RT: D=T/4, C/D=1.

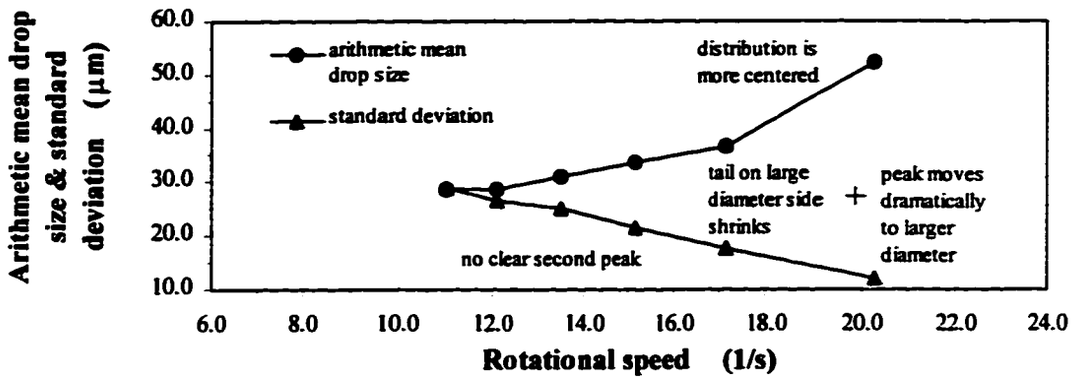

4g) RT: D=T/4, C/D=1/2.

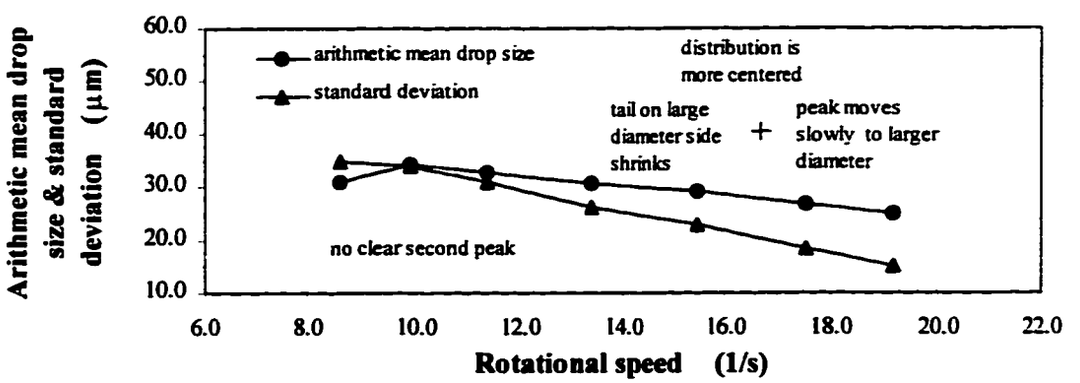

Figure 8-5 Comparison of experimental distribution and fit distribution. A310, N_f=4, D=0.350T, C/D=1.

5a) Double peak distribution

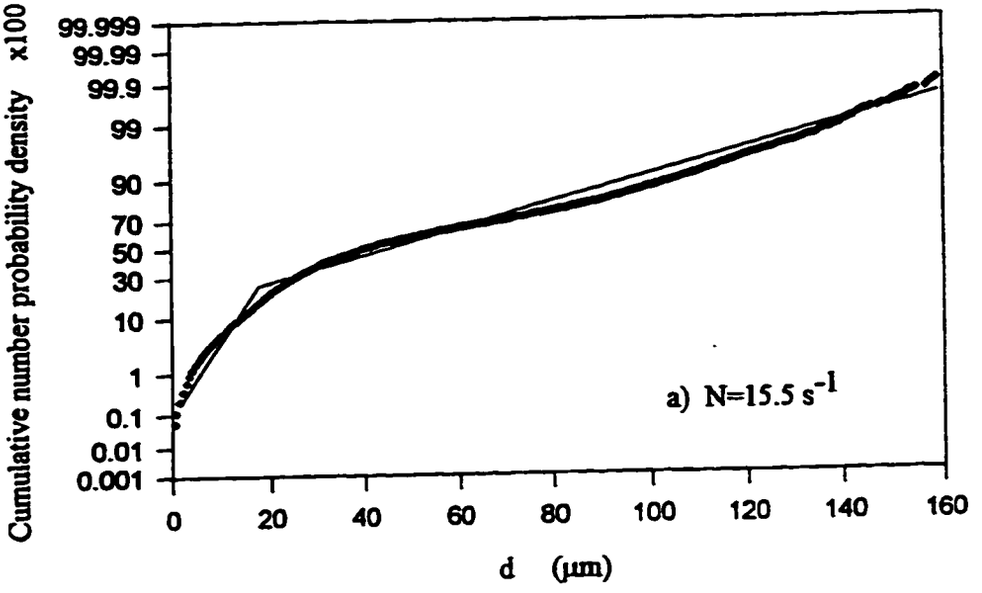

5b) Skew distribution

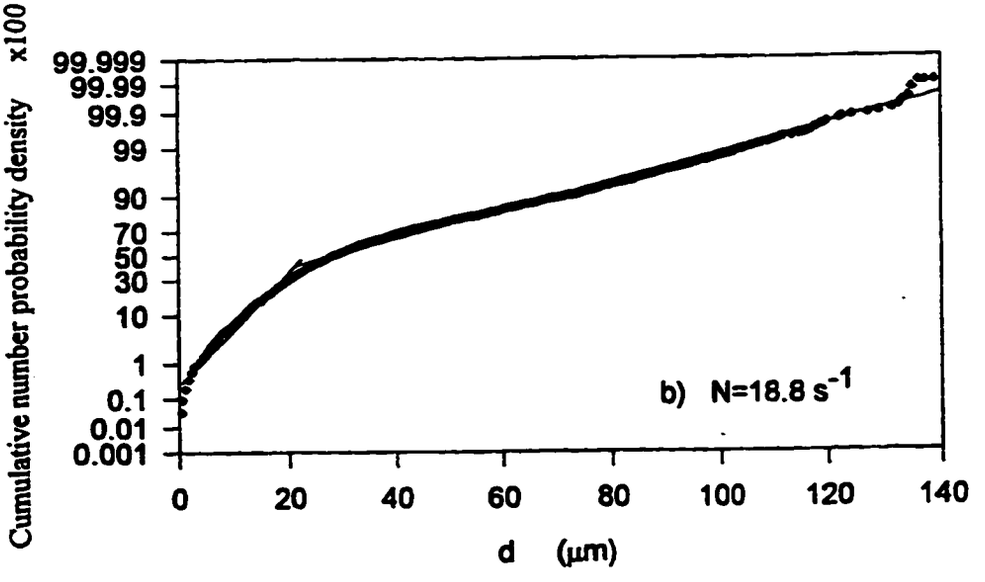

Cont'd **Figure 8-5**

5c) Skew-normal distribution

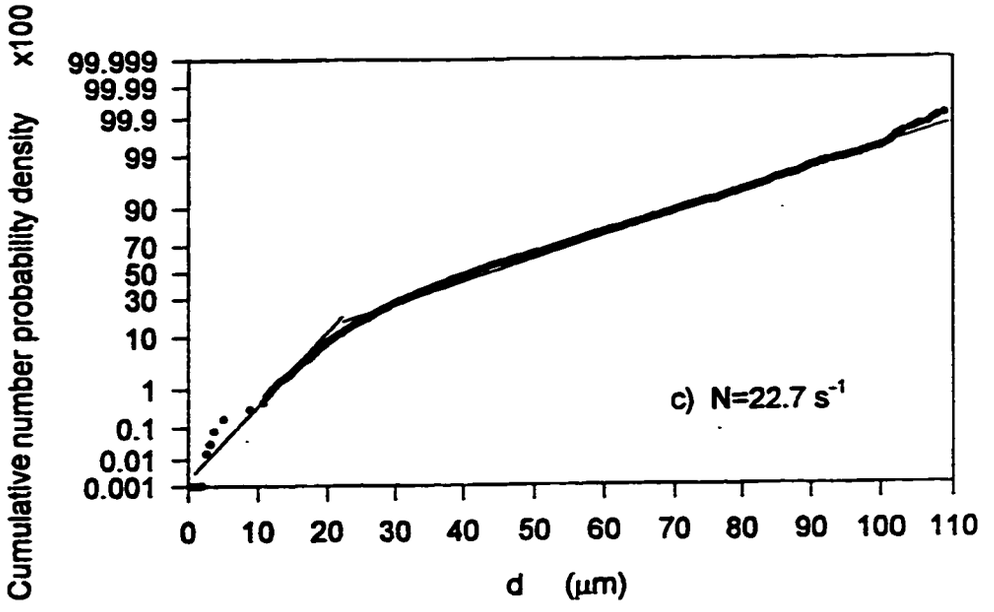

Figure 8-6 Kolmogoroff length η vs turbulence energy dissipation rate ε

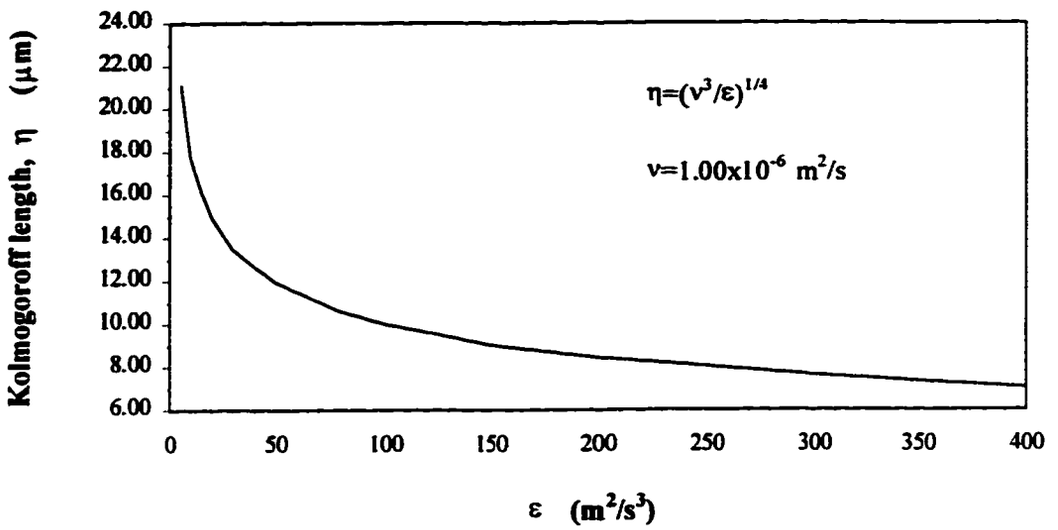

Figure 8-7 Plots of cumulative number probability density vs d at different rotational speeds. PBT: D=T/4, C/D=1, 2r/D=0.30.

a)

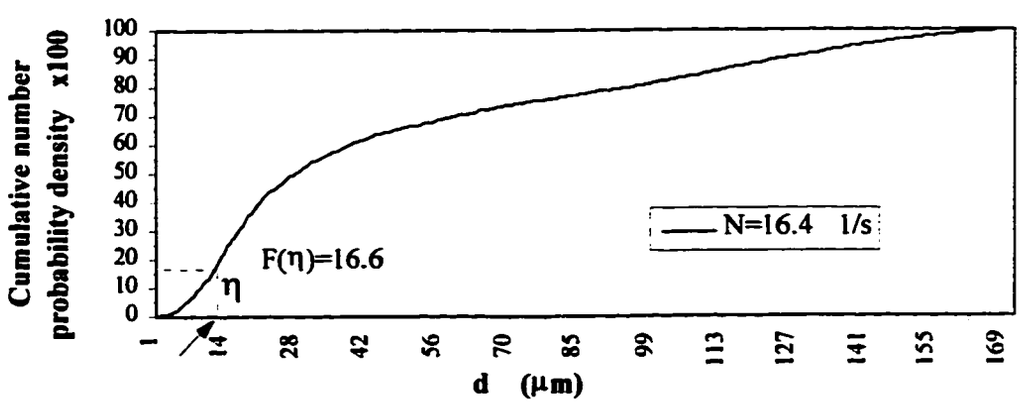

Cont'd **Figure 8-7**

b)

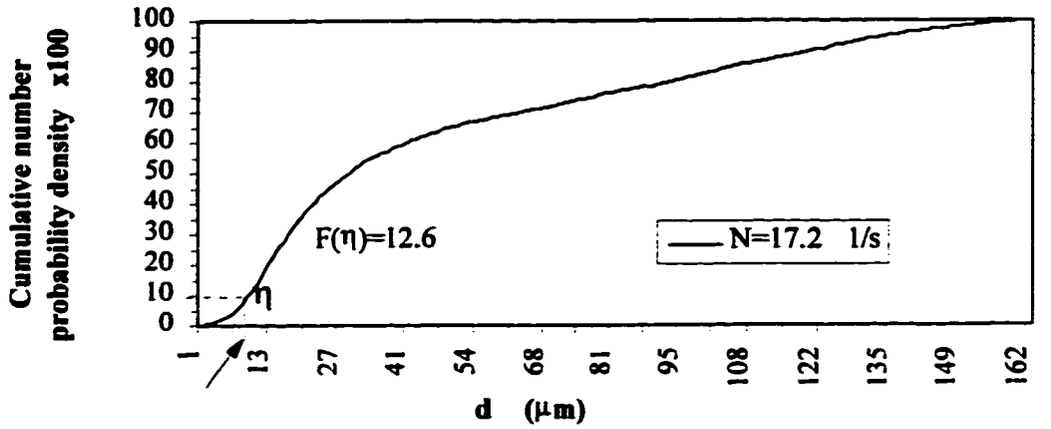

c)

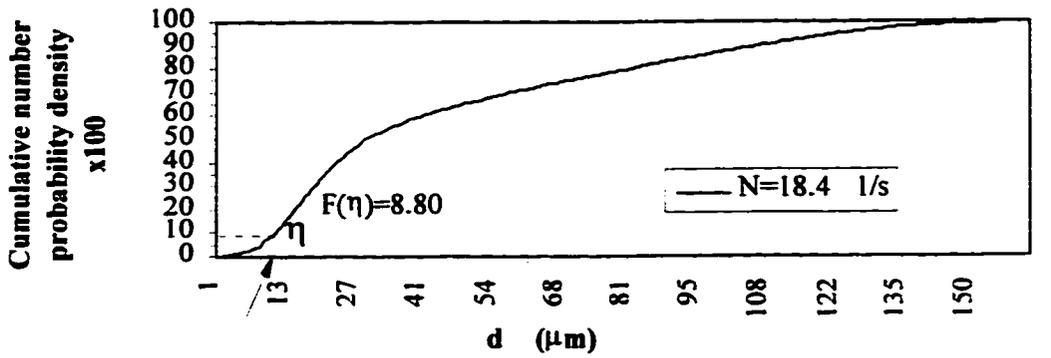

d)

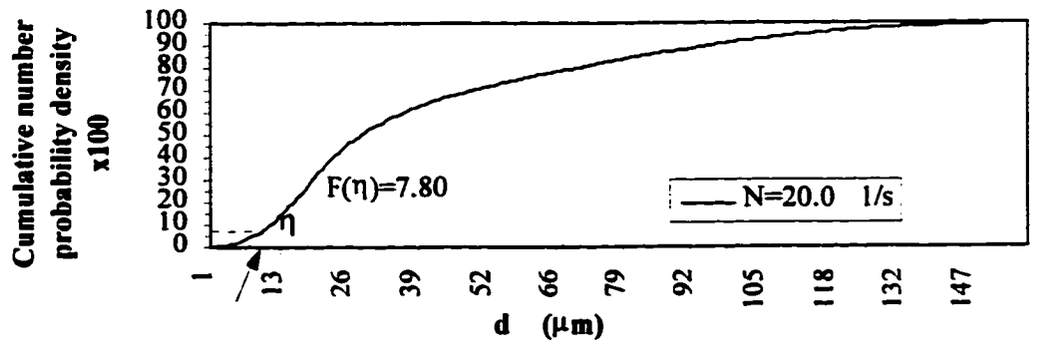

Cont'd **Figure 8-7**

e)

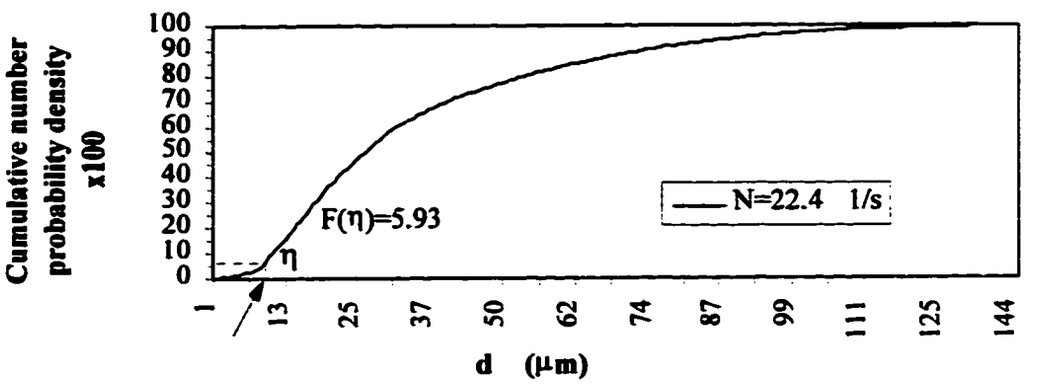

f)

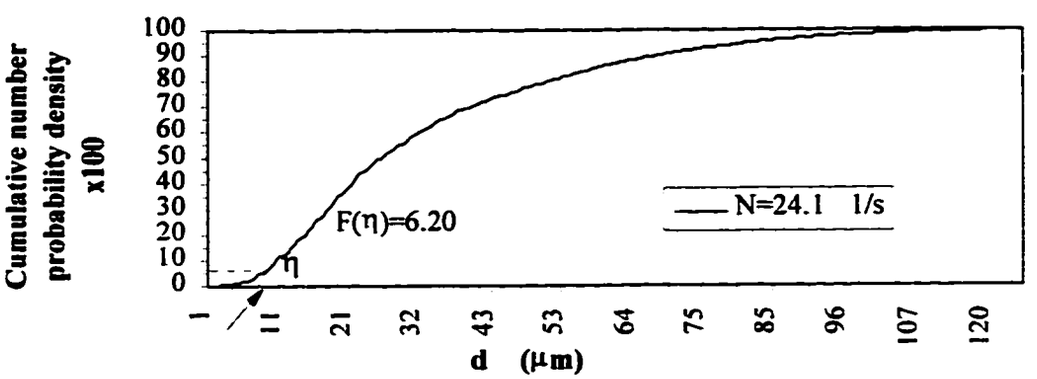

g)

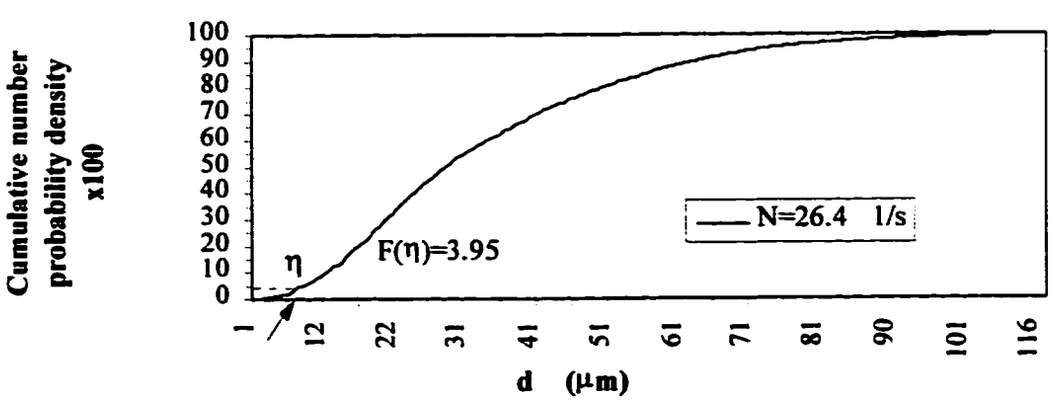

Cont'd **Figure 8-7**

h)

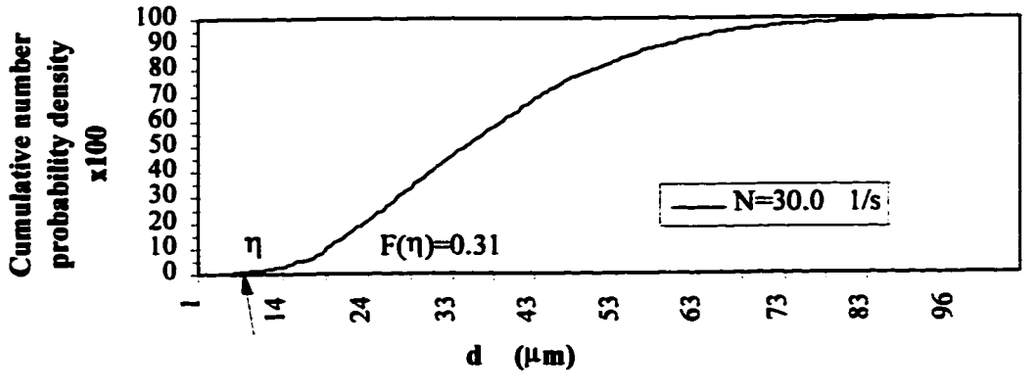

Figure 8-8 Correlation of F(η) with the flow.

8a) Plots of F(η) vs N for all seven cases

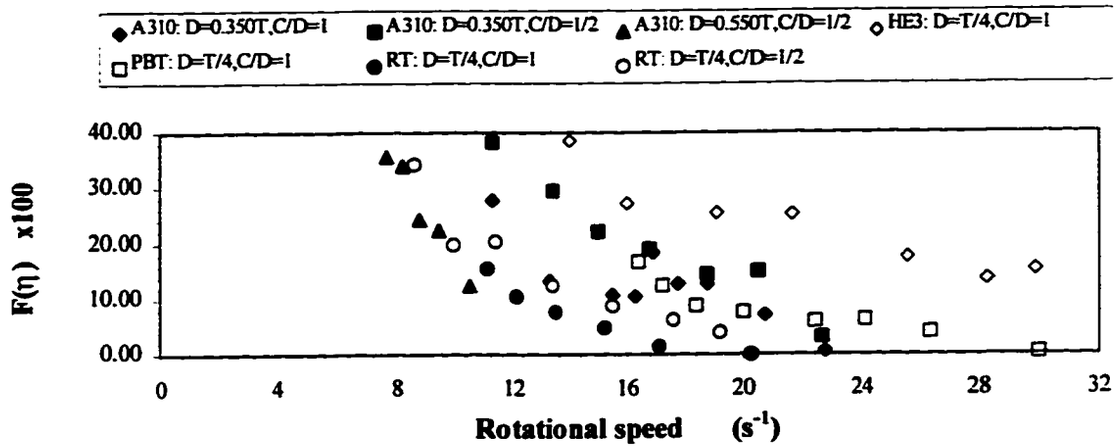

8b) Plots of F(η) vs ND for all seven cases.

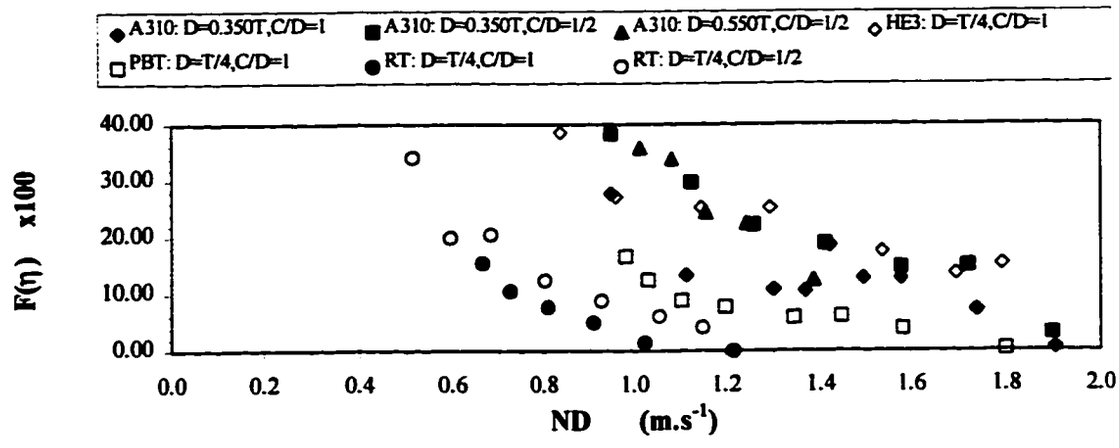

8c) Plots of F(η) vs Re for all seven cases.

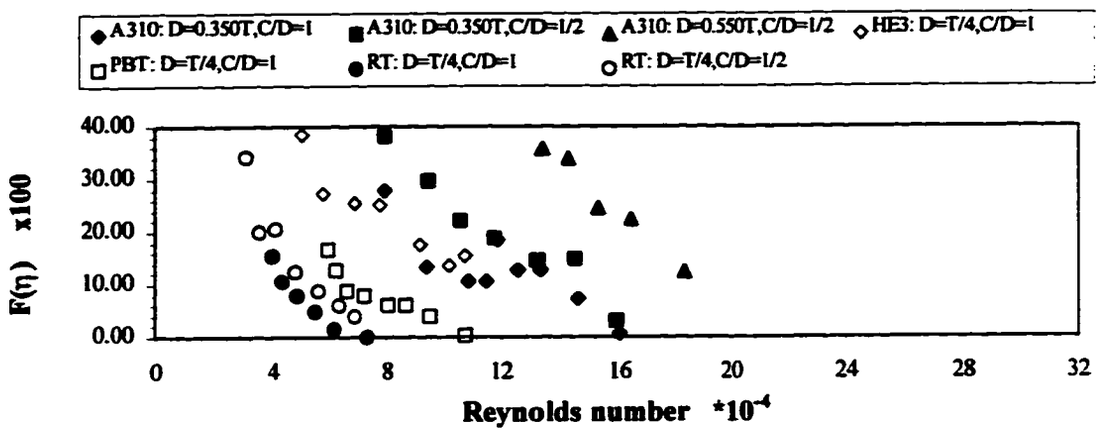

8d) Plots of F(η) vs ε_{max} for all seven cases.

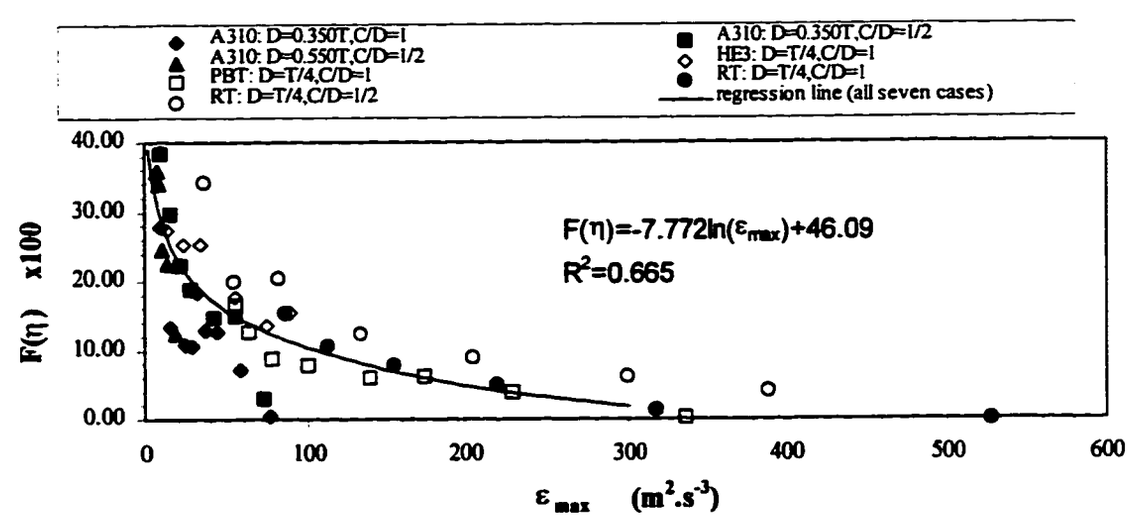

8e) Plots of $F(\eta)$ vs $P/\rho V_T$ for all seven cases.

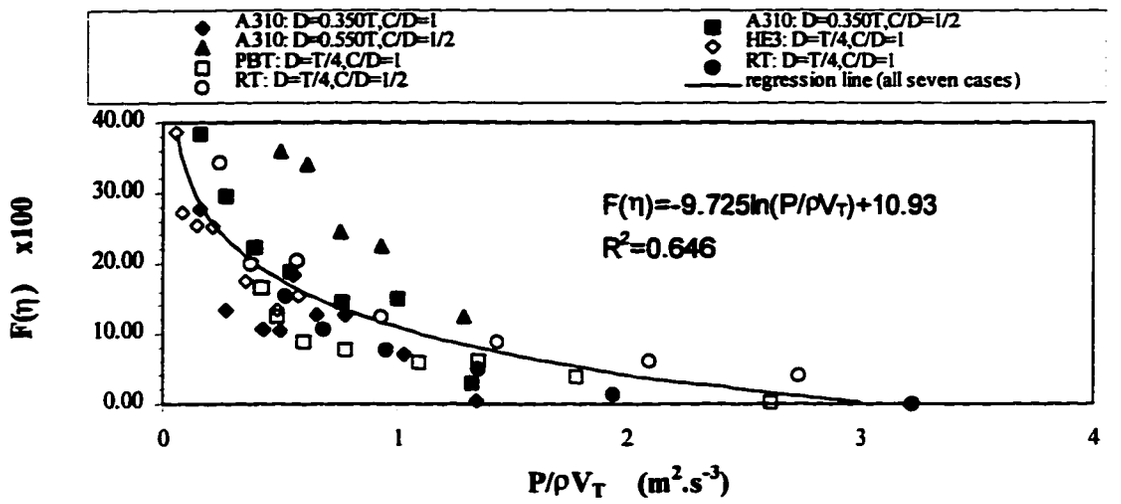

Figure 8-9 Correlation of $F(\eta)$ with mean drop sizes.

9a) Plots of $F(\eta)$ vs d_{10} for all seven cases

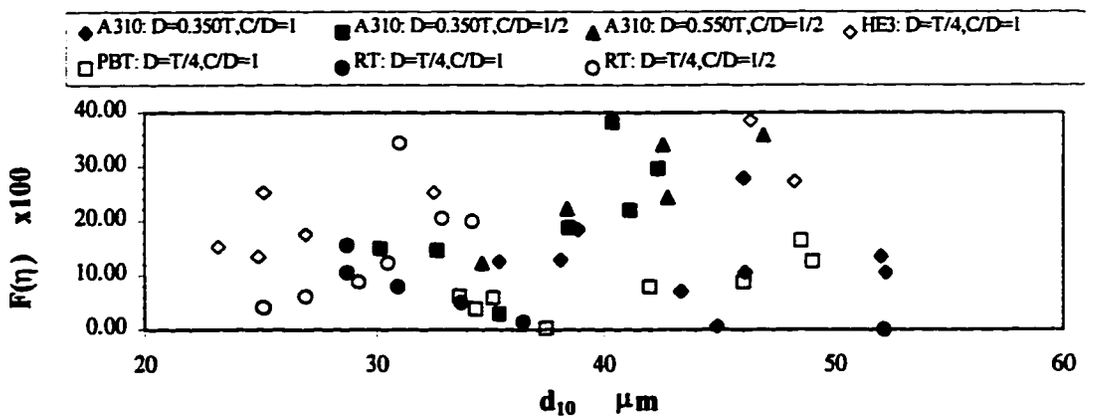

9b) Plots of F(η) vs d_{30} for all seven cases.

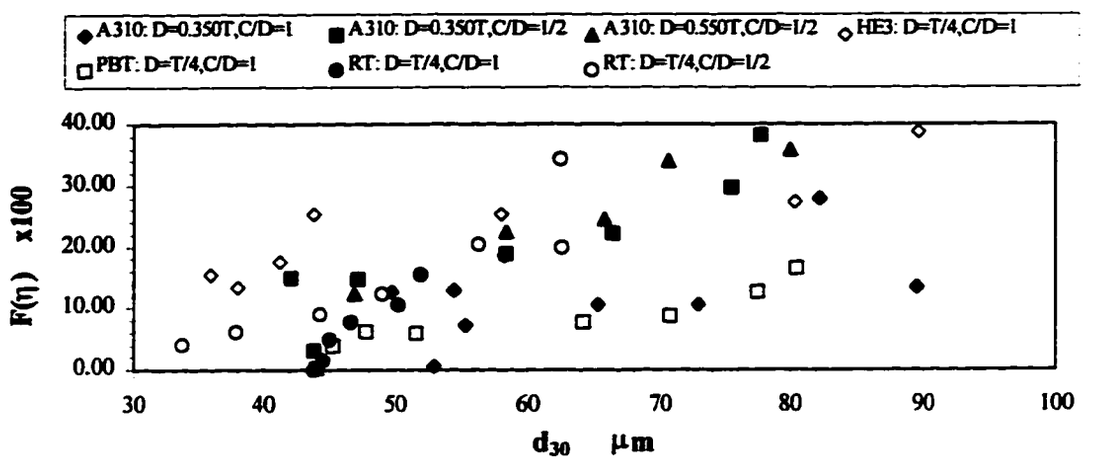

9c) Plots of F(η) vs d_{32} for all seven cases.

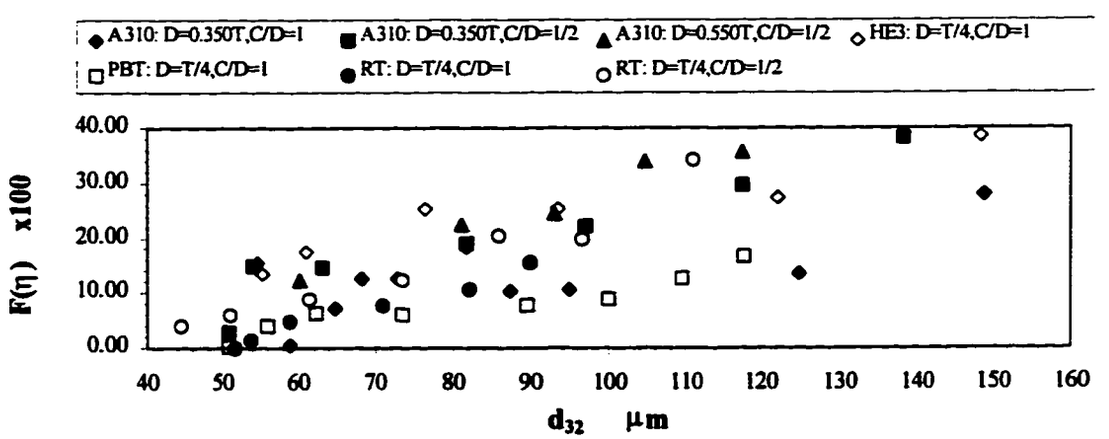

Figure 8-10 Correlation of $F(\eta)$ with scaled d_{30} and d_{32}.

10a) Plots of $F(\eta)$ vs d_{30}/d_{10} for all seven cases

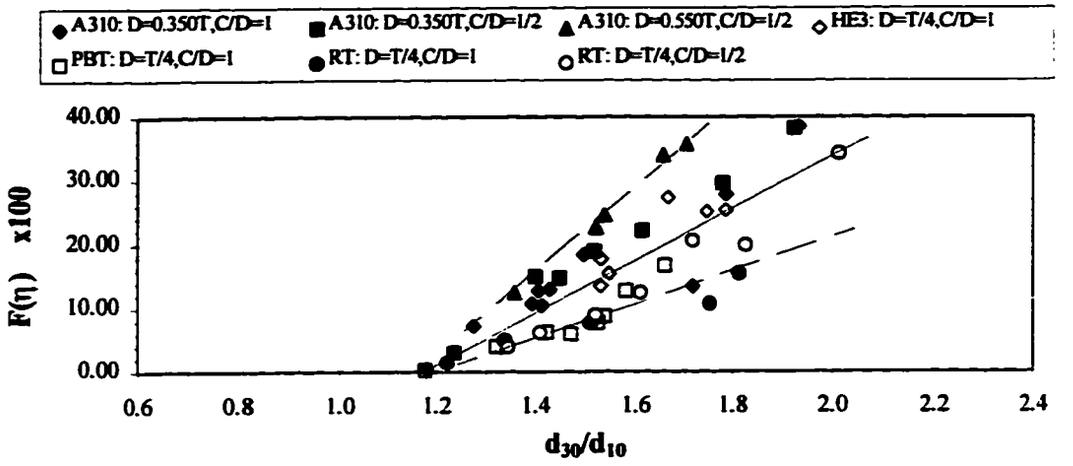

10b) Plots of $F(\eta)$ vs d_{32}/d_{10} for all seven cases.

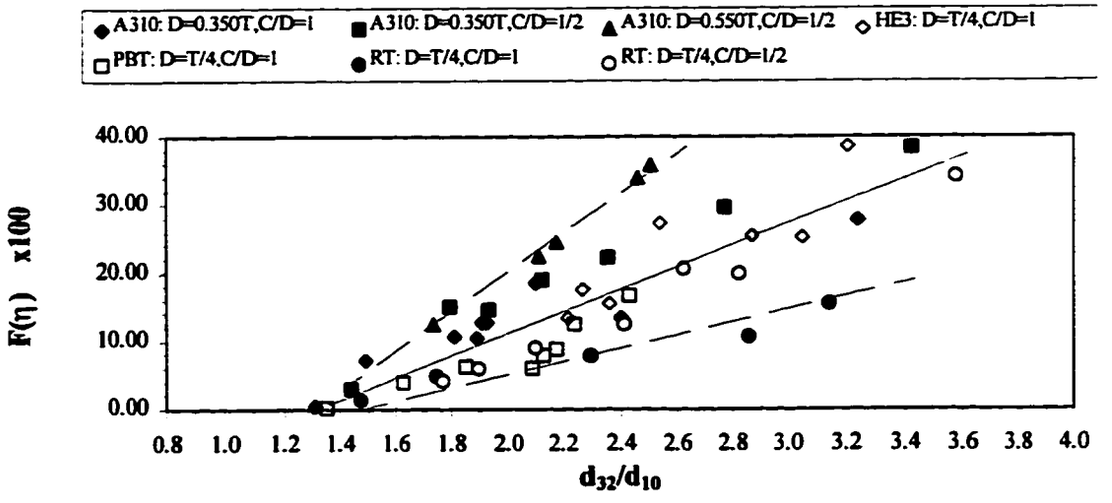

Figure 8-11 Correlation of the constant c with the flow.

11a) Plot of the constant c vs N for all seven cases.

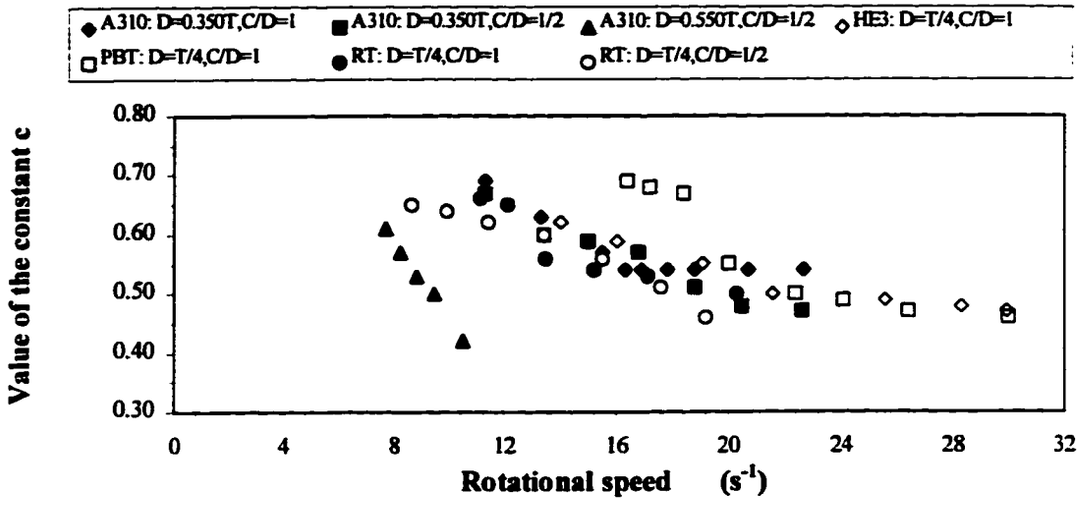

11b) Plot of the constant c vs ND for all seven cases.

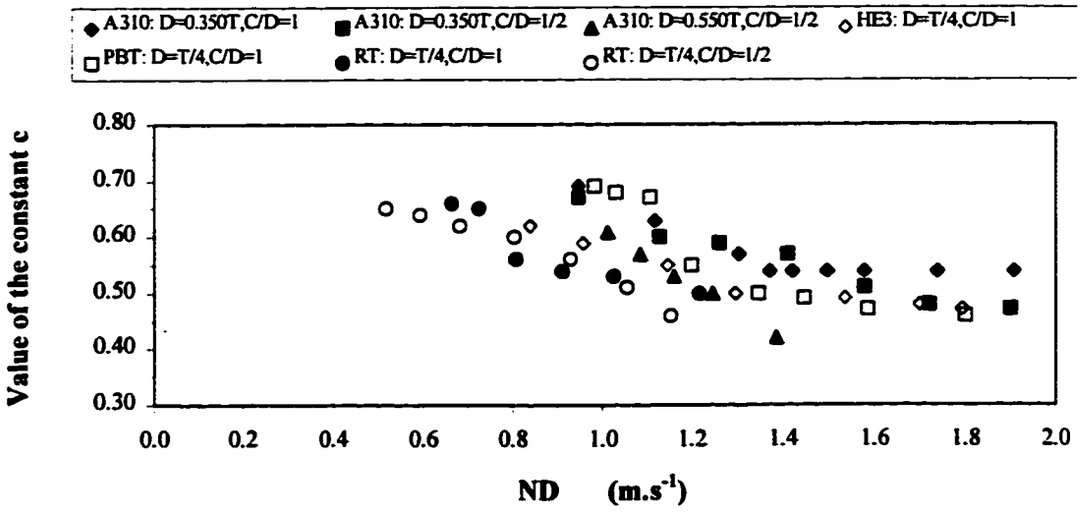

11c) Plot of the constant c vs Re for all seven cases.

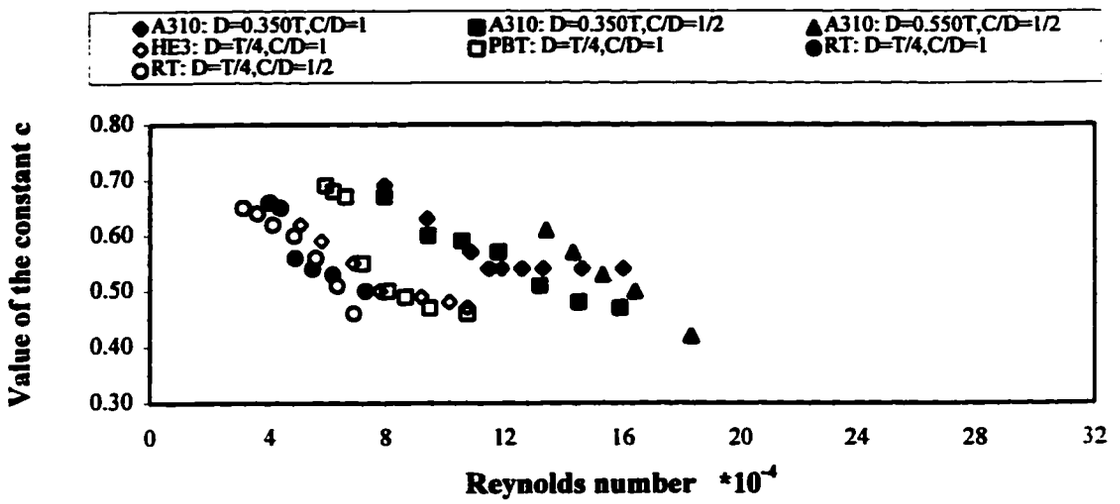

11d) Plot of the constant c vs ε_{max} for all seven cases.

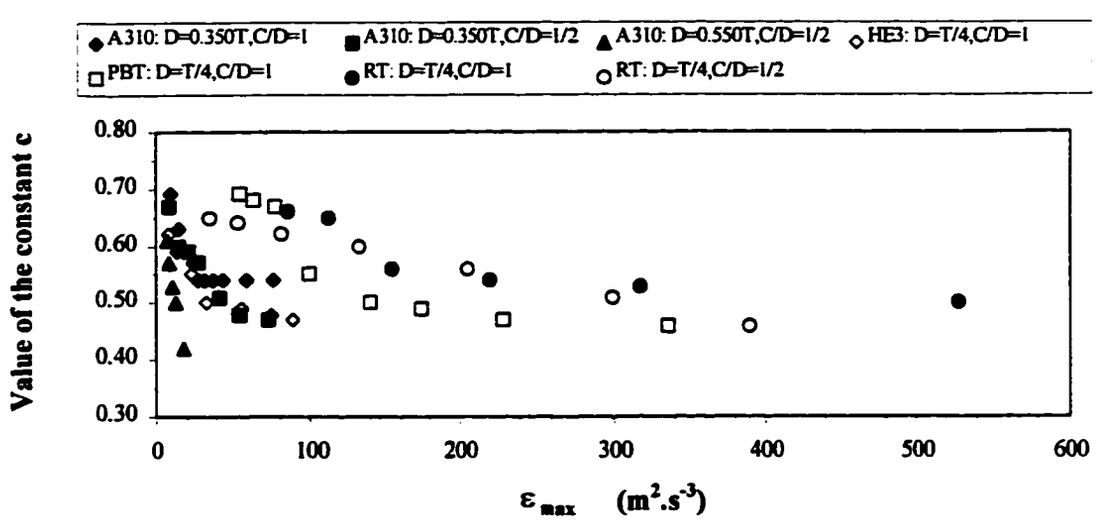

11e) Plot of the constant c vs $P/\rho V_T$ for all seven cases.

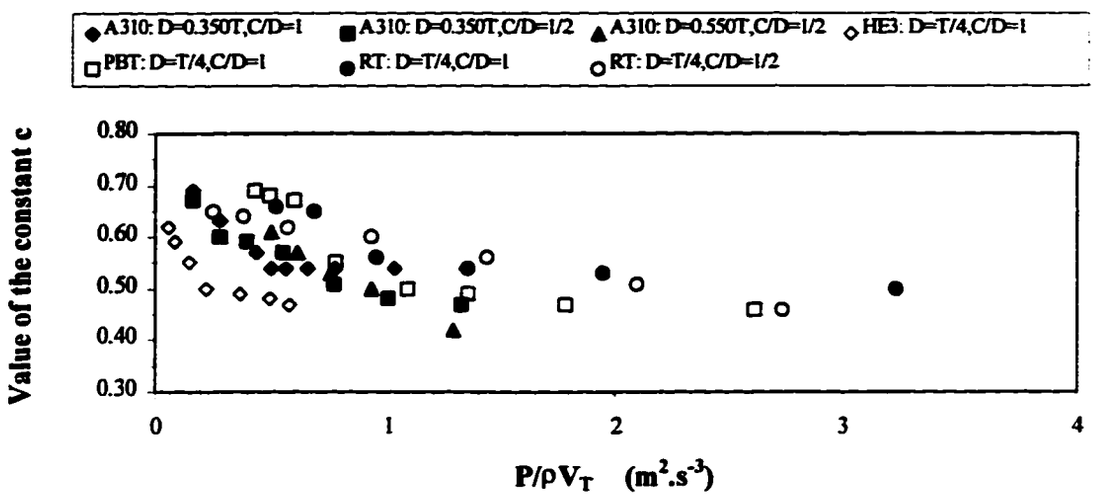

Figure 8-12 Correlation of Sauter mean diameter with the flow.

12a) Plot of Sauter mean diameter vs ND for all seven cases.

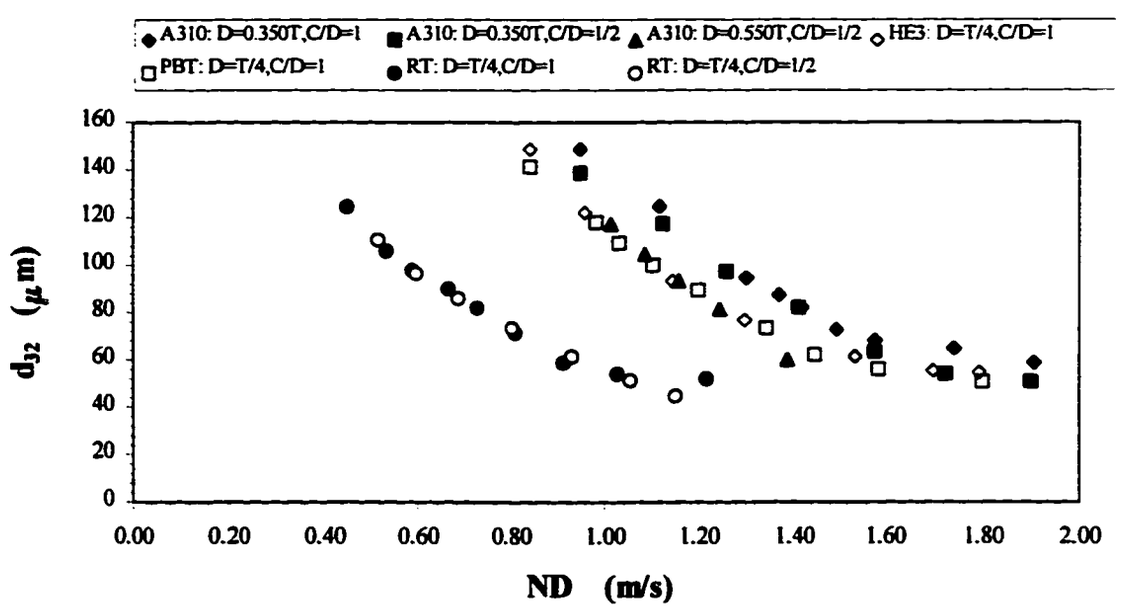

12b) Plot of Sauter mean diameter vs ε_{max} for all seven cases.

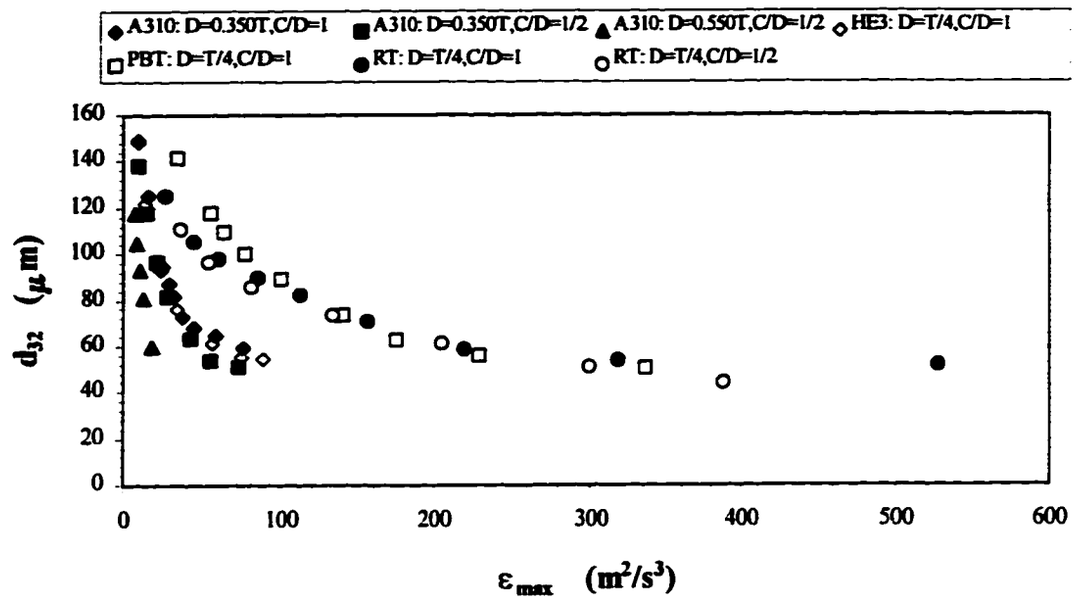

12c) Plot of Sauter mean diameter vs $P/\rho V_T$ for all seven cases.

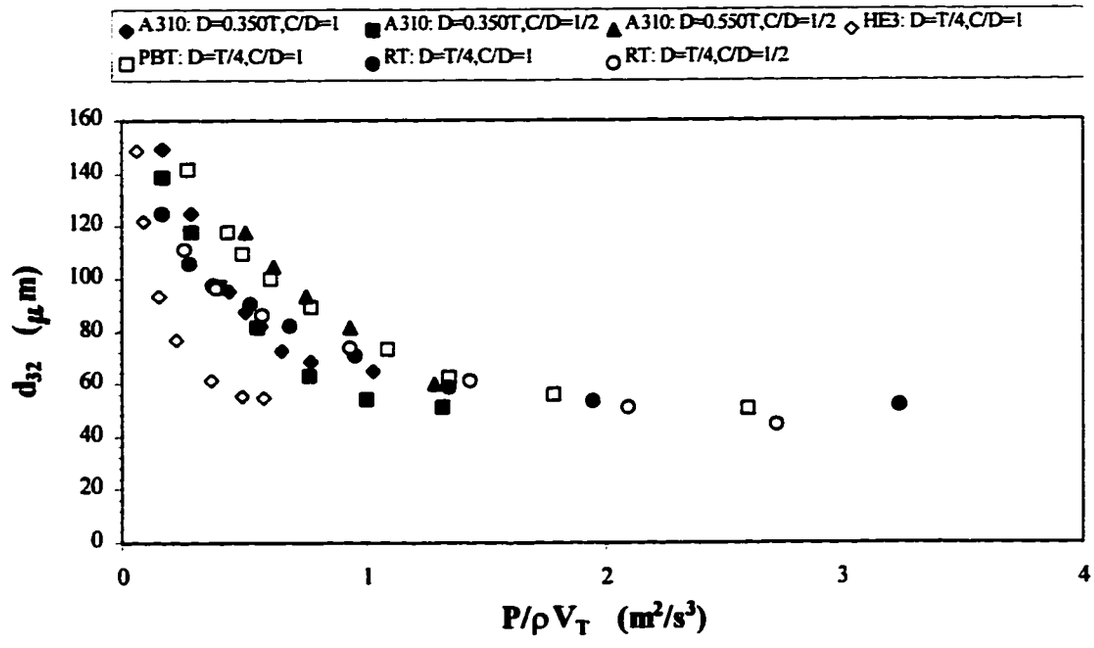

Figure 8-13 Plot of Sauter mean diameter vs $\varepsilon_{max}\cdot(D/D_0)^2$ for the A310, D_0=0.350T.

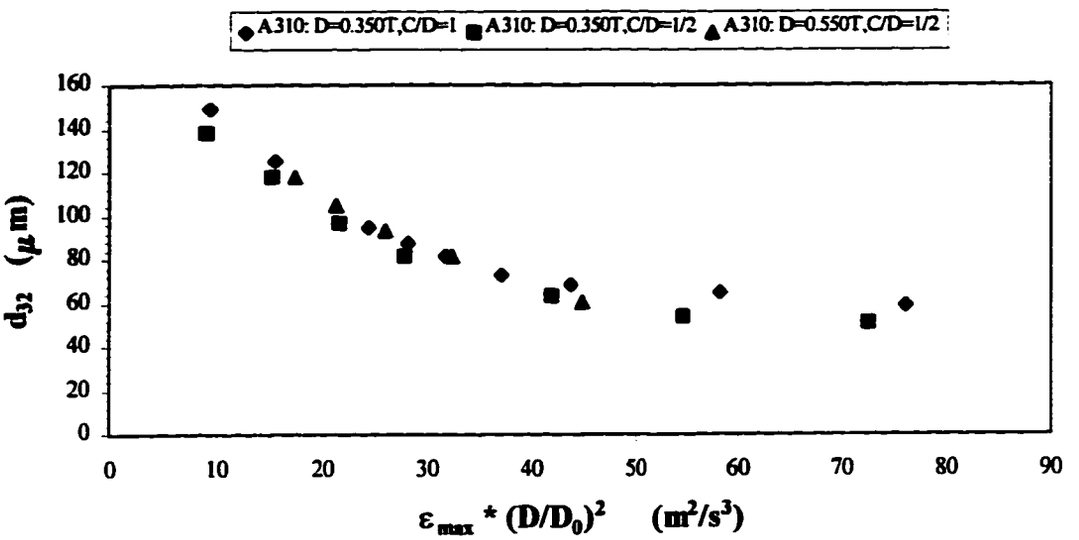

Figure 8-14 Plot of Sauter mean diameter vs $\varepsilon_{max}\cdot(D/D_0)^{-8/3}$ for the A310, D_0=0.350T.

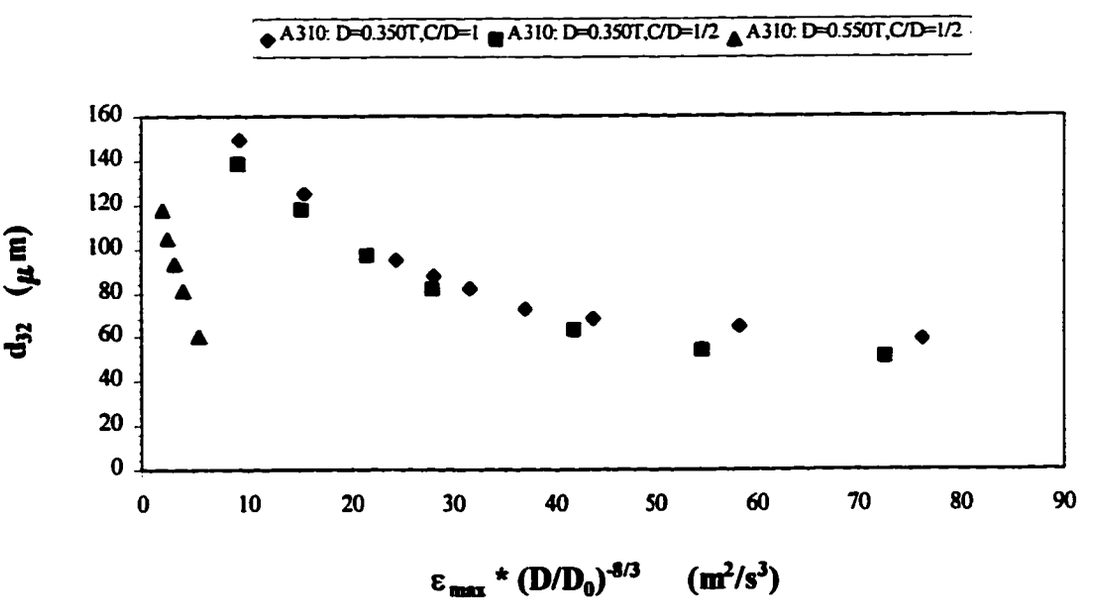

Figure 8-15a Plot of Sauter mean diameter vs ε_{max}·ND for all seven cases.

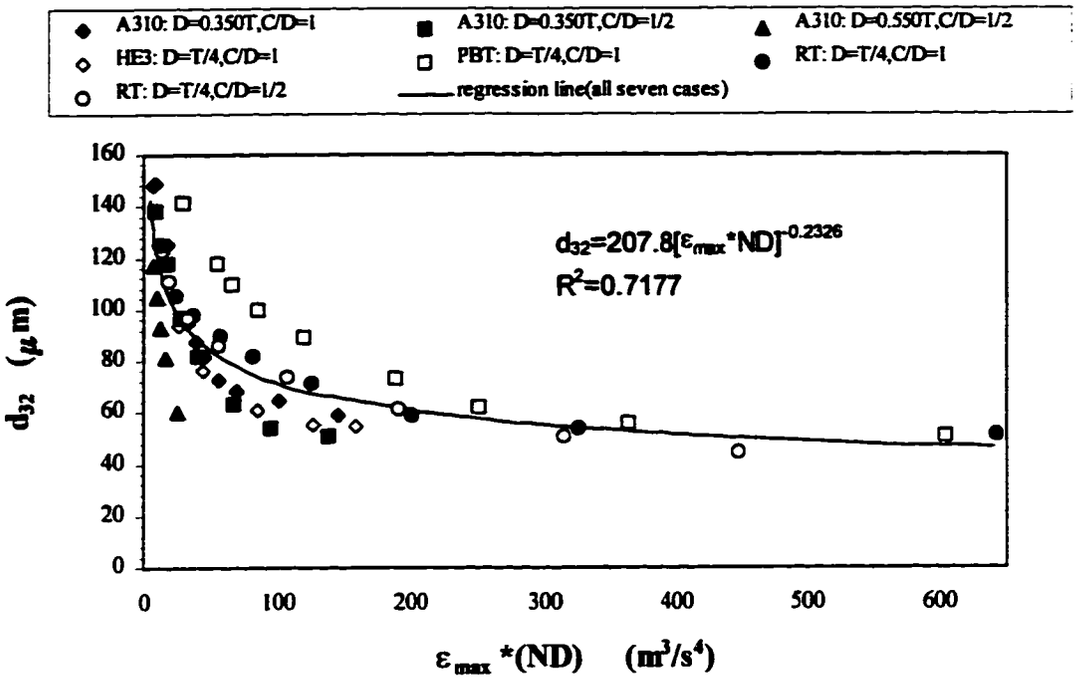

Figure 8-15b Plot of Sauter mean diameter vs ε_{max}·ND^2 for all seven cases.

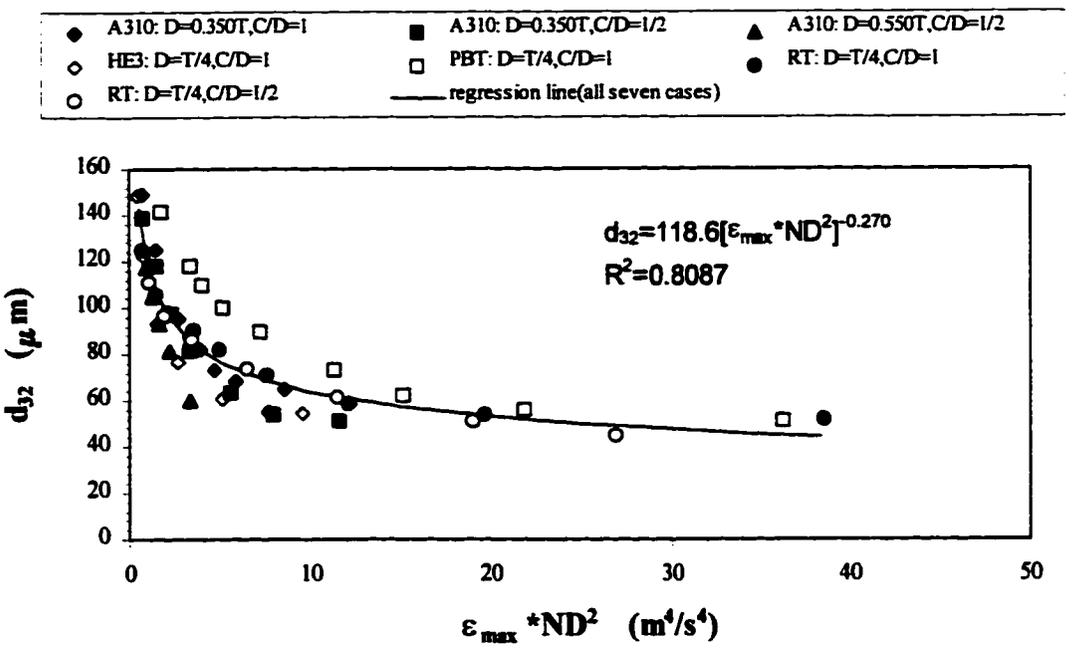

Figure 8-15c Plot of Sauter mean diameter vs $\varepsilon_{max}\cdot(ND)^2$ for all seven cases.

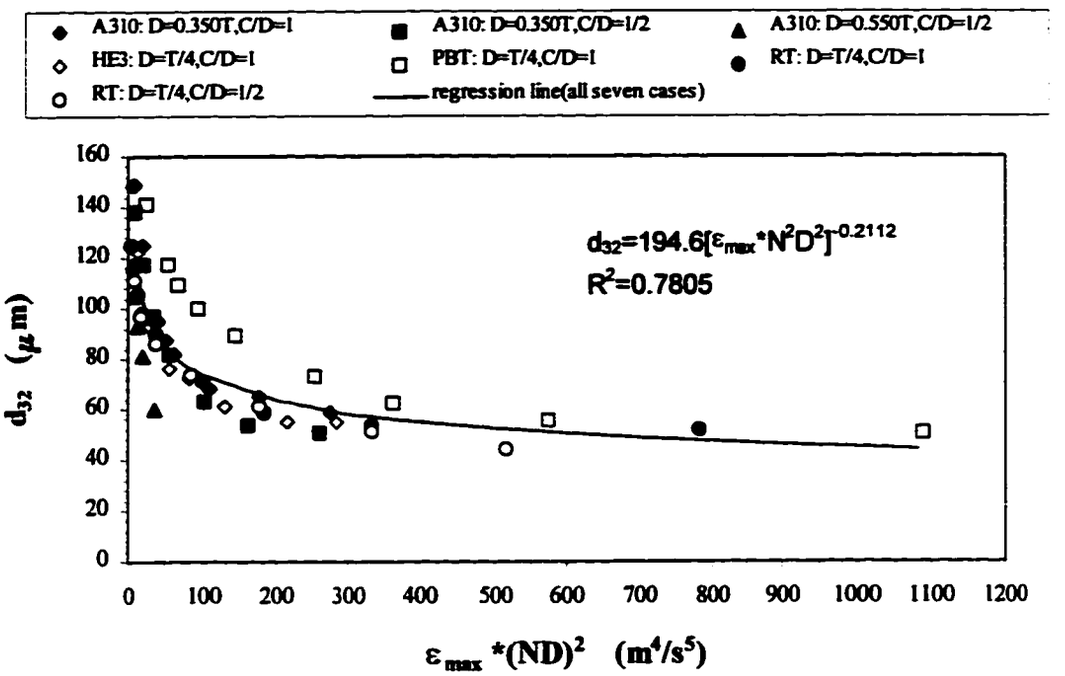

Figure 8-16a Plot of Sauter mean diameter vs $(P/\rho V_T)\cdot ND$ for all seven cases.

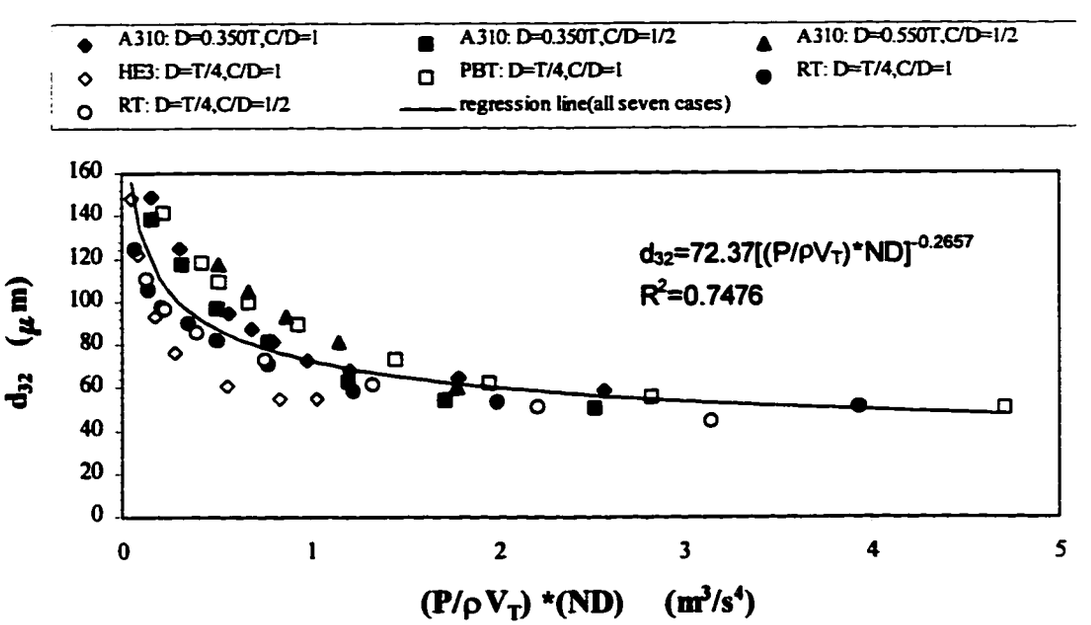

Figure 8-16b Plot of Sauter mean diameter vs $(P/\rho V_T)\cdot ND^2$ for all seven cases.

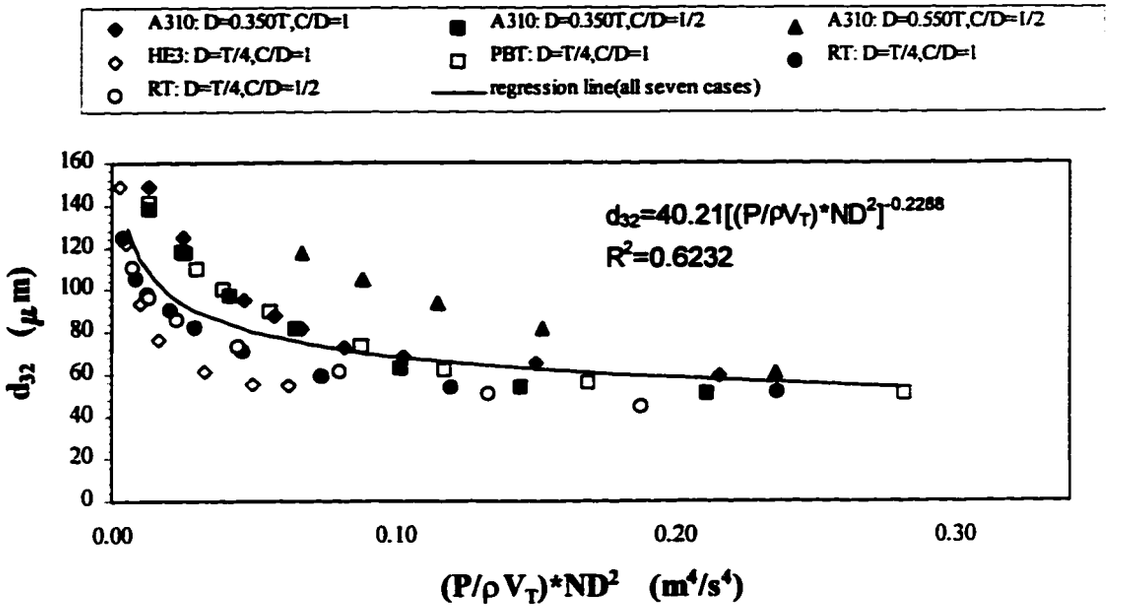

Figure 8-16c Plot of Sauter mean diameter vs $(P/\rho V_T)\cdot (ND)^2$ for all seven cases.

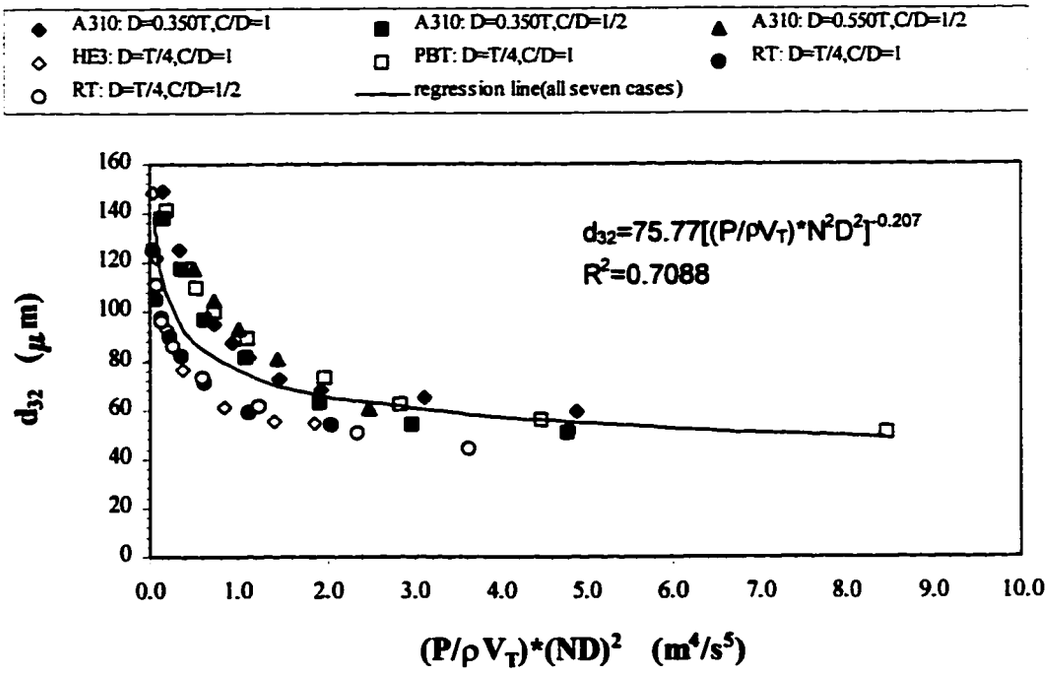

References

Berkman, P. D. and Calabrese, R. V., 1988, Dispersion of viscous liquids by turbulent flow in a static mixer. *AIChE J.* **34**, 602-609.

Blount, J. M. and Calabrese, R. V., Prediction of drop size in dilute agitated liquid-liquid systems: Further considerations. Page No. 120f, AIChE Annual Meeting, Miami Beach, FL, November, 1995.

Brown, D. E. and Pitt, K., 1972, Drop size distribution of stirred non-coalescing liquid-liquid system. *Chem. Eng. Sci.***27**, 577-583.

Brown, D. E. and Pitt, K., 1974, Effect of impeller geometry on drop break-up in a stirred liquid-liquid contactors. *Chem. Eng. Sci.* **29**, 345-348.

Calabrese, R. V., Wang, C. Y. and Bryner, N. P., 1986, Drop breakup in turbulent stirred-tank contactors, Part III: Correlations for mean size and drop size distribution. *AIChE J.* **32**, 677-681.

Chen, H. S. and Middleman, S., 1967, Drop size distribution in agitated liquid-liquid systems. *AIChE J* **13**, 989-995.

Costes, J. and Couderc, J. P., 1988, Study by laser Doppler anemometry of the turbulent flow induced by a Rushton turbine in a stirred tank: influence of the size of the units-I. mean flow and turbulence. *Chem. Eng. Sci.* **43**, 2751-2764.

Coulaloglou, C. A. and Tavlarides, L. L., 1976, Drop size distribution and coalescence frequencies of liquid-liquid dispersions in flow vessels. *AIChE J.* **22**, 289-297.

Cutter, L. A., 1966, Flow and turbulence in a stirred tank. *AIChE J.* 12, 35-45.

Gunkel, A.A. and Weber, M.E., 1975, Flow phenomena in stirred tanks: Part I. the impeller stream. *AIChE J.* **21**, 931-949.

Hinze, J. O., 1955, Fundamentals of the hydrodynamic Mechanism of splitting in dispersion processes. *AIChE J.* **1**,.289-295.

Hinze, J. O., 1987, *Turbulence*, Second Edition, McGraw-Hill, New York.

Kim, W. J. and Manning, F. S., 1964, Turbulence energy and intensity spectra in a baffled, stirred vessel. *AIChE J.* **10**, 747-752.

Komasawa, I., Kuboi R. and Otake, T., 1974, Fluid and particle motion in turbulent dispersion. *Chem. Eng. Sci.* **29**, 641.

Kresta, S. M., and Wood, P. E., 1991, Prediction of the three-dimensional turbulent flow in stirred tank. *AIChE J.* **37**, 448.

Kresta, S. M. and Wood, P. E., 1993, The mean flow field produced by a 45° pitched blade turbine: changes in the circulation pattern due to off bottom clearance. *Can. J. Chem. Eng.***71**, 42-53.

Nishikawa, M., Mori, F., Kayama, T. and Nishioka, S, 1991, Drop size distribution in a liquid-liquid phase mixing vessel. *J. Chem. Eng. Japan* **24**, 88-94.

Nishikawa, M., Okamoto, Y., Hashimoto, K. and Nagase, S., 1976, Turbulence energy spectra in baffled mixing vessels. *J. Chem. Eng. Japan* **9**, 489-494.

Nishikawa, M., Mori, F. and Fujieda, S., 1987, Average drop size in a liquid-liquid phase mixing vessel. *J. Chem. Eng. Japan* **20**, 82-88.

Okamoto, Y., Nishikawa, M. and Hashimoto, K., 1981, Energy dissipation rate distribution in mixing vessels and its effects on liquid-liquid dispersion and solid-liquid mass transfer. *Int. Chem. Eng.***21**, 88-94.

Okufi, S., Perez de Ortiz, E. S. and Sawistowski, H., 1990, Scale-up of liquid-liquid dispersions in stirred tanks. *Can. J. Chem. Eng.* **68**, 400-406.

Pacek, A. W. and Nienow, A. W., 1995, Measurement of drop size distribution in concentrated liquid-liquid dispersions: video and capillary techniques. *Trans IChemE.* **73**, 512-518.

Parthasarathy, R. and Ahmed, N., 1994, Bubble size distribution in a gas sparged vessel agitated by a Rushton turbine. *Ind. Eng. Chem. Res.* **33**, 703-711.

Sprow, F. B., 1967a, Drop size distributions in strongly coalescing agitated liquid-liquid systems. *AIChE J.* **13**, 995-998.

Sprow, F. B., 1967b, Distribution of drop sizes produced in turbulent liquid-liquid dispersion. *Chem. Eng. Sci.***22**, 435-442.

Tavlarides, L. L. and Stamatoudis, M., 1981, The analysis of interphase reactions and mass transfer in liquid-liquid dispersions. *Adv. Chem. Eng.* **11**, 199-273.

Wu, H. and Patterson, G. K., 1989, Laser Doppler measurements of turbulent-flow parameters in a stirred mixer. *Chem. Eng. Sci.* **44**, 2207-2221.

Chapter 9

Synthesis

This dissertation research had the following objectives:

a) to investigate the turbulence energy dissipation (average and local) in the impeller regions where the bulk of the input power is dissipated and the maximum turbulence dissipation rate exists; and to investigate where the power input goes and the energy distribution between the convective and the turbulent energy.

b) to investigate the effect of tank geometry on the maximum turbulence energy dissipation rate, ε_{max}.

c) to characterize liquid-liquid dispersions generated by different impellers with various tank geometries.

d) to examine the suitability of the two existing scaleup principles - constant tip speed of an impeller or constant average power input per unit mass, and to improve the understanding of fluid flow fundamentals of scaling up liquid-liquid dispersions.

Characterization of the Turbulence Energy Dissipation in the Impeller Regions

To determine the average turbulence energy dissipation rate, a macroscopic mechanical energy balance equation was re-derived since discrepancies were found in published works of previous investigators. The LDA was first validated and then used to measure all three components of instantaneous velocities for the three impellers (the RT, the PBT and the A310). The average turbulence energy dissipation rate in the impeller regions was calculated using the energy balance and the LDA data.

For the local turbulence energy dissipation rate, ε, the equation ($\varepsilon=Av^3/L$) was verified in the impeller regions by first examining the assumption of isotropic flow which is inherent in the equation; then the length scale L and the constant A were determined using tuft visualization experiments and a comparison between energy balance results and integration of the estimated local ε's.

Experimental results show that the flow in the impeller and impeller discharge stream is approximately locally isotropic for the three impellers examined (the RT, PBT and A310). The two equations (Eqs.(5-42) and (5-43)) for the average turbulence energy dissipation, $\dot{E}_v$, agree well for the three impellers. The equation ($\varepsilon=Av^3/L$) with A=1 and L=D/10 gives a reliable estimate of the local turbulence energy dissipation rate. The constant A in the equation can be determined by comparison of the macroscopic energy balance (Eq.(5-42)) with the integrated local dissipation (Eq.(5-43)) for any impeller, and is very close to 1 for the three impellers examined.

The dissipation is always very high in the impeller region and in the impeller discharge stream. The bulk of the energy is dissipated in the small volume occupied by the impeller and the impeller discharge for all three impellers: in order of increasing percentages 38.1% (A310, 13.1% of the tank volume), 43.5% (RT, 9.83% of the tank volume) and 70.5% (PBT, 13.1% of the tank volume). The dominant characteristics of energy distribution are different for each impeller. The A310 is most efficient at generating convective flow. The RT generates the most turbulent kinetic energy (TKE), and the PBT derives a much larger portion of its energy from the return flow. These differences should be taken into account when selecting an impeller for a specific application.

Effects of Tank Geometry on ε_{max}

The maximum turbulence energy dissipation rate, ε_{max}, was estimated using the equation $\varepsilon=Av^3/L$. First, the location of ε_{max} in the flow field was determined for each of the four impellers (the PBT, the A310, the HE3 and the RT). Then, the effects of geometric variables (number of baffles, (N_f), impeller diameter, (D), off bottom clearance, (C, or the ratio of C/D)) on ε_{max} were investigated using three different factorial designs. The dominant effects and interactions were highlighted and used in the study of liquid-liquid dispersions.

Experimental results show that the local dissipation scales exactly with N^3, when the tank geometry is held constant. The maximum dissipation is located on the traverse immediately below the impeller for the three axial impellers (the PBT, the A310 and the

HE3), and on the traverse at the tip of the impeller blades for the RT. The maximum local dissipation is larger for impellers with a larger power number.

Comparison of the scaled ε_{max} values for all geometries considered shows significant variation between the results both when constant power input per unit mass ($P/\rho V_T$) is used as the scaling criterion, and when ε_{max} is scaled with N^3D^2. Taking the results of all three factorial designs together, several important conclusions can be drawn about the effect of tank geometry on ε_{max}:

1) The dominant variable was shown to be the impeller diameter. This effect is in addition to the expected scaling with D^2. This can only be due to interactions between the impeller and the tank walls; put another way, significant changes in the turbulent flow field occur when the D/T ratio is changed.
2) A substantial dependence on the off bottom clearance was also demonstrated. This dependence is best quantified when a dimensionless form, C/D is used. The off bottom clearance often interacts strongly with the impeller diameter, and thus should not be considered as an independent variable.
3) The number of baffles, N_f, has no significant effect on ε_{max}, either as an independent variable, or in the form of interactions with other geometric variables. This is true for all four impellers, and all three factorial designs.
4) To maintain a roughly constant ε_{max}, scale up which is not geometrically exact should be based on D^2, not on D^5. This is the scaling predicted from theory, rather than the constant $P/\rho V_T$ (equivalently constant power per unit mass, or average dissipation) which is commonly used in the literature.

Characterization of Liquid-Liquid Dispersions

Drop sizes were measured over a wide range of rotational speeds using the PDPA. First, the PDPA was validated by checking the repeatability of the instrument and the experiment and using standard particles. The initial analysis of the drop size was focused on the drop size distribution; on the minimum drop size in oil/water dispersions and its relationship to turbulent flow, especially the ε_{max}; and on the Sauter mean diameter and its relationship to ND, ε_{max} and $P/\rho V_T$. Four impellers (the A310, HE3, PBT and RT)

with varying tank geometries were used. The two scale-up rules (constant impeller tip speed and constant power input per unit mass) were examined using all the data obtained for the four impellers and varying tank geometries. Three sets of conclusions can be drawn from the analysis of experimental results:

a) Drop size distribution

The drop size distributions (normal or log-normal, mono-modal or bimodal) for dispersions proposed by previous investigators is only true for the dispersions under the specific operation conditions used. By checking a wide range of rotational speeds for the four different impellers, four types of drop size distribution were found in the evolution of drop size distribution with N: the long tail distribution; the double peak distribution; the skew distribution and the skew-normal distribution. Excepting the long tail distribution, the drop size distribution can be predicted using two superimposed normal distributions with different parameters of (d_{10}, $\sigma(d)$) and two diameter subranges at different N's.

b) Minimum drop size

Use of the Kolmogoroff length scale as an estimate of the minimum drop size is not accurate. The flow in agitated tanks is in an inertial subrange. The Kolmogoroff length scale is generally suitable as an estimate of the *magnitude* of the drops, but it cannot be used as an estimate of the minimum drop size in the dispersion. A significant number of drops smaller than the Kolmogoroff length scale were measured in the seven tank geometries investigated. When N is low, the number percentage of drops smaller than the Kolmogoroff length scale, $F(\eta)$, is high due to drop breakup dominating in the dispersion; $F(\eta)$ decreases with an increase in N since coalescence coexists in the enhanced flow. Only at very high N's where coalescence may become significant does $F(\eta)$ approach zero. $F(\eta)$ is clearly related to ε_{max} and the drop size distribution. When d_{30}/d_{10}=1.19, $F(\eta)$ drops to 0 and the minimum drop size may be estimated by the Kolmogoroff length scale.

c) Sauter mean diameter

The assumption that d_{32} is directly proportional to the maximum stable drop diameter is not valid when the operating conditions change dramatically. Relating d_{32} to the flow requires consideration of the effect of the flow on the constant c in the equation $d_{32}=c \cdot d_{max}$, and the interaction between ε_{max} and the mean flow on drop breakup in agitated tanks. Scale up using constant tip speed is not suitable, and constant power input per unit mass is not as good a scale-up criterion as ε_{max} for scale up of the dispersions studied. The correlation given in Eq. (8-12) is suggested from this work. The effect of σ and ρ_c on d_{32} needs to be verified, together with the constant in Eq. (8-12), when different dispersions are used.

Advancements in Knowledge

This work represents the first effort to characterize the turbulence energy dissipation in the impeller regions by combining both the average and local dissipation, and by analyzing its distribution between convective flow and turbulent flow. A method to determine the constant A and the length scale L in Eq. (2-41) is proposed: comparison of the macroscopic energy balance (Eq.(5-42)) with the integrated local dissipation (Eq.(5-43)). This method is suitable for any impeller or impeller regions. It avoids the difficulty of measuring velocities in the baffle regions which previous investigators explicitly avoid mentioning. The energy distribution between the convective flow and the turbulent flow for the three impellers (the RT, the PBT and the A310) explains the differences among different impellers, and presents useful information for selecting an impeller for a specific application. The A310 has not been used in such an investigation before.

This work represents the first extensive analysis of the effect of tank geometry on the maximum turbulence energy dissipation rate, ε_{max}. The four impellers (the RT, PBT, A310 and HE3) represent the full spectrum of impellers currently used for turbulent mixing in industry. The results of the effect of tank geometry on ε_{max} provide some

guidance as to when these effects will be most important, and what values of ε_{max} can be expected for some standard impellers and tank configurations.

The Kolmogoroff length scale has commonly been used as the estimate of minimum drop size in dispersions in agitated tanks. For the first time this belief is questioned and rejected, based on the experimental results obtained in this work.

Also, the constant c in equation $d_{32}=c \cdot d_{max}$ has never been examined. The constant c is found to be related to the flow when the operating conditions change dramatically. For the first time it is proposed that relating d_{32} to the flow requires consideration of the effect of the flow on the constant c.

This work represents the first effort to compare the suitability of ND, $P/\rho V_T$ and ε_{max} in the scale-up of liquid-liquid dispersions. Experimental results show that d_{32} depends both on ε_{max} and the circulation. This is most accurately represented by $\varepsilon_{max} \cdot ND^2$.

Future Research Needs Related to This Work

At least four projects may be devised from this work:

a) the characteristics of the flow at high Reynolds numbers. When N is very high in three out of the seven cases investigated in drop size measurement, $F(\eta)$ appears to agree with what Kolmogoroff length scale predicts, which is assumed to be applicable for the flow in viscous subrange: it may be meaningful to investigate the turbulence characteristics of flow agitated by different impellers in tanks when the Reynolds number is very high and determine if it is possible that the flow is in the viscous subrange by checking the energy spectrum. This effort may be not easily accomplished because of the high wavenumbers present in the viscous subrange, but it would be helpful to better understand the characteristics of the flow in agitated tanks and to determine the suitability of Kolmogoroff length scale for dispersions in flow fields in viscous subrange.

b) the evolution of the drop size distribution with N for *different dispersions* with various tank geometries and with *different volume fractions* of dispersed phases. The drop size distribution determines both the mean drop diameter and size distribution on both sides of the mean diameter. It holds all the information about the droplets in a

dispersion. Therefore, the evolution of the drop size distribution with N needs to be investigated extensively.

c) minimum drop size in different dispersions.

d) test of the correlation of $d_{32} \propto (\varepsilon_{max}\ ND^2)$ with varying tank diameters and fluid properties. In this work, although the ratio D/T was changed for the A310, the tank diameter was kept the same; and the dispersed phase was also unchanged. To develop a reliable scale-up rule requires study not only of different ratios of D/T but also different T's, and different dispersed fluids. For the correlation of d_{32} with physical properties of a dispersed phase fluid, a lot of work done by previous investigators can be used (Arai, et al., 1977, Calabrese, et al., 1986a, Calabrese et al., 1986b, Lagisetty, et al., 1986. Nishikawa, et al., 1991, Wang and Calabrese, 1986).

References

Arai, K., Konno, M., Matunaga, Y. and Saito, S., 1977, Effect of dispersed-phase viscosity on the maximum stable drop size for breakup in turbulent flow. *J. Chem. Eng. Japan* **10**, 325-330.

Calabrese, R. V., Chang, T. P. K. and Dang, P. T., 1986a, Drop breakup in turbulent stirred-tank contactors, Part I: Effect of dispersed-phase viscosity. *AIChE J.* **32**, 657-666.

Calabrese, R. V., Wang, C. Y. and Bryner, N. P., 1986b, Drop breakup in turbulent stirred-tank contactors, Part III: Correlations for mean size and drop size distribution. *AIChE J.* **32**, 677-681.

Lagisetty, J. S., Das, P. K., Kumar, R. and Gandhi, K. S., 1986, Breakage of viscous and non-Newtonian drops in stirred dispersions. *Chem. Eng. Sci.* **41**, 65-72.

Nishikawa, M., Mori, F., Kayama, T. and Nishioka, S, 1991, Drop size distribution in a liquid-liquid phase mixing vessel. *J. Chem. Eng. Japan* **24**, 88-94.

Wang, C. Y. and Calabrese, R. V., 1986, Drop breakup in turbulent stirred-tank contactors, Part II: Relative influence of viscosity and interfacial tension. *AIChE J.* **32**, 667-676.

Appendix-1

Drop Size Distribution Data

Figure A-1 Plots of drop size distributions at different rotational speeds.

a) A310: D=0.350T, C/D=1/2, 2r/D=0.50.

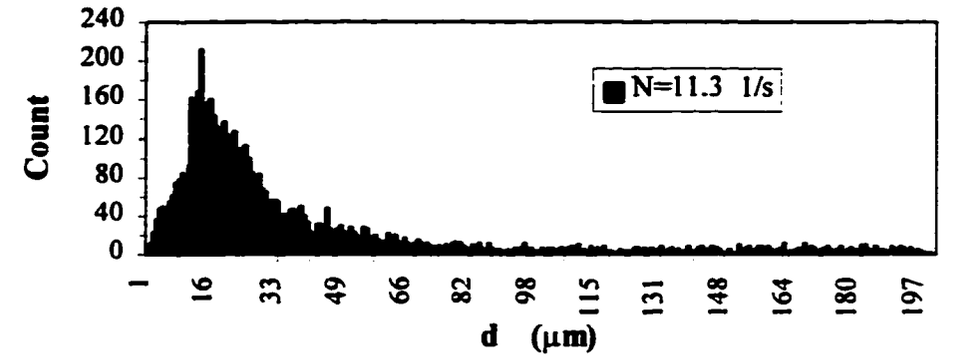

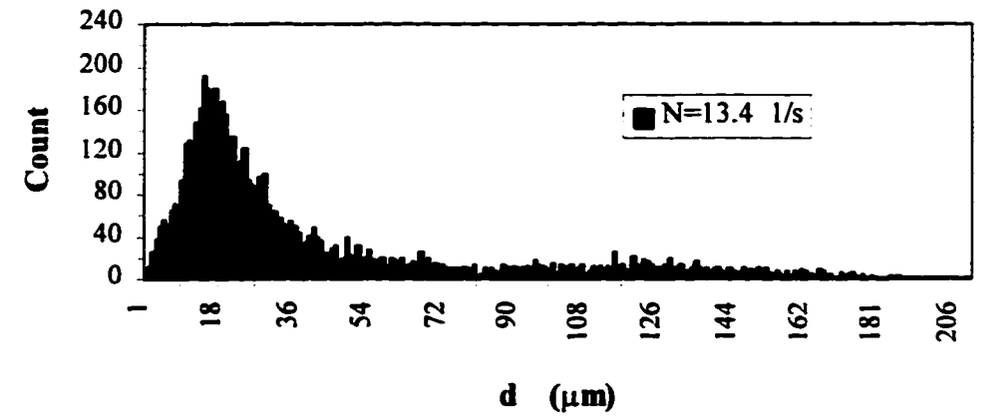

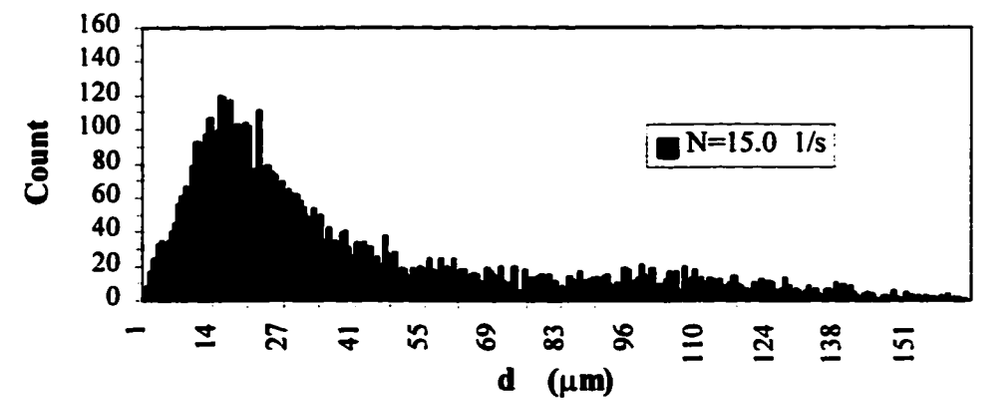

Cont'd **Figure A-1a**

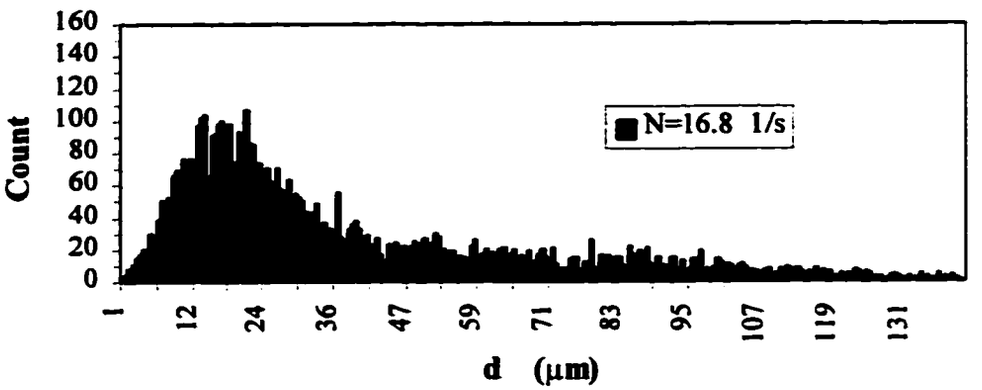

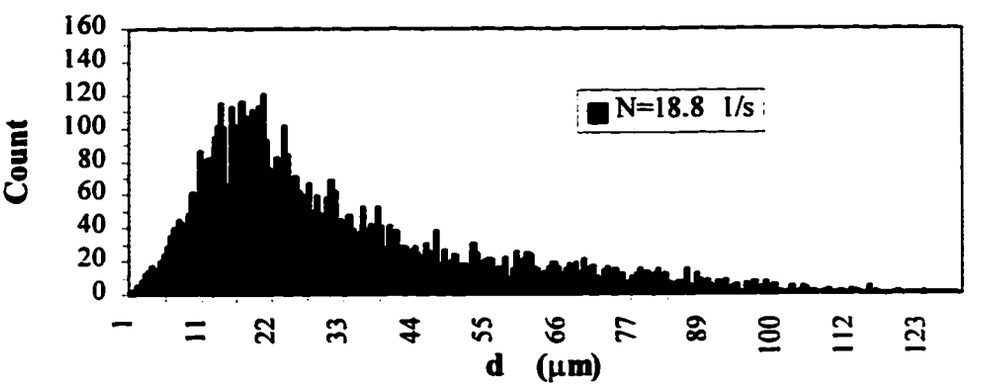

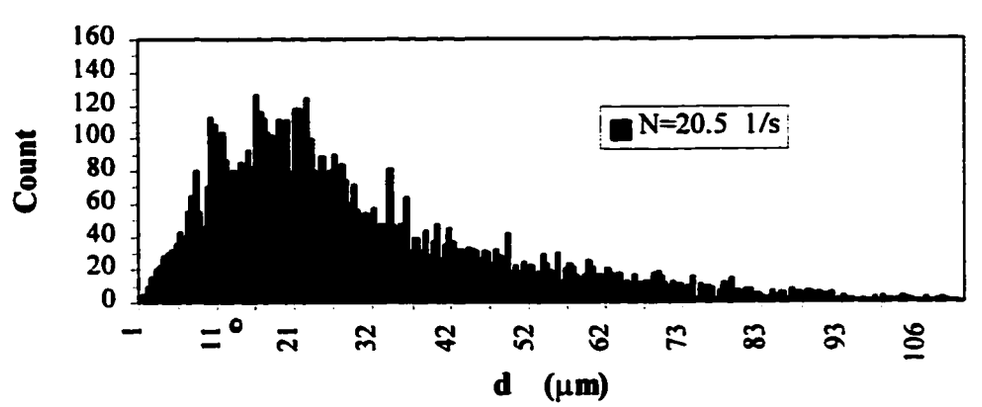

Cont'd **Figure A-1a**

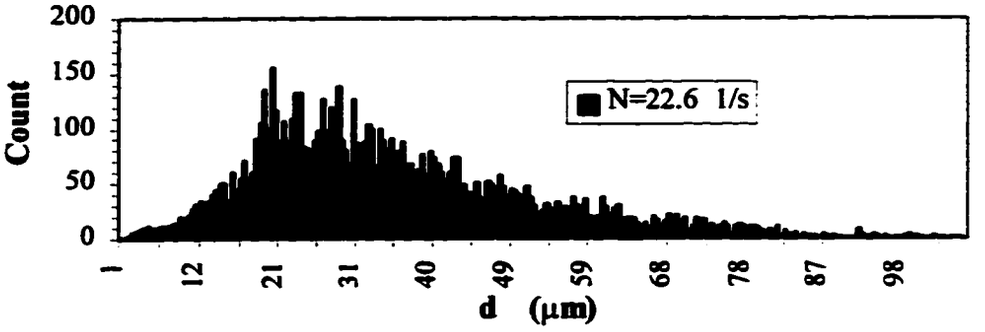

b) A310: D=0.550T, C/D=1/2, 2r/D=0.55.

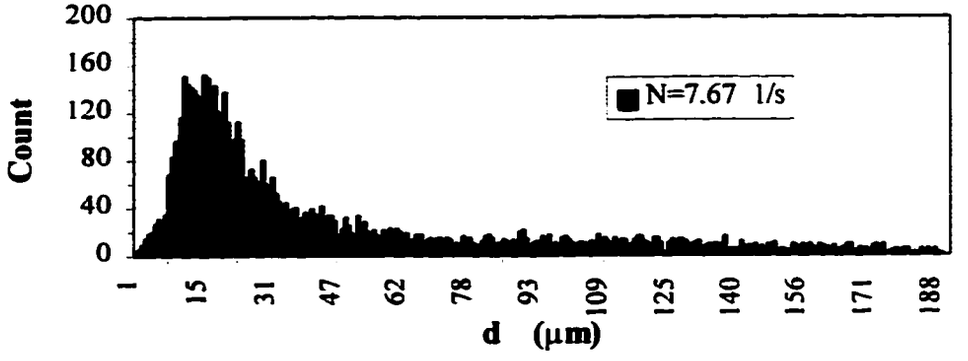

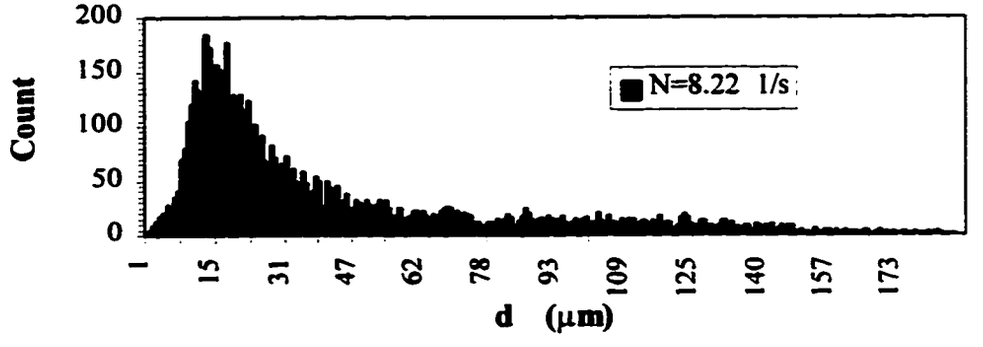

Cont'd **Figure A-1b**

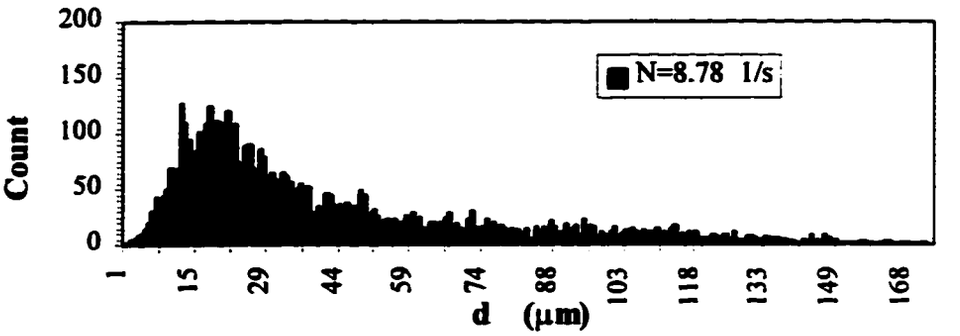

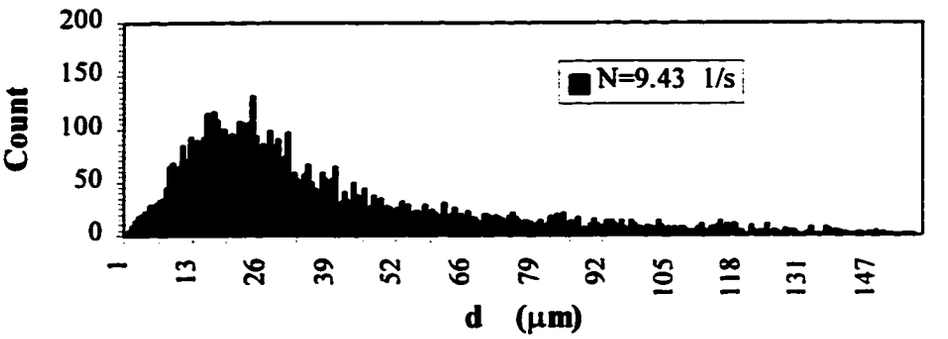

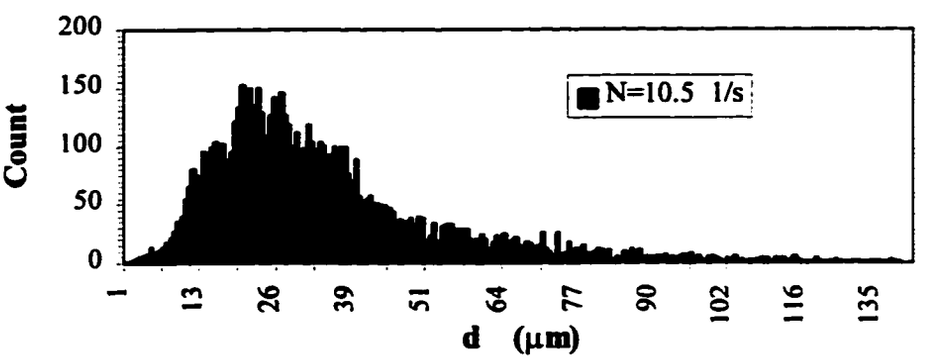

c) HE3: D=T/4, C/D=1, 2r/D=0.30.

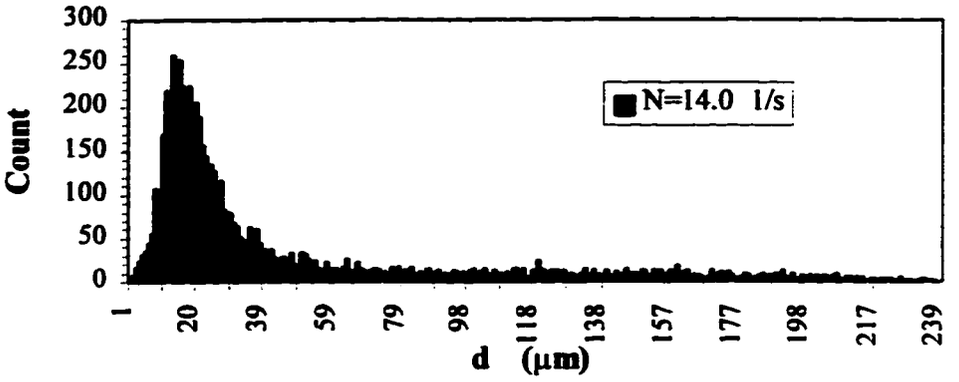

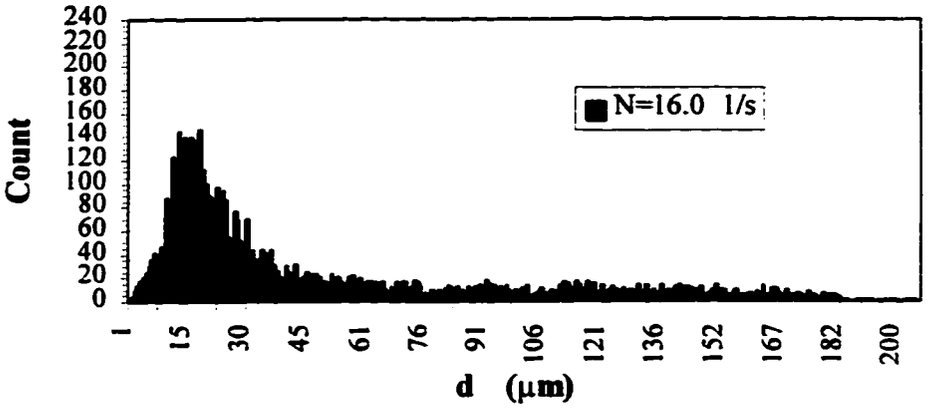

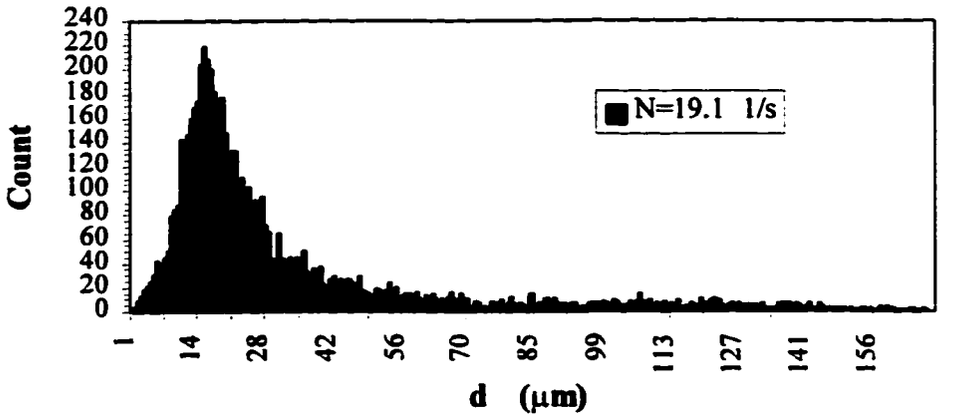

Cont'd **Figure A-1c**

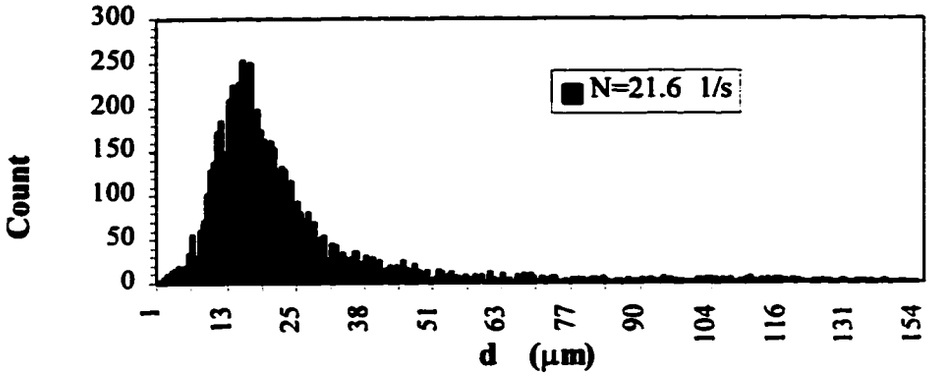

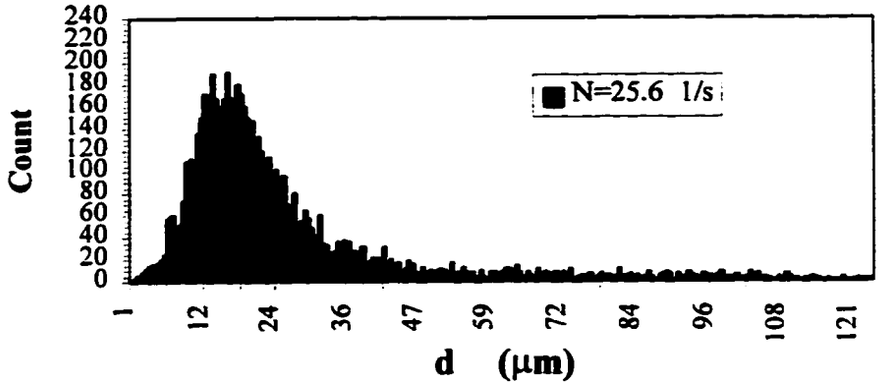

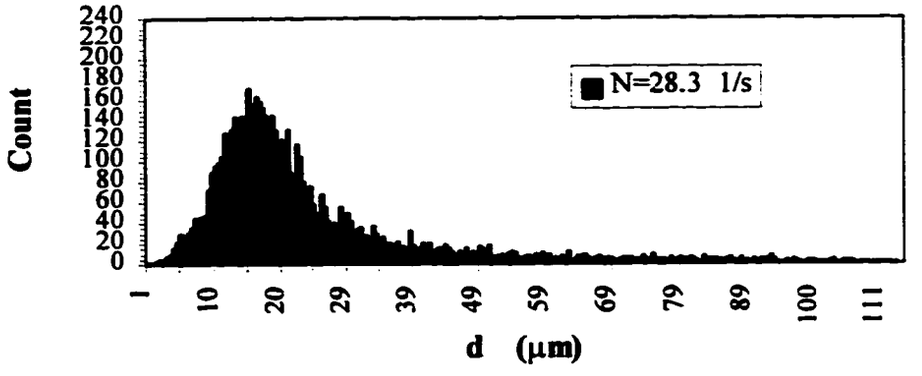

Cont'd **Figure A-1c**

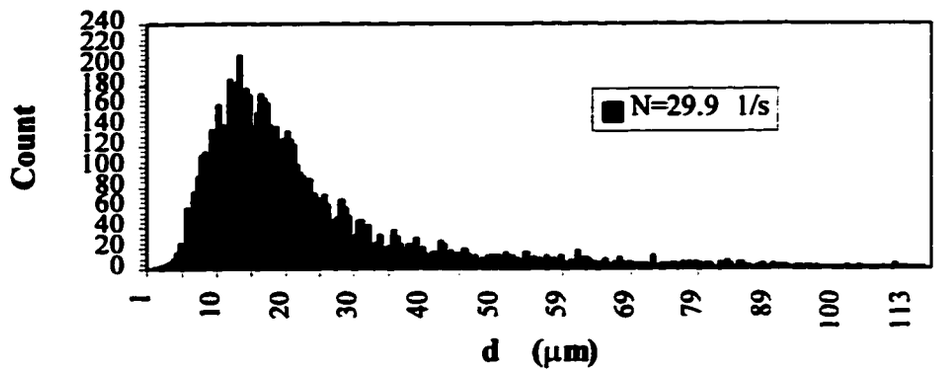

d) PBT: D=T/4, C/D=1, 2r/D=0.30.

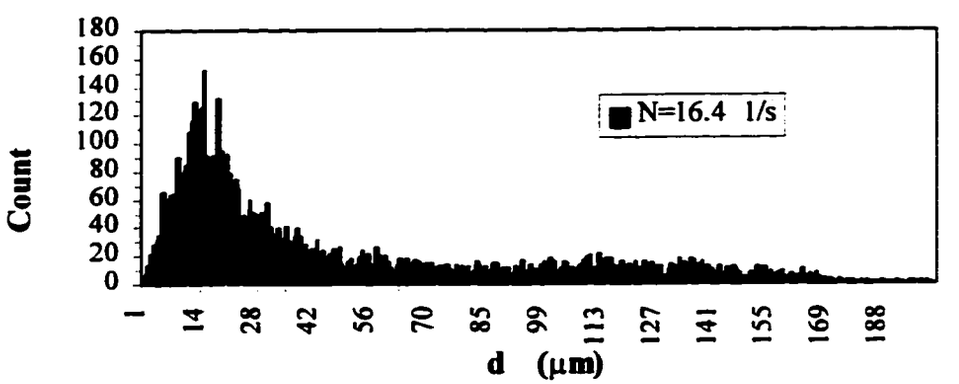

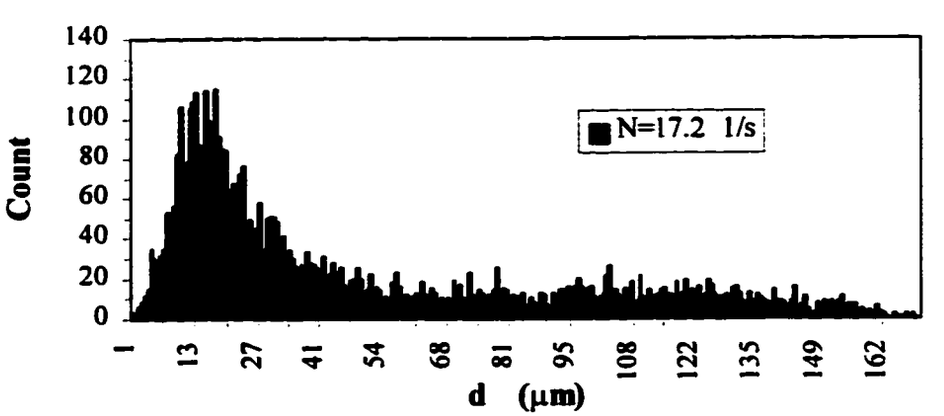

Cont'd **Figure A-1d**

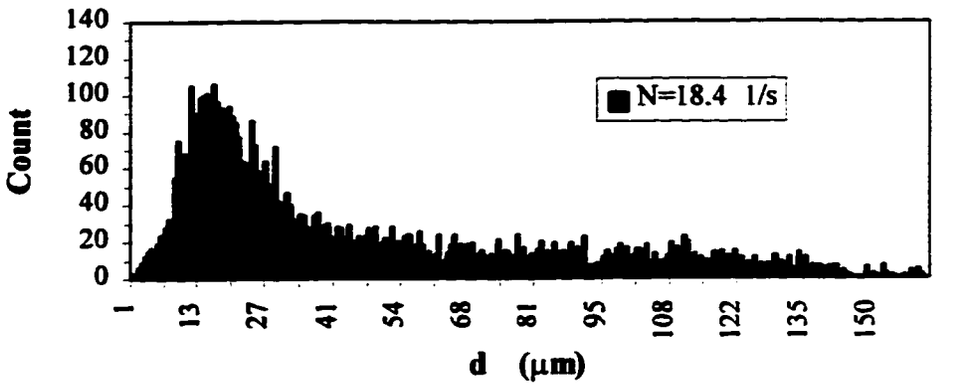

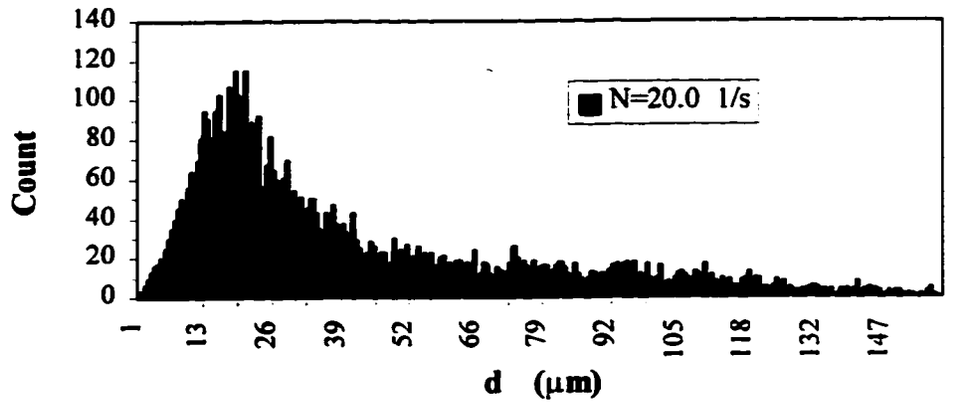

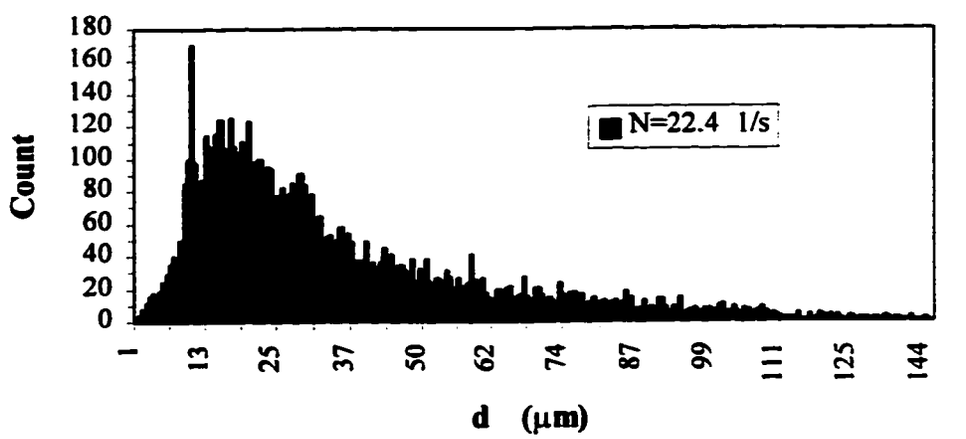

Cont'd **Figure A-1d**

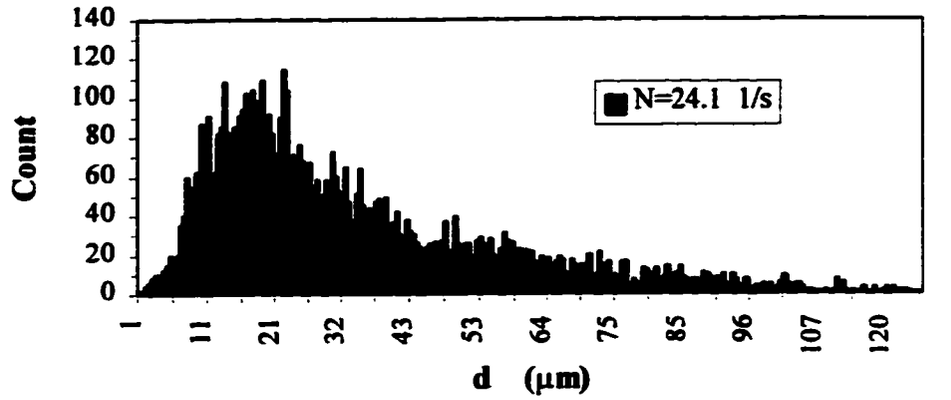

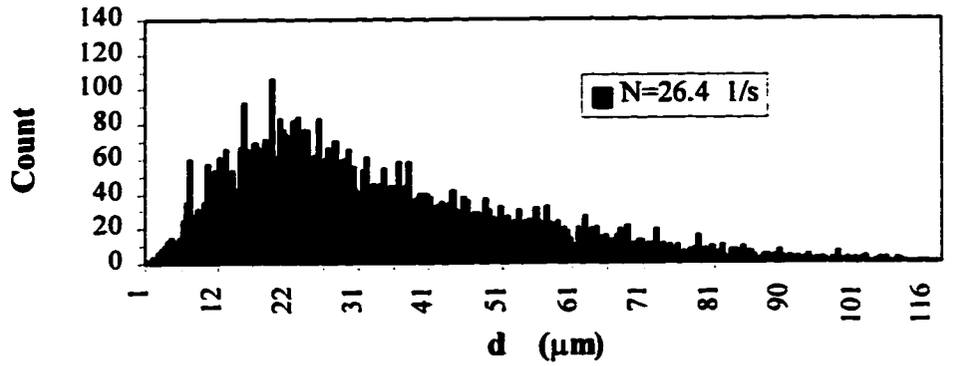

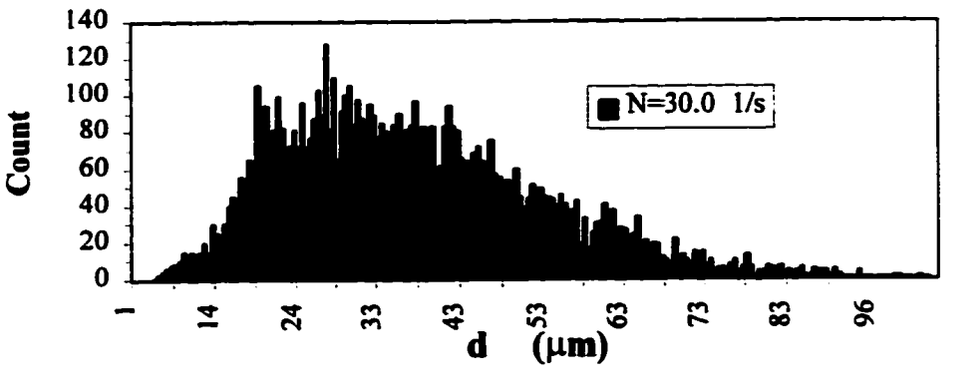

e) RT: D=T/4, C/D=1, 2r/D=0.70.

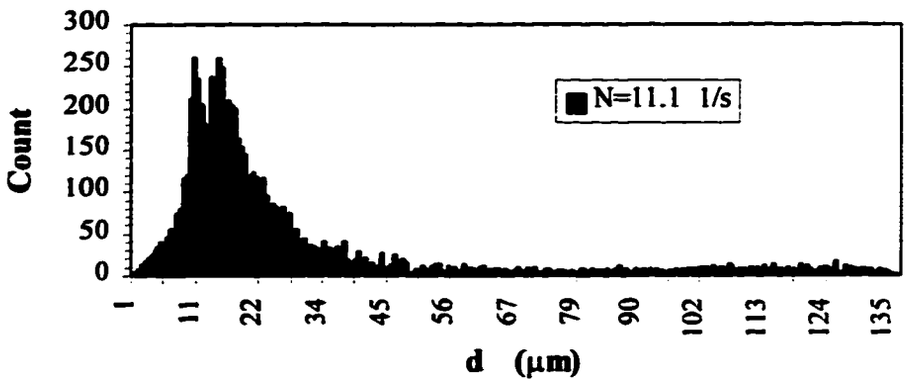

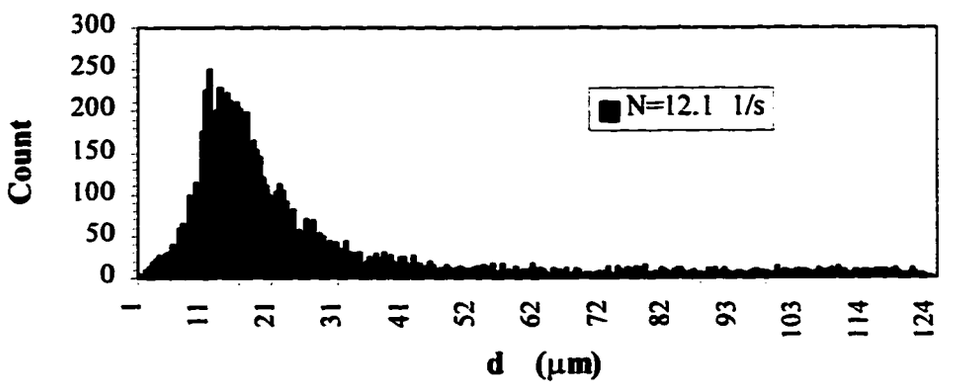

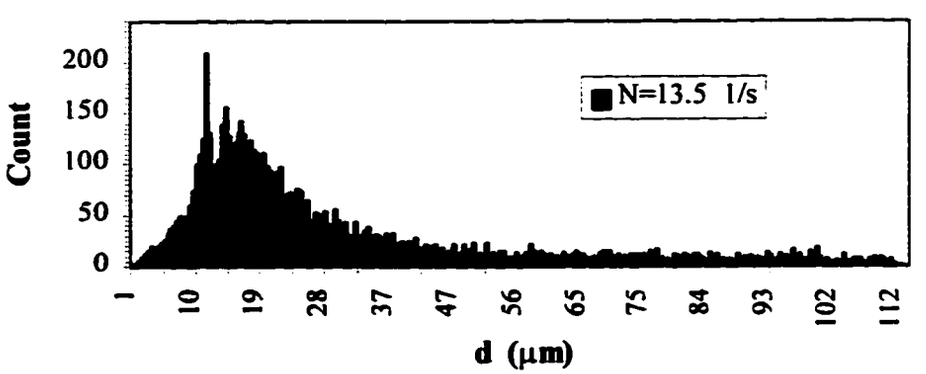

Cont'd **Figure A-1e**

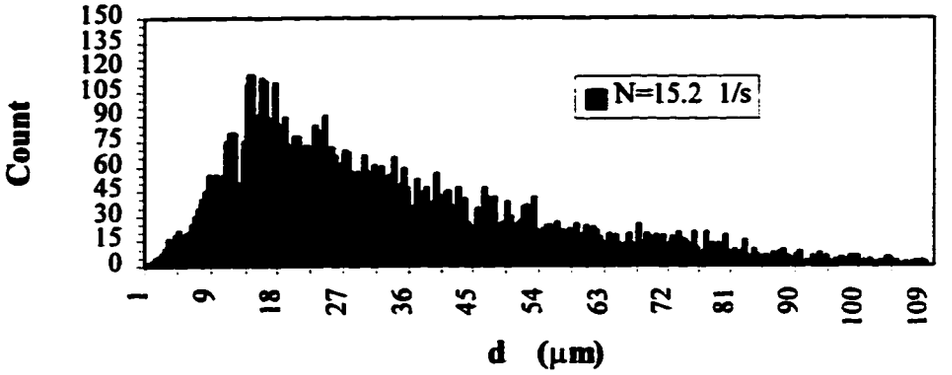

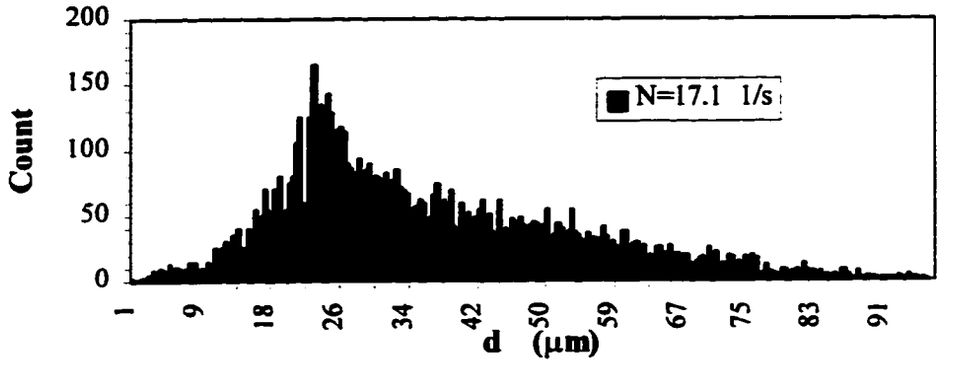

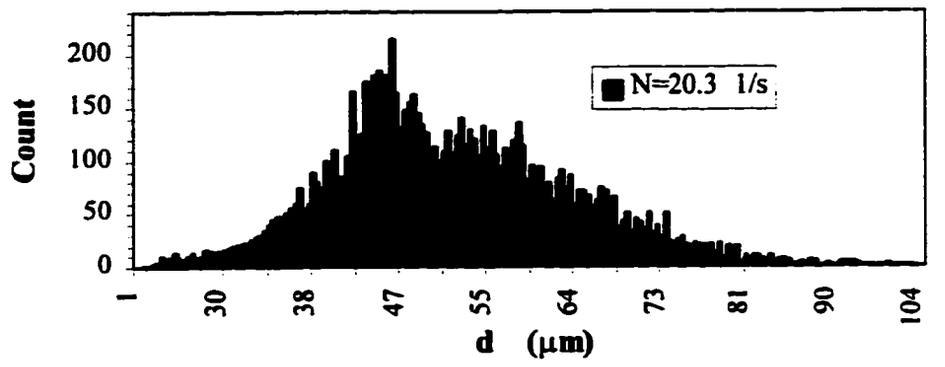

f) RT: D=T/4, C/D=1/2, 2r/D=0.30.

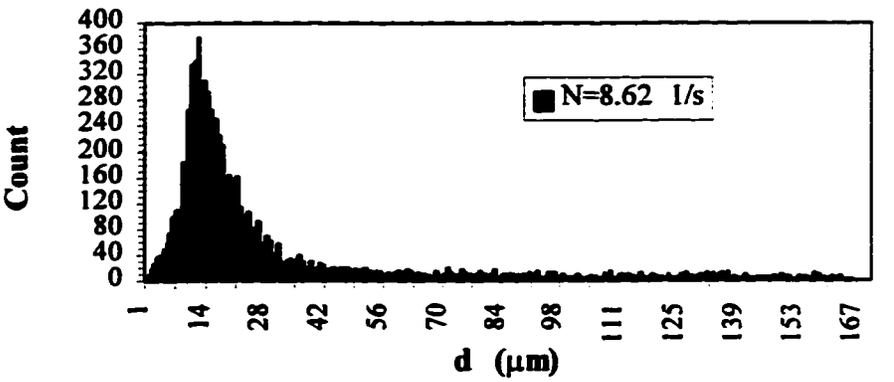

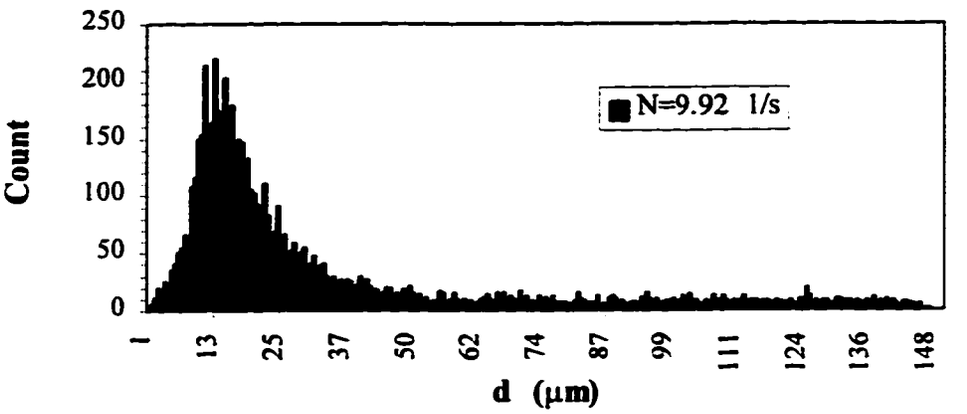

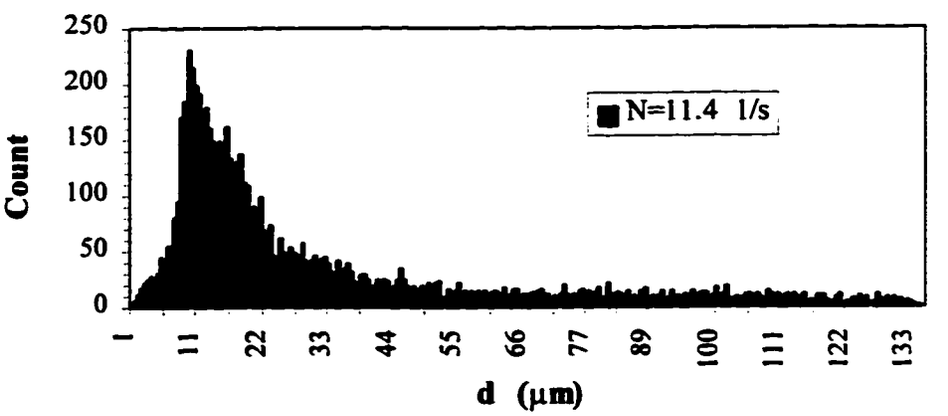

Cont'd **Figure A-1f**

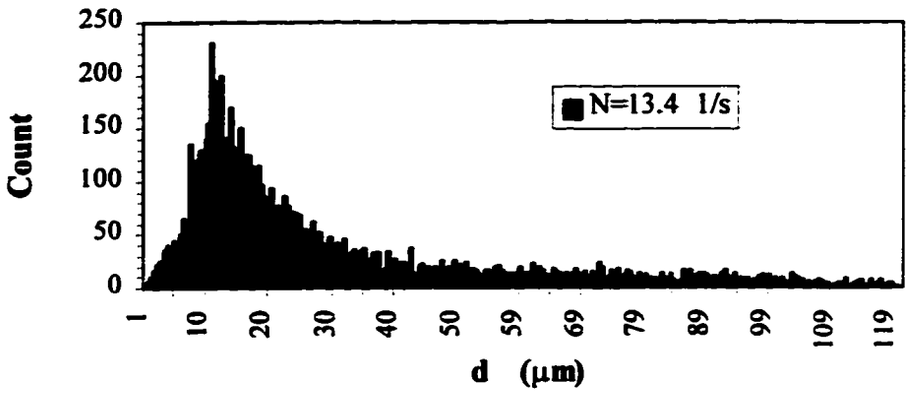

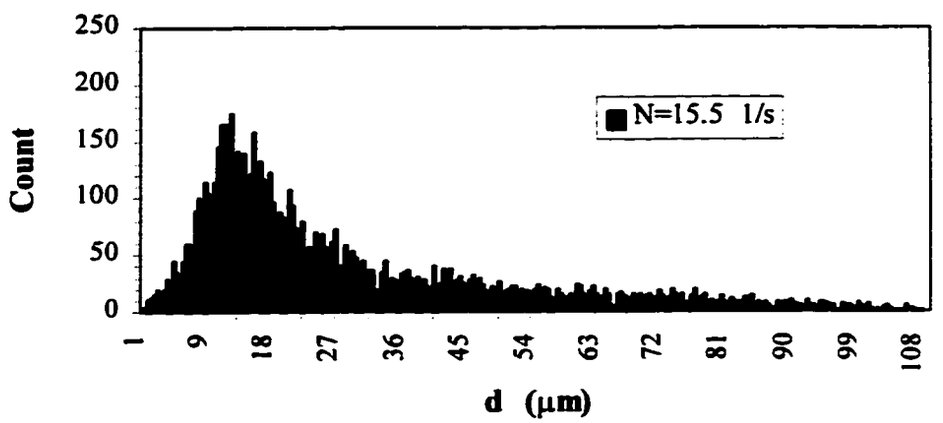

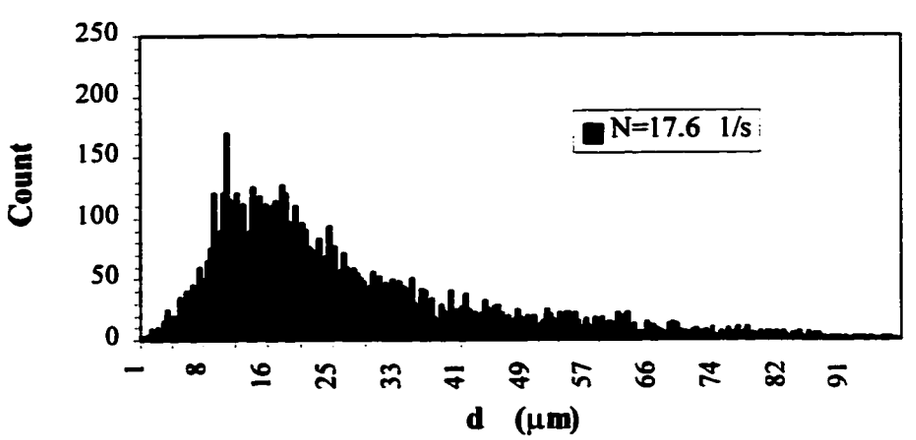

Cont'd **Figure A-1f**

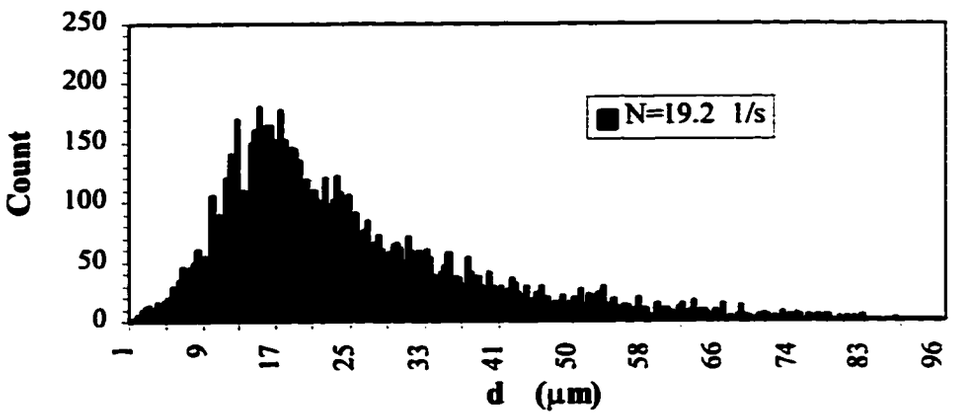

Appendix-2

Cumulative Number Probability Density Data

Figure A-2 Plots of cumulative number probability density vs d at different rotational speeds.

a) A310: D=0.350T, C/D=1, 2r/D=0.50.

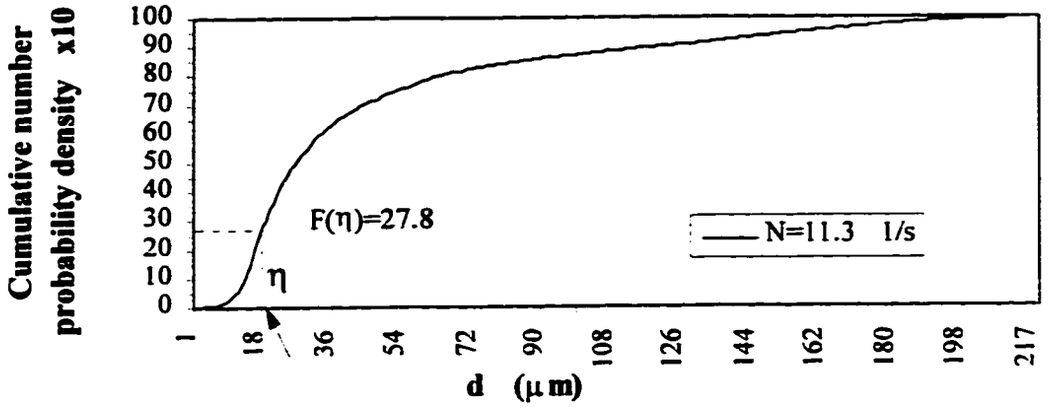

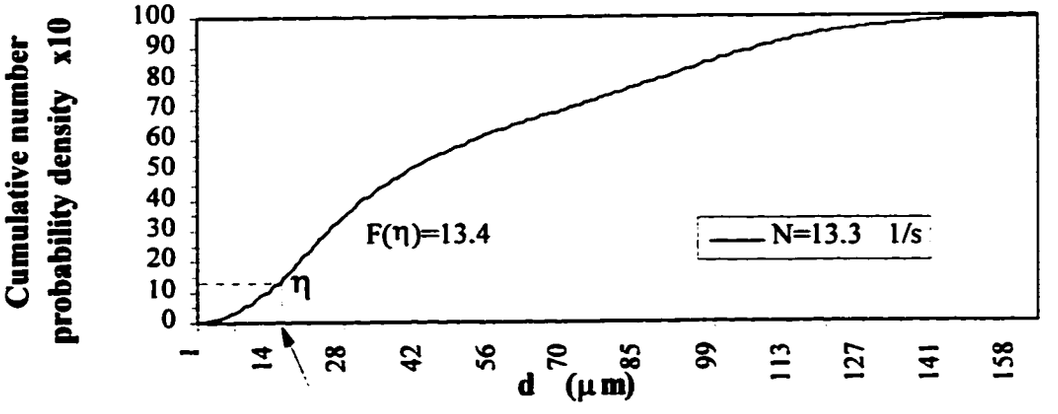

Cont'd **Figure A-2a**

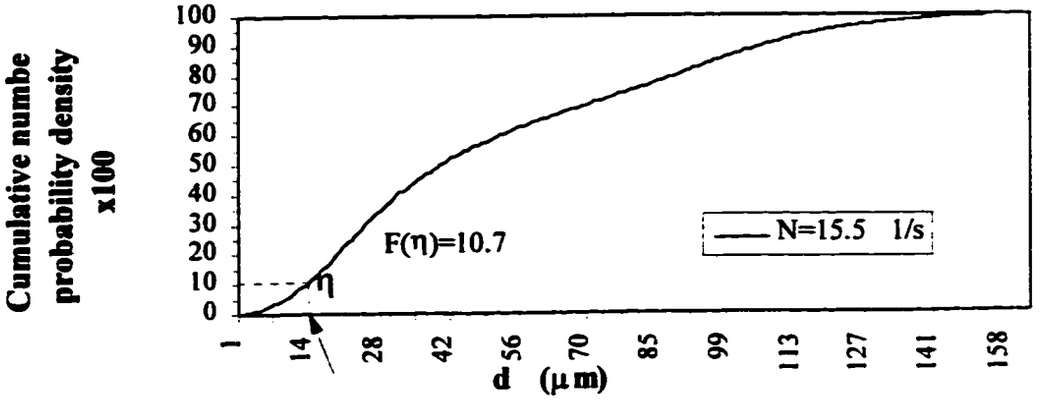

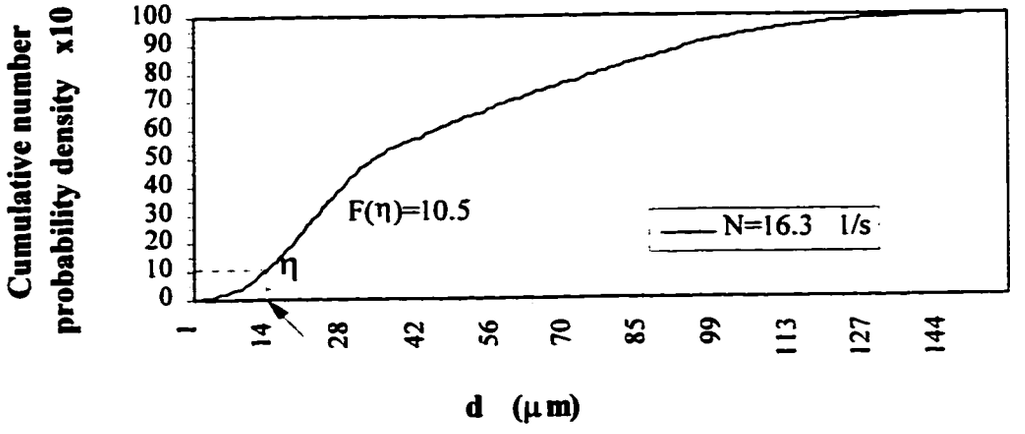

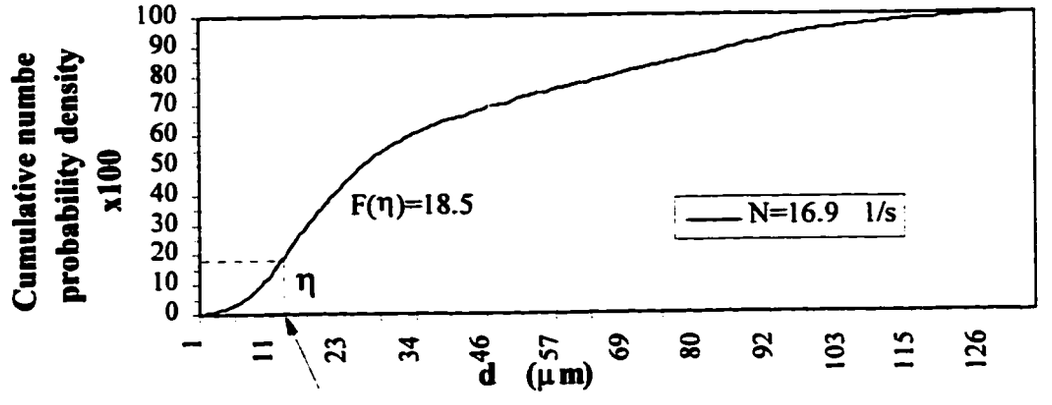

Cont'd **Figure A-2a**

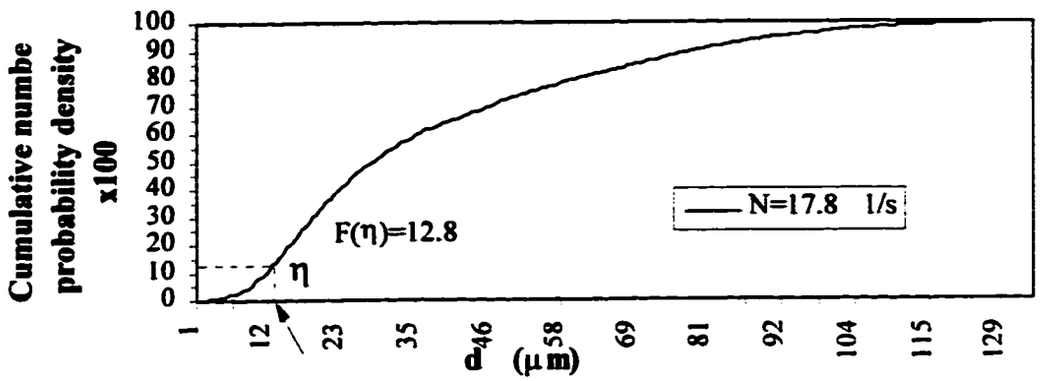

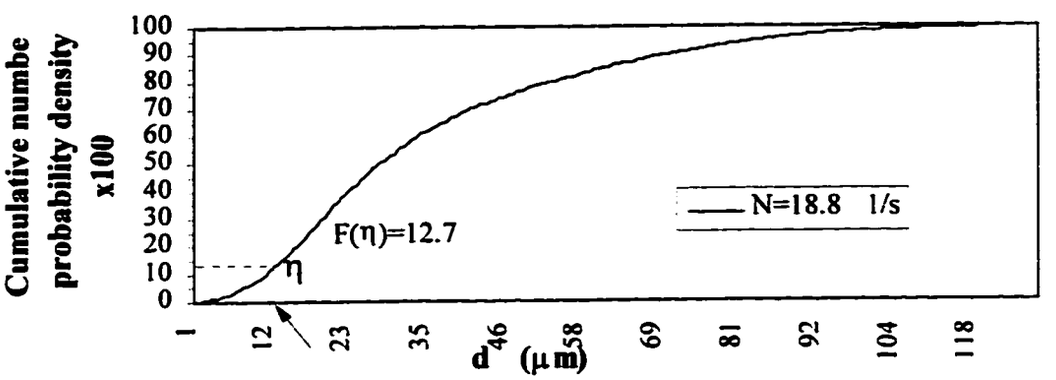

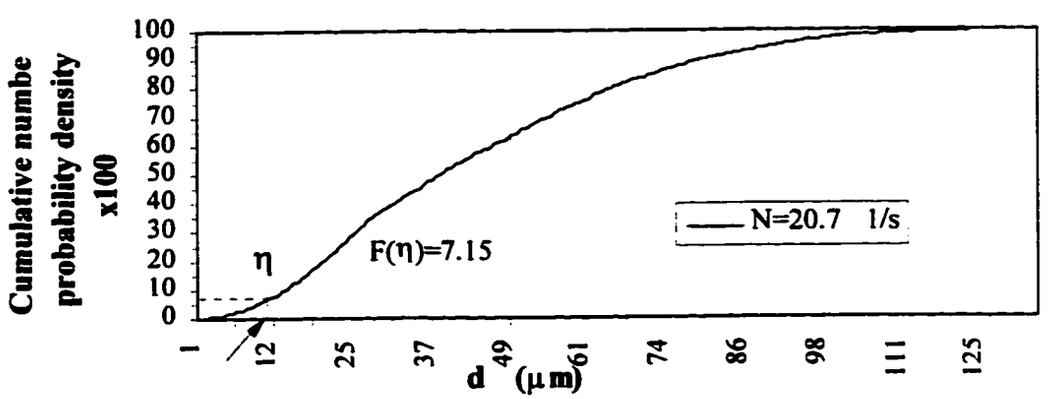

Cont'd **Figure A-2a**

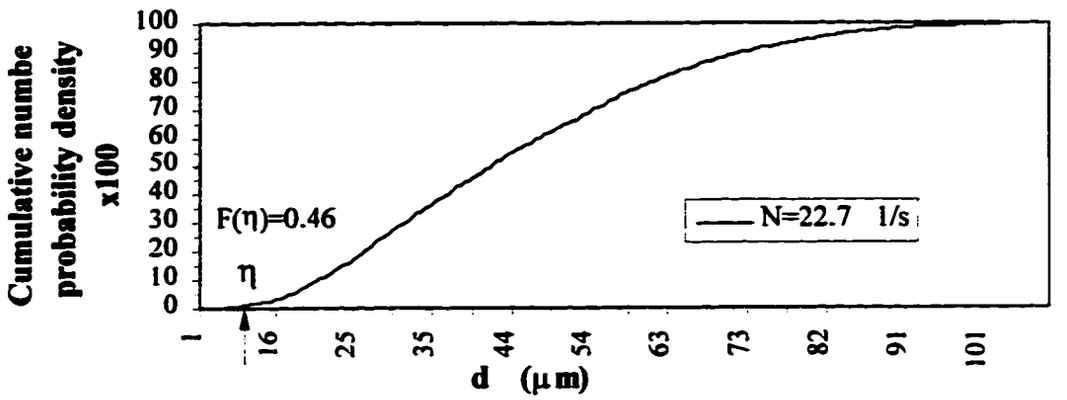

b) A310: D=0.350T, C/D=1/2, 2r/D=0.50.

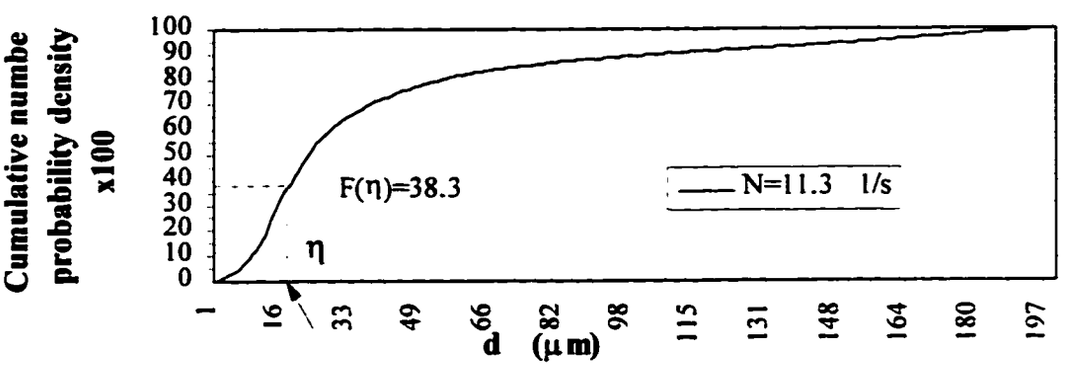

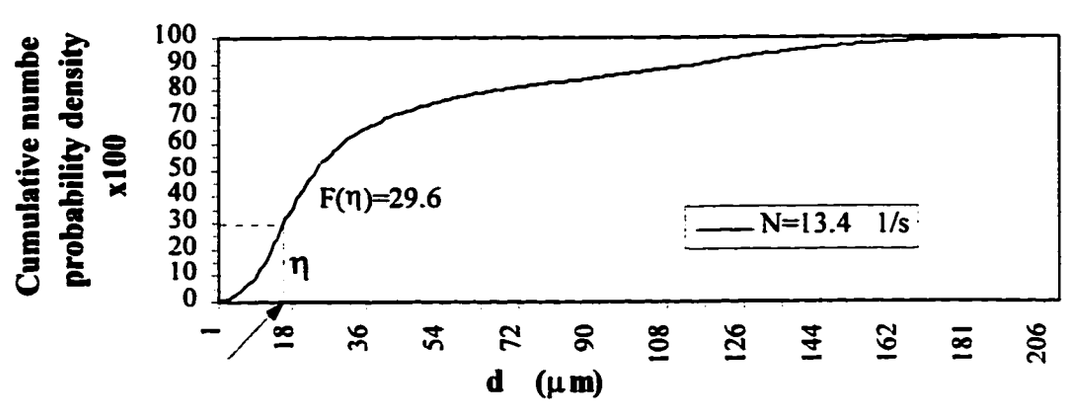

Cont'd **Figure A-2b**

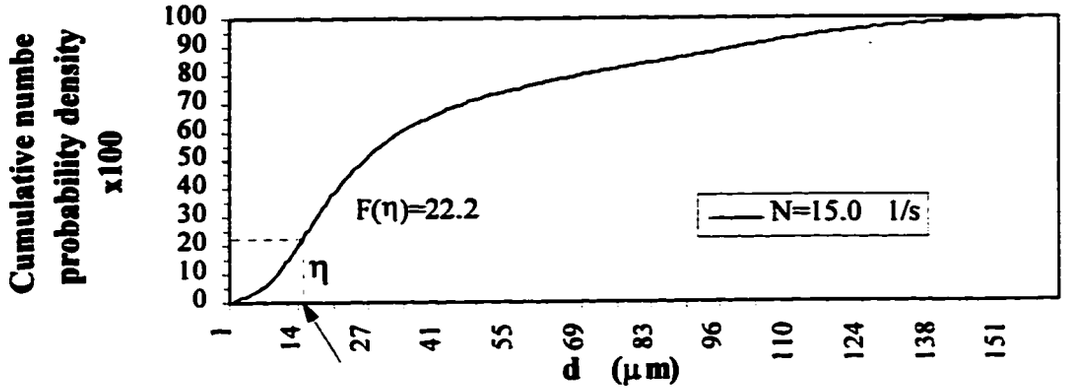

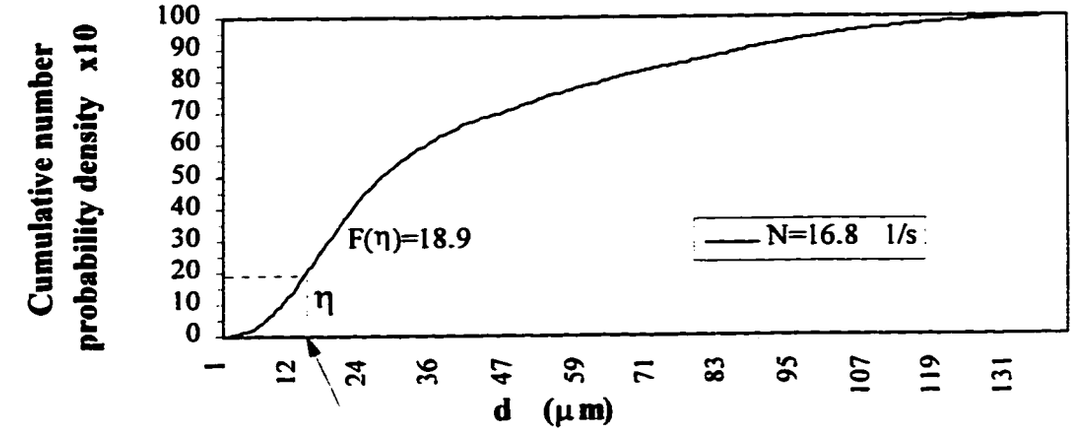

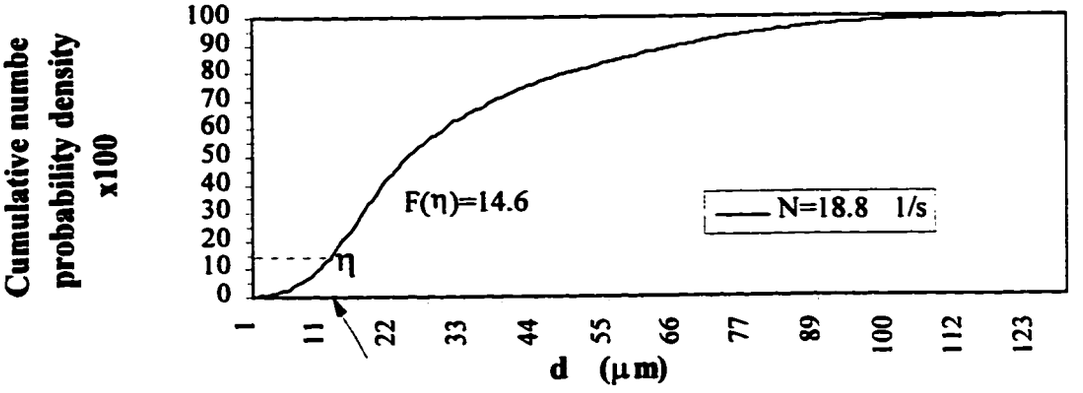

Cont'd **Figure A-2b**

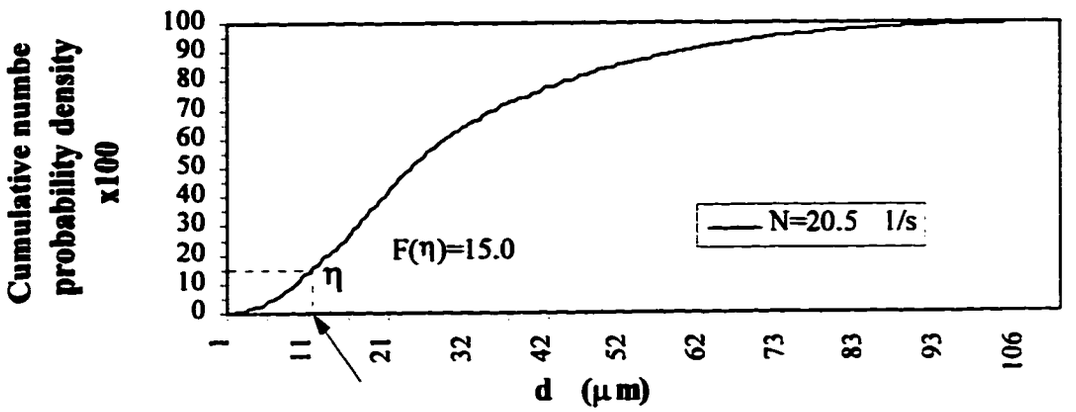

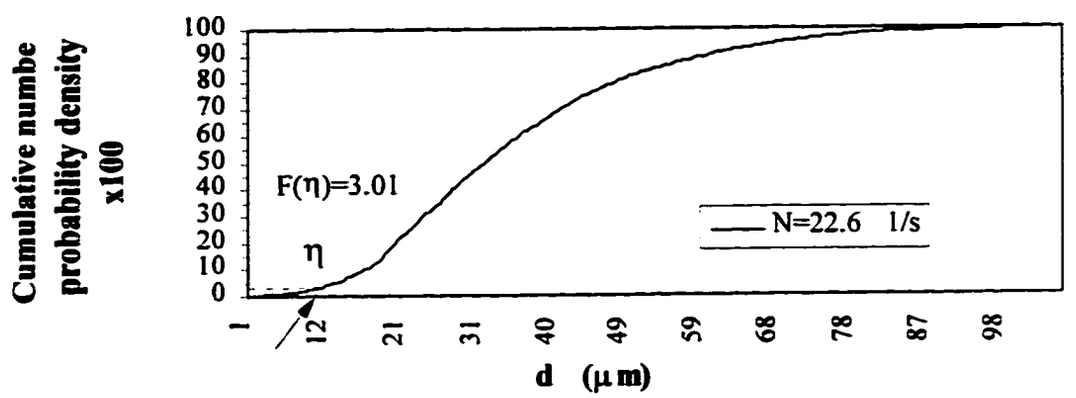

c) A310: D=0.550T, C/D=1/2, 2r/D=0.55.

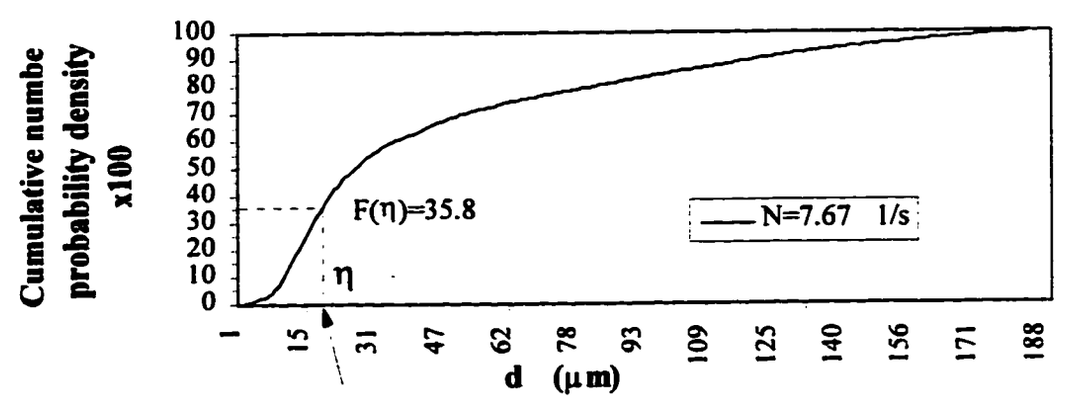

Cont'd **Figure A-2c**

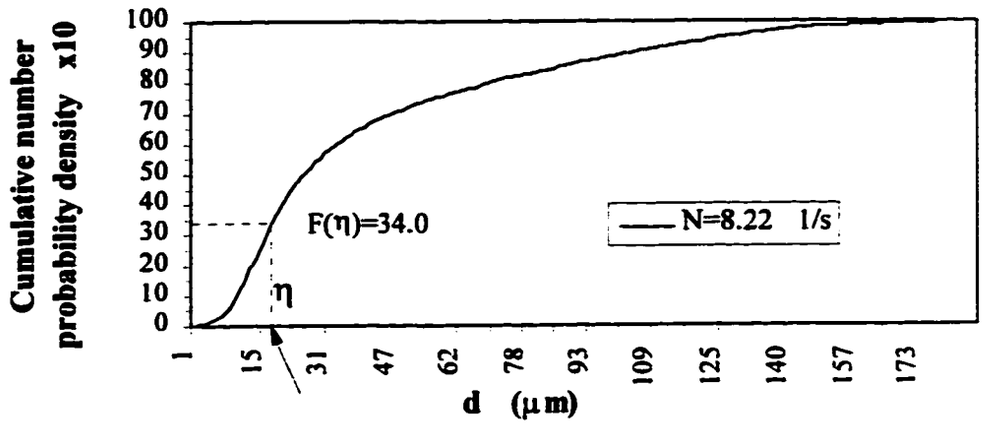

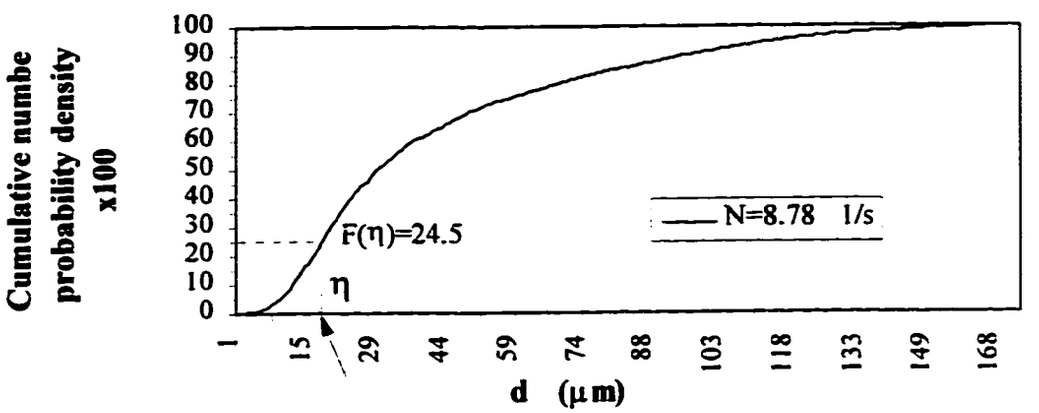

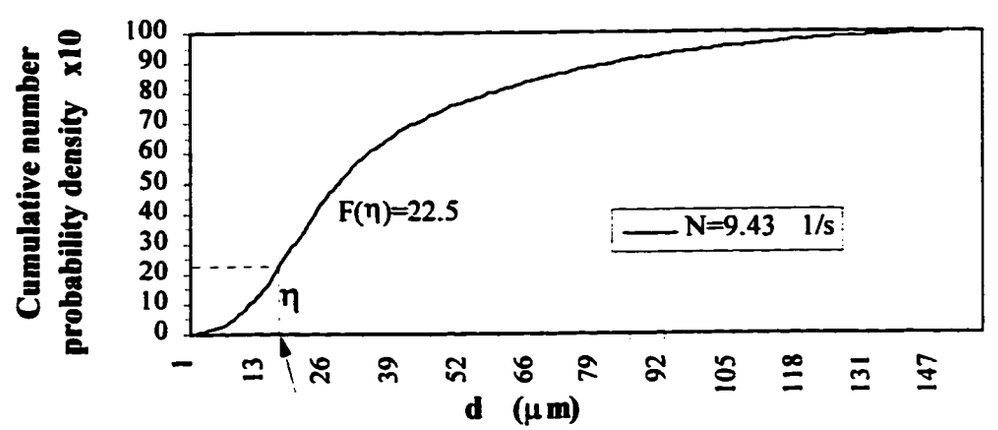

Cont'd **Figure A-2c**

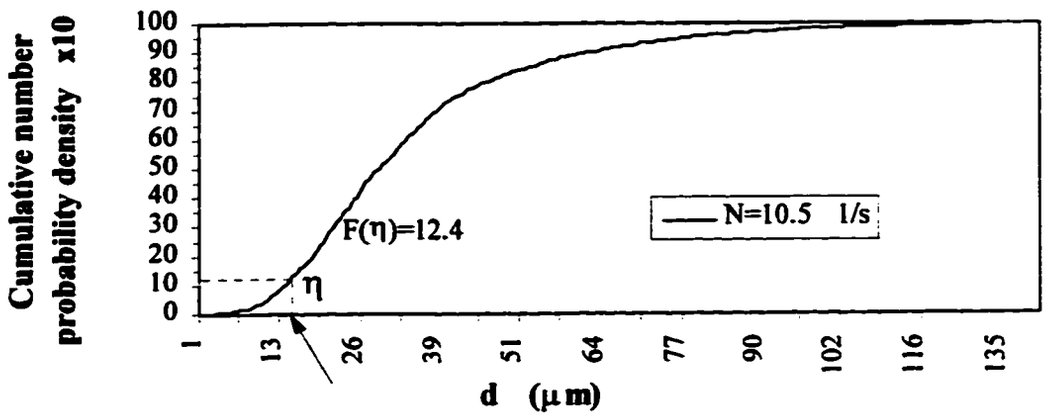

d) HE3: D=T/4, C/D=1, 2r/D=0.30.

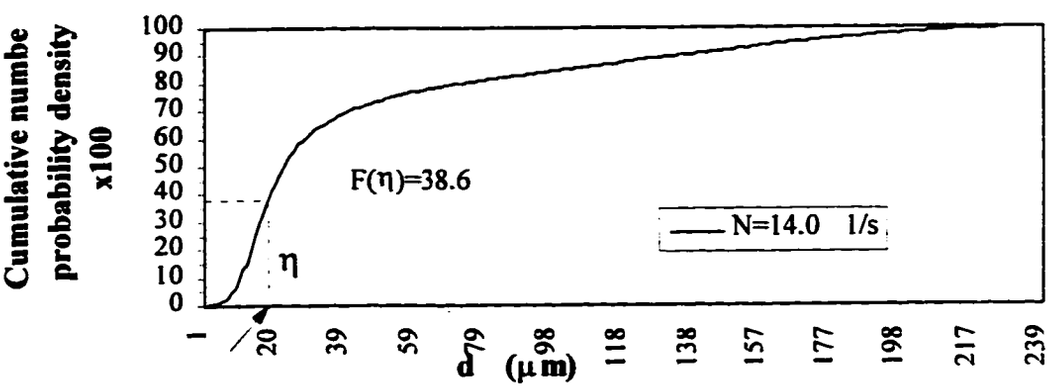

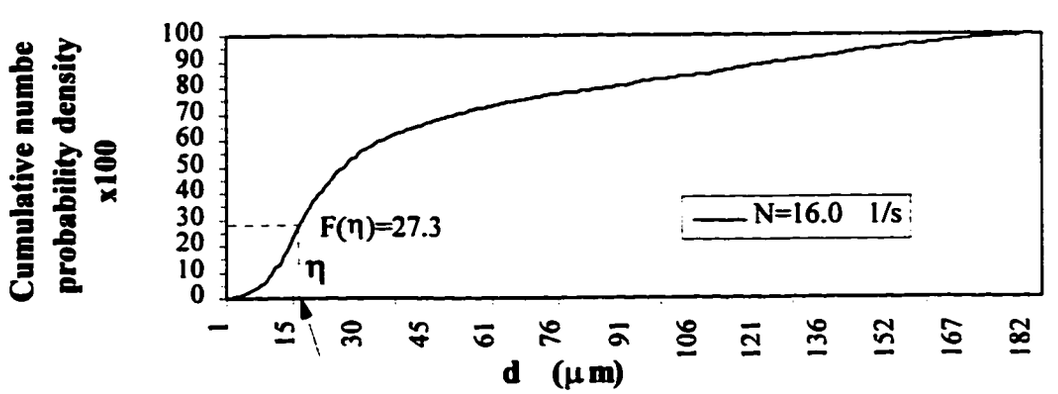

Cont'd **Figure A-2d**

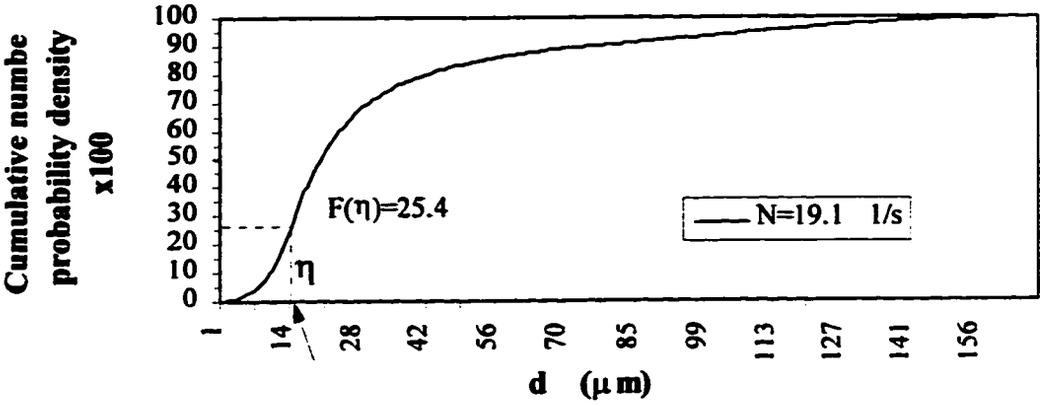

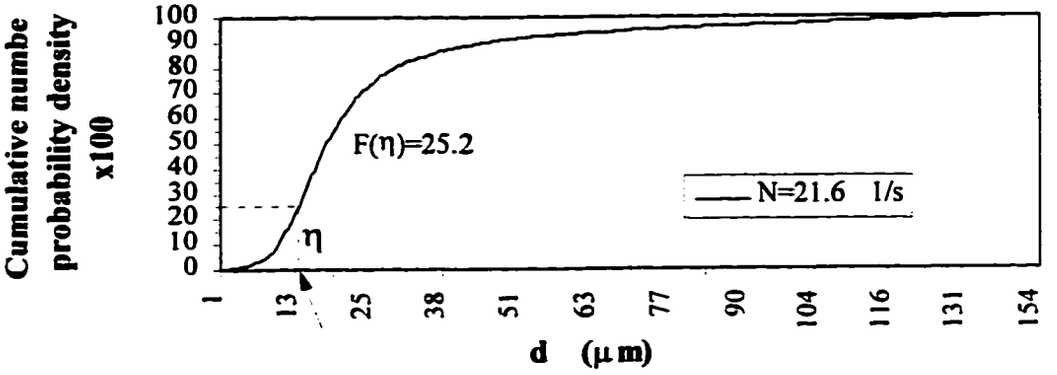

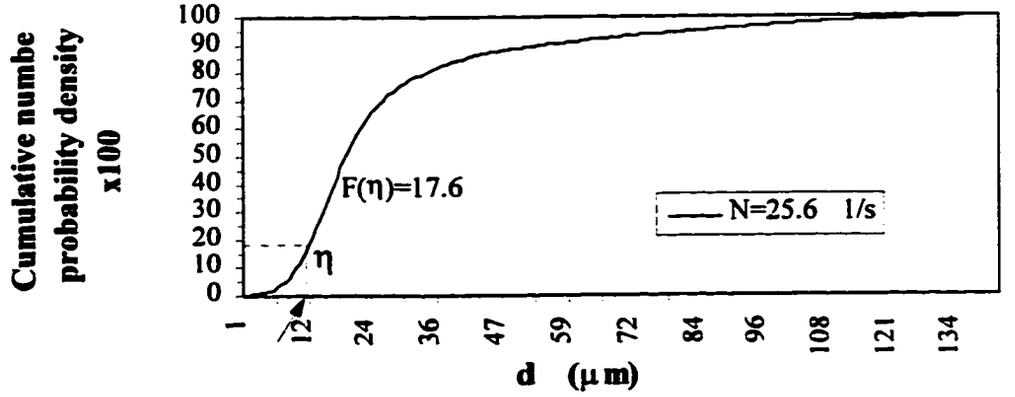

Cont'd **Figure A-2d**

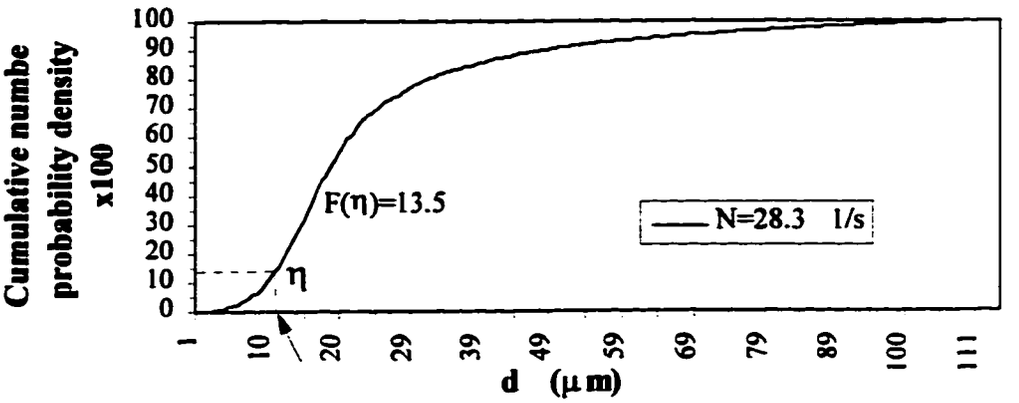

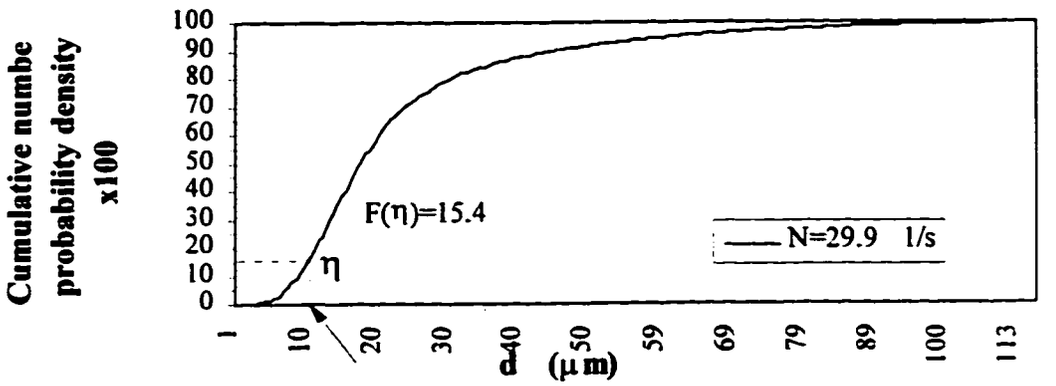

e) RT: D=T/4, C/D=1, 2r/D=0.70.

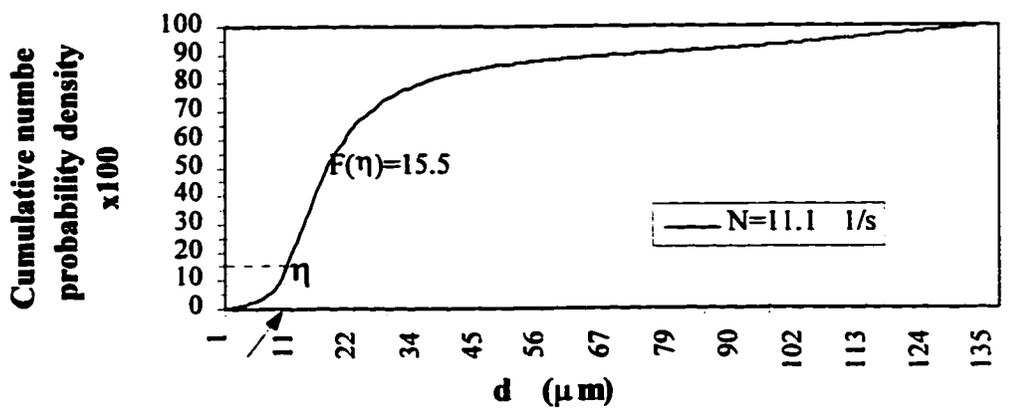

Cont'd **Figure A-2e**

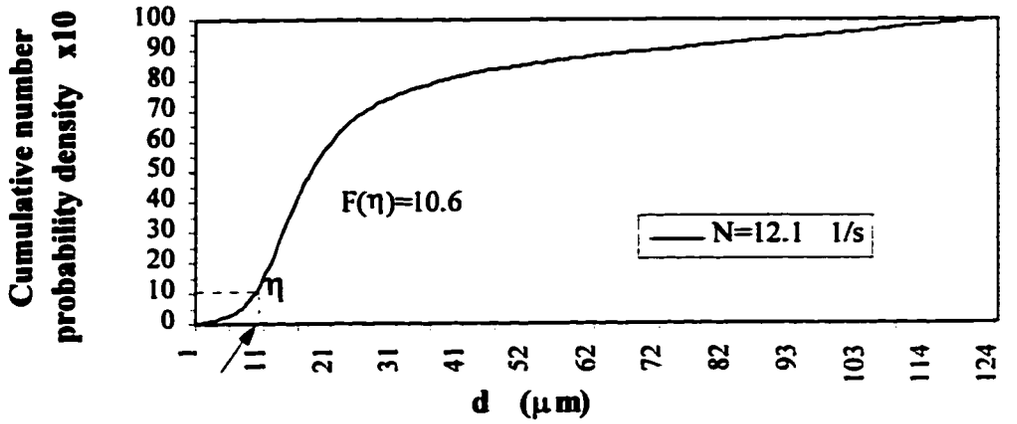

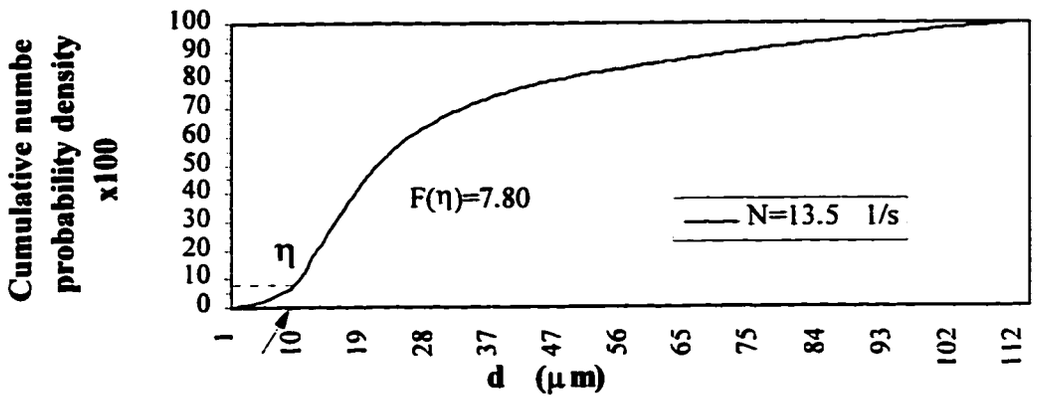

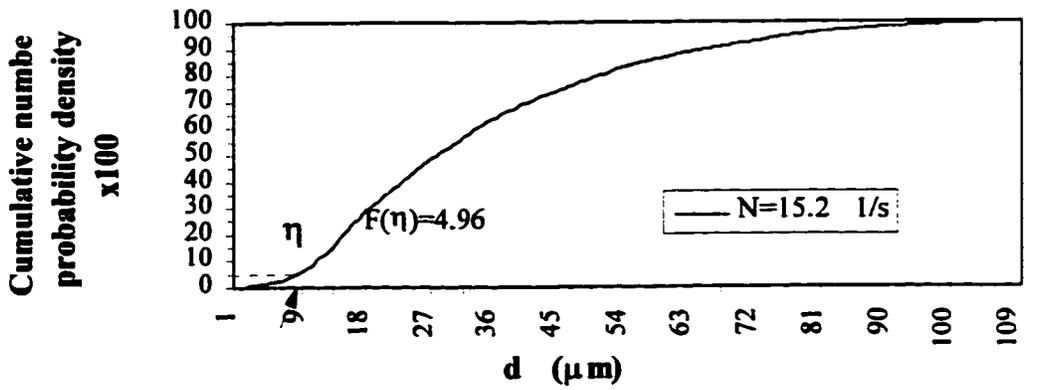

Cont'd **Figure A-2e**

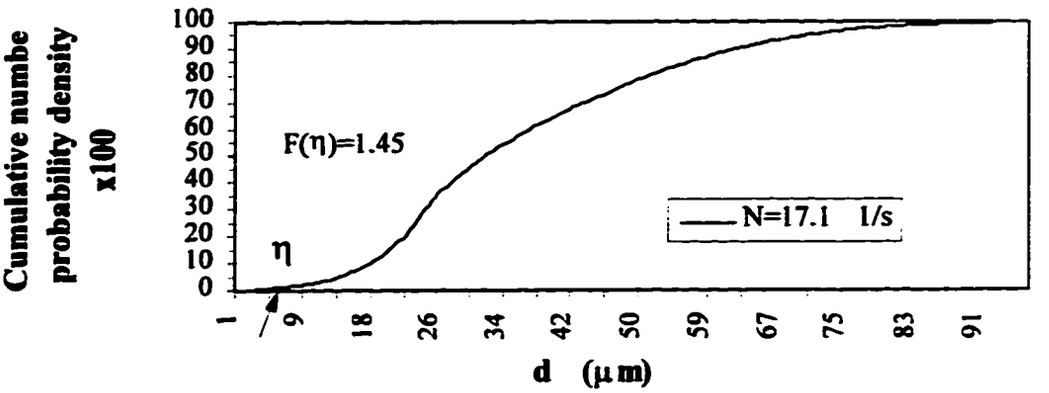

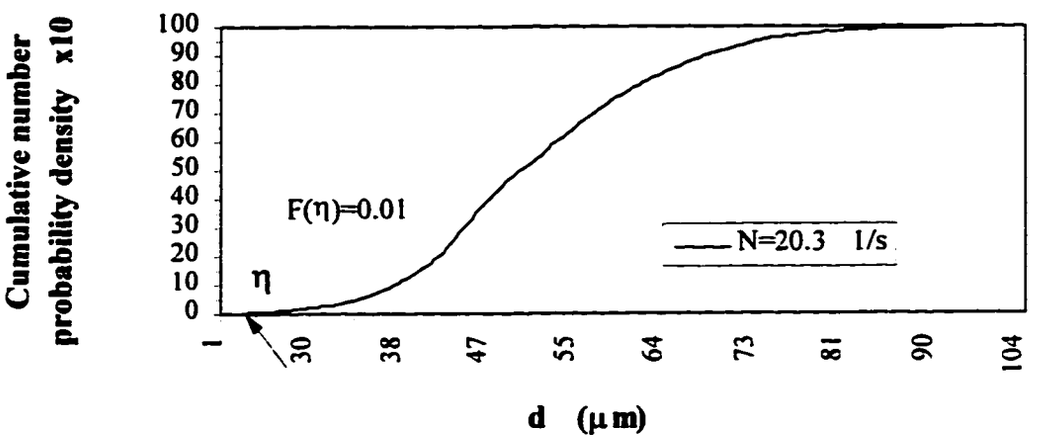

f) RT: D=T/4, C/D=1/2, 2r/D=0.30.

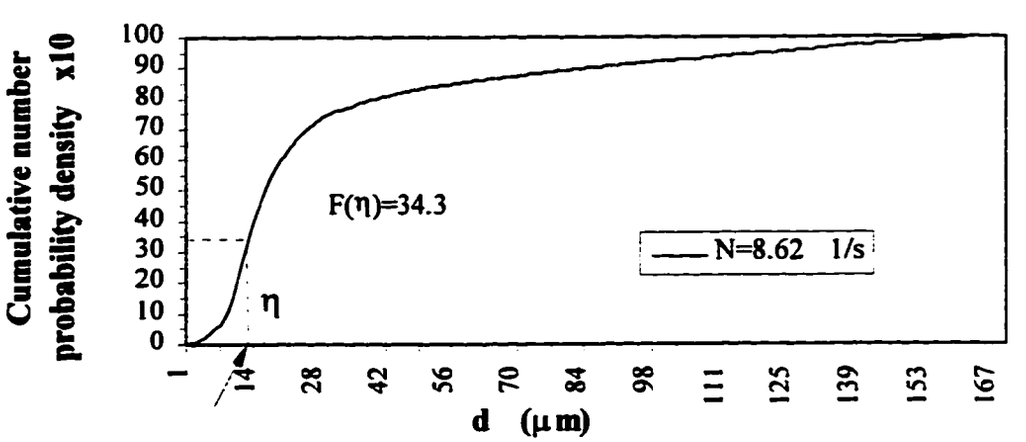

Cont'd **Figure A-2f**

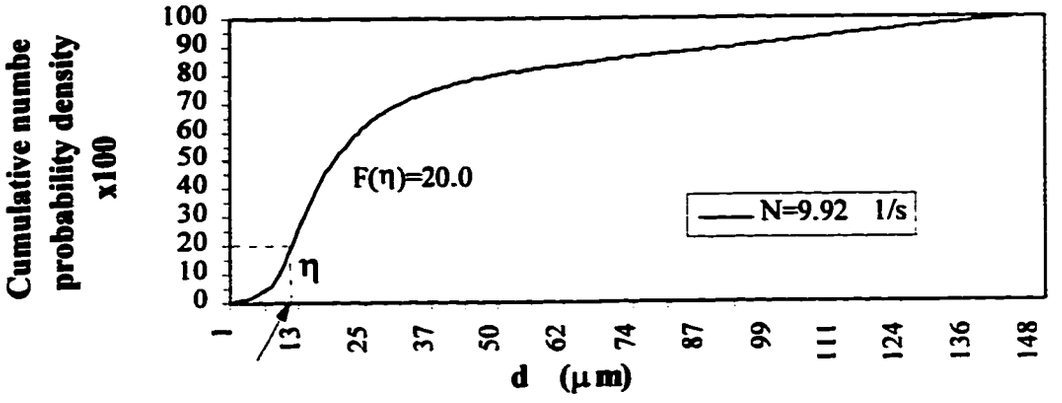

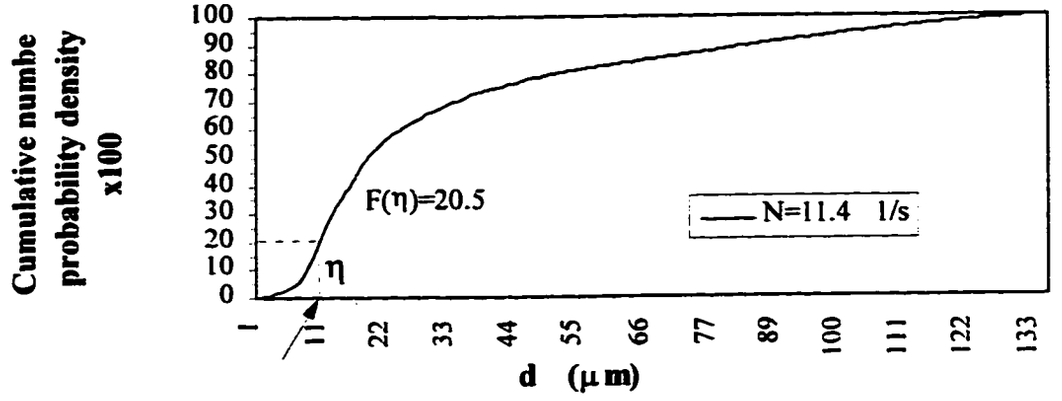

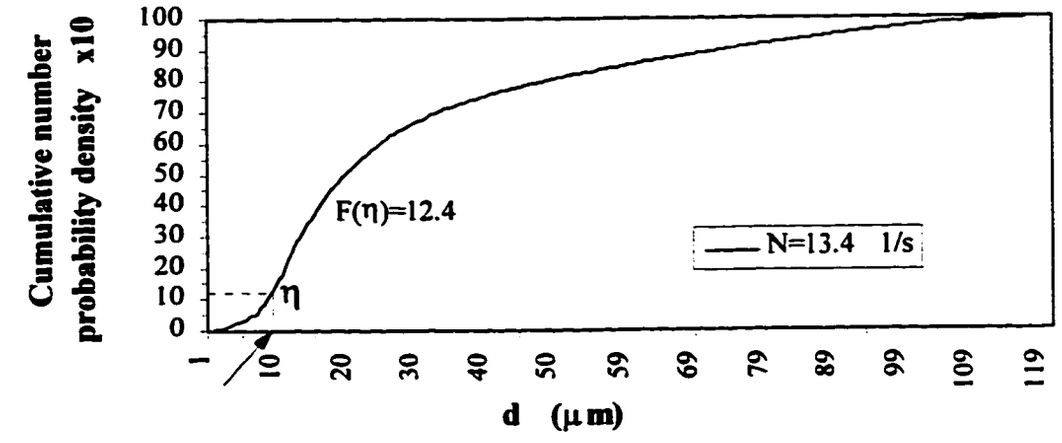

Cont'd **Figure A-2f**

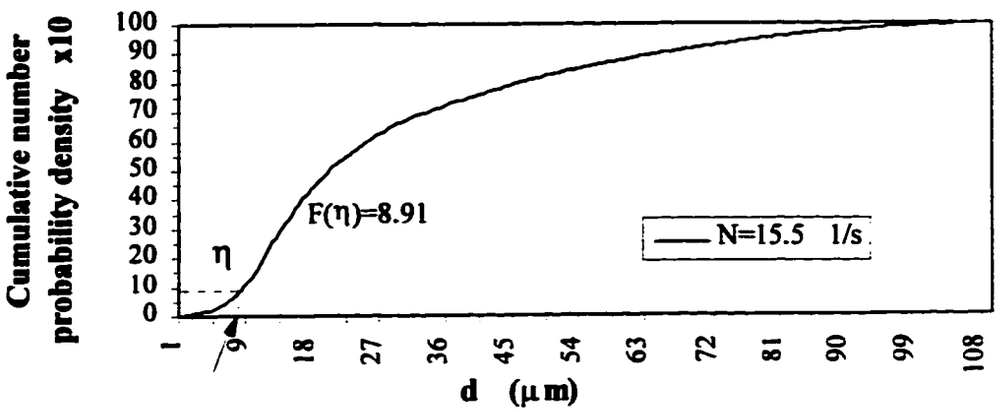

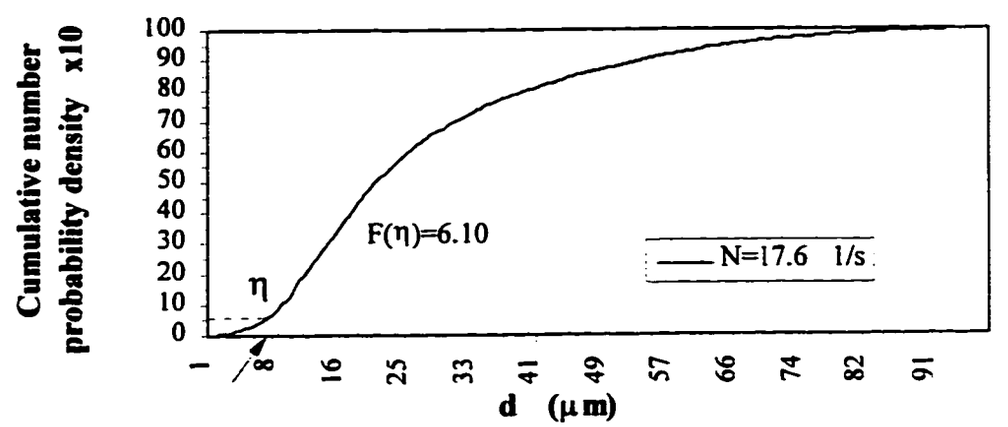

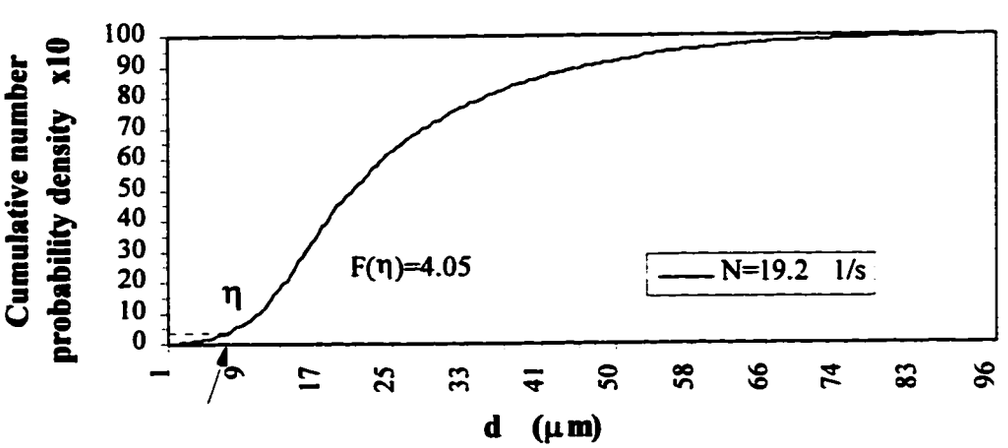

Appendix-3

Parameters of the Regression for Each Case

Table A-3.1 Parameters of the regression of d_{32} with tip speed (ND).

Impeller	Geometry		Regression equation			
	D	C/D	d_{32} (μm), N (s^{-1}), D (m)	α	β	R^2
A310	0.350T	1	$d_{32}=\alpha(ND)^{\beta}$	137.5	-1.4126	0.978
	0.350T	1/2		134.6	-1.5685	0.983
	0.550T	1/2		123.9	-2.0926	0.986
HE3	T/4	1		114.1	-1.3659	0.991
PBT	T/4	1		112.9	-1.445	0.990
RT	T/4	1		58.26	-0.9634	0.978
	T/4	1/2		54.71	-1.1233	0.989

Table A-3.2 Parameters of the regression of d_{32} with maximum turbulence energy dissipation rate, ε_{max}

Impeller	Geometry		Regression equation			
	D	C/D	d_{32} (μm), N (s^{-1}), D (m)	α	β	R^2
A310	0.350T	1	$d_{32}=\alpha(\varepsilon_{max})^{\beta}$	426.1	-0.4709	0.978
	0.350T	1/2		461.1	-0.5227	0.985
	0.550T	1/2		468.4	-0.6963	0.985
HE3	T/4	1		394.7	-0.4552	0.991
PBT	T/4	1		794.4	-0.4814	0.990
RT	T/4	1		361.0	-0.3212	0.978
	T/4	1/2		436.3	-0.3746	0.988

Table A-3.3 Parameters of the regression of d_{32} with $P/\rho V_T$

Impeller	Geometry		Regression equation			
	D	C/D	d_{32} (μm), N (s^{-1}), D (m)	α	β	R^2
A310	0.350T	1	$d_{32}=\alpha(P/\rho V_T)^{\beta}$	63.67	-0.4715	0.978
	0.350T	1/2		57.24	-0.5226	0.983
	0.550T	1/2		74.38	-0.6975	0.985
HE3	T/4	1		39.62	-0.4554	0.991
PBT	T/4	1		76.66	-0.4808	0.990
RT	T/4	1		70.19	-0.3194	0.978
	T/4	1/2		68.04	-0.3743	0.988

Appendix-4
Viscosity of Silicone Oil

Rheomat with MS-O115 — **Silicone oil @ 20 °C**

Setting	Speed (min^-1)	D (s^-1)	n % (mPa.s)	Reading (%)	Stress (mPa)	Viscosity (mPa.s)
Constants	⟹	4.439	14.786		65.64	
1	5.15	23	2.87	62	4070	178.01
2	7.37	33	2.01	87.5	5744	175.55
3	10.54	47	1.40	124	8139	173.95
4	15.09	67	0.98	177	11618	173.43
5	21.6	96	0.68	253	16607	173.19
6	30.9	137	0.48	361	23696	172.74
7	44.3	197	0.33	516	33870	172.23
8	63.4	281	0.23	740	48574	172.58
9	90.7	403	0.16	1052.5	69086	171.58
10	129.8	576	0.11	1247	81853	142.05
11	185.8	825	0.08			
12	266	1181	0.06			
13	381	1691	0.04			
14	545	2419	0.03			

Stress vs. Shear Rate

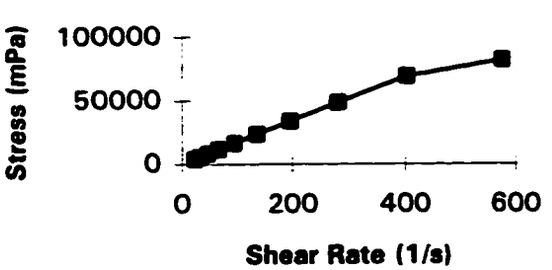

Stress vs. Shear Rate

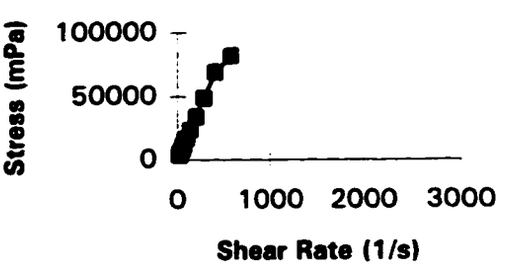

Viscosity vs. Shear Rate

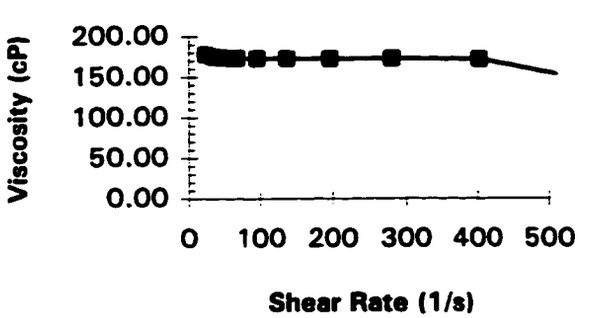

Silicone oil was bought from Aldrich Chemical Company, Inc..
Catalog No. 17,563-3

n_D^{20} 1.495

ρ 1.050

More information about this oil can be found on page 1252, in Catalog Handbook of Fine Chemicals, Aldrich (1994-1995).